MODELING, DESIGN AND CONTROL OF A SMALL MARINE CURRENT ENERGY CONVERSION SYSTEM

A thesis presented to the School of Graduate Studies of

Memorial University of Newfoundland in partial fulfillment of the

requirement leading to the award Doctor of Philosophy in

ELECTRICAL ENGINEERING

By

© MD NAHIDUL ISLAM KHAN

Department of Electrical Engineering

Faculty of Engineering & Applied Science

Memorial University of Newfoundland

Dedications

To my grandparents, parents and my loving daughter

Noshin Khan

Acknowledgement

I wish to thank all those who have contributed to my work and supported me during my work. This research was supported by an Atlantic Innovation Fund or AIF Grant for the 'Seaformatics' project. The project was also supported by a scholarship from the Research and Development Corporation or RDC.

I would like to thank my supervisor, Dr. Michael Hinchey for introducing me to the field of Marine Energy Technology, keeping me on the right track and also helping me in this research work when I was facing some unexpected challenges. His judicious suggestions made the successful completion of this dissertation possible. He has been the best possible mentor in every sense of the word. He initiated the founding ideas behind this thesis and provided insight and valuable information into many of the problems that were encountered. This thesis would not have been possible without him.

I would like to thank supervisory committee member, Dr. Tariq Iqbal for his advice, encouragement and unwavering optimism. His positive attitude throughout the duration of this thesis always put things into perspective whenever difficulties arose. Thanks also to supervisory committee member Dr. Vlastimil Masek for the support, funding and encouragement during my work.

I give my special appreciation to Dr. Azizur Rahman and Sheikh Rabbi for their help in setting up the simulations and experiments. Thanks to David Jones for careful proof-reading of my dissertation. I would like to thank the Technical Services staff, Ken Brown and Dave Snook, who manufactured the prototypes. Thanks also to Trevor Clark who helped me setup and test the models in the tow tank.

There are many other people that have contributed directly or indirectly to this thesis. Some acting as sounding boards, sources of information, or providing resources that contributed to the development of my electronics. While their individual contributions have been small, their efforts have still been greatly appreciated.

I would like to thank all my family members. My parents and grandfather deserve special recognition for their continuous encouragement and selfless support. I would like to also give thanks to my wife for whom the struggle was hardly less arduous, but suffered with good humor and unfailing support. I am very grateful to my daughter Noshin Khan. Her cheerful smile and lovely voice made my hard moments bearable. Lastly, and most importantly, I thank Almighty for His grace and love.

Abstract

The Seaformatics project is a five year AIF project that intends to develop wireless marine sensors for use in monitoring seabed processes. The sensor pods will be self-powered through ocean bottom currents and will be able to communicate with each other

This research is focused on development of a device to harvest energy from water currents near the ocean floor to power such seabed marine technologies. The research is very interdisciplinary in nature and involves design, structures, fluid dynamics, nonlinear control and power electronics, which makes it very challenging. A major outcome of the research is a robust small marine current energy conversion system that can extract power from the low marine current.

A prototype was designed and constructed. It was tested in the towing tank in the Faculty of Engineering at Memorial University of Newfoundland. Power output was controlled using a DSP PI controller. The device consisted of a watertight hull. An electric generator was installed inside the hull and the turbine rotor was installed outside. The rotor of the device has blades like conventional wind turbines but the blades face forward into the flow and not perpendicular to it. This unique arrangement of the blades ensures high starting torque even in low currents. It used simple flat plate blades. A unique magnetic torque coupler was used to connect the generator to the turbine. This used sets of magnets inside and outside that repelled each other. Besides acting as a coupler, this arrangement of magnets also acted as a bearing. Ideally, it would have been good to use a generator designed specifically for the device but that would have been expensive and beyond the project budget so we used a commercial generator. To increase the rotational speed of

this generator, a set of gears was inserted between the turbine and generator shafts.

Computational Fluid Dynamics analysis and Potential Flow Hydrodynamics Theory were used to study the hydrodynamics of the rotor. This allowed us to explore geometry variations too expensive to study experimentally. For example, it showed that curved blades would give significantly more power than flat blades.

This dissertation also presents an adaptive back stepping nonlinear maximum power point tracking (MPPT) control strategy for the system. Because of tow tank scheduling constraints, this was tested in simulation only. The proposed control strategy does not require any flow sensors and also does not need the parameters of a PMSG. A Lyapunov based online estimation approach is used to continually estimate the input voltage and the output load resistance of the converter. Detailed simulation results of the proposed adaptive back stepping control are presented and fully analyzed. Simulation results demonstrate that the proposed nonlinear controller can incessantly extract maximum power from the ocean current at various flow speeds.

Table of Contents

List of Figures

Chapter I

Introduction

1.0 Background

The Seaformatics project is a five year Atlantic Innovation Fund project that intends to develop to a proof of-concept seafloor array of wireless marine sensors for use in monitoring seabed processes, including applications such as geological imaging and earthquake detection. Individual low cost sensor pods will be self-powered through ocean bottom currents and will be able to communicate with each other and to the Internet through surface master units to facilitate observation of the ocean floor from shore.

Towards the end of the 1970s there was a significant interest in developing renewable energy sources. This interest resulted in research into several conventional turbines, such as the vertical axis Darrius rotor type, to experiment with different mechanisms for removing energy from fluid flows. There were also several novel designs developed from unsteady aerodynamic theory. For instance, Jeffery developed a model for a vertically-mounted pivoting wing which flapped in the wind. At around the same time Wilson and Lissaman at the National Research Council developed a cyclogryo-type device which, through articulation of pitch, was able to extract energy from the flow.

Currently most of the world's energy demand is met by fossil fuels with their attended devastating effects on the environment, most notably the emission of carbon dioxide (CO2) leading to climate change. According to the Kyoto agreement countries, agreed to reduce the emission of greenhouse gases to the atmosphere [1]. In additions according to

the International Panel on Climate Change (IPCC), atmospheric concentrations of CO2 resulting from burning of fossil fuels and deforestation have increased by more than one third in the past 150 years and are at the highest levels for at least the past 420,000 years (Singer 2003). Fossil fuels that took many years to be formed by geological processes are now being burned in one year. Therefore, efforts should be made to meet the present and future energy demands cleanly and efficiently. To provide a sustainable power production in the future, and at the same time respecting the Kyoto protocol, there is a growing demand for energy from renewable sources such as wind, geothermal, solar and ocean.

The oceans cover 75% of the world surface and as such ocean energy is a global resource. There are different forms of renewable energy available in the oceans, including waves, currents, thermal gradients, salinity gradients and tides. Ways to exploit these high energy densities resources are being investigated worldwide. Renewable energy sources, most notably, wind energy, solar energy and small scale hydro power schemes have undergone major developments. Their potential to meet the world's energy demand for the 21st century and beyond, cleanly, safely and economically is high. However, the intermittency and weather dependency of most of them still poses a challenge and calls for extensive and diligent research and development effort. One other form of renewable energy which has attracted great interest is marine current or tidal stream energy. This energy resource has a great potential to be exploited on a large scale because of its predictability and intensity.

1.1 Thesis Objectives

The 'Seaformatics' sensor pod consumes power in the range of 5~8 watts. The goal of the thesis project was to develop a power source for the pod. Power generation in harsh

seafloor conditions is the major challenge. Batteries cannot store power for a long time. Closed cycle engines need storage of fuel and oxygen for a long time that is not possible in seafloor conditions. Light often does not reach that area therefore photovoltaic is not an option. Temperature differential is nominal, therefore ocean thermal energy cannot be exploited. The only remaining options are wire linked floating wave energy converter and ocean current converter. A fundamental requirement for the success of the power system is the presence of ocean currents of sufficient velocity near the seafloor to permit self-contained energy generation. The objectives of this research is to design, fabricate and test an autonomous, lightweight, low-cost, pressure-resistant energy generation system which can optimize power 'harvesting' from ocean current sources and deliver electric power to the communication pod.

This work also presents modeling, control and experimental testing of a standalone marine current energy conversion system. The energy conversion system consists of a marine current turbine, a surface-mounted slow speed permanent magnet synchronous generator, magnetic coupler, gearbox, rectifier, dc-dc converter. In this research a multi-bladed horizontal axis turbine has been designed to provide sufficient starting torque for the generator, and also to harness the required power from the marine current at low velocities. The performance analysis of the turbine has been studied using computational fluid dynamics (CFD). The complete marine energy conversion system is developed and simulated in Matlab/Simulink for various flow speeds. The mathematical modeling of permanent magnet synchronous generator, rectifier and the dc-dc converter has been combined to analyze the conversion unit. The design of a repulsion-type magnetic coupler with Nd-B-Fe permanent magnets has been built for non-contact integration

between turbine and generator. Because of the inclusion of a magnetic coupler, the system does not need any mechanical bearings, and also becomes more compact, robust and water insulated as there is no protruding part of the shaft.

Maximum power point tracking (MPPT) is indispensable for stand-alone energy conversion systems. Many researchers have proposed various control strategies for extracting maximum power from PMSG based energy conversion systems. Most of their control strategies use linearization approach that results in reduced system reliability and poor tracking performance. Few researchers have applied adaptive nonlinear control techniques like passivity based control, sliding mode control, artificial neural networks, fuzzy logic etc. to incorporate the nonlinearity into the overall system dynamics and also to reduce the total number of sensors. However, their control strategies require estimated values of specific parameters (d-q axis inductances) of a PMSG that sometimes are not readily available and also make the overall control methods very complicated. Their control approaches require the application of a flow sensor or a predictive resource modeling and also require fast powerful processors. However, a fundamental requirement in marine current energy conversion system is not to have any external rotatory parts such as flow sensors, protruding part of the shaft, etc. in order to make the system more compact and more insulated. Application of traditional control methodologies found in the literature does not meet the requirements of highly reliable and efficient marine current energy conversion systems.

In very recent years, sensorless maximum power point tracking control using a switch mode rectifier for variable speed permanent magnet synchronous generator (PMSG) based stand-alone wind energy conversion systems has been proposed by many

researchers. In their control approach, a linear proportional integral (PI) control has been used to regulate the duty cycle of a dc-dc converter. Although their control technique does not require the parameters of a PMSG, it does not consider the system nonlinearities into account.

A small scale laboratory prototype (MCECS) has been developed and tested in a flume tank. Proportional Integral (PI) based sensorless maximum power point tracking (MPPT) control algorithm has been implemented in real time using digital signal processing board DS1104. The stability of the overall system has been also studied. Although the classical control technique does not require the parameters of a PMSG but cannot take into account the system nonlinearities. This research work also proposes a simplified online estimation based adaptive backstepping based maximum power point tracking control algorithm. The proposed controller takes into account the uncertainties of change in parameters and system nonlinearities.

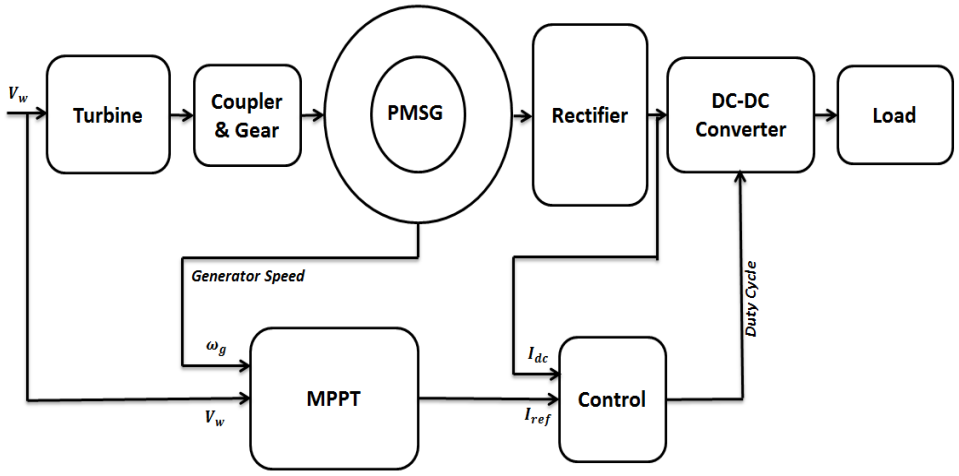

Fig. 1.1 Block diagram of Marine Power Conversion System

Fig. 1.1 represents the block diagram of the proposed model. The following are the objectives of this research to develop such a system are:

1. System sizing based on the resource available (1.25m/s).

2. Design of an efficient turbine responsive to low marine current and can extract 20W at 1.0m/s.

3. Integration of a suitable generator that can convert mechanical power into usable electrical power.

4. Design of a simple, compact marine energy conversion system.

5. Design of a maximum power point tracking (MPPT) control strategy based on two types of classical and nonlinear control.

6. Develop a simulation model of the MCECS to analyze system behavior.

7. Testing of the prototype in the tow tank at different flow speed.

1.2 Outline of Thesis

This thesis is made up of eight chapters. A brief description of the content of each chapter is as follows:

Chapter I give a background to marine current energy. The need to meet increasing energy demand cleanly and safely was highlighted. The marine current resource, the technology status and challenges were briefly discussed resulting in the definition of objectives of this thesis.

Chapter II focuses at more detailed study of the marine current resource dynamics and estimation making reference to past studies. The mode of operation of the technologies is highlighted. Prototypes undergoing testing and refinement were also discussed briefly and the enumerating engineering challenges facing them.

Chapter III illustrates the design of different types of water turbine that includes both vertical and horizontal axis turbine. It also illustrates the complete design of marine current energy conversion system.

Chapter IV deals with developing a mathematical model of the proposed energy conversion system and the device performance analyzed based on the simulation results. The chapter illustrates theories to develop a numerical model of water current turbine. It deals with the development of a Matlab/ Simulink® model of a marine current turbine system through the modeling of the resource, the rotor, and the generator.

Chapter V proposes a series of control strategies for maximum power point tracking algorithm. It also illustrates online estimation based adaptive backstepping MPPT controller

Chapter VI shows the simulation results of the proposed model. The performance evaluation of the turbine is conducted using computational fluid dynamics. It describes the main results, based on the developed marine current turbine simulation tools, and is presented along with illustration by case studies and Matlab/Simulink® simulation assessment.

Chapter VII presents the testing results of the prototype in the tow tank facility.

Chapter VIII presents the overall research summary and also some notes for future work that could be carried out for a better understanding of the various aspects involved in the marine current energy conversion process.

Chapter II

The Energy Potential of Marine Currents

2.0 Introduction

Tidal currents are recognized as a resource to be exploited for the sustainable generation of electrical energy. As with all energy generation developments they have to be considered and analyzed in entirety; energy, economics and environmental concerns.

2.1 Marine Currents

Oceans of the world can be regarded as an abundant source of energy. A portion of the total energy from the oceans is due to the marine currents including tidal currents, currents caused by salinity or temperature gradients, and/or the Coriolis effect caused by the earth's rotation [11]. Generally the water current movements are slow but the seabed topography can increase the current velocities to up to 7 m/s [12], particularly between islands and the mainland, around ends of headlands and in river estuaries.

The current velocity is an important factor in the design of a marine current power plant, because it sets the limits for both the power output as well as the forces acting on the turbine and support structures. The available power from the ocean increases rapidly with increasing current velocity. It can be assumed that approximately 75 percent of the energy is found in the upper 50 percent of the flow [13].

2.2 Tidal Currents

The global marine current energy resource is generally driven by the tides and to a lesser extent by thermal and density effects. The tides cause the water to flow inwards twice

each day (flood tide) and seawards twice each day (ebb tide) with a period of approximately 12 hours and 24 minutes (a semi-diurnal tide), or once both inwards and seawards in approximately 24 hours and 48 minutes (a diurnal tide). In most locations the tides are a combination of the semi-diurnal and diurnal effects, with the tide being named after the most dominant type.

Tides are generated by gravitational forces of the sun and moon on the ocean waters of the rotating earth. The proximity of the moon and sun relative to Earth has a significant effect on the tides. The magnitude of the tide-generating force is about 68% moon and 32% sun due to their respective masses and distance from Earth (Open University, 1989). The gravitational forces of the sun and moon create two "bulges" in the earth's ocean waters: one directly under or closest to the moon and other on the opposite side of the earth. These "bulges" are the two tides a day observed in many places in the world. Unfortunately, this simple concept is complicated by the fact that the earth's axis is tilted at 23.5 degrees to the moon's orbit; the two bulges in the ocean are not equal unless the moon is over the equator. This difference in tidal height between the two daily tides is called the diurnal inequality or declinational tides and they repeat on a 14 day cycle as the moon rotates around the earth.

Where the semi-diurnal tide is dominant, the largest marine currents occur at new moon and full moon (spring tides), which is when gravitational pull of the sun and moon is aligned. The lowest, occurs at the first and third quarters of the moon (neap tides), where the sun and moon's gravitational pull are 90 degrees out of phase.

When diurnal tides happen then the current strength varies with the declination. Generally the largest and lowest currents occur at the extreme declination of the moon

and zero declination respectively. Thus the differences in currents occur due to changes between the distances of the moon and sun from Earth, the relative positions with reference to Earth and varying angles of declination. This phenomenon happens with a periodicity of two weeks, one month, and one year or may be longer and is predictable entirely [15,16]. This means that the strength of the marine currents generated by the tide varies, depending on the position of the site on the earth. The other factors such as the shape of the coastline and the bathymetry (shape of the sea bed) are also responsible to affect the strength of marine currents. Along straight coastlines and in the middle of deep oceans, the tidal range and marine currents are typically low. Another factor that has impact upon the magnitude of marine currents is the presence of narrow passages or straits between islands and around headlands. These passages result in a narrowing and concentration of tidal flow. The flow through a passage is affected by the loss of energy due to friction. The entrances to lochs, bays and large harbors cause high marine current flows.

Generally, but not always, the strength of the currents is dependent on the tidal height of the location. It's not essential that large marine currents do not necessarily require a large tidal range or height. In land-locked seas such as the Mediterranean, where the tidal range is small, some sizeable marine currents exist (BC Hydro, 2002). Some of the largest tidal flows are found on the east side of the Philippines where the tidal range is small.

Generally the marine current resource follows an approximate sinusoidal pattern with the largest currents generated during the mid-tide. The flood tide often has slightly larger currents than the ebb tide. The flood and ebb flows are generally 180 degrees out of face with no flow at the turn of the tide (slack tide). However there are some locations where

the water flows continuously in one direction only, the strength being largely independent of the moon's phase. These currents are dependent on large thermal movements and run generally from the equator to cooler areas. A not too far fetching example is the Gulf Stream, which moves approximately 80 million cubic meters of water per second (BC Hydro, 2002). Another example is the Strait of Gibraltar where in the upper layer, a constant flow of water passes into the Mediterranean basin from the Atlantic and a constant outflow in the lower layer (BC Hydro. 2002).

2.3 Ocean Currents

The more constant water movements are also found in the oceans. There is a dynamic relationship between constant ocean movements and the slope of the mean sea level (MSL) surface. The MSL is the average level of the sea surface measured relative to a fixed level on land. The greatest surface slopes and deviation from the MSL surface are found in areas of great ocean currents for example the Gulf Stream, the Kuroshio Current and the Antarctic Circumpolar Current shown in Figure 2.1. The relationship between the current velocity and the mean sea level surface slope for a steady current is given in (2.1).

$$vf_c = g\beta \tag{2.1}$$

where v is the current velocity, β is the slope of the MSL, g is the gravitational acceleration and f_c is the Coriolis parameter given by:

$$f_c = 2\omega_s \sin \emptyset_l = 1.459 \times 10^{-4} \sin \emptyset_l \tag{2.2}$$

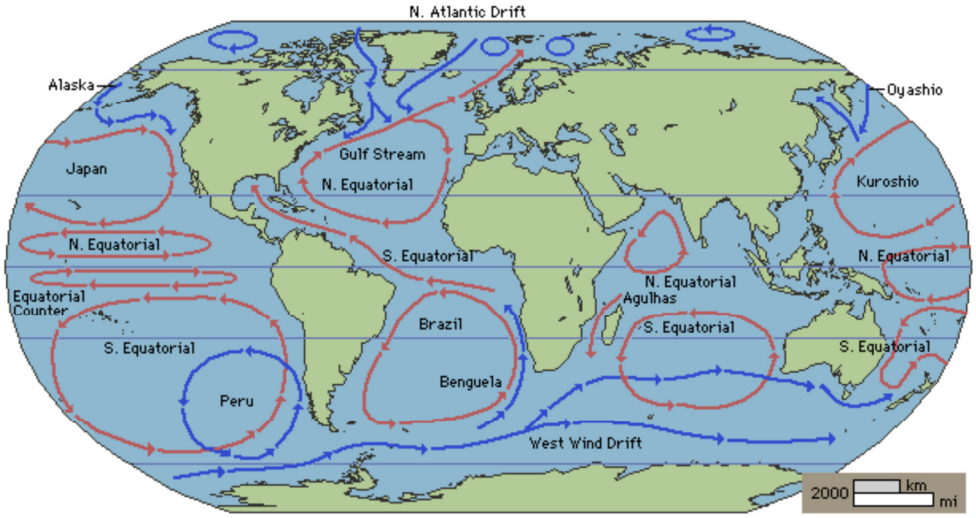

Fig. 2.1 The major ocean currents, the red arrows illustrate warm water currents and the blue are cold water currents[17].

In eq. (2.2) ω_s is the angular speed of earth's rotation and Φ_l is the latitude [17]. In the Gulf Stream an average current velocity of 2.1 m/s has been measured [18] and the Kuroshio Current has a maximum velocity of 1 m/s around Taiwan and slightly higher outside Japan [19, 20].

2.4 Gradient Currents

In some places nearly constant currents occur due to density differences caused by salinity or temperature gradients. These types of currents exist, for example, in the Mediterranean in the strait of the Dardanelles and in the sites of Samos, Kafirea, Kea and Kithos in Greek waters. In Skagerak/Kattegatt current velocities of up to 1.4 m/s have been measured. These currents are mainly due to barotropic flows and salinity gradients when the brackish water from the Baltic Sea meets the Atlantic Ocean. According to [21] the currents in this area are strongest along the Danish coast.

2.5 Conclusion

This chapter illustrates different types of current available in ocean around the world. The next chapter describes the existing technologies in the market to extract power from marine current.

Chapter III

A Status Review of Marine Current Systems

3.0 Introduction

This chapter looks at the nature of the marine current resource and the technology required exploiting it. Prototypes which have been developed and undergoing testing have been highlighted as well as possible environmental impacts. Focus is placed on three physical factors of the aquatic environment which are likely to be affected.

3.1 Scaling Laws for Turbines

In order to evaluate the performance of turbine we are interested mainly in the power of the device as a function of its rotational speed. The simplest way to develop a non-dimensional power is to divide power **P** by something which has the units of power. The power in a flow is its dynamic pressure P times volumetric flow rate. For a flow, the dynamic pressure P can be expressed as:

$$P = \rho \frac{S^2}{2} \tag{3.1}$$

where ρ denotes the density of fluid and S is the speed of the flow. Volumetric flow is the speed of the flow speed S times the profile area of the turbine A. So, a reference power can be calculated as:

$$\boldsymbol{P} = \rho \frac{S^2}{2} SA \tag{3.2}$$

Also, we can define a power coefficient $\boldsymbol{C_P}$

$$\boldsymbol{C_P} = \frac{\boldsymbol{P}}{\rho \frac{S^3}{2} A} \tag{3.3}$$

To develop a non-dimensional version of the rotational speed of the turbine, we can divide the tip speed of the blades rω by the flow speed S. So, we can define a tip speed $\boldsymbol{\lambda}$ as:

$$\boldsymbol{\lambda} = \frac{\omega r}{S} \tag{3.4}$$

These coefficients can be found in most papers on turbines. It is customary to use the symbol λ instead of C_S. For a turbine, the flow speed S is something imposed by the surroundings, and it is appropriate to use it for dynamic pressure. One could derive the power and speed coefficients using a more formal procedure known as the Method of Indices. Most fluids text books call this the Buckingham π Theorem. For this, the variables and parameters of interest are divided into primary and secondary categories. Power would be primary. Things like the properties of the fluid and conditions imposed by the surroundings would be secondary. When using the Buckingham π Theorem, each non-dimensional coefficient is known as a π. For power, the goal is to find $\boldsymbol{\pi_P}$ where

$$\pi_p = \boldsymbol{P}\, S^a\, \rho^b\, A^c \tag{3.5}$$

We need to find the coefficients *a b c* that makes the right hand side dimensionless. In terms of the basic units of mass M and length L and time T, one can write as:

$$M^0 L^0 T^0 = M \frac{L}{T^2} \times \frac{L}{T} \qquad \left[\frac{L}{T}\right]^a \left[\frac{M}{L^3}\right]^b \qquad [L^2]^c$$

Inspection shows that

a=-3 *b=-1* *c=-1*

With this, π_P becomes

$$\pi_p = \frac{\boldsymbol{P}}{\rho S^3 A} \tag{3.6}$$

Similarly, for speed, the goal is to find π_S where

$$\pi_s = \omega S^a \rho^b r^c \tag{3.7}$$

Manipulation shows that

a=-1 *b=0* *c=+1*

With this, π_S becomes

$$\pi_s = \frac{\omega r}{S} \tag{3.8}$$

As can be seen, the π coefficients are basically the same as the **C** coefficients. If we had included the viscosity μ in the list of variables, the π theorem would have produced the Reynolds Number R_e as a non-dimensional parameter. One might expect this to be important, but it turns out that this is not the case. The character of the flow is not a strong function of R_e.

3.2 Water Current Turbines

The water turbines are generally classified into two groups, horizontal axis and vertical axis. Horizontal axis turbines are the most popular geometry for two primary reasons. Firstly it can produce constant positive torque from the flow. Secondly it can operate at higher rotational speeds. A fast rotating rotor is very suitable for electrical power generators, which operate on an order of hundreds for low speed operating system. Turbines may be anchored to the ocean floor in a variety of ways. Mechanisms such as posts, cables, or anchors are required to keep the turbines stationary relative to the currents with which they interact. They may be tethered with cables, with the relatively constant current interacting with the turbine used to maintain location and stability. In some areas with powerful currents, it would be possible to install water turbines in groups or clusters to create a "marine current facility," similar in design approach to a wind turbine farm. Generally the turbines used for the first marine current energy conversion system have relatively shorter, thicker blades than wind turbines to withstand larger stresses due to higher density of water. The axial flow rotors always require facing the incoming current and thus need a mechanism that allows the turbine to operate with the flow in both directions. This can be achieved either by pitch control of the rotor blades through one hundred eighty degree at turn of tide or by using a tail. Common to all different designs are that they have the axis of rotation along the flow. Most of the turbine designs have been adapted from the applied wind turbine geometry. One of the advantages of vertical axis rotor is that it does not need to be oriented to the flow. This design also allows with ease to mount the gearbox and generator above or below the rotor

avoiding interference with the flow across the rotor. Regardless of the design a turbine can only harness a fraction of the available power in the free flowing water.

Blade designs are based upon either the principle of drag or lift. In drag type turbines the blade shape is employed to have a higher drag coefficient on one side of the incident current than on the other. The drag powered turbines are designed to produce high torque capabilities. The downward drag force on the retreating blades is greater than the retarding force on the advancing blades and thus a net torque is produced. The speed of the rotor is inherently limited because the retreating blades cannot travel faster than water speed. They generally said to operate at low tip speed ratio (TSR) less than one. It is a limitation of drag type turbines that higher speeds and higher peak efficiencies can never be achieved. Moreover, relatively large amount of material are required for a given swept area. The construction is very simple and inexpensive compared to other turbines.

Lift type turbines incorporates aero foil section blades to produce lift. The blades can turn sufficiently fast relative to free stream flow and converts the lift into positive torque. These turbines can operate at TSR up to ten and can achieve better efficiencies than drag turbines. The following Table 3.1 shows a comparison study of lift and drag type turbines.

Table 3.1 Lift and Drag Horizontal and Vertical axis Turbines

Rotor Type	**Hydrodynamic**	**Axis**	**Self-start**	**Cp**	**Keynotes**
Propeller	Lift	HAWT	Good	High	Noisy, Turbulence, Low torque, High speed
Darrieus	Lift	VAWT	Poor	High	Low torque
Savonius	Drag	VAWT	Good	Low	High torque, Low speed, Poor efficiency

When designing a rotor for marine current generation the author considered both vertical and horizontal axis turbine. The reasons to consider vertical axis rotor initially over other types are stated below:

1. Simple and low cost to build.
2. Most vertical axis turbines cannot rotate faster than the water speed. On the other hand some horizontal turbine gains momentum and can exceed the water speed. It can cause mechanical stress on motor due to overvoltage in the windings and can cause rotor damage. In order to prevent this, a separate braking system must be designed to compensate the issue.
3. Vertical axis rotors accept flow from any direction and they are easier to install.
4. Generator can be easily mounted on the top of vertical turbine. Another aspect of rotor design is to consider the connection method between generator and turbine to extract power. The horizontal turbine needs to have a strong connection in order to compensate for the weight of the rotor itself. The vertical axis rotor can be configured so that the generator can sit on top. For this reason one could use a simpler coupler, which would act as the connection between the axle of the rotor and the motor shaft. When considering which option to choose, it is important to figure in the flexibility of each option, and plan accordingly. Due to the fact that the vertical axis turbine does not actually have to be welded into place on the generator shaft, it could be replaced easily, thus adding the flexibility desired for low power applications.
5. High starting torque helps to start at lower speed.

6. Relatively low operating speed and may require a gearbox.
7. Maintenance to maintain a clean leading edge is not necessary.

The above advantages still outweigh its low efficiency and slow running speed makes it an ideal economical choice to meet small-scale power requirement [35]. This is essentially due to the low hydrodynamic performances of such rotors, based on the difference between the drag forces on the paddles. The calculations of Professor Betz gave 20 % as the highest theoretical maximum for drag type vertical axis turbines, which under the best of circumstances could not produce more than 10% in practical output [36]. The expected performance curves of different turbines for wind are shown in Fig. 3.1.

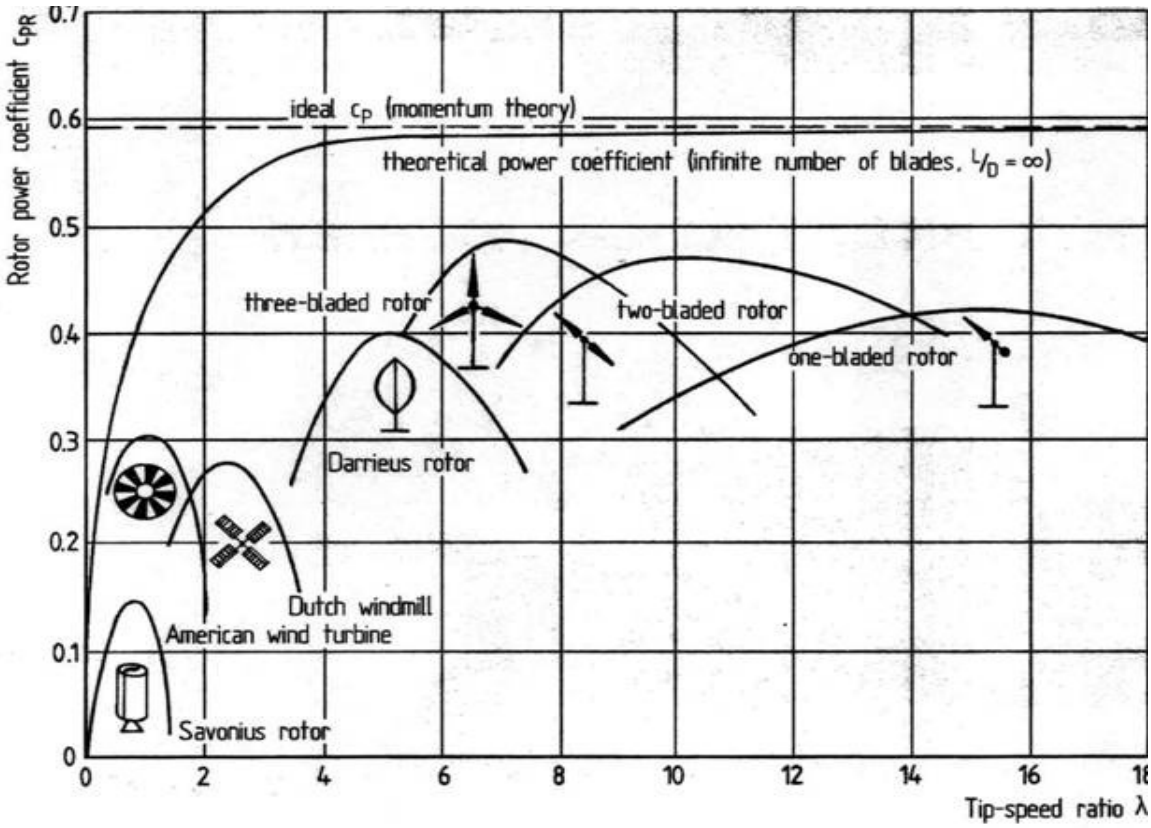

Fig. 3.1 Expected performances of different types of turbines [36]

3.3 Marine Current Energy Extraction Technologies

Within the last few decades, developers have shifted towards technologies that capture the tidally-driven coastal currents or tidal stream. Indeed, very large amounts of energy are available in coastal waters [22-28]. The simplest and oldest technology involves building a dam, known as a barrage, across a bay or estuary that has large differences in elevation between high and low tides. When the tide comes in, the water fills the area behind the barrage. When the tide starts to ebb, the gates of the barrage shut to hold back the water at its maximum height. Once the tide is out, the water is allowed to flow through holes near the bottom of the barrage where the turbine is located. The water, now running with great energy, turns the blades of the turbine that, in turn, generate electricity.

The first commercial scale tidal generating barrage rated at 250MW was built in La Rance, France in 1960.The plant continues to operate today just as another smaller plant constructed in 1984 in Nova Scotia, and Canada rated at 20MW. All these first generation tidal power plants have faced the hash marine environment and have been in continuous emission-free operation for many years. The high capital and environmental problems from accumulation of silt within the catchments area of the dam makes it no longer feasible for energy generation. Two new developed concepts can be described as follows:

- The first and the most advanced, adapted from wind energy industry can be considered as an underwater turbine. It can be categorized into Horizontal and Vertical axis turbines, depending on the orientation of the rotating shaft.
- The second one adapted is a system of oscillating hydroplanes linked to a hydraulic motor and generator arrangement.

Presently these concepts and the prototypes are being considered for commercialization. Most of them are still now in the experimental stages.

3.4 Prototypes

In general technology development in the marine current energy sector has been slow worldwide. Ocean current energy is at an early stage of development, with only a small number of prototypes and demonstration units having been tested to date. The high costs coupled with the harsh nature of the marine environment made it difficult to develop the technology. Recent advances in offshore installations and innovation have translated into real prototypes or field trial models. But still these technologies are not well developed into full commercialization. The focus is to prove the technologies that can be made to work reliably. Investigation shows that there is no small scale system available that is suitable to extract power from exceedingly low marine current. Some of the most promising ones are described in this literature. As these developing technologies are being commercialized, there is reluctance to release information due to competitive advantage. Moreover no research article has been found on small scale marine current energy conversion that can be used to develop power autonomously.

3.4.1 Seaflow

The unit consists of a two-bladed rotor mounted on a steel pile set into a socket drilled in the seabed. The dimension of rotor diameter is 11 m with full span pitch control thereby making it capable of generating power for both directions of flow. It is currently being operated in one direction of flow and a dump load is being used instead of grid connection due to economic reasons. The power train consists of a gearbox and an induction generator. It makes the unit an integral, sealed, watertight unit. The system

operates at variable speed and the control system and power conditioning, together with the dump load ballast are located in the housing above the pile [29-30]. An important feature of this technology is that the rotor and drive train (i.e. gearbox and generator) can be raised completely above the surface as shown in Fig. 3.2. In this position easy maintenance can be carried out.

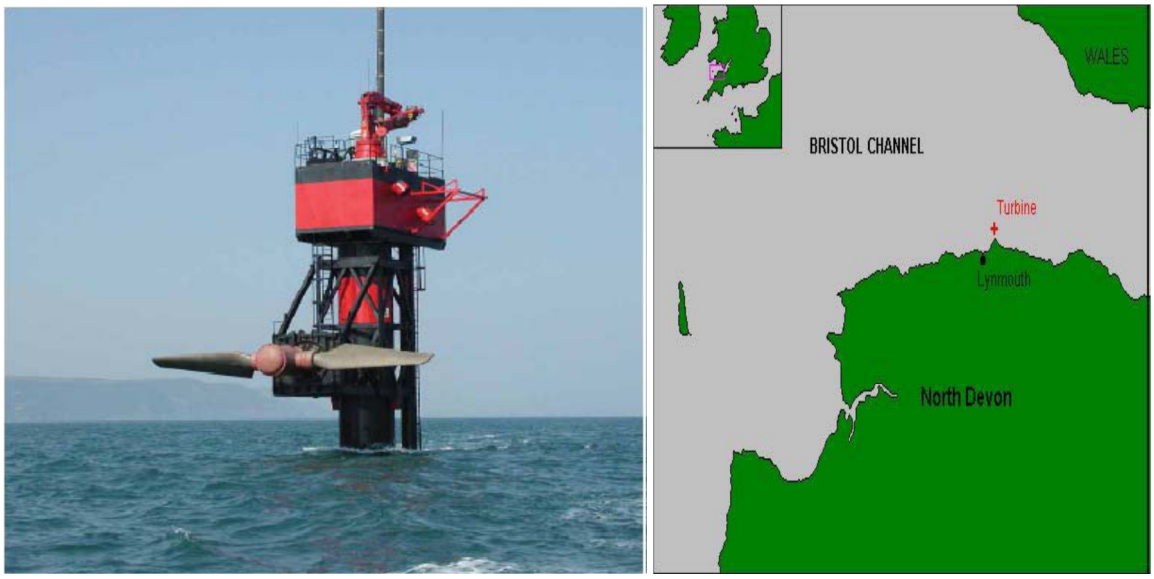

Source: www.marineturbines.com

Fig. 3.2 Seaflow in position for maintenance and location in Bristol Channel, UK[29]

The prototype (experimental unit) is installed in the channel between Foreland Ledge and Foreland Point on the North Devon coast. It is 3 km to the North-East of Lynmouth, UK. It has a rated output power of 300 kW at a current speed of 2.7 m/s. The Foreland Point was chosen due to favorable tidal stream speeds. According to an independent consultancy in marine environmental science Coastal Research, this location has tidal streams in excess of 2.5 m/s during spring tides.

3.4.3 Tidal Stream Turbine

Fig. 3.3 shows the prototype which is expected to supply 700 MWhr per year. The submerged structure weighs 120 tons. It is a three-bladed turbine made up of glass fiber-reinforced plastic measured 10 meters from hub to tip. By rotating the blades around their own axis by 180 degrees at slack water, the machine is ready for the reversing current [31]. The average current velocity at this location is 1.8 m/s. The strait has a width of 400 m at its narrowest cross section and a maximum depth of 50 m allowing a sailing depth of 19 m.

Source: www.e-tidevannsenergi.com

Fig. 3.3 Deployment of the first grid connected tidal turbine in Kval Sound, Norway [31]

3.4.3 Tidal Fence (Davis Hydro Turbine)

Blue Energy has over two decades developed a floating vertical axis turbine known as Davis Hydro Turbine. The Blue Energy Ocean Turbine acts as a highly efficient underwater vertical-axis windmill. Four fixed hydrofoil blades of the Blue Energy Ocean Turbine are connected to a rotor that drives an integrated gearbox and electrical generator assembly. The turbine is mounted in a durable concrete marine caisson, which anchors

the unit to the ocean floor, directs flow through the turbine further concentrating the resource supporting the coupler, gearbox, and generator above it. The hydrofoil blades employ a hydrodynamic lift principal that causes the turbine foils to move proportionately faster than the speed of the surrounding water. Prototypes ranging from 4 kW to 100 kW have been tested mostly in rivers [32].

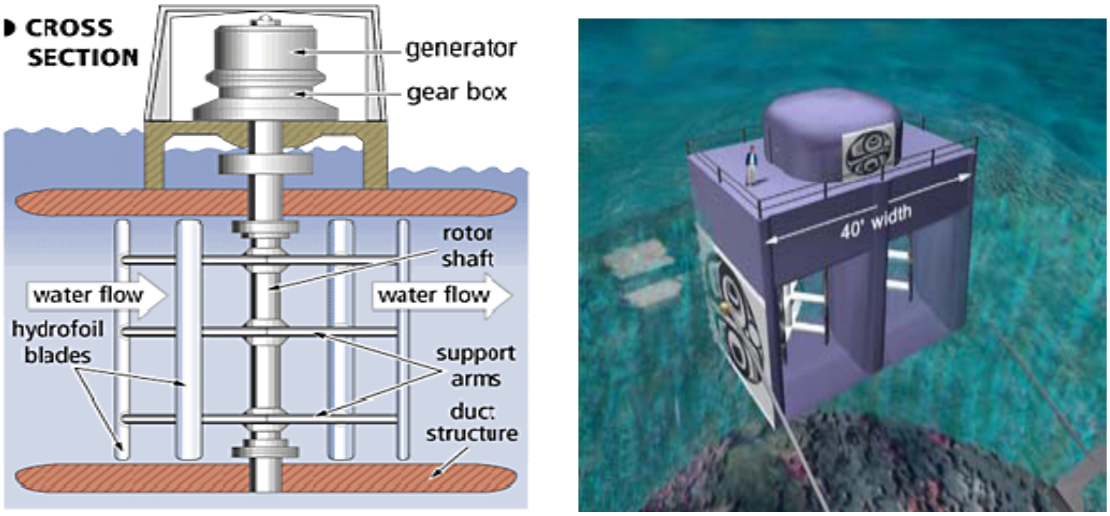

Source: www.bluenergy.com

Fig. 3.4 Computer rendering of the twin (2 x 250 kW) floating units [32]

Blue Energy is currently pursuing the development of a 500kW pre-commercial demonstration project off the coast of British Columbia, Canada. The project is comprised of two floating 250kW units of the type shown in Fig. 3.4. The unit will be viable in ocean currents of 1.75 m/s.

3.4.4 The Stingray Tidal Stream Generator

Fig. 3.5 shows the stingray generator converts the kinetic energy of moving water into hydraulic power and turns an electrical generator by means of a hydraulic motor. It consists of a stack of large hydroplanes attached by a linkage. The hydroplanes change its face relative to the approaching water stream by a simple mechanism. The lift and drag

force causes the arm to oscillate vertically [33]. The oscillating motion is used to directly operate hydraulic cylinders to produce a flow of oil. This can be used to drive a hydraulic motor which in turn drives an electrical generator. A yaw arrangement ensures that the hydroplane is directly aligned with the flow of water. The whole structure is fully submerged and is fixed rigidly onto the sea bed.

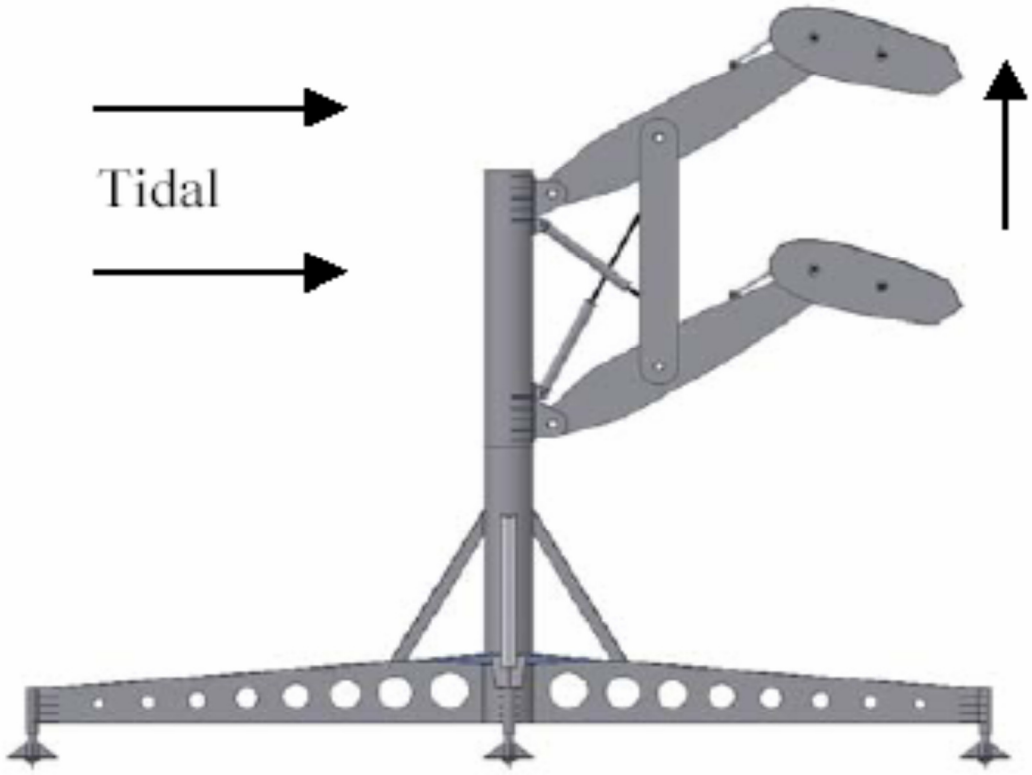

Fig. 3.5 Principle of operation of the Stingray Generator [33]

Initial power cycles completed with 'manual' control of the hydroplane angle produced a peak hydraulic power of 250kW and a time averaged electrical power output of 90kW in a 1.5 m/s measured current. The deployment of the Stingray tidal stream generator is shown in Fig. 3.6.

Fig. 3.6 Deployment of Stingray in Yell Sound, Scotland [33]

3.4.5 MOOS Power System

The MOOS power system is designed to collect and store energy from the buoy environment, transmit power to distant loads over the riser and seafloor cables, and make clean power available to buoy and seafloor loads via a standardized electrical interface. The system block diagram is shown in Fig. 3.7. The capability of the power system was made based on goals established during the user requirements survey**.** These goals included a continuous-average power delivery capability between 10 and 100 watts, the ability to transmit power of 300W peak down a 4-km mooring riser, and the ability to transmit power of 10 W peaks to the end of a 10-km benthic extension cable.

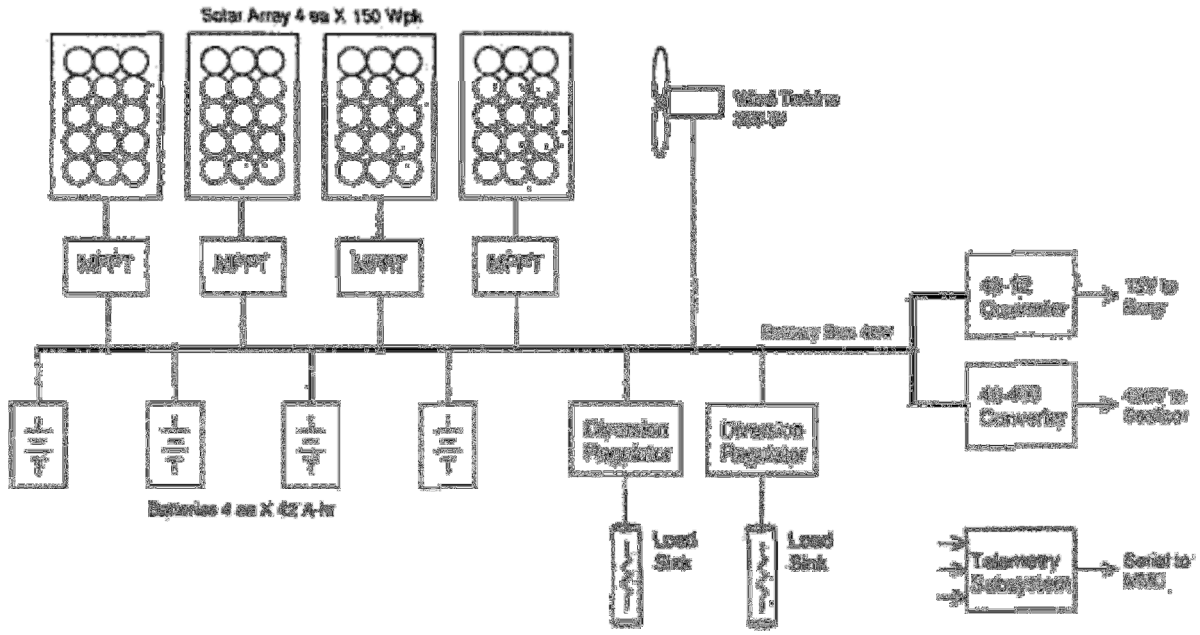

Fig. 3.7 Block diagram of the power system [34]

3.5 Emerging Technologies

There are a couple of additional concept variants currently in development. Some of them are worth noting as they may emerge as strong options for future.

3.5.1 TidEI Tidal Stream Generator

The TidEI concept is a pair of contra-rotating turbines, mounted on a single crossbeam. It is buoyant and tethered to the seabed by a series of mooring chains. The floating system allows the turbines to align in the direction of the tide automatically, i.e. following the tide backwards and forwards as it changes direction. The turbine blades are fixed pitch and variable speed operated.

Fig. 3.8 1/10th scale TidEI tidal stream generator [34]

A commercial size, 1000 kW (2 x 500 kW), prototype with 15 m diameter is at the development stage for offshore testing. It is likely to be tested in an offshore environment with peak tidal speed of 2.5 m/s or more and a water depth of 30m [34]. This will help to prove its viability and numerous perceived advantages. Meanwhile a 1:10 scale system as shown in Fig. 3.8, partly funded by DTI, and has undergone a seven week trial program at the New and Renewable Energy Centre (NaREC) in Blyth.

3.5.2 Lunar system

This technology being developed by Lunar Energy features a ducted turbine, fixed to the seabed by a gravity foundation. The blades are bi-directional rather than variable pitch, and there is no yaw mechanism which maximizes the energy from the water flow, even when flow is not parallel to the turbine axis. This reduces complexity and allows

improved reliability. Moreover it is likely to be deployed in deep waters without impacting shipping traffic.

3.6 Technology Challenges

In the early stage, all new technology challenges are bound to be faced .Some of the most pressing ones are being discussed here. As prototypes are being tested, and the technology matures, most of them, if not all, are bound to be addressed. Though some of them may be unique to certain technologies, most of them are common to most, if not all the technologies under development.

A. *Installation, Foundation and Moorings*:

The installation of marine current machines will present their own unique difficulties. The constructions of foundations and installation during water movement are challenging. Slack water can be expected each day only for a few minutes. Scouring around the base of temporary support structures can be significant, even over very short periods. Most devices may have similar installation, foundation and mooring problems and so there is scope for generic research in this area.

B. *Maintenance Requirements*:

It is very important to have easy access to the unit for maintenance. Two concepts have been proposed so far. The first is a hoist system based on a hydraulic unit, similar to the system used to raise marine platform legs. The second one is a semi-submersible system which allows the rotor and power train to float on the water surface for access. The size and shape of the assembly is likely to make removal and replacement a difficult operation requiring calm sea conditions which may be hard to find. Due to economic reasons it will

be wise to design the turbines in such a way that it a requires minimum level of maintenance.

C. *Cavitation*:

Relatively high velocities at the tips of the rotor blades cause formation of cavities along the blade. To avoid this different approach is needed for marine current turbines because of its larger plane or rotor area. Cavitation is sensitive to water depth and can be avoided by placing units in deeper water at potential cavitation sites. Hence, research is needed to understand the problems of cavitation and whether selection of blade profiles and materials can bring a difference in cavitation efficiency loss and damage problems.

D. *Packing Density*:

A good understanding of the impact of quantity and size cause on the marine environment and flow pattern can be a basis of design guidelines for system sizing. Some of the factors to be taken into consideration include seabed structure, depth, flow pattern and available area. This will help designers to locate suitable sites, and investor to understand the implications of these farms.

E. *Turbulence*:

The velocity of the flow at a given location can sometimes vary across the actuator area. This can cause significant variations in loading across the actuator and associated fatigue and vibration problems. The study of turbulence levels is important for installation of individual units in an area with strong flow. The turbulent structure of the flow field is another important factor design affecting the design of components to resist fatigue. Design codes for marine current devices considering turbulence levels are important in setting realistic limits to design.

F. *Biofouling*:

Many devices installed in the sea become artificial reefs, attracting a wide variety of marine organisms. These cover the structures and can cause significant fouling. Fouling of moving parts could affect the performance of devices. Several methods for preventing fouling have been proposed. These include the use of antifouling paints and sonic and ultra-sonic systems. Both methods have their challenges and drawbacks calling for further research.

3.7 Conclusion

This chapter has reviewed state of the art of marine tidal turbines. The strength and the weakness of the major tidal turbine technologies have been described. It has been found that technologies for the exploitation of marine tidal currents are still in their infancy stage. Next chapter discusses the different types of marine current turbine and design of of a complete marine current energy conversion system.

Chapter IV

Design of Marine Current Energy Conversion System

4.0 Introduction

The author considered several alternatives for the Seaformatics marine current energy device. Initially, as part of M.Eng program, I worked on a Savonius rotor. This had very low efficiency. Early in PhD program, I considered a flapping wing device. It was concluded that energy extraction from this device would be extremely difficult. Also the device was quite fragile and not very robust. The author finally settled on a horizontal axis turbine with a novel blade arrangement and a unique magnetic coupler between the turbine and the electric generator. This chapter describes the design work that was done on each of these devices.

4.1 Vertical Axis Turbine

The idea of Savonius rotor was first developed by Flettner. The easiest way to build a Savonius rotor is to cut a cylinder into two halves along the central plane and moving the two semi cylindrical surfaces sideways along the cutting plane so that it looks like alphabet "S." In the early stage of this research the author considered Savonius rotor as the vertical axis turbine for energy conversion system. Fig 4.1 shows a typical Savonius rotor with two blades.

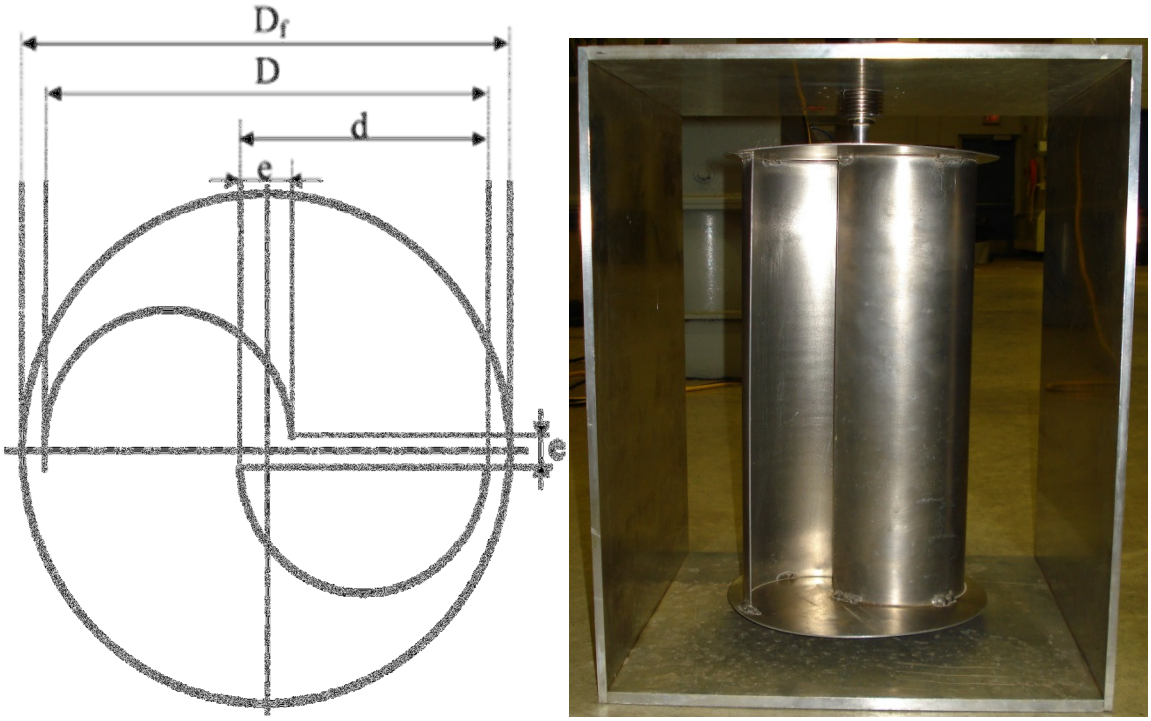

Fig. 4.1 Typical stationary Savonius rotor with round edge

Menet et al. have shown that the Savonius rotors are in fact more resistant to mechanical stresses than all fast running wind turbines [37-39]. The basic idea is to compare the mechanical power obtained by a vertical axis turbine with the one produced by a horizontal turbine. The comparison is done by considering the same front width of fluid (i.e. diameter of the rotor) and the same mechanical stresses produced due to the centrifugal forces on the paddles for the two turbines. The Savonius turbine relies on stagnation principles to convert current into rotational energy. The Savonius rotor uses stagnation pressure on one side to promote rotation around a central vertical axis. The blade turning redirects water around itself with its rounded shape. Any tangential flow of water will produce a positive force on the rotor; vertical axis turbines operate in turbulent water better than horizontal designs. A Savonius design relies on the pressure of the

current against the rotor blade to produce torque. As such, a Savonius design cannot exceed the speed of the water and operates at a lower RPM range than would a horizontal axis turbine. It has the benefit of producing a larger torque. The basic Savonius rotor is a drag turbine. It consists of two semicircular buckets with a small overlap between them. There are two ways such a turbine can extract power from a flow. Imagine that the flow is moving upwards from the bottom left. Such a flow would produce a wake drag load top of left bucket and stagnation pressure load below right bucket. Each load has a moment arm r which creates a torque about the rotor axis. Multiplying each torque by rotation speed gives power. The net power is

$$P_{Savonius} = I\,A\,\frac{\rho}{2}\,(S - \omega r)^2\,r\omega \;-\; J\,A\,\frac{\rho}{2}\,(S + \omega r)^2\,r\,\omega \qquad (4.1)$$

where *I* and *J* are drag coefficients. Fluids texts suggest that for the bucket moving away from the flow *I* is around 2.3 while for the bucket moving into the flow *J* is around 1.0 [45]. However, the presence of a jet in the wake region could make J much lower: the ideal would be *J=0*. For the turbine, there would also be impulse load where a sheet of water moves first along the inside of the left bucket and then along the inside of the right bucket. One can imagine the turbine absorbs momentum when it hits the left bucket and expels momentum where it leaves the right bucket. Each momentum has a moment arm *r* which creates a torque about the rotor axis. Multiplying each torque by rotation speed gives power. Here we assume that the flow going into the turbine moves at the current speed S. The speed of the flow relative to the bucket is *S* minus $r\omega$ the speed of the bucket. The speed of the flow at the exit would be the relative speed minus the bucket speed.

Let the rotor flow area be A. The impulse momentum absorbed is calculated by:

$$Impulse\ Momentum\ Absorbed = \rho SA \times S \tag{4.2}$$

while the impulse momentum expelled is written as:

$$Impulse\ Momentum\ expelled = \rho SA\ (S - r\omega - r\omega) \tag{4.3}$$

The net developed power can be expressed as:

$$Net\ Power = 2\rho SA\ (S - r\omega) r\omega \tag{4.4}$$

This equation shows that the power is zero when the bucket speed ωr is zero and when it is equal to S. Differentiation shows that the power peaks when the bucket speed is half *S*. The typical efficiency of the rotor is shown in Fig 4.2. The turbine shows a higher cut in speed and efficiency less than 10% when tested in tow tank. Due to poor performance and the stalling effect of the blades in the dead zone it was decided not to use single stage Savonius turbine for low speed application. In M.Eng research the author also designed and built two stage and three stage Savonius rotors to improve torque pulsations, overcome dead zones and omnidirectional. The efficiency of all the rotors was found to be less than 10%. In the same research work by another graduate student at MUN a twisted Savonius rotor was proposed to improve the efficiency and starting torque. The complex geometry and high manufacturing cost of the twisted Savonius brought an end to further research work in this type of turbine.

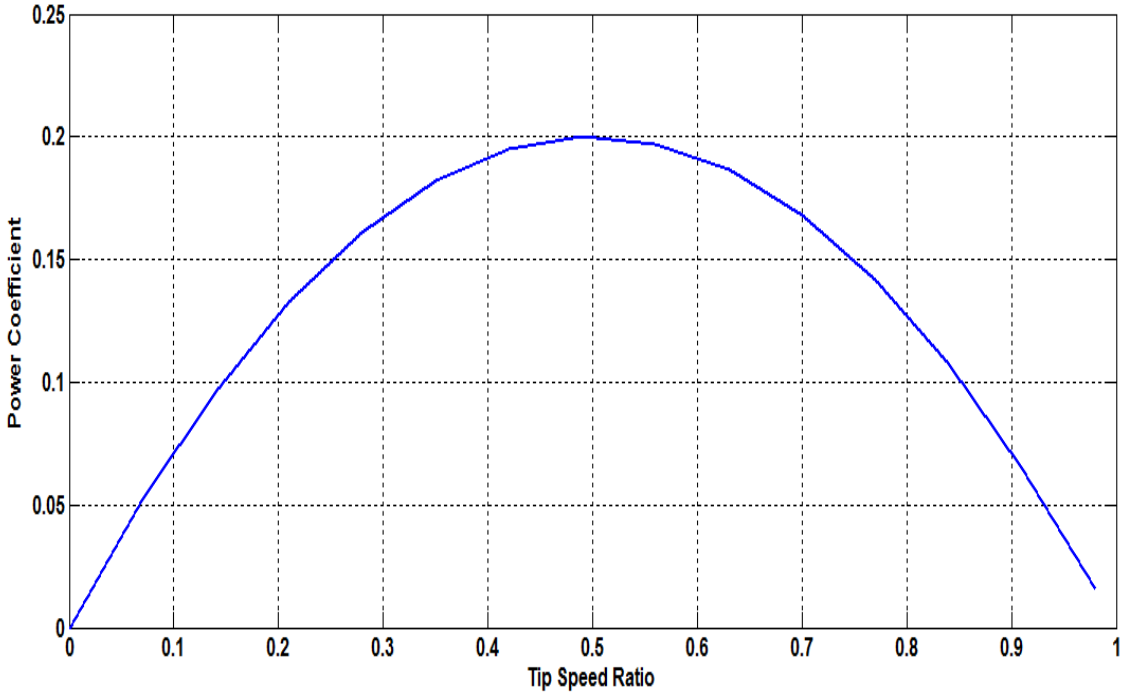

Fig. 4.2 Efficiency of Savonius Rotor

4.2 Oscillating Turbine

In order to reduce the cut in speed of the vertical axis turbine the author investigated different geometries. Extensive study shows that there are some novel designs developed from unsteady aerodynamic theory. For instance, Jeffery developed a model for a vertically-mounted pivoting wing which flapped in the wind [46-50]. Based on this idea, we designed an oscillating water turbine that can operate in excessively low speed. The mechanism consists of an airfoil or a flat plate that is able to move in a coupled pitch and plunge motion. In case of airfoil it is obvious to use a symmetrical one to have the same angle of attack for both sides. The airfoil selected is based on Jukowsky foil which resembles a symmetrical NACA 4 digit foil. The symmetrical airfoil with a cusped trailing edge is approximately 14% thick and maximum thickness at about 0.25 times the chord length. The chord length is 0.25m and the span is 0.25m resulting in an aspect ratio

of one and a cross sectional area of 0.0625m^2. Aspect ratio is the principal parameter affecting lift production in a streamlined foil. High aspect ratio wings provide high lift capacity. A rectangular bar of length 1m and 0.00635m has been used as a torque arm. A small shaft is attached to the foil which is connected to one end the torque arm by a bushing and a cap. Generally the pivot point for a flat plate is at the half of the chord length but in case of an airfoil it's at the quarter of the chord length. A locking arrangement has been made so that a maximum angular displacement of the foil is ± 30 degrees. In order to balance the device and add drag effects so that the device can oscillate smoothly, tabs are used on the other end of torque arm. To reduce the effect of tip vortices, end appendages have been proposed, which have an effect similar to end walls to a certain degree. In practice, it has been found that end plates are useful only for high lift coefficient, above 0.3. Trailing vanes, winglets, and tip sails, are good for improving performance of existing wings, but a to-be-designed wing can always be made as good without them, by proper aspect ratio choice [50-59]. Additionally, it is intended that the device will be fully compatible with existing marine production techniques and tooling. Fig 4.3 shows the CAD schematic of the oscillating water current turbine. The functionality of water current device was tested in to flume tank as shown in Fig 4.4. Due to the complexity of the instrumentation and power take off requires more research to make it suitable for the application.

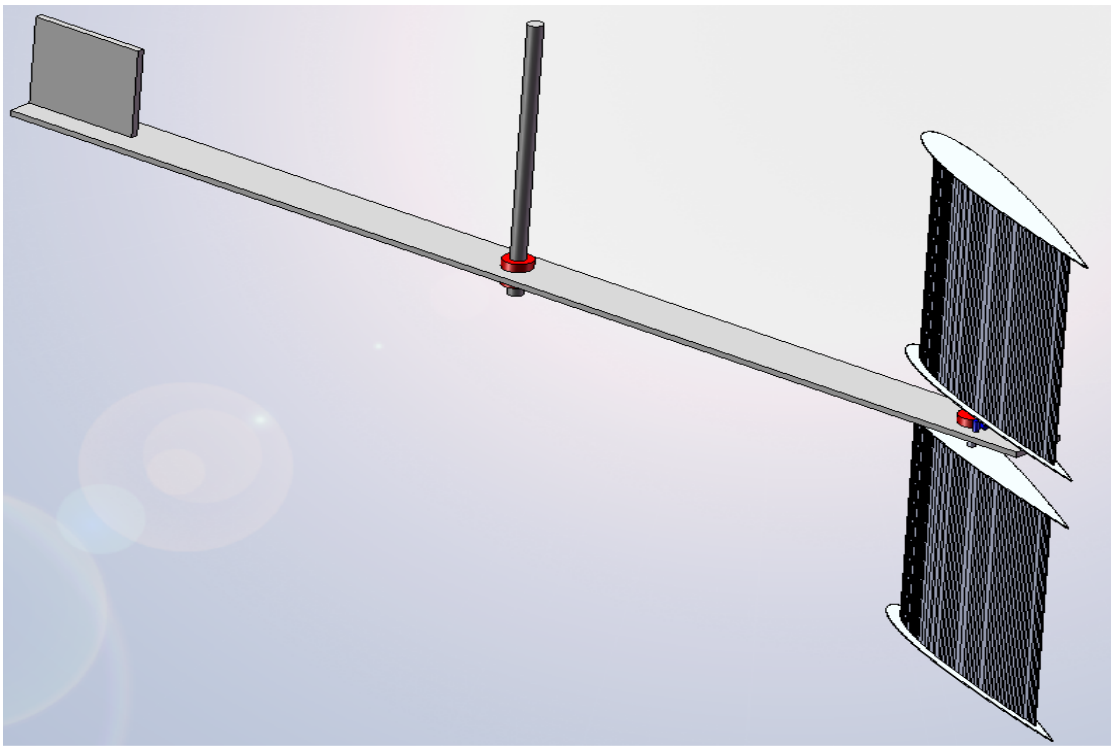

Fig. 4.3 CAD Drawing of Oscillating Water Current Turbine

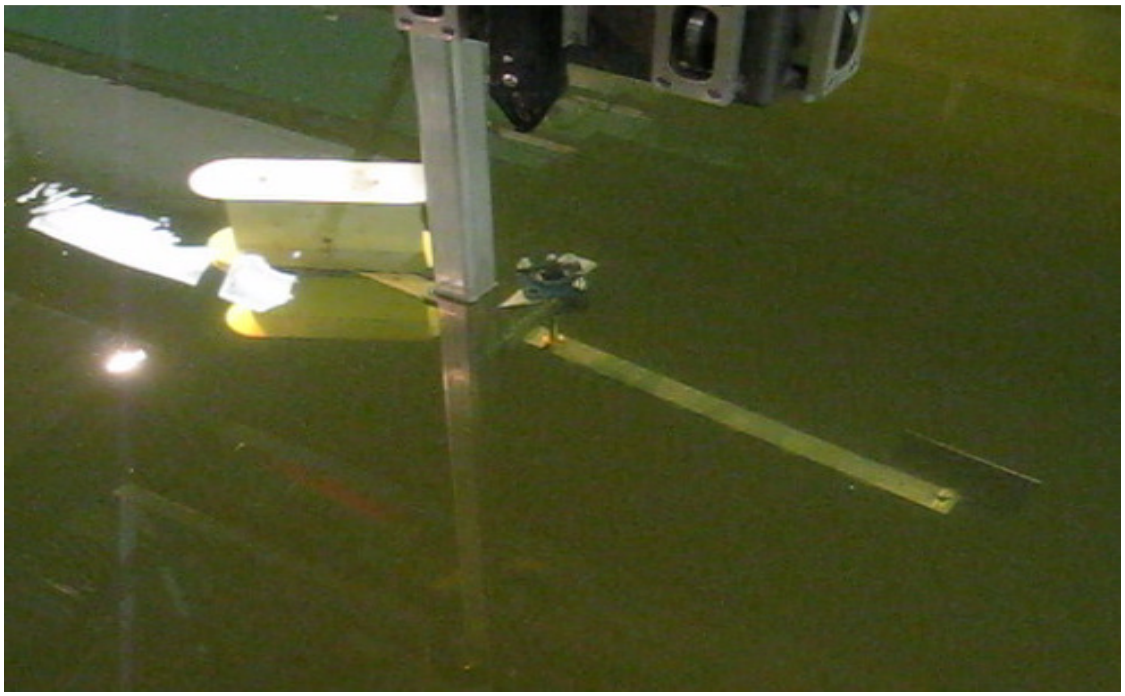

Fig. 4.4 Testing of Oscillating Water Current Tank in Tow Tank

The equations of motion for the device can be derived fully and easily using the Lagrange energy equation. The Lagrangian Formulation is based on the "Principle of Virtual Work". This states that when a body in static, load equilibrium undergoes small virtual or imaginary displacements consistent with constraints that the net work done by the loads is zero. Dynamic loads due to inertia are included using "D'Alemberts Principle". This states that reaction loads due to inertia can be treated as static loads in the virtual work statement. For a general multi degree of freedom system, virtual work gives the equation of motion:

$$\frac{d}{dt}\left(\frac{\partial L}{\partial \dot{q}}\right) - \frac{\partial L}{\partial q} = Q \qquad (4.5)$$

where $L = T - V$ is known as the system Lagrangian, $T = K.E$ is the total kinetic energy of the system, $V = P.E$ is its total potential energy, Q is a generalized load and q is a generalized displacement. The energy equations should yield the same equations of motion as a small perturbation force analysis using Newton's second law, and are in general, better suited to use with multiple degree of freedom systems as the method is less algebraically bulky. The choice of generalized coordinates must be such that there is no redundancy, and should be minimum required to completely describe the state of the system and as such, in the case of this device, it can be seen from the diagram that they are α and β. Thus any conceivable system state can be determined from consideration of these two ordinates and their derivatives. The geometry of the device with resolved forces is shown in Fig.4.5. A detailed derivation of the Lagrangian equation of the device is outlined in Appendix A.

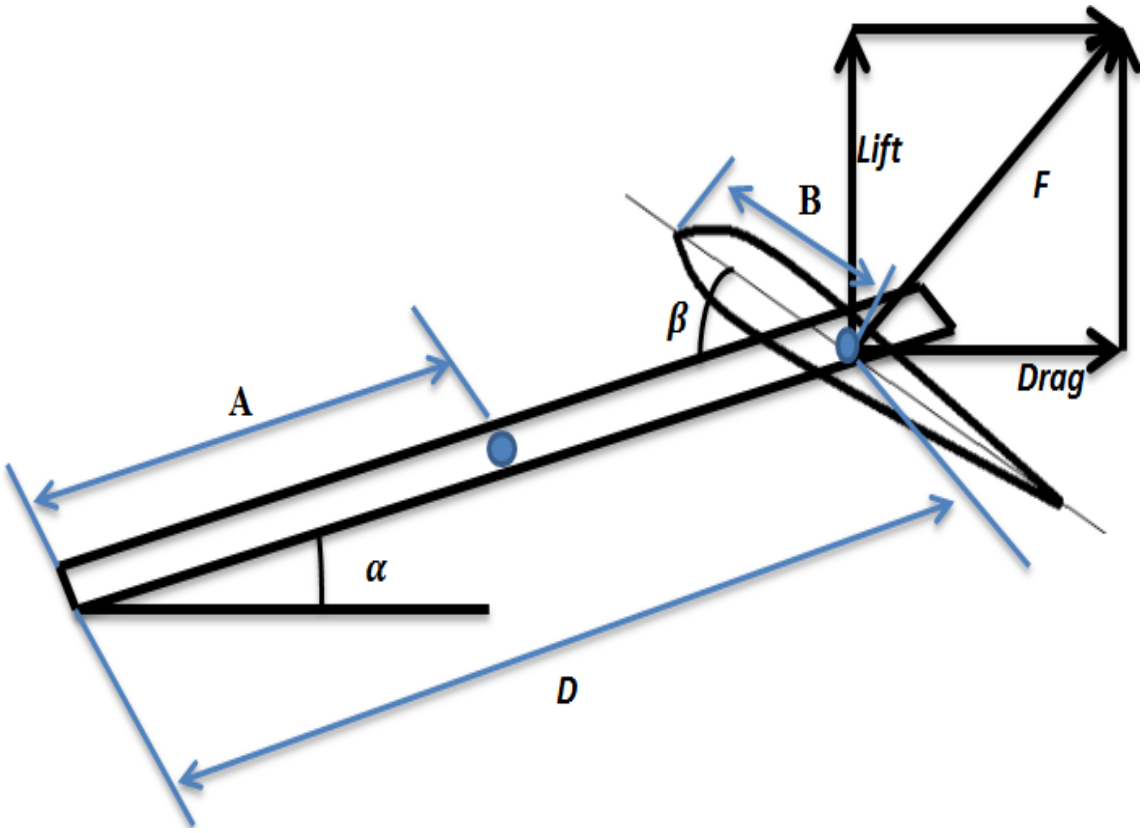

Fig. 4.5 Geometry of Oscillating Water Current Turbine

The arm equation of motion can be calculated as:

$$[\,M_F\,(\,B^2\,+\,D^2\,-\,2\,B\,D\,\cos\beta)+\,I_F\,]\ddot{\alpha}\;\;-\,[\,M_F\,(\,B^2\,-\,B\,D\,\cos\beta)+\,I_F\,]\ddot{\beta}$$

$$+\,[\,M_A\,A^2\,+\,I_A\,]\ddot{\alpha}\;+\,2\,M_F\,B\,D\,\sin\beta\;\dot{\alpha}\;\dot{\beta}\;-\,M_F\,B\,D\,\sin\beta\,\dot{\beta}^2$$

$$=\,\varphi \qquad (4.6)$$

The load across the arm is expressed as:

$$\varphi\;=\;lift\,(D\,\cos\alpha\,-B\,\cos\kappa)+\;drag\,(D\,\sin\alpha\;+B\,\sin\kappa) \qquad (4.7)$$

The foil equation of motion can be written as:

$$-[\,M_F\,(\,B^2\,+\,D^2\,-\,2\,B\,D\,\cos\beta)+\,I_F\,]\ddot{\alpha}\;\;+\,[\,M_F\;B^2\,+\,I_F\,]\ddot{\beta}$$

$$+\;M_F\,B\,D\,\sin\beta\,\dot{\alpha}^2\;=\psi \qquad (4.8)$$

The load across the foil can be written as:

$$\psi = Lift \times B\cos\kappa + Drag \times B\sin\kappa \quad (4.9)$$

The parameter β is the instantaneous angle of attack of the foil $\frac{3C}{4}$ back from its leading edge. It is made up of three components. The first component is the pitch angle α. The second component is due to the change in flow direction caused by the heave rate $\frac{\partial h}{\partial t}$. The third component is due to the change in flow direction caused by the pitch rate $\frac{\partial \alpha}{\partial t}$ at the $\frac{3C}{4}$ location. The $\frac{3C}{4}$ location is suggested by flat plate foil theory. Theory shows that the centre of pressure on a foil is at $\frac{C}{4}$ back from the leading edge.

$$\beta = \alpha + \frac{\frac{\partial h}{\partial t}}{U} + \left(\frac{3C}{4} - b\right)\frac{\frac{\partial \alpha}{\partial t}}{U} \quad (4.10)$$

In order to understand the behaviour of the device a simulation model was developed.

Fig. 4.6 shows the angular displacement of the torque arm and the fin. The simulation is done with and without the effect of vortices and pitching moment of the foil. In both cases the simulation result has been found to be the same. This explains the fact the vortices didn't have any considerable effect on the system. The device performs the semi-circular reciprocating motion. Later the prototype was tested in tow tank and found that the fin has a tendency to stall. The extraction of power from the oscillating turbine can be complicated and needs further research. In simulation, we did try a PI control torque which was set to zero in the stall zones and it suggested good control was possible. However one of the techniques is that the flapping motion of the arm of the device can be used to energize a piston which in turn operates a check valves and causes the fluid to move back and forth in a small diameter pipe leading to a miniature rotary turbine. This

will amplify the flow speed to a level suitable for energy extraction by a rotary generator. The fluid that can be used can be either sea water or vegetable oil which is not threatening to environment. This is a very commonly used technique by developers of wave energy devices which also operate at low speed. The working principle of oscillating turbine leads to an idea of design a horizontal axis turbine discussed in next chapter.

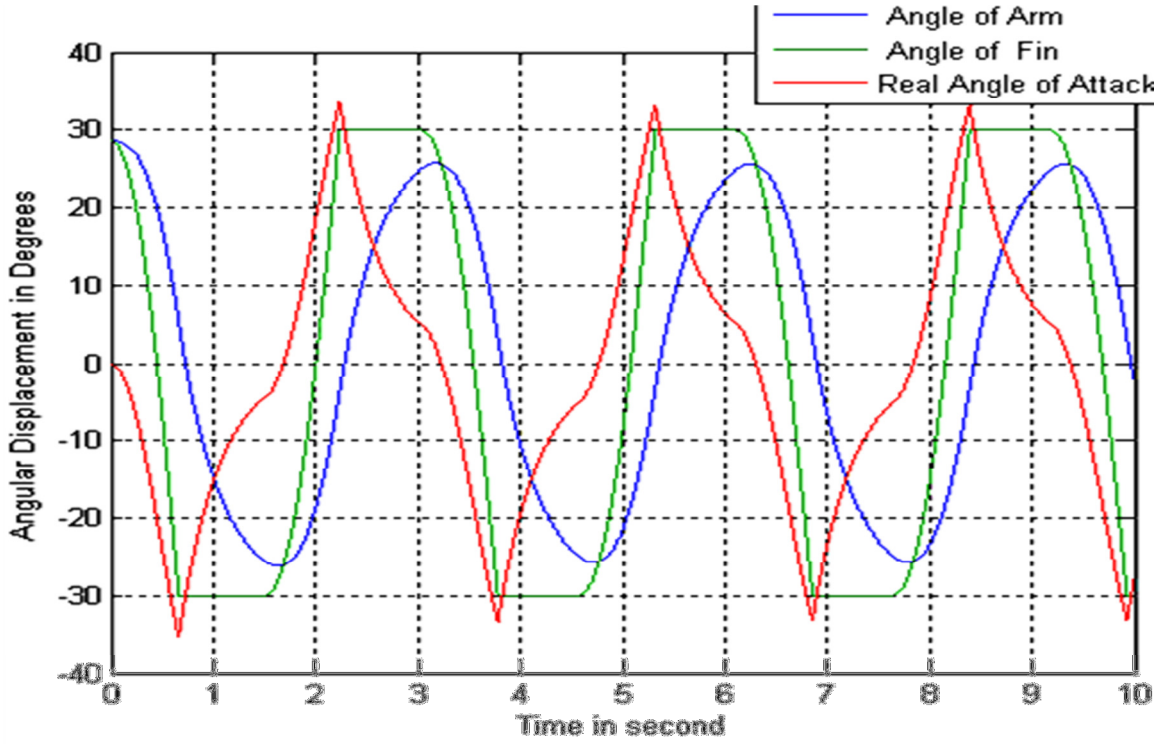

Fig. 4.6 Angular displacements of the Arm and Fin

4.3 Horizontal Axis Turbine

The idea of oscillating turbine leads to the design of a horizontal axis turbine. The design space for horizontal axis marine current turbine is quite large. Ratio of total rotor blade area to swept area (solidity), blade number, foil characteristics and tip speed ratio are all

factors that will determine the hydrodynamic performance of the rotor. Reference [61] presented a comparison of approximate turbine power coefficient versus tip speed ratio for a wide range of machines, including horizontal and vertical axis turbines and is shown in Fig. 3.1. It can be seen that the highest performance is exhibited by a two-bladed and three bladed high speed rotor with tip speed ratios in the range of $\boldsymbol{\lambda}$=7-10. Most modern three-bladed horizontal axis has similar characteristics, and is designed with low solidities, typically less than 7%. Fig. 3.1 exhibits that the American multiblade turbine shows poor performance at a lower tip-speed ratio ranges than the high-speed two and three-bladed horizontal axis turbine. Multiblade turbines, typically, have high solidities and use drag to develop high torques for mechanical water-pumping applications [62]. The four-bladed Dutch turbine shows low-performance space between the previously mentioned horizontal axis types, likely because they did not employ the airfoil or rotor design methodologies of modern horizontal axis turbine. A large difference in the performance and operating range can be found between the multiblade and low blade number turbines. Moreover, the ideal efficiency curve presented in Fig.3.1 is based on the General Momentum theory. It is theoretically possible for a properly designed rotor to exhibit higher characteristics than the current high speed turbines at approximately half of the tip speed ratios. A study was therefore conducted to explore the design space that exists between high-solidity water-pumping turbines and the high-speed two and three-bladed turbines [63-64]. In particular, the study focussed on using the same design principles used in the high-speed turbine designs to investigate the impact of solidity and turbine blade number on the performance of a small horizontal axis turbine.

4.4 Effect of Blade and Solidity Ratio

A blade-element momentum (BEM)-based optimum design routine was used to investigate the impact of solidity and turbine blade number on the performance of a small horizontal axis turbine with optimally designed blades [65-66]. Fig. 4.7 shows maximum power coefficient versus tip speed ratio at for each optimum design. A three-bladed turbine, designed for a high tip speed ratio more than one should have solidity less than 7%. In most cases high tip speed ratios are found to be more optimal for a three-bladed rotor. As shown in Fig. 4.8 for the 6 and 12-bladed cases, increasing the blade number at the high design point would increase power coefficient with low tip speed ratio. Moreover, decreasing the design tip speed ratio would increase power coefficient. It should be noted that these results are based on an idealized blade-element technique [65].

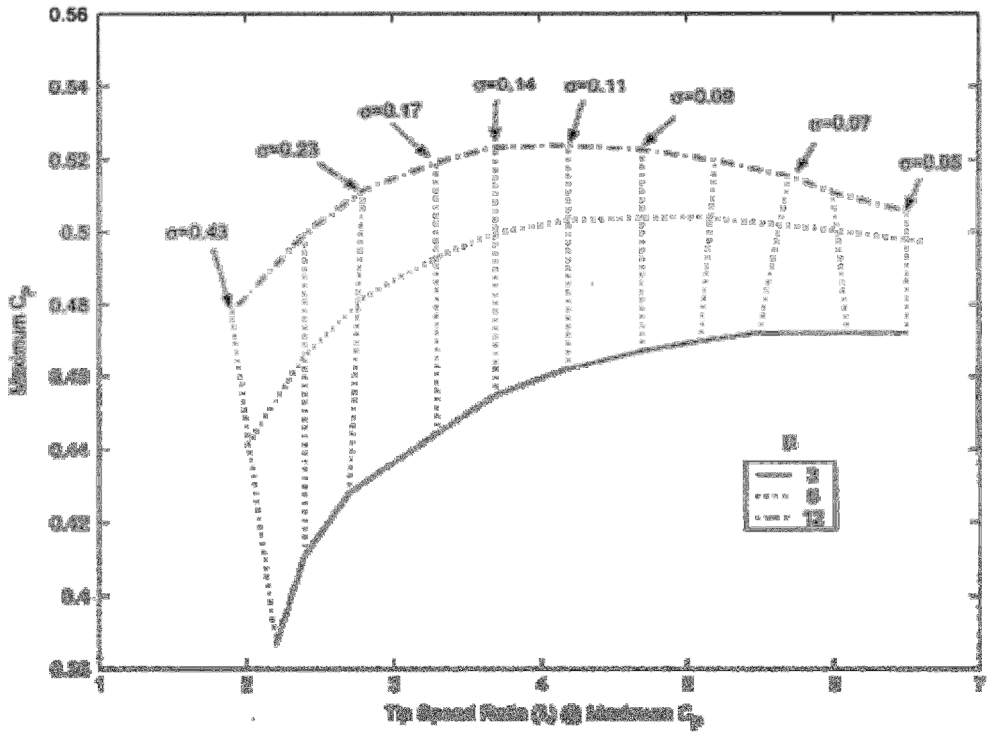

Fig. 4.7 Effect of turbine blade number (B) and solidity (σ) on C_P and $\boldsymbol{\lambda}_{opt}$, for a small HAWT with optimally designed rotor blades [65-66].

Optimum designs use complicated nonlinear twist and chord distributions, but small horizontal are often constructed with non-twisted, constant chord blades for ease of manufacture. Blades are then pitched at an angle that gives best overall performance. A comparison of maximum power coefficient for different solidity ratio non-twisted, constant chord blades [65-66] is shown in Fig 4.8.

Fig. 4.8 shows effect of turbine blade number and solidity ratio on C_P and $\boldsymbol{\lambda}_{opt}$, for a small HAWT with optimally designed rotor blades [65-66]. The curves in Fig. 4.8 were obtained from a BEM analysis technique described in [65], and are shown for comparison. Unlike the optimum designs in Fig. 4.8, constant-chord, untwisted blades were observed to produce the highest points of maximum at a higher solidity than the optimum design solution in both the three and 12-bladed cases. The difference in maximum power coefficient is small for different solidity ratio. Fig. 4.8 shows that the tip speed ratio decreases with increasing solidity and independently of the blade number. Several experiments conducted on a small horizontal axis turbine in wind tunnel with flat-plate, constant-chord, non-twisted blades, to experimentally verify the trends in versus solidity and blade number [65-66]. The experimental data confirmed that increasing solidity increases power coefficient and decreasing tip speed ratio at the point of maximum. The experiments also indicated that changes in blade number had little effect on the characteristics at a given solidity [66].

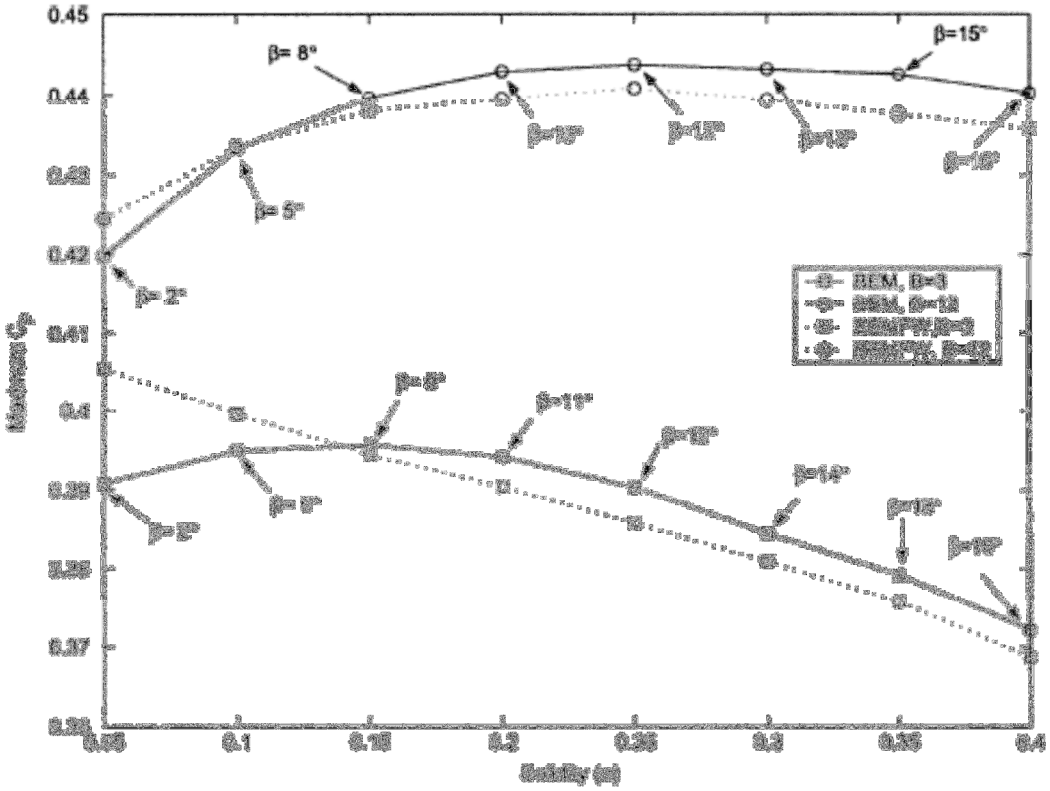

Fig. 4.8 Effect of turbine blade number (B), blade pitch angle (β), and solidity (σ) on C_P of a small HAWT [65-66].

With reference to Figs. 4.7 and 4.8, the highest power coefficient is obtained for multi blade turbines with high solidity ratio. In other words the same turbine blade diameter and flow speed conditions, the multi blade turbine will capture more energy than the three-bladed turbine when each are operated at the respective tip speed ratios which ensure maximum energy capture. For the same output-power rating, a generator coupled to the multi blade turbine will therefore be required to develop more torque.

4.5 Proposed Marine Current Energy Conversion System

The proposed energy conversion system is composed of a permanent magnet generator, rectifier, and dc-dc converter. The voltage generated by the permanent magnet machine is rectified using a three-phase passive rectifier, which converts the AC voltage generated by the PMSG to a DC voltage. The DC output voltage is boosted to a higher dc voltage.

4.5.1 Marine Current Turbine

Fig. 4.9 shows the design of a proposed horizontal axis marine turbine which has blades like conventional wind turbines but the blades face forward into the flow. The size of the blades was determined based on the fact that it can capture 20W at 1m/s. The proposed turbine has a radius of 0.15m. In order to optimize the number of blades a simulation was conducted in CFD with blade numbers 2, 4, 8 and 10. Investigation of CFD results shows that turbine with 8 number of blades provides higher tip speed ratio and torque. The angle of attack of the blades was set up for 45 degrees. This ensures high starting torque even in low flow speeds. For simplicity of the design and manufacturing, the blade chosen is a flat plate with a thickness of 0.2 inch. This arrangement of the blades around the circumference of the hub has the ability to produce reasonable torque even with smaller dimensions. The orientation of the rotor is fixed which means the blades can't change the pitch angle. This proposed system is designed to be installed in a site where the flow rate is greater than a knot (0.5m/s).

Fig. 4.9 Proposed Marine Current Turbine

4.5.2 Permanent Magnet Synchronous Generator

In this case to convert mechanical power into electrical power from the permanent magnet synchronous generator has been used. Permanent magnet electric machine is a synchronous machine which is magnetized from permanent magnets placed on the rotor instead of using a DC excitation circuit. In this case having the magnets on the rotor the electrical losses of the machine are reduced and the absence of the field losses improves the thermal characteristics of the PM machines. The absence of mechanical components such as slip rings and brushes make the machine lighter, having a high power to weight ratio which means a higher efficiency and reliability. With the advantages describe above permanent magnet synchronous generator is an attractive solution for water turbine applications. Like always, PM machines have some disadvantages: at high temperature the PM are demagnetized, difficulties to handle in manufacture, high cost of PM material. It is important to reduce the cogging torque in a PM generator because it affects self-starting ability and produces noise and mechanical vibration. Cogging is a phenomena occurring due to the non-homogenous stator reluctance and therefore the magnets tends to cling to the stator teeth [67-68]. Cogging torque is the torque produced by the shaft when the rotor of a PM generator is rotated with respect to the stator at no load condition. Cogging torque is an inherent characteristic of PM generators and is caused by the geometry of the generator. During start-up, when the rotor speed is very low the TSR is also low. At low TSR, the resulting power coefficient is very low, thus the hydrodynamic power is low. Hence it is desirable that during start-up the cogging torque of the PM generator is low enough that the hydrodynamic power can overcome it. Otherwise, with a large cogging torque, the turbine may never start. Small turbines, typically, have lower

rotor inertia than large turbines because of their shorter blades and lower mass [69-70]. Thus, the cogging torque excites the structure of the water turbine and the smoothing effect of inertia is not very dominant. Noise and mechanical vibration may be excited by the cogging torque. This type of vibration may threaten the integrity of the mechanical structure of an improperly designed small wind turbine. In terms of high marine current, the amount of torque and the kinetic energy stored in the rotor is sufficiently large that the cogging torque is insignificant. In this research a surface mounted permanent magnet generator suitable for low speed application has been used shown in Fig.4.10.This arrangement appeared as a low cost alternative solution given that there is no standard off-the shelf generator to match the requirements of this rather unique turbine. An ideal solution would have been to design a low speed, high efficiency, low-cogging generator as discussed in Appendix C.

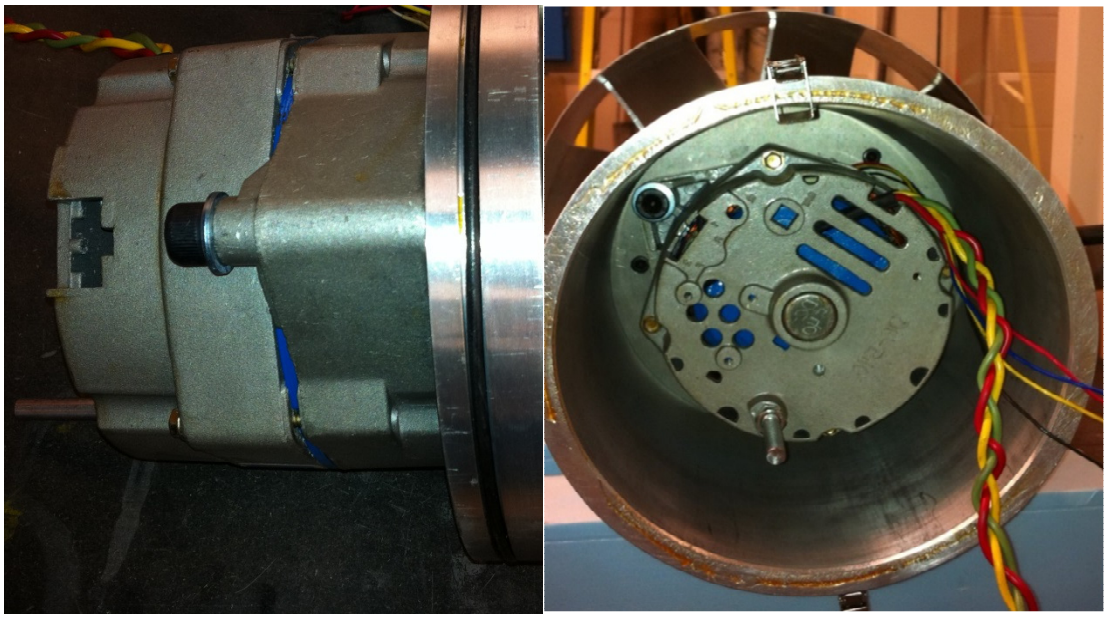

Fig. 4.10 Permanent Magnet Synchronous Generator mounted in chamber

4.5.3 Permanent Magnet Couplings

In the design of MCECS magnetic coupling is used to couple turbine and generator. Magnetic couplers are generally used to transmit torque between two rotating parts without any mechanical contact. Radial couplings are constituted of two concentric sets of magnets. Each set is ring-shaped and presents radial magnetic polarizations [71-74]. It is generally obtained by assembling radially polarized tile permanent magnets constituting pole pairs. Both turbine and generator rotate about the same axis. One set is driven by the turbine. The torque is transmitted via the second set to the load. When the leading set rotates, the torque existing between both sets forces the led one into rotation. Both turbine and generator rotate synchronously but with an angular shift. Furthermore, the torque transmitted between the two rotors depends on the number of pole pairs and their design, on the geometrical dimensions of the coupling and on the relative angular position of the rotors. The developments of synchronous couplings are tightly related to the appearance of the rare-earth permanent magnets [75-79]. The magnetic coupler also ensures that the system is completely water tight with zero leakage. Fig 4.11(a) shows that he magnets are oriented around the circumference with similar polarity to produce repulsion type force between the two sets of rings. In this particular work eight sets of rectangular neodymium magnets were used to build the coupler. Fig. 4.11(b) shows the mounting of the magnets in the structure.

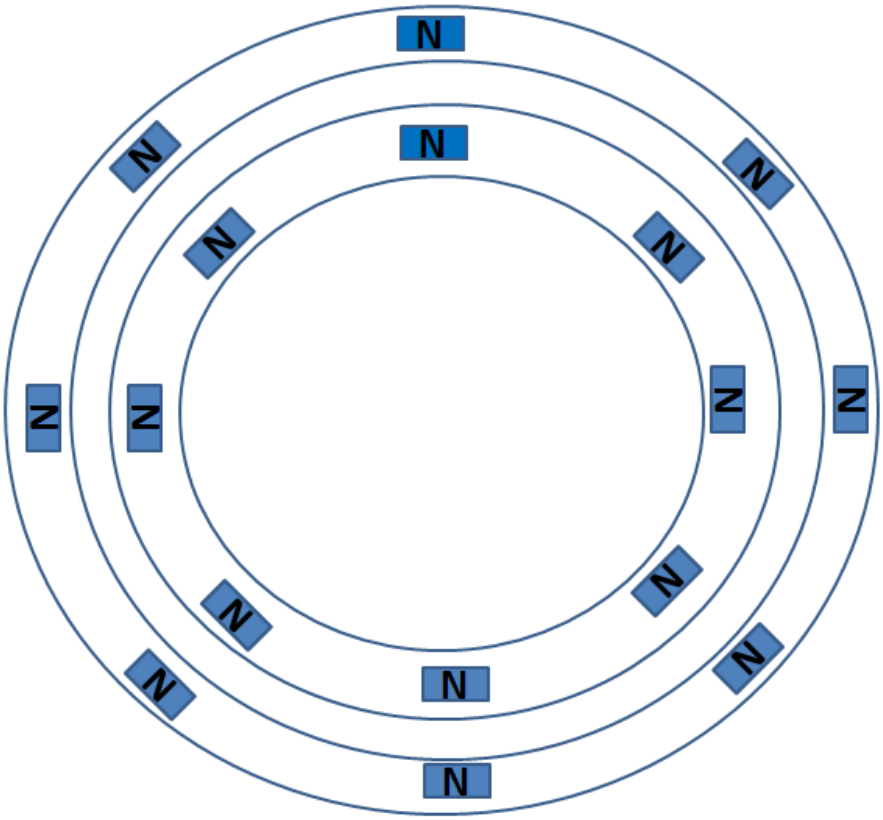

Fig 4.11(a)

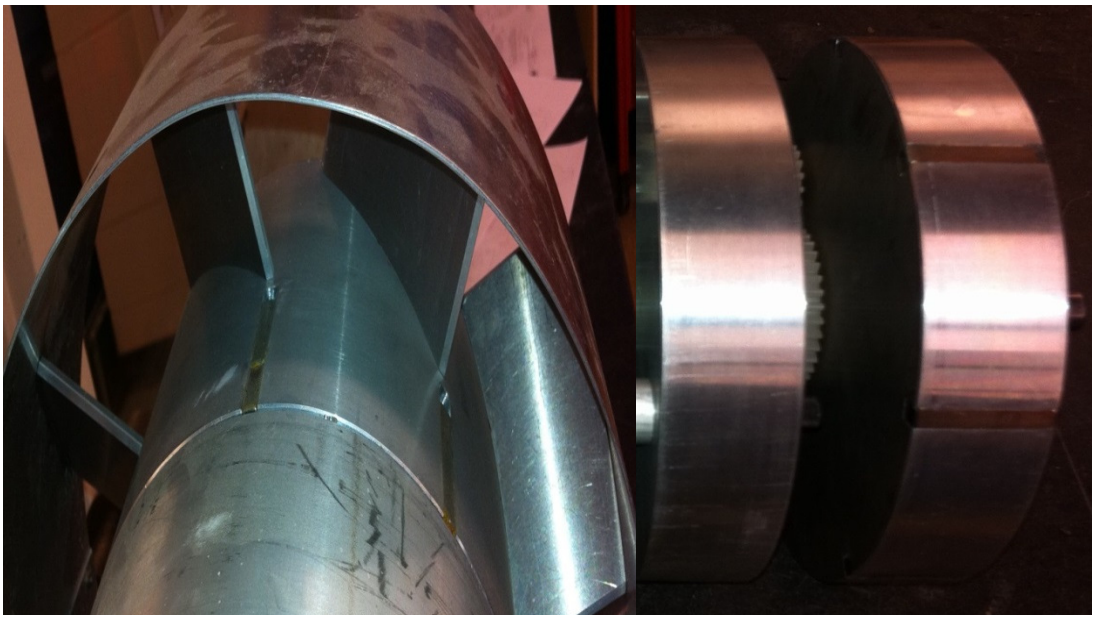

Fig 4.11(b)

Fig. 4.11(a) Geometry of magnetic coupling (b) Coupling Turbine and Generator using permanent magnets

4.5.4 Marine Current Turbine Chamber

The chamber of MCECS is cylindrical in shape and consists of components that sit underneath the water. The dimension of the chamber is 0.22m × 0.35m with a wall thickness of 0.0125m. A complete stress analysis of the chamber is given in Appendix D. For simplicity and easy maintenance the number of components inside the chamber has been minimized. The components inside the water tight chamber consist of a magnetic coupler, generator, gearbox and optical encoder. The chamber housing is made up of aluminum and protects the internal components from the environment. The main frame structure is heavy aluminum metal, able to withstand large hydrostatic loads. The heart of the marine current turbine is its electricity generating system. Inside the chamber the gearbox steps up the revolutions per minute to a speed suitable for the electrical generator. In this particular work the gears are designed with a ratio of 4 as shown in Fig 4.12.

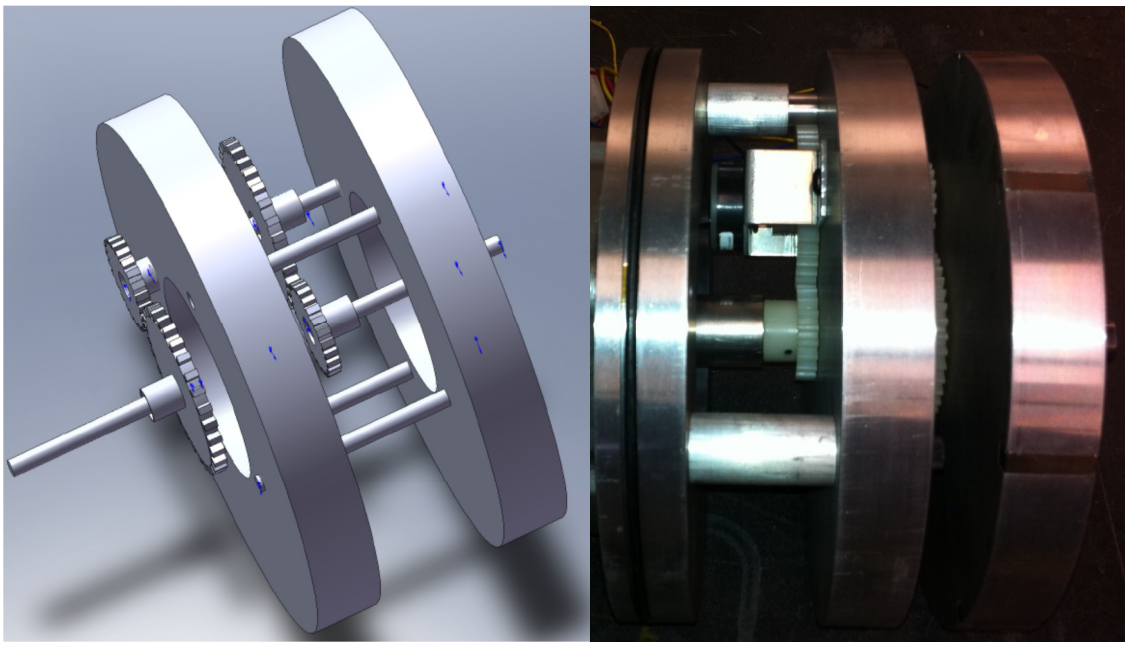

Fig. 4.12 MCECS Gear Orientation to ramp up the turbine speed

4.5.5 Power Electronics

To extract maximum power from the water current by varying the generator speed, a power electronics interface between the generator and the DC load side must be used, to provide the system with a control parameter. Ultimately, the generator speed is controlled by changing the loading of the generator by means of the power electronic converter. The two most common types of power electronics rectifiers found is the PWM rectifier and the single phase boost converter. The advantage of using a PWM rectifier is that it does not require any inductors or capacitors in the circuit. Also, by applying PWM techniques to the rectifier, good control flexibility can be obtained. However, since the PWM rectifier requires six switches in the circuit, the control scheme would be quite complicated. Since the purpose of this thesis is to build an efficient MCECS, a single phase boost converter is used. Compared to the PWM rectifier, the single phase boost converter requires only one switch in the circuit to be controlled. As a result, a simple duty ratio control loop can be used to adjust the pulse width of the switch to control the loading of the generator. Mostly the output voltage from the PMG is very low because of low marine currents [80]. In this regard, a boost converter is one of the possible solutions, where, by controlling the duty cycle of the converter the apparent load seen by the generator will be adjusted and thus, its output voltage and shaft speed. Fig. 4.13 shows the customized DC-DC switching boost converter which is designed to provide an efficient method of supplying power and boosting the voltage level. The customized converter allows changing the duty cycle based on the control algorithm.

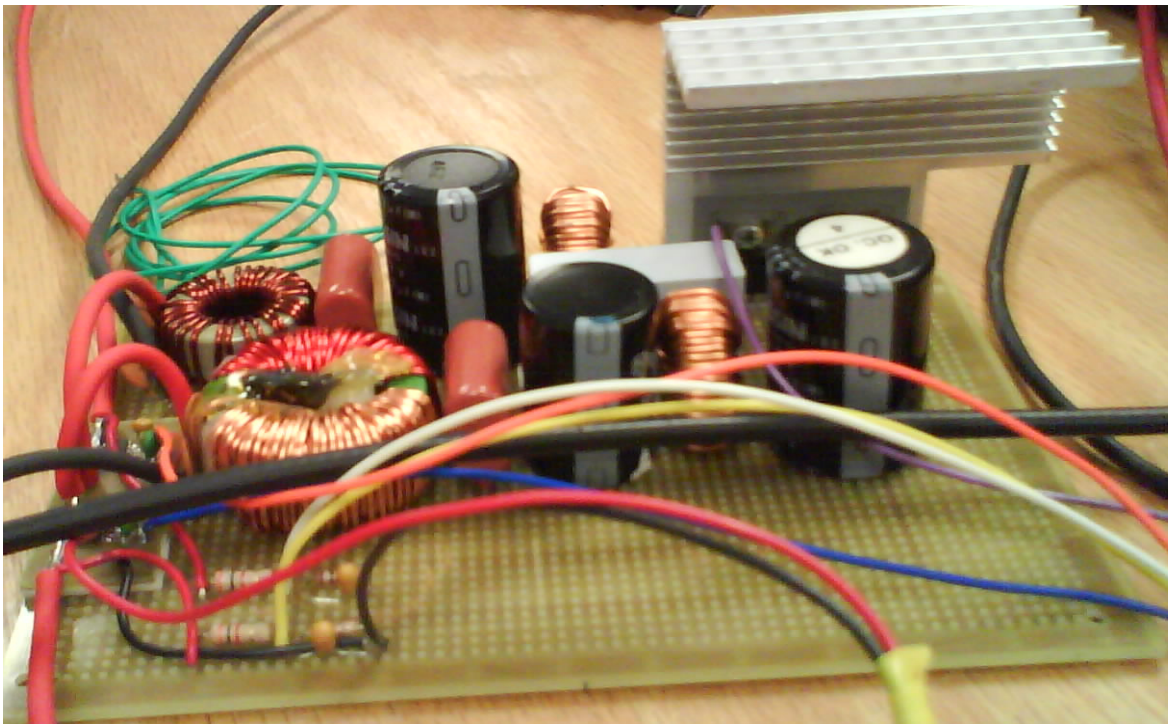

Fig. 4.13 DC -DC switching Boost Converter

Fig. 4.14 shows the overall energy harvesting system, with the focus here on the energy source, mechanical conversion, and electrical power conversion. Fig 4.14(a) shows the CAD drawing of the complete energy conversion system which consists of turbine, magnetic coupler, gears and the generator. Fig 4.14 (b) shows the actual components of the prototype assembled for functional testing.

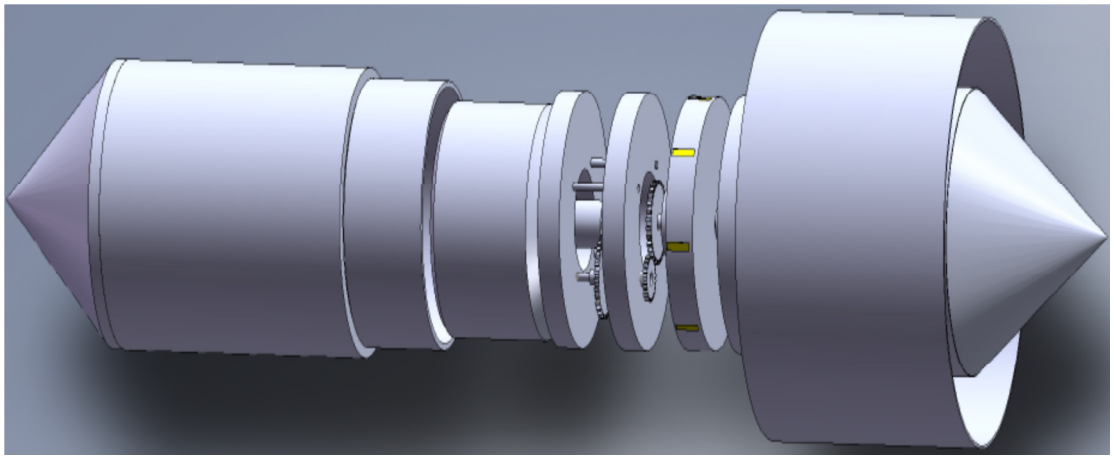

Fig. 4.14(a)

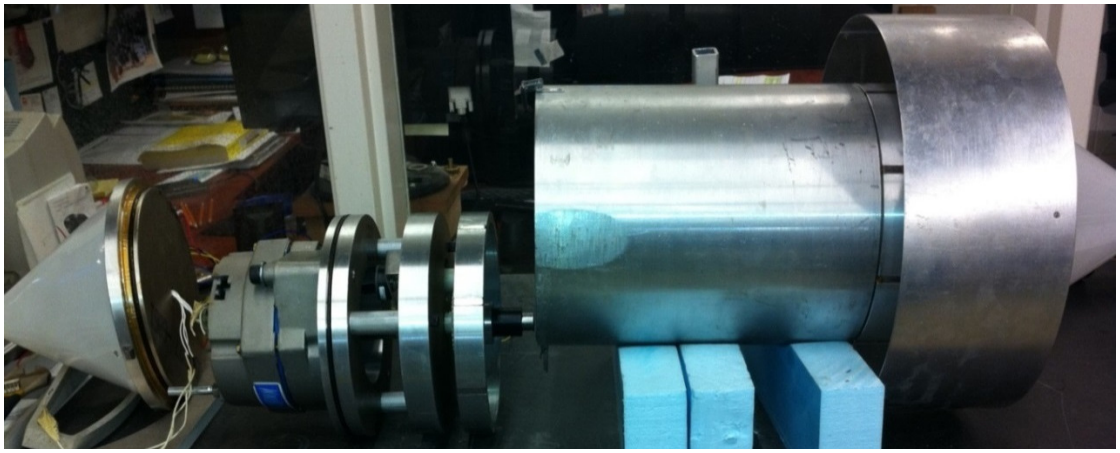

Fig. 4.14(b)

Fig. 4.14 (a) CAD drawing showing the assembly of the prototype (b) Components of Marine Current Energy Conversion System

4.6 Conclusion

This chapter highlighted the various types of turbine built and tested in a tow tank for low flow speed application. After all the investigations, a horizontal axis turbine with blades has been found to be more suitable for the application. Based on the proposed turbine, a complete energy conversion has been discussed here. A detailed mathematical model of the complete energy conversion system is carried out in the next chapter. In addition a CFD model of the turbine has also been discussed.

Chapter V

Modeling of Marine Current Energy Conversion System

5.0 Introduction

This chapter deals with the development of a Matlab/Simulink model of a small marine current energy system through the modeling of the resource, rotor, generator and dc-dc converter. The simulation model has been used as a sizing and site evaluation tool for installation of the marine current energy conversion system. An algorithm based on the Potential Flow Theory approach is used to establish a hydrodynamic turbine model.

5.1 Modeling of MCECS

Modelling is a basic tool for analysis, such as optimization, design and control. MCECS are very different in nature and therefore dynamic studies must be addressed in order to integrate marine power. Models utilised for steady-state analysis are extremely simple, while the dynamic models for MCECS are not easy to develop. Dynamic modelling is needed for various types of analysis related to system dynamics, stability, control system and optimization. In case of marine turbine modelling, researchers face problems related to the lack of data and lack of control-system structures. This leads to the situation in which many researchers model the MCECS in relatively simple form, almost neglecting the control systems, which significantly influence the reliability of the analytical results. The design of marine current turbine falls under this category equipped with a control system, which enables the power generated by the marine current to be controlled.

The dynamic performance analysis of marine current energy conversion system (MCECS) is done by developing computational models. The model usually represents the nonlinear differential equations of the various system components. It is challenging to incorporate different types of sub-models with variety timescale for hydrodynamic loads (turbine, mechanical transmission, generators, power electronics and load). Each of the models in the energy conversion system has different time scales. It is possible to develop a simulation model of MCECS that includes all dynamic effects from slow to fast hydrodynamic loads using Matlab/Simulink. Sometimes, to make it simpler, engineering practice prefers incorporating dynamic effects relevant to the problem at hand. Computational Fluid Dynamics (CFD) is nowadays considered as one of the most powerful and accurate tool for studying flow over both marine turbines. It has the capability of being able to resolve the full flow field as well as limiting the assumptions needed in calculations. Although CFD adds more computational expense compared to any numerical codes such as potential flow codes.

5.1.1 Resource Modeling

The marine current is mostly driven by the tides and to a lesser extent by thermal and density effects. The tidal current flow is always been very predictable with high degree of accuracy. This makes the available power from marine current more reliable. The Atlantic currents are primarily wind driven, but are also affected by the rotation of the earth. A resource modeling is necessary to assess the extractable power from a particular site. A suitable site should have strong current and enough depth to deploy a marine current turbine. In most cases the velocity profile for most of the time is greater than minimum, estimated to be 1.0m/s required for economic deployment of marine current

turbines. Fig. 5.1a illustrates the tidal velocity profile in eastern Canada. The red marked circle in Fig 5.1a shows region, where the root mean square current velocity is roughly 1.25 m/s. A theoretical model of tidal velocity is being developed understand flow characteristics. Fig 5.1b shows the plot of theoretical tidal velocity of magnitude 1.25m/s. The tidal period can be represented by a double sinusoid; one with a period of 12.4 h representing the diurnal tidal ebb and flow cycle, and the second one with a period of 353h representing the fortnightly spring neap period [81-83]. The equation that can be used as a model for predicting the velocity of a tidal current.

$$V = \left[V_0 + V_I \cos\frac{2\pi t}{T_1}\right]\cos\frac{2\pi t}{T_0} \quad (5.1)$$

where V_0 and V_I are constants determined from the mean spring peak and the ratio between the mean spring peak and the mean neap peak currents, T_1 is the spring neap period (353h) and T_0 is the diurnal tidal period (12.4h). The marine current will also vary in velocity as a function of the depth. The velocity varies with the depth and the velocity profile approximately follows:

$$V_h = \left(\frac{h}{H}\right)^{\alpha} V_{peak} \quad (5.2)$$

where h is the total water depth and H is any height above the seabed, α is a constant and V_{peak} is the current velocity at the surface [84-85]. The factor α is generally taken equal to $\frac{1}{7}$ and is different for different locations. The time series of depth averaged power density can be calculated as:

$$P(t) = \frac{1}{2}\rho k_s k_N {V_{peak}}^3 \quad (5.3)$$

where ρ is the density, A the cross-sectional area of flow, k_s a velocity shape factor

(0.424 for a sinusoidal flow), k_N a spring neap factor (e.g. for maximum neap stream of 60 percent of spring, $k_N = 0.57$) and V_{peak} is the maximum spring tide velocity [86].

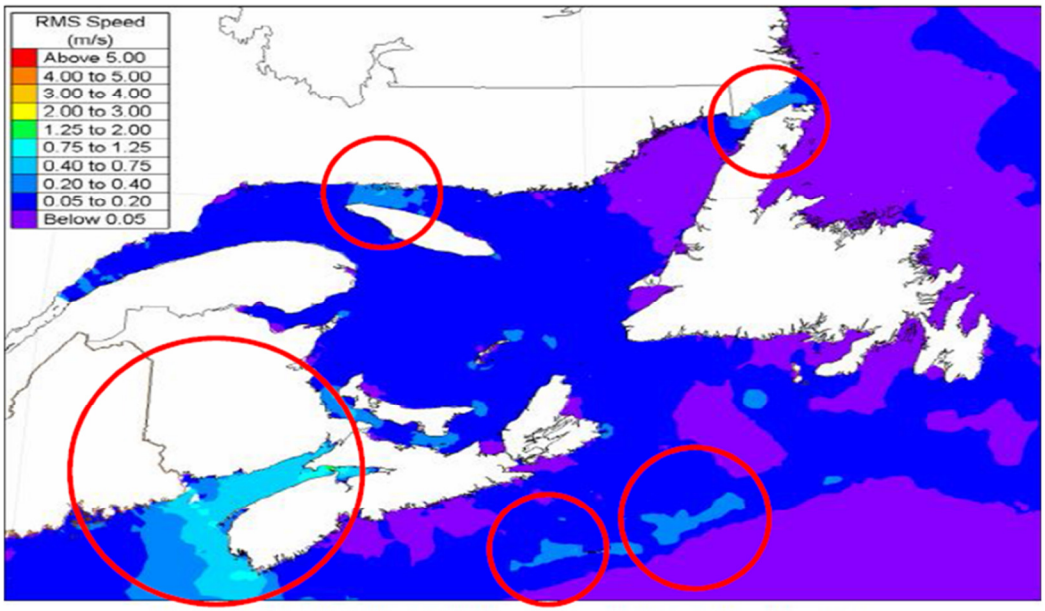

Fig. 5.1 (a)

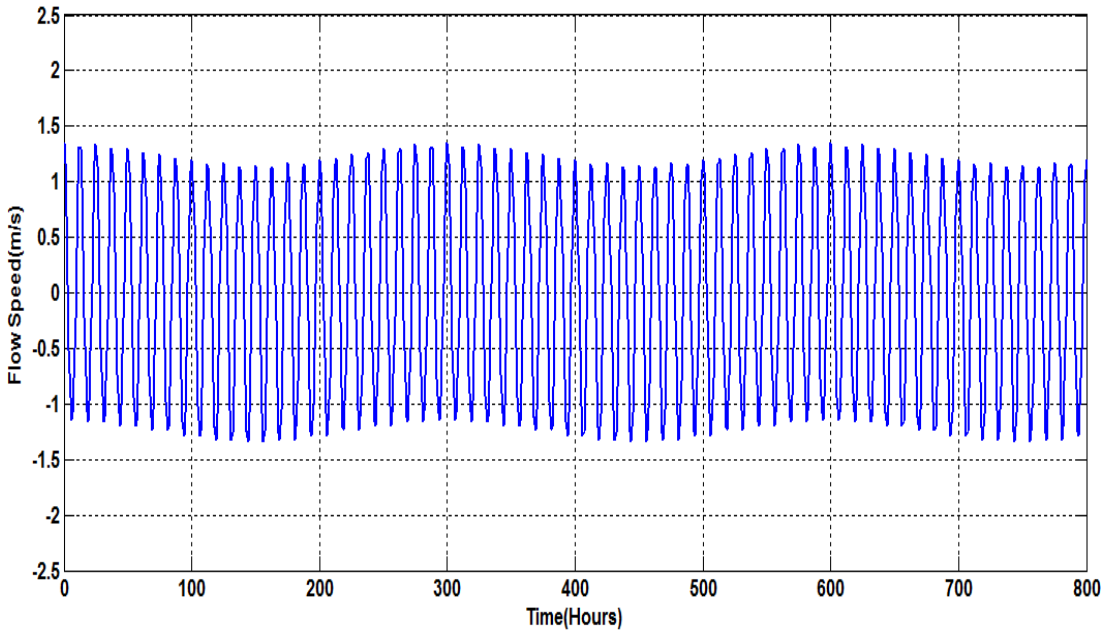

Fig.5.1(b)

Fig.5.1 (a) Root tidal current speed, Eastern Canada (b) Tidal Velocity of sites with flow speed 1.25m/s.

5.1.2 Swell Effect

The sea is usually assumed to be calm without significant swell waves. However, the real marine current modeling should include the effect of internal waves, which formed from the interfaces of water layers and difference in density and temperatures in layers. The marine turbine should be installed at a certain depth under the sea-surface so that normal sea waves will have negligible influence for the MCT system. In this case, high marine current speed is caused only by strong tidal current at spring tides.

The swell effect should be taken into account as it can cause marine current speed to fluctuate. Swell refers to long-length ocean waves usually over 150m generated from distant storms [87]. Long distance dispersion makes the swell spectrum narrower and the energy more accumulated than local wind-generated waves. Swells can propagate very deep below the sea surface and therefore have a non-negligible effect on the MCECS system. However the swell effect can lead to marine current speed fluctuations on a short period about 10 to 20s [88]. The swell-induced marine current speed variations can be based on location parameters which include sea depth, turbine installation depth, and sea state.

First order Stokes model can be used to calculate horizontal speed oscillations induced by swell waves [89-90]. The total effect on marine current speed is then calculated by the combination of predicted tidal speed and swells effect as follows:

$$V(t) = V_0 + \sum_{i=1} \frac{2\pi a_i}{T_i} \frac{\cosh(2\pi \frac{z+d}{L_i})}{sinh(2\pi \frac{d}{L_i})} \cos 2\pi \left(\frac{t}{T_i} - \frac{x}{L_i} + \varphi_i \right) \quad (5.4)$$

The first item in eq.5.4, V_o represents the predicted tidal speed, which can be regarded as a constant during a period of a few minutes; the second term represents the current speed oscillation caused by the swell. Fig. 5.2 shows the variation in the ocean current due to swell effect. It is always recommended that more than one frequency component should be considered to model a realistic swell effect. Each swell frequency component should be calculated based on the swell spectrum and ocean wave theories; φ_i represents the initial phase angle of each frequency component which is given randomly. The effects of the cross interaction between current and swell are not taken into account in this simple model. In this case JONSWAP spectrum is chosen as the swell spectrum due to its sharp peak characteristic. The JONSWAP spectrum can be expressed as:

$$S(f) = \beta_J \frac{{H_s}^2}{{T_p}^4} \frac{1}{f^5} \exp\left(-\frac{4}{5}\frac{1}{{T_p}^4}\frac{1}{f^5}\right)\gamma^Y \tag{5.5}$$

$$Y = \exp\left[-\frac{\left(T_p f - 1\right)^2}{2\sigma^2}\right] \tag{5.6}$$

$$\sigma = 0.07, \leq \frac{1}{T_P}$$

$$\sigma = 0.09, f \geq \frac{1}{T_P}$$

where γ is called peak enhancement factor which controls the sharpness of the spectral peak. Larger value can be chosen to reflect the sharp peak characteristic of swell waves. The swell spectrum with the peak enhancement factor being chosen between γ = 3~10, depending on the distance that the swell has traveled [91]. The amplitude of each

frequency components can be calculated by $a_i = \sqrt{2S(f_i)f_i}$. The narrow frequency range and sharp spectral peak illustrates the swell characteristics.

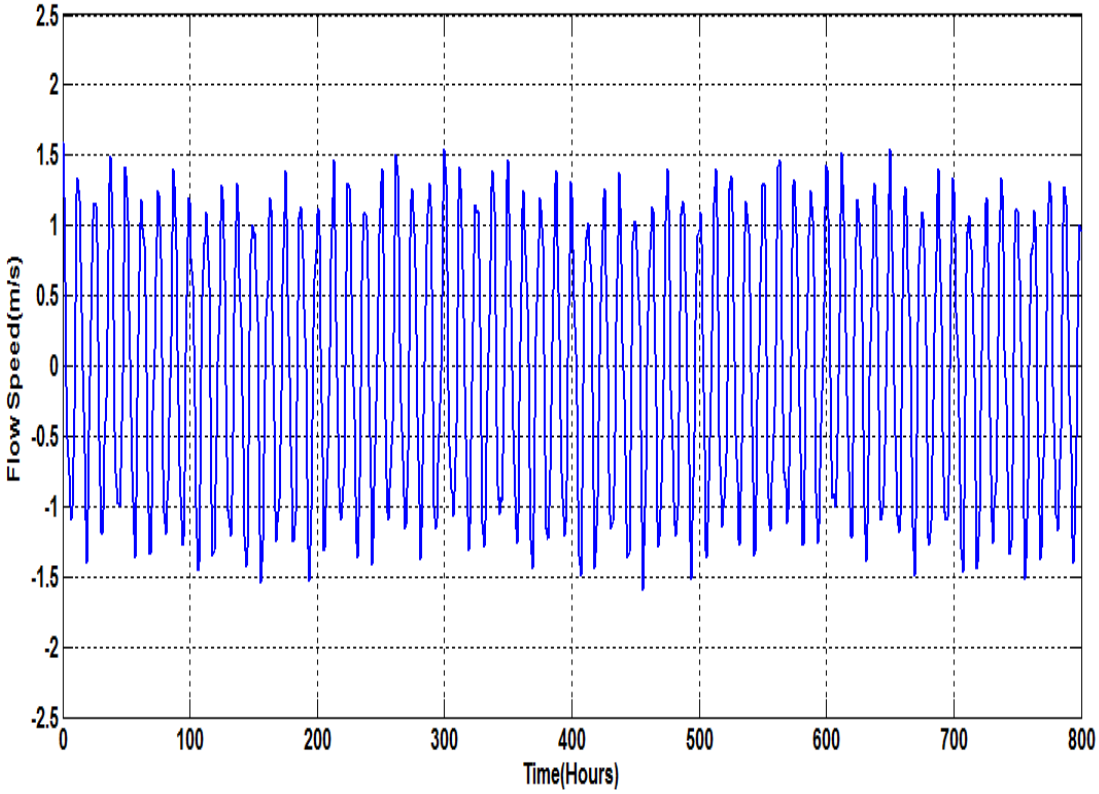

Fig.5.2 Fluctuation in flow speed due to swell effect

The swell effect can induce large oscillations in the marine current speed for any given depth. Therefore marine current speed oscillations can cause very high fluctuations in the power harnessed by marine current turbine.

5.1.3 Marine Current Turbine

The hydrodynamic modeling of the turbine takes into account the diameter, pitch and speed for a particular application. Further the design criteria can include the pitch or twist distribution across the blade span, the stall characteristics. The design becomes more complicated by changes in the non uniform speed, the current direction, the shear profile in the tidal flow, and the influences of water depth and the free surface.

The mathematical model of the turbine should represent accurately the performance and dynamic characteristics in different condition. The modeling of the turbine rotor is done using the following theories to make a comparison study :

A.1 Actuator Disk Model Theory

A.2 Blade Element Momentum Theory

A.3 Potential Flow Theory

A.4 Deflector Theory

A.5 Computational Fluid Dynamics

The author made a mathematical model of the tubine based on the above theories and compared the results.

A.1 Actuator Disk Model Theory

Literature study shows that the concept of hydrodynamics of marine current turbines has its roots in the momentum theories developed for ships propellers by Rankine and Froude, and later proposed by Betz to make estimation for efficiency (Golding 1955). Alfred Betz developed the actuator disk model based on axial momentum theory to determine the optimal power extraction of turbine. The theory uses an expression for the momentum of a stream of moving air on an actuator disc and considers the pressures and velocities of air on the free upstream side of the disc and also in the disc wake [92]. The following assumptions are made to formulate the theory:

a. The turbine consisting of infinite number of blades is represented as an actuator disk producing a discontinuity in pressure in a stream tube.
b. The fluid is incompressible and non viscous.
c. The flow is steady and non rotational i.e. translational flow is considered.

d. For air downstream of the actuator disc, the velocity is axial and constant over the stream tube section, and there is no pressure discontinuity across the stream tube boundary.

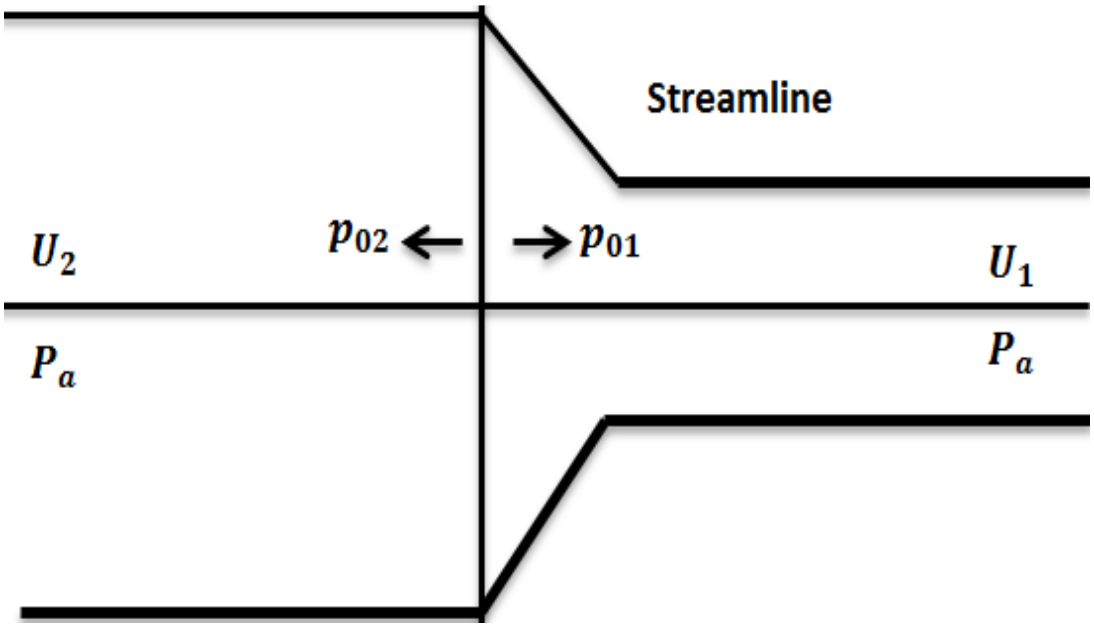

Fig. 5.3 Actuator Disk Model

Fig.5.3 shows different zones in an actuator disk which corresponds to upstream and downstream side of turbine. Applying Bernoulli's theory between the free stream and the upstream side of the turbine and also between the downstream side of the turbine and the wake.

$$H_a = p_a + \frac{{U_1}^2}{2} = p_{01} + \frac{U^2}{2} \tag{5.7}$$

$$H_d = p_a + \frac{{U_2}^2}{2} = p_{02} + \frac{U^2}{2} \tag{5.8}$$

where H_u and H_d is the upstream head and downstream head. From the momentum theory one can estimate the thrust on the disc as:

$$T \doteq \dot{m}(U_1 - U_2) = A(p_{01} - p_{02}) \quad (5.9)$$

$$T = \rho A U (U_1 - U_2) \quad (5.10)$$

The power extracted by the turbine can be expressed as:

$$P = AU (p_{01} - p_{02}) \quad (5.11)$$

Combining equations 4.7 -4.11 we can write the expression of power as below:

$$P = \frac{1}{2}\rho A U \left({U_1}^2 - {U_2}^2\right) \quad (5.12)$$

$$P = \frac{1}{4}\rho A (U_1 + U_2)\left({U_1}^2 - {U_2}^2\right) \quad (5.13)$$

Where $U = \frac{1}{2}(U_1 + U_2)$.

A rotor axial factor can be expressed as below:

$$\alpha = \frac{U_1 - U}{U_1} \quad (5.14)$$

The axial factor can be introduced to establish a relationship such that:

$$U = U_1(1 - a) \quad (5.15)$$

$$U_2 = U_1(1 - 2a) \quad (5.16)$$

Equating (5.12), (5.14), (5.15) and (5.16) one can establish the following relationship:

$$P = \frac{1}{2}\mathrm{A}\,\rho 4a\,(1-a)^2 {U_1}^3 \tag{5.17}$$

$$T = \frac{1}{2}\mathrm{A}\,\rho 4a\,\,(1-a){U_1}^2 \tag{5.18}$$

$$P = \frac{1}{2}\mathrm{A}\,\rho\, C_P {U_1}^3 \tag{5.19}$$

$$T = \frac{1}{2}A\,\rho\, C_t\, {U_1}^2 \tag{5.20}$$

$\boldsymbol{C_p}$ *i*s known as the power coefficient of the turbine and can attain a theoretical maximum value of $\frac{16}{27}$ when $\boldsymbol{a = \frac{1}{3}}$**.** The maximum value of '***a'*** can be found when the final wake velocity $\boldsymbol{U_2}$ is zero. The power coefficient can be affected because of associated phenomenon such as friction, imperfect construction, etc. and can get reduced to a small value. Similarly, $\boldsymbol{C_t}$ is known as the torque coefficient and has theoretical maximum value of $\frac{8}{9}$. The above formulas can be used to make an estimation of the upper limit performance of turbine. The theory is applicable when the rotor is modeled as disk in ideal. It is not appropriate for marine current turbines as the flow characteristics around ocean current turbine are highly complex due to turbulence caused by the blades.

A.2 Blade Element Momentum Theory

BEM theory calculates the axial and circumferential forces on a blade strip using momentum theory and using blade element theory. It then equates the axial forces on the strip and the circumferential forces on the strip to get equations for the axial induction factor and the angular induction factor. Once these are known for a strip, the forces on the strip can be calculated. The circumferential force on a strip times the radius out to it from

the axis of rotation gives the torque on the strip. Torque times rotational velocity gives the power from the strip [93-94]. BEM theory ignores the interaction between blade strips. The interaction gives horse shoe vortices in the wake. It uses 2D lift and drag foil data for the blade strips. It ignores bound and shed vortex phenomena associated with the turbine or the current speeding up or slowing down Bernoulli Equation. Let the upstream current speed be V and the downstream current speed be W as shown in Fig 4.4. Let the current speed at the turbine blades be U. Let the pressure far upstream and far downstream be P_O. Let the pressure just upstream of the turbine blades be P_A and the pressure just downstream be P_B. Application of Bernoulli upstream and downstream gives the following expression:

$$\frac{1}{2}V^2 + \frac{P_0}{\rho} = \frac{1}{2}U^2 + \frac{P_A}{\rho} \tag{5.21}$$

$$\frac{1}{2}U^2 + \frac{P_B}{\rho} = \frac{1}{2}W^2 + \frac{P_0}{\rho} \tag{5.22}$$

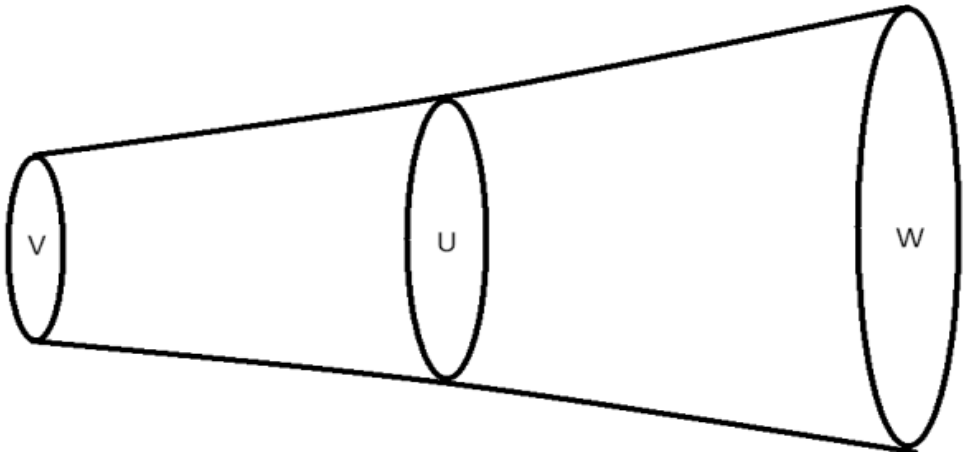

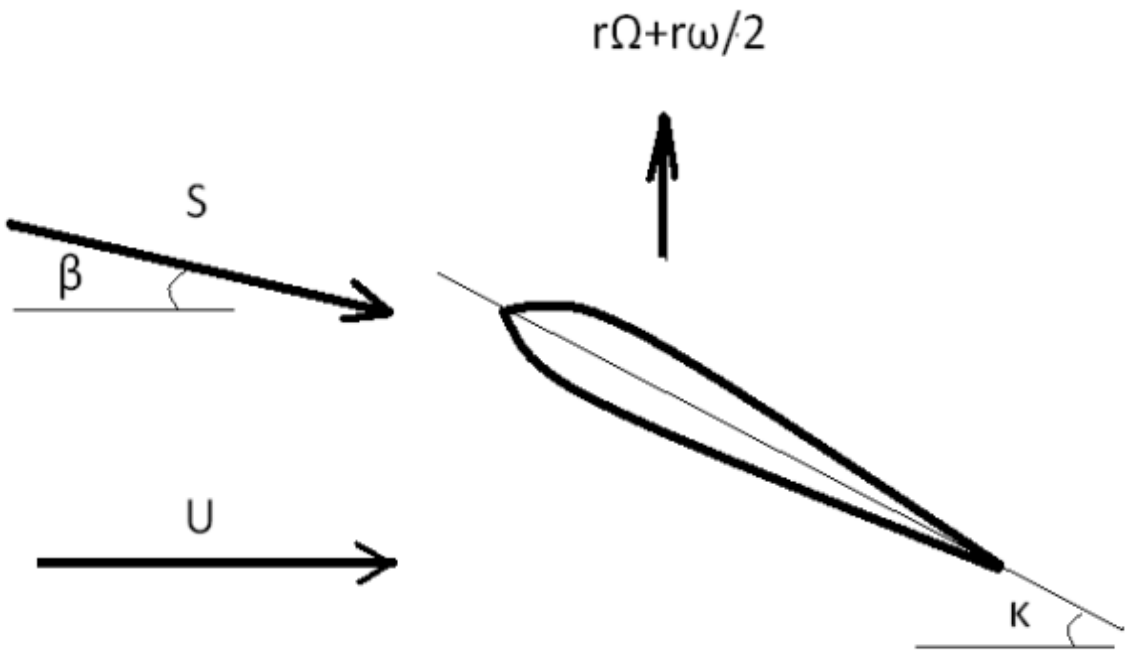

Figure 5.4 Blade Element Momentum Theories

Manipulation of eq. 5.21 and 5.22 gives the following

$$P_A - P_B = \frac{1}{2}\rho\,(V^2 - W^2) \tag{5.23}$$

Standard practice is to assume that U is the average of V and W:

$$U = \frac{1}{2}\,(V + W) \tag{5.24}$$

One can break the stream tube that encloses the turbine into to annular strips with area $2\pi r \times \Delta r$. Pressure times area gives the axial force which can be expressed as:

$$\Delta G = \frac{1}{2}\,\rho\,(V^2 - W^2)\,2\pi r\,\Delta r \tag{5.25}$$

One can define an axial induction factor α as follows

$$\alpha = \frac{V - U}{V} \tag{5.26}$$

One can write the following expression:

$$U = V(1 - \alpha) \tag{5.27}$$

$$W = V(1 - 2\alpha) \tag{5.28}$$

With this the axial force becomes:

$$\Delta G = \frac{1}{2} \rho V^2 [4\alpha (1 - \alpha)] 2\pi r \Delta r \tag{5.29}$$

When the water passes through the turbine, it takes on an angular speed ω. Upstream of the turbine the angular speed is zero. So the average angular speed is $\frac{\omega}{2}$. The rotational speed of the turbine is Ω. With this, one can define an angular induction factor ε as follows:

$$\varepsilon = \frac{\omega}{2\Omega} \tag{5.30}$$

The mass flow rate moving through an annular strip is $\rho U 2\pi r \times \Delta r$. The angular flow speed associated with rotation is ωr. The circumferential momentum is $\rho U 2\pi r \Delta r \, r\omega$. The force associated with this is

$$\Delta H = \rho U 2\pi r \Delta r \, r\omega \tag{5.31}$$

Again this can be rewritten as below:

$$\Delta H = 4\varepsilon (1 - \alpha) \rho V \Omega r 2 \pi \Delta r \tag{5.32}$$

The stream speed coming at a blade is

$$U = V(1-\alpha) \tag{5.33}$$

The speed due to rotation and downstream vortex is $r\Omega + r\omega/2 = r\Omega(1+\varepsilon)$. From geometry we can write:

$$\text{Tan}\,\beta = \frac{r\Omega(1+\varepsilon)}{V(1-\alpha)} \tag{5.34}$$

where β is the apparent flow angle. The tip speed ratio is

$$\lambda = \frac{r\Omega}{V} \tag{5.35}$$

With this the geometry equation becomes

$$\text{Tan}\,\beta = \frac{\lambda(1+\varepsilon)}{(1-\alpha)} \tag{5.36}$$

The total flow speed can be calculated as below:

$$S = \frac{U}{cos\,\beta} = \frac{V(1-\alpha)}{\cos\beta} \tag{5.37}$$

The lift force is perpendicular to S and the drag force is parallel to S. The axial and circumferential forces on a blade strip are

$$\Delta G = \Delta L\, sin\beta + \Delta D\, cos\beta \tag{5.38}$$

$$\Delta H = \Delta L\, cos\beta - \Delta D\, sin\beta \tag{5.39}$$

The lift and drag forces are

$$\Delta L = \frac{1}{2} C_L \rho\, S^2\, c\, \Delta r \tag{5.40}$$

$$\Delta D = \frac{1}{2} C_D \rho\, S^2\, c\, \Delta r \tag{5.41}$$

The lift and drag coefficients C_L and C_D would be calculated based on the apparent angle of attack θ. Let the blade angle relative to the current direction be κ. The apparent angle of attack is

$$\Theta = \kappa - \beta \tag{5.42}$$

With this the axial and circumferential forces become

$$\Delta G = \frac{1}{2} \rho S^2 (C_L Cos\beta + C_D Sin\beta) c \Delta r \tag{5.43}$$

$$\Delta H = \frac{1}{2} \rho S^2 (C_L Cos\beta - C_D Sin\beta) c \Delta r \tag{5.44}$$

If there are N blades then the forces can be written as:

$$\Delta G = \frac{1}{2} N \rho S^2 (C_L Cos\beta + C_D Sin\beta) c \Delta r \tag{5.45}$$

$$\Delta H = \frac{1}{2} N \rho S^2 (C_L Cos\beta - C_D Sin\beta) c \Delta r \tag{5.46}$$

One can define a solidarity ratio as follows

$$\sigma = \frac{Nc}{2\pi r} \tag{5.47}$$

With this the axial and circumferential forces become

$$\Delta G = \sigma \pi \rho S^2 (C_L Sin\beta + C_D Cos\beta) r \Delta r \tag{5.48}$$

$$\Delta H = \sigma \pi \rho S^2 (C_L Cos\beta - C_D Sin\beta) r \Delta r \tag{5.49}$$

Substitution of *S* into equations 5.46 and 5.47 gives

$$\Delta G = \sigma \pi \rho \left[\frac{V(1-\alpha)}{Cos\beta}\right]^2 (C_L Sin\beta + C_D Cos\beta) r \Delta r \quad (5.50)$$

$$\Delta H = \sigma \pi \rho \left[\frac{V(1-\alpha)}{Cos\beta}\right]^2 (C_L Cos\beta - C_D Sin\beta) r \Delta r \quad (5.51)$$

The equations based on momentum can be expressed as:

$$\Delta G = \frac{1}{2} Q \rho V^2 [4\alpha(1-\alpha)] 2\pi r \Delta r \quad (5.52)$$

$$\Delta H = Q 4\varepsilon (1-\alpha)\rho V \Omega r^2 \pi \Delta r \quad (5.53)$$

where Q is a correction factor for losses due to vortices. Equating the ΔG equations gives

$$\frac{1}{2} Q \rho V^2 [4\alpha(1-\alpha)]2\pi r \Delta r = \sigma \pi \rho \left[\frac{V(1-\alpha)}{Cos\beta}\right]^2 (C_L Sin\beta + C_D Cos\beta) r \Delta r \quad (5.54)$$

$$\frac{\alpha}{1-\alpha} = \frac{\sigma}{4Q\,Cos^2\beta} (C_L Sin\beta + C_D Cos\beta) \quad (5.55)$$

Equating equation 5.52 gives following expression:

$$Q\ 4\varepsilon\ (1-\alpha)\ \rho\ V\ \Omega r^2\ \pi\Delta r = \sigma\ \pi\ \rho \left[\frac{V(1-\alpha)}{Cos\beta}\right]^2 (C_L Cos\beta - C_D Sin\beta) r \Delta r \quad (5.56)$$

$$\frac{\epsilon}{1-\alpha} = \frac{\sigma}{4Q\,\lambda Cos^2\beta} (C_L Cos\beta - C_D Sin\beta) \quad (5.57)$$

The final equations can be written as below:

$$Tan\beta = \frac{\lambda(1+\varepsilon)}{(1-\alpha)} \quad (5.58)$$

$$\frac{\alpha}{1-\alpha} = \frac{\sigma}{4Q\ Cos^2\beta}\ (\ C_L\ Sin\beta + \ C_D\ Cos\beta\ ) \tag{5.59}$$

$$\frac{\epsilon}{1-\alpha} = \frac{\sigma}{4Q\ \lambda Cos^2\beta}(\ C_L\ Cos\beta\ -\ C_D\ Sin\beta\ ) \tag{5.60}$$

Iteration gives α and ε and β for each strip. Once these are known one can then calculate the axial and circumferential forces on the strip. The theory has its limitations which have been described earlier. To account for the assumptions in the theory the aero elastic codes for wind turbine are modified by incorporating number of empirical corrections. The estimated power coefficient and tip speed ratio of the turbine using BEM has been shown in Fig 5.5.

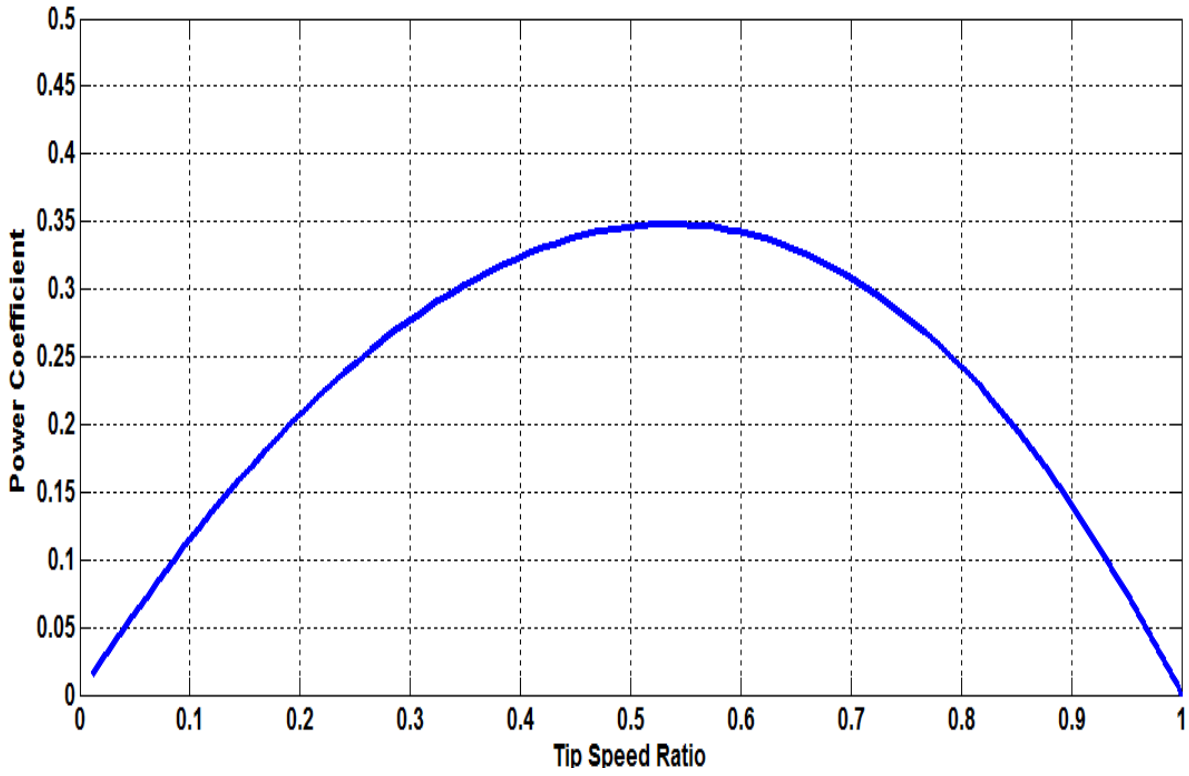

Fig. 5.5 Efficiency of the turbine using BEM theory

A.3 Deflector Theory

Due to the limitations in the blade element momentum theory, the author considers the deflector theory to model the turbine. A turbo machine is a device that takes in momentum at an inlet and gives out momentum at an output. Only tangential or circumferential components of momentum have a moment arm around the axis of rotation of a turbo machine so only those components can contribute to torque and thus power. The force due to momentum moves at the translational speed of the blade. The blade speed is the radius out to the blade times the rotational speed of the turbo machine. The power is force times speed or torque times rotational speed. The important equations are:

$$Momentum\ Force = \ \rho Q\ V_T \tag{5.61}$$

$$Translational\ Speed = \ R\ \omega \tag{5.62}$$

$$Power = \ \rho Q\ V_T\ R\ \omega \tag{5.63}$$

The power of the turbo machine can be expressed as:

$$\boldsymbol{P} \ = \ \Delta\ (\rho Q\ V_T\ R\ \omega) \ = \ \Delta\ (T\ \omega) \tag{5.64}$$

Fluid power theory assumes that a turbo machine has an infinite number of infinitesimally thin blades. A schematic of a single blade showing all the inlet and outlet flow is shown in Fig 5.6.

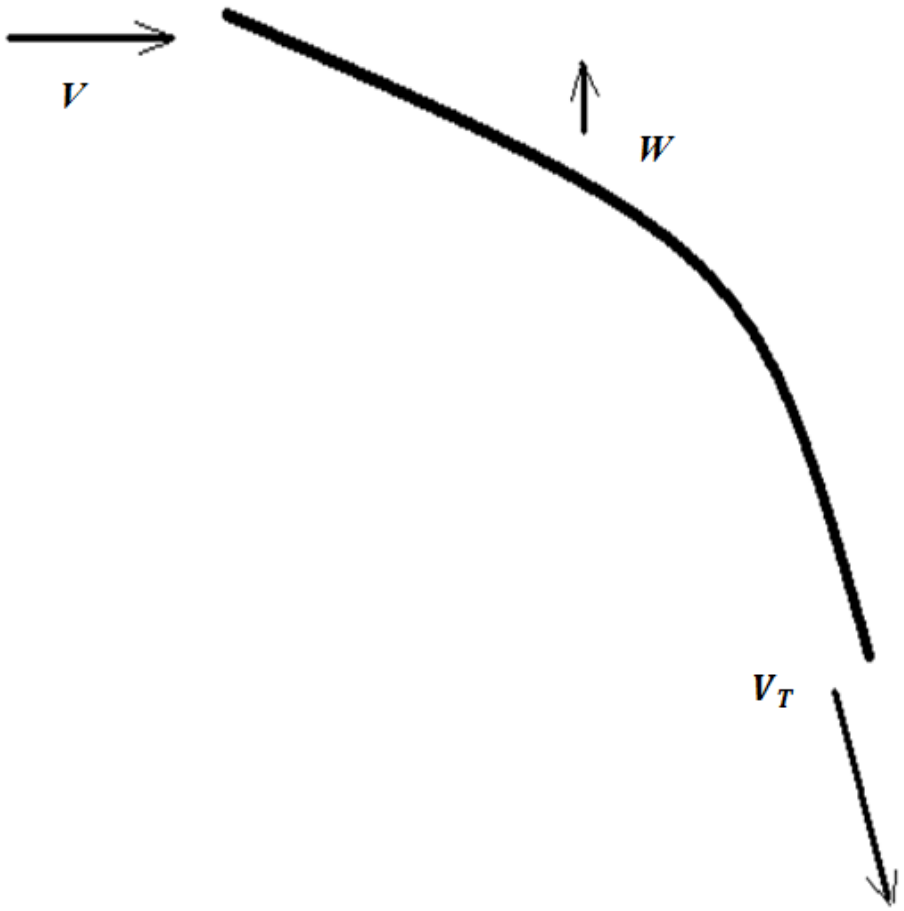

Fig 5.6 Curved blade showing flow deflection.

Assume that the flow V at the inlet is axial without any swirl. This means its tangential component V_T is zero. The speed of the blade is:

$$W = \omega R \tag{5.65}$$

The flow speed at the inlet relative to the blade is:

$$U = \sqrt{[V^2 + W^2]} \tag{5.66}$$

The blade angle can be expressed as:

$$\beta_{in} = \tan^{-1}\frac{W}{V} \tag{5.67}$$

If we set β_{in} and V then we can calculate the optimum ω to make the relative flow line up with the blade. Also if we ignore friction, the relative speed would be constant along the blade. The tangential speed at the outlet can be calculated as:

$$V_T = U\,Sin\beta_{out} - W \tag{5.68}$$

If the stream speed is S and the shroud area is A_S and the blade profile area is A_B then the flow though the turbine and the inlet speed are:

$$Q = SA_S \;; \quad V = \frac{Q}{A_B}$$

The output power of the turbine can be written as

$$\boldsymbol{P} = \rho Q\, V_T\, R\, \omega \tag{5.69}$$

The calculated power coefficient of the turbine using deflector theory has been shown in Fig 5.7. The power coefficient and tip speed ratio shows very little variation in the tip speed ratio obtained in BEM analysis.

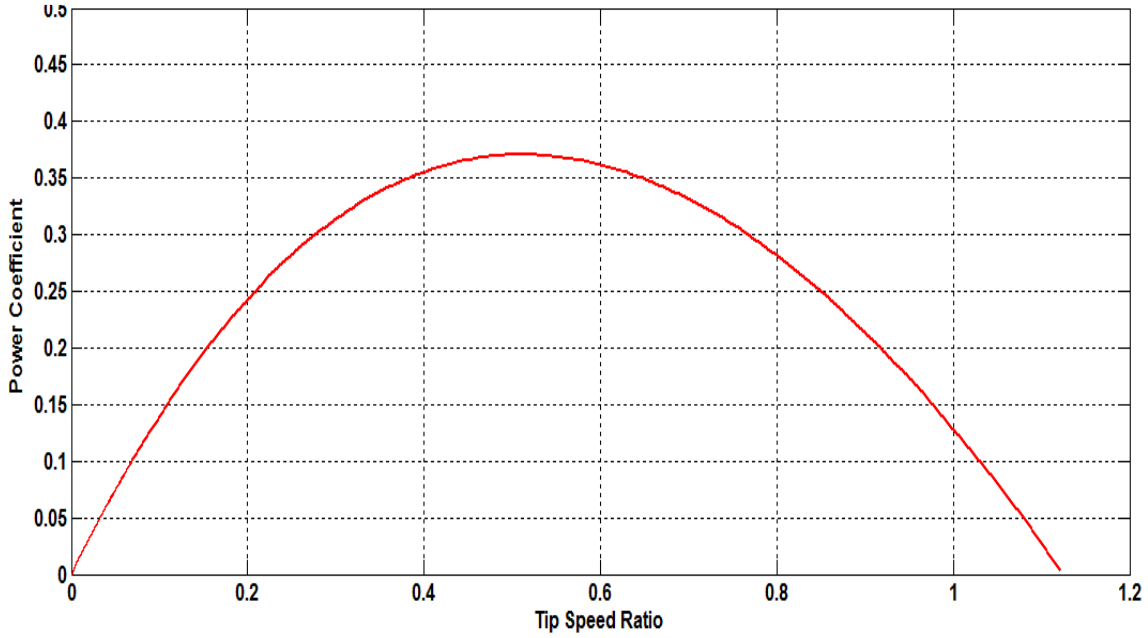

Fig 5.7 Efficiency of the turbine using deflector theory

A.4 Potential Flow Theories

The modeling of the turbine can also be done using the very popular and well known potential flow theory. The fluid is said to be ideal and can be compressible or incompressible. For flows around water current energy devices, the fluid can be considered to be incompressible [95-96]. When a body moves through an ideal fluid at steady speed, theory states that the net load acting on the body will be zero. This phenomenon includes bodies that in reality have lift and drag forces acting on them. This is known as D'Alemberts Paradox.

Ideal fluid theory determines that for a foil the fluid is able to turn the sharp corner at the trailing edge and move back over the top of the foil to join with fluid that moved around the leading edge and over the top. The two bits of fluid would then pass through two stagnation or zero velocity points, one on the bottom and one on the top. In reality, the fluid has to undergo infinite deceleration and acceleration to turn the sharp corner, which is not possible. Associated with this is an infinite suction pressure. As a real fluid tries to moves away from this into a higher pressure region on top of the foil, it moves inside a boundary layer. Within it, energy is taken from the fluid by viscous drag forces. The low to high pressure is known as an adverse pressure gradient. It turns out that fluid in a boundary layer would not be able to move into such a strong gradient and would be stopped at the trailing edge. The fluid is said to separate. The trailing edge becomes a stagnation point and a separation point. The fluid can be seen to leave the trailing edge smoothly. It turns out that the loads on the foil in this case are not zero. Note that this happens because of the behavior of a boundary layer, which is a purely viscous phenomenon. One can use a potential vortex to force the ideal flow over a foil to mimic a

real flow and leave the trailing edge smoothly. The vortex drags the stagnation point normally on top of the foil back to the trailing edge. When this is done, loads are no longer zero. A fundamental theorem of potential flow theory is that the net circulation or rotation in the flow must be constant. For a foil which started from rest, this would be zero. When a foil starts to move, a circulation is set up to make the flow leave the trailing edge smoothly. Theory suggests that an equal amount in opposite direction must be shed in a vortex sheet to keep the net circulation zero. Every time the circulation changes around the foil a vortex must be shed. These vortices are carried back from the foil by the flow. Each causes an up wash or a downwash on the foil depending on how it is rotating. Its effect gets smaller as it is carried further downstream by the flow. The vortex flows change the apparent angle of attack of the foil and thus its lift. Unsteady foil theory tries to account for the shed vortices. Probably the biggest effect of foil motion is it changes the apparent angle of attack of the foil. The load on the foil is always perpendicular to this so the load can lean forward or backward. If it leans backward, it gives rise to a drag on the foil, whereas if it leans forward, it gives rise to a thrust on the foil. There are two foil theories for steady foils. Both are based on potential flow theory. One theory superimposes a stream with a doublet to get a circular dividing streamline. A vortex is then superimposed onto this flow. The stream/doublet/vortex flow is then mapped to get the flow around a foil.

Consider the rotor of a horizontal axis turbine with radius R rotating with constant angular speed when placed in a flow. The turbine consist of N_B blades distributed symetrically around the rotor hub. For simplicity the presence of any boundaries of the flow other than the turbine blades and hub is negligible. Potential Flow Theory has been

used to develop a numerical model for the hydrodynamics of the turbine rotor blade that takes the vortices into account to estimate the apparent angle of attack on the blade at every instant. Strip theory has been used to break the span of the blade into several strips assuming that there is no interaction between the strips. Lift and drag forces on each of the strips using the apparent angle of attack are calculated to determine the total lift and drag forces on the blade. Total load, moment and torque on the blade have been calculated from the lift and drag forces. The performance characteristics curve of the turbine is generated using computational fluid dynamics. Strip theory breaks the span of a blade up into strips. Basic strip theory assumes that there is no interaction between strips and the load can be expressed as:

$$Load\ \ upon\ foil = \ \rho\ \Gamma\ V\ \partial r \tag{5.68}$$

where ρ is fluid density, V is the local flow speed and Γ is the local circulation. The local flow speed flowing toward the blade is related by :

$$\boldsymbol{S} = \sqrt{V^2 + v^2} \tag{5.69}$$

where $\boldsymbol{S}$ is the stream speed and v is the local strip speed due to rotation. The strip speed can be represented as below:

$$v = \omega r \tag{5.70}$$

where r is the radius out to the strip and ω is the rotation speed of the rotor. The circulation Γ around the blade is expressed as:

$$\Gamma\ = \ c\ \pi\ \boldsymbol{S}\ Sin\ \Theta \tag{5.71}$$

where c is the local chord and Θ is the local angle of attack.

The local angle of attack is related to the real and apparent angle of attack of the blade by:

$$\Theta = \Phi - \phi \tag{5.72}$$

where Φ is the geometrical angle of attack and ϕ is the angle of attack reduction due to blade speed. The angle of attack reduction can be written as:

$$\phi = tan^{-1}\frac{v}{S} \tag{5.73}$$

As circulation changes from one strip to the next, it induces another flow onto the strips. This can be an up wash or downwash. This changes $\boldsymbol{S}$ and v and thus the circulation itself. A horseshoe vortex is formed on each strip. Each leg of the vortex induces a flow at the center of each strip. The outer leg causes a downwash on each inner strip and an up wash on each outer strip: the inner leg does the reverse. One can add up all of these flows due to the horseshoe vortices and use them to modify v. The differential lift force is normal to the resultant velocity of the blade relative to the fluid and the differential drag force is opposite of the resultant blade velocity. Fig 5.8 shows the velocity and force triangle in a blade.

$$\partial L = \rho\, \Gamma\, \boldsymbol{S} Cos\phi\, dr \tag{5.74}$$

$$\partial D = \rho\, \Gamma\, \boldsymbol{S} Sin\phi\, dr \tag{5.75}$$

The lift and drag force components resolved in directions parallel and perpendicular to the flow is denoted as ∂T and ∂H respectively.

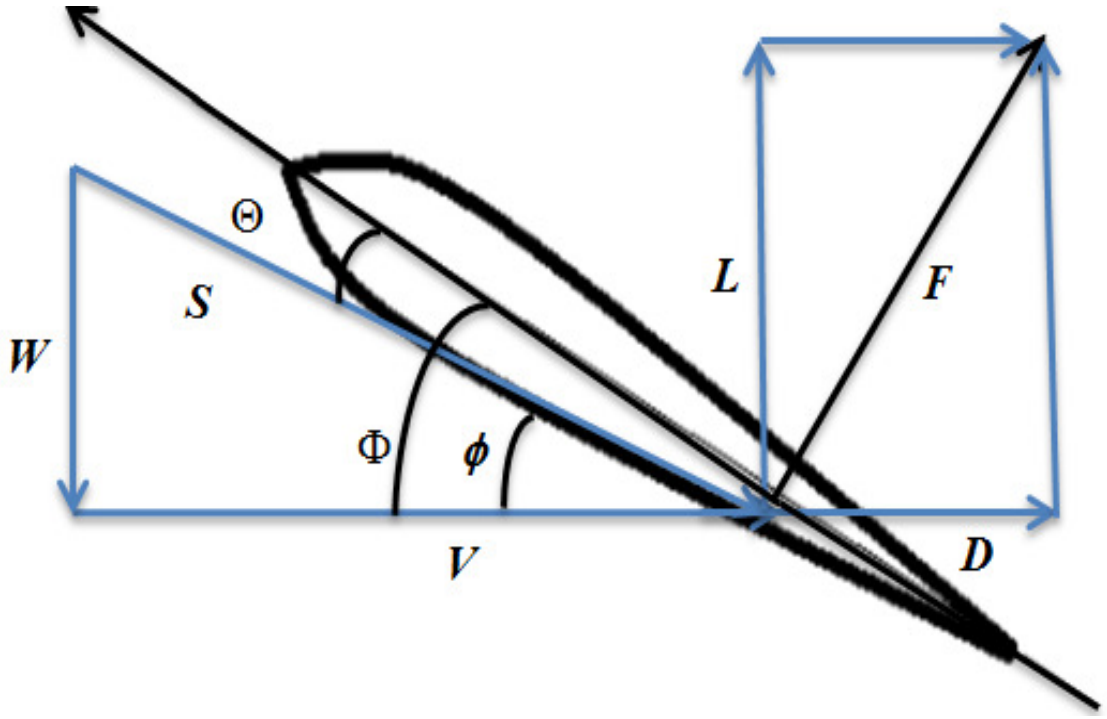

Fig 4.8 Velocity and force triangles in blade section

The term ∂M is the moment of ∂T that can be expressed as:

$$\partial P = \omega \times \partial M = 2\pi n \times r \times \partial L \tag{5.76}$$

By integration the total torque and power developed by the turbine can be written as:

$$T = \sum \partial L \tag{5.77}$$

$$M = \sum r \times \partial L \tag{5.78}$$

$$P = \sum 2\pi n \times r \times \partial L \tag{5.79}$$

For the turbine rotor, the non-dimensional quantities used to express the general performance characteristics are the tip speed ratio λ and the power coefficient C_P as follows:

$$C_P = \frac{P}{\frac{1}{2}\rho A V^3} \tag{5.80}$$

$$\lambda = \frac{\omega r}{V} \tag{5.81}$$

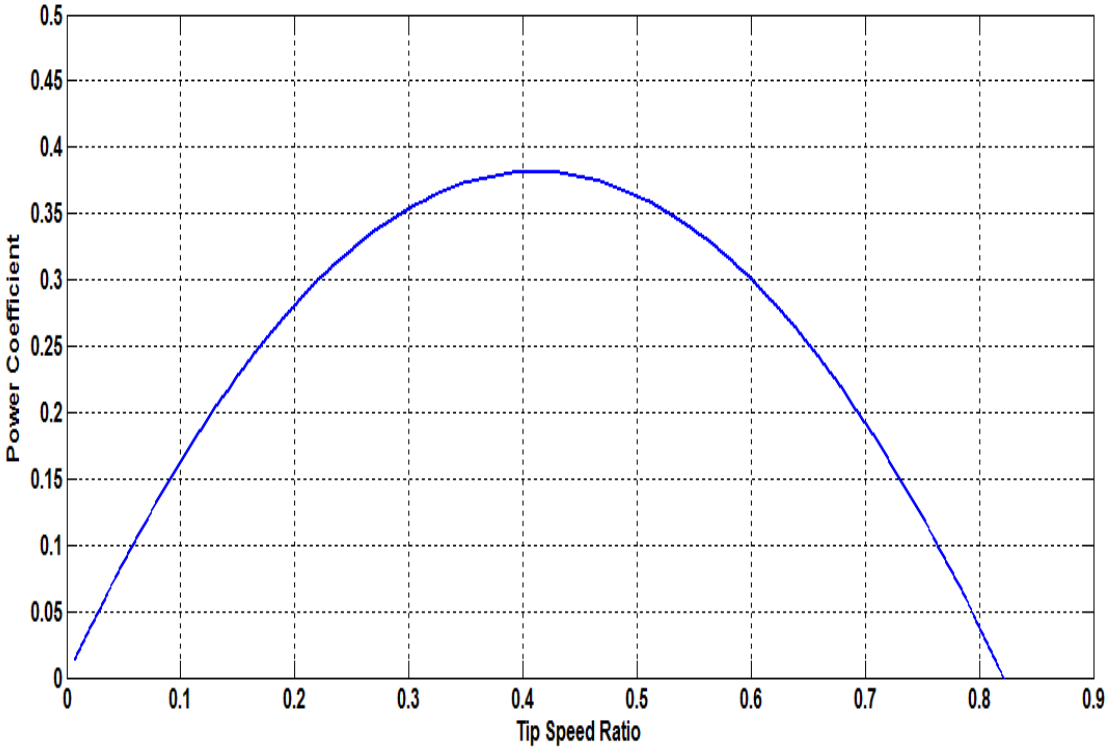

Fig. 5.9 Efficiency of the Turbine using Potential Flow Theory

Fig 5.9 shows the calculated efficiency of the turbine using potential flow theory. The simulation results closely resembles with BEM analysis. Thus the numerical model of the turbine is validated using potential flow theory.

A.5 Computational Fluid Dynamics

Computational Fluid Dynamics (CFD) has become very popular tool for studying flow over marine current turbines. It has the ability to resolve the full flow field as well as limiting the assumption needed in calculations. In CFD analysis the flow field is discretized by a Cartesian or xyz system of grid lines. Small volumes or cells surround points where grid lines cross. Conservation of momentum considerations give:

$$\rho\left(\frac{\partial U}{\partial t}+U\frac{\partial U}{\partial x}+V\frac{\partial U}{\partial y}+W\frac{\partial U}{\partial z}\right)+A = \frac{\partial P}{\partial x}+\left[\frac{\partial}{\partial x}\left(\mu\frac{\partial U}{\partial x}\right)+\frac{\partial}{\partial y}\left(\mu\frac{\partial U}{\partial y}\right)+\frac{\partial}{\partial z}\left(\mu\frac{\partial U}{\partial z}\right)\right. \quad (5.82)$$

$$\rho\left(\frac{\partial V}{\partial t}+U\frac{\partial U}{\partial x}+V\frac{\partial V}{\partial y}+W\frac{\partial V}{\partial z}\right)+B = -\frac{\partial P}{\partial y}+\left[\frac{\partial}{\partial x}\left(\mu\frac{\partial V}{\partial x}\right)+\frac{\partial}{\partial y}\left(\mu\frac{\partial V}{\partial y}\right)+\frac{\partial}{\partial z}\left(\mu\frac{\partial V}{\partial z}\right)\right] \quad (5.83)$$

$$\rho\left(\frac{\partial W}{\partial t}+U\frac{\partial W}{\partial x}+V\frac{\partial W}{\partial y}+W\frac{\partial W}{\partial z}\right)+C = -\frac{\partial P}{\partial z}-\rho g+\frac{\partial}{\partial x}\left(\mu\frac{\partial W}{\partial x}\right)+\frac{\partial}{\partial y}\left(\mu\frac{\partial W}{\partial y}\right)+\frac{\partial}{\partial z}\left(\mu\frac{\partial W}{\partial z}\right)] \quad (5.84)$$

Where $U\ V\ W$ is the velocity components in the $x\ y\ z$ directions, P is pressure, ρ is the density of water and μ is its effective viscosity. The time averaging process introduces source like terms A B C into the momentum equations. Each is a complex function of velocity and viscosity gradients as indicated below:

$$A=\frac{\partial\mu}{\partial y}\frac{\partial V}{\partial x}-\frac{\partial\mu}{\partial x}\frac{\partial V}{\partial y}-\frac{\partial\mu}{\partial z}\frac{\partial W}{\partial x}-\frac{\partial\mu}{\partial x}\frac{\partial W}{\partial z} \quad (5.85)$$

$$B = \frac{\partial \mu}{\partial x}\frac{\partial U}{\partial y} - \frac{\partial \mu}{\partial y}\frac{\partial U}{\partial x} + \frac{\partial \mu}{\partial z}\frac{\partial W}{\partial y} - \frac{\partial \mu}{\partial y}\frac{\partial W}{\partial z} \tag{5.86}$$

$$C = \frac{\partial \mu}{\partial y}\frac{\partial V}{\partial z} - \frac{\partial \mu}{\partial z}\frac{\partial V}{\partial y} - \frac{\partial \mu}{\partial x}\frac{\partial U}{\partial z} - \frac{\partial \mu}{\partial z}\frac{\partial U}{\partial x} \tag{5.87}$$

Conservation of mass considerations give:

$$\frac{\partial P}{\partial t} + \rho c^2 \left(\frac{\partial U}{\partial x} + \frac{\partial V}{\partial y} + \frac{\partial W}{\partial z} \right) = 0 \tag{5.88}$$

where c is the speed of sound in water. Although water is basically incompressible, for mass conservation, CFD takes it to be compressible. A special function F known as the Volume of Fluid or VOF function is used to locate the water surface. Material volume considerations give for F the governing equation:

$$\frac{\partial F}{\partial t} + U\frac{\partial F}{\partial x} + V\frac{\partial F}{\partial y} + W\frac{\partial F}{\partial z} = 0 \tag{5.89}$$

For water, F is taken to be unity. For air, it is taken to be zero. Regions with F between unity and zero must contain the water surface. This feature could be used to model operation of the rotor in a river. Hydrodynamics flows are generally turbulent. Engineers are usually not interested in the details of the eddy motion in a turbulent flow. Instead they need models which account for their diffusive character. One such model is known as the *k-ε* model where *k* is the local intensity of turbulence and *ε* is its local dissipation rate. Its governing equations are:

$$\frac{\partial k}{\partial t} + U\frac{\partial k}{\partial x} + V\frac{\partial k}{\partial y} + W\frac{\partial k}{\partial z}$$

$$= T_P - T_D + \left[\frac{\partial}{\partial x}\left(\alpha \frac{\partial k}{\partial x} \right) + \frac{\partial}{\partial y}\left(\alpha \frac{\partial k}{\partial y} \right) + \frac{\partial}{\partial z}\left(\alpha \frac{\partial k}{\partial z} \right) \right] \tag{5.90}$$

$$\frac{\partial \varepsilon}{\partial t} + U\frac{\partial \varepsilon}{\partial x} + V\frac{\partial \varepsilon}{\partial y} + W\frac{\partial \varepsilon}{\partial z}$$

$$= D_P - D_D + [\frac{\partial}{\partial x}\left(\beta\frac{\partial \varepsilon}{\partial x}\right) + \frac{\partial}{\partial y}\left(\beta\frac{\partial \varepsilon}{\partial y}\right) + \frac{\partial}{\partial z}\left(\beta\frac{\partial \varepsilon}{\partial z}\right)] \quad (5.91)$$

Where

$$T_D = C_D\varepsilon \quad D_D = C_2\frac{\varepsilon^2}{k}$$

$$T_p = \frac{G\mu_t}{\rho} \quad D_p = T_pC_1\frac{\varepsilon}{k}$$

$$\mu_t = C_3\frac{k^2}{\varepsilon} \quad \mu = \mu_t + \mu_l$$

$$\alpha = \frac{\mu}{a} \quad \beta = \frac{\mu}{b}$$

$$G = 2\left[\left(\frac{\partial U}{\partial x}\right)^2 + \left(\frac{\partial V}{\partial y}\right)^2 + \left(\frac{\partial W}{\partial z}\right)^2\right]$$

$$+ \left[\left(\frac{\partial U}{\partial y} + \frac{\partial V}{\partial x}\right)^2 + \left(\frac{\partial U}{\partial y} + \frac{\partial W}{\partial y}\right)^2 + \left(\frac{\partial W}{\partial y} + \frac{\partial V}{\partial y}\right)^2\right] \quad (5.92)$$

where C_D=1.0 C_1=1.44 C_2=1.92 C_3=0.9 a=1.0 b=1.3 are constants based on data from geometrically simple experiments, μ_l is the laminar viscosity, μ_t is extra viscosity due to eddy motion and G is a production function. The k-ε equations account for the convection, diffusion, production and dissipation of turbulence. The production term in the k equation is T_P while the dissipation term there is T_D. The production term in the ε equation is D_P while the dissipation term there is D_D. The function G in the production terms is a complex function of velocity gradients. The time averaging process introduces source like terms into the momentum equations. These are the A B C terms. Each is a complex function of velocity gradients. Special wall functions are used to simplify consideration of the sharp

normal gradients in velocity and turbulence near walls. A new feature known as the General Moving Object or GMO allows for moving bodies in a flow. For CFD, each governing equation is put into the form:

$$\frac{\partial M}{\partial t} = N \tag{5.93}$$

At points within the CFD grid, each governing equation is integrated numerically across a time step to get:

$$M(t + \Delta t) = M(t) + \Delta t\, N(t) \tag{5.94}$$

where the various derivatives in N are discretized using finite difference approximations. The discretization gives algebraic equations for the scalars P F k ε at points where grid lines cross and algebraic equations for the velocity components at staggered positions between the grid points. Central differences are used to discretize the viscous terms in the momentum and turbulence equations. To ensure numerical stability, a combination of central and upwind differences is used for the convective terms. Collocation or lumping is used for the T and D terms. To march the unknowns forward in time, the momentum equations are used to update U V W, the mass equation is used to update P and correct U V W, the VOF equation is used to update F and the location of the water surface, and the turbulence equations are used to update k-ε.

5.1.4 Permanent Magnet Synchronous Generator

The permanent magnet synchronous generator has been considered as the generator which can produce electricity from the mechanical energy obtained from the turbine. The dynamic model of the PMSG is generally derived from the two phase synchronous

reference frame, where the *q*-axis is 90° ahead of the *d*-axis with respect to the direction of rotation [96-98]. The synchronization between the *d-q* rotating reference frame and the *abc* 3- phase frame is maintained by phase locked loop [99-102]. Fig. 4.10 shows the *d-q* reference frame used in a salient-pole synchronous machine (similar for PMSG), where θ is the mechanical angle, also known as the angle between the rotor d-axis and the stator axis. The PMSG is modeled with the simplifying assumptionsthe stator windings are positioned sinusoidal along the air-gap as far as the mutual effect with the rotor is concerned; the stator slots cause no appreciable variations of the rotor inductances with rotor position; magnetic hysteresis and saturation effects are negligible; the stator winding is symmetrical; damping windings are not considered; the capacitance of all the windings can be neglected and the resistances are constant (this means that power losses are considered constant) [103]. A simpler model can be obtained in *d-q* rotor coordinates. The conversion between (*a,b,c*) and *d-q* coordinates can be realized by means of the Park transform [Appendix C].

$$v_q = R_s i_q + L_q \frac{di_q}{dt} + L_d \omega_e i_d + \lambda_m \omega_e \tag{5.95}$$

$$v_d = R_s i_d + L_d \frac{di_d}{dt} - L_q i_q \omega_e \tag{5.96}$$

$$\omega_e = p\omega_r \tag{5.97}$$

where subscripts d and q refer to the physical quantities that have been transformed into the d-q synchronous rotating reference frame, R_S is the stator resistance, L_d and L_q are the inductances of the generator on the d and q axis, ω_r is the generator speed and ω_e is the electrical rotating speed.

The output stator voltages of the generator are assumed sinusoidal and the equations are given below:

$$V_a = V_s \cos(\theta_r) \tag{5.98}$$

$$V_b = V_s \cos\left(\theta_r - \frac{2\pi}{3}\right) \tag{5.99}$$

$$V_c = V_s \cos\left(\theta_r + \frac{2\pi}{3}\right) \tag{5.100}$$

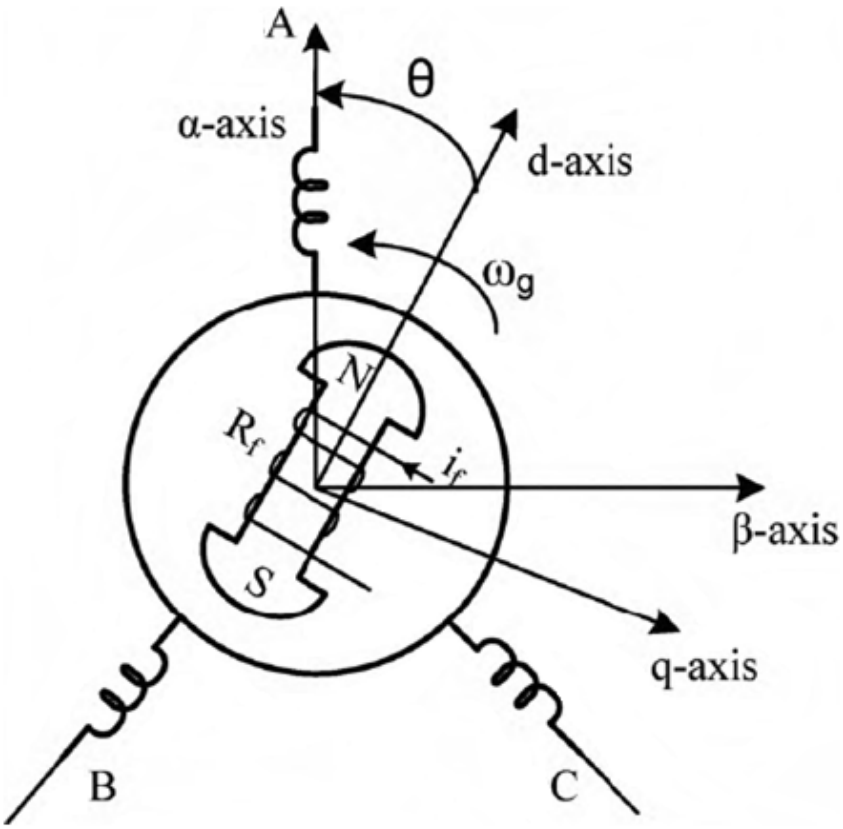

Fig.5.10 *d-q* and *a-β* axis of a typical salient-pole synchronous machine.

As the output voltages are sinusoidal, the d and q axis voltages become:

$V_q = V_s$

$V_d = 0$

The electromagnetic torque T_g of the generator can be expressed as:

$$T_g = \frac{3}{2} p \left[\lambda_m i_q + (L_d - L_q) i_d i_q \right] \quad (5.101)$$

In this particular case a surface mounted permanent magnet generator has been used which makes $L_d = L_q$.

$$T_g = \frac{3}{2} p \, \lambda_m i_q \quad (5.102)$$

For all these conditions the permanent magnet synchronous generator Park model is illustrated in Fig.5.11. The model shows that the PMSG speed can be controlled by regulating the rotor current I_q.

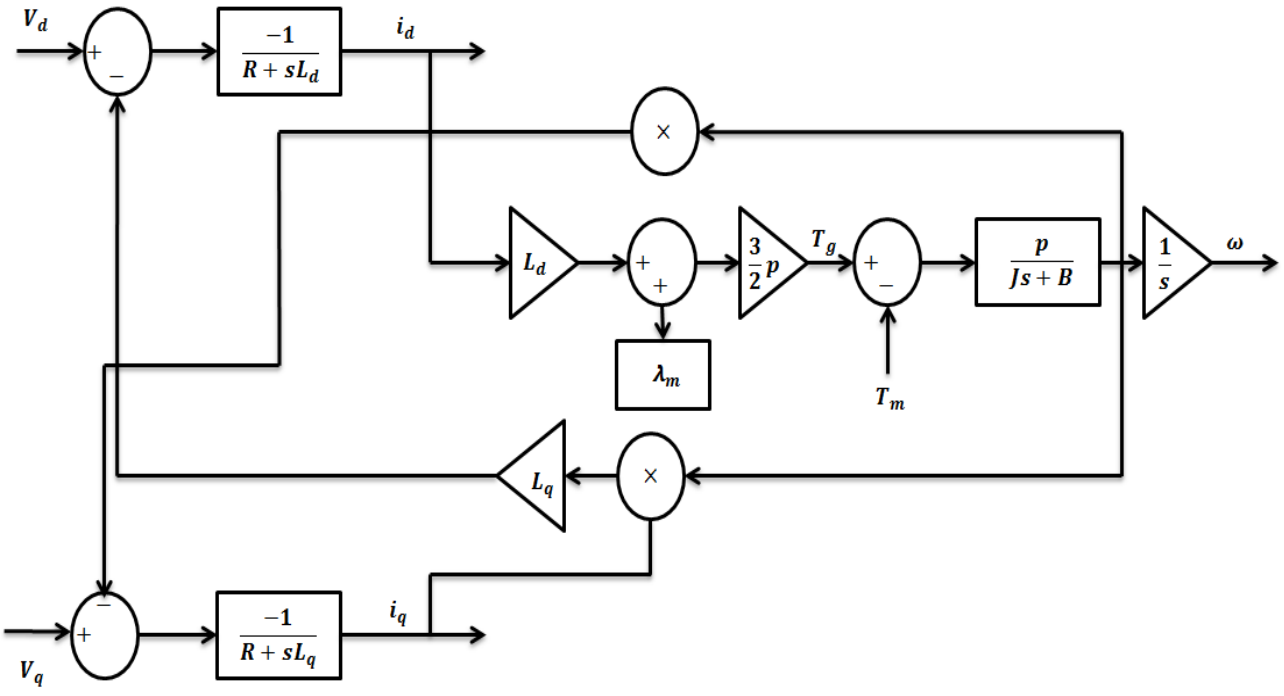

Fig 5.11 Permanent Magnet Synchronous Generator Park model

5.1.5 Drive Train

The drive train of a marine current energy conversion system consists of a turbine with multiple number of blades, magnetic coupler, a gearbox with generator. Torque equations representing the mechanical behaviour of the marine current turbine are derived, based on the two-mass model. The hydrodynamic torque from the marine turbine rotor and the electromechanical torque from the permanent magnet synchronous generator act in opposition to each other. The low speed torque T_{lm} acts as a braking torque on the rotor. The generator is driven by the high speed torque T_{hg} and braked by the generator electromagnetic torque T_g. Fig 5.12 shows the drive train model of MCECS. The the pull-out torque T_c of the magnetic coupler depends directly on the geometrical parameters. The simplest way to express the pull out torque of the magnets is:

$$T_c = T_{max} \sin p\,\delta \tag{5.103}$$

where δ known as torque angle is the relative angular position between the two magnets.

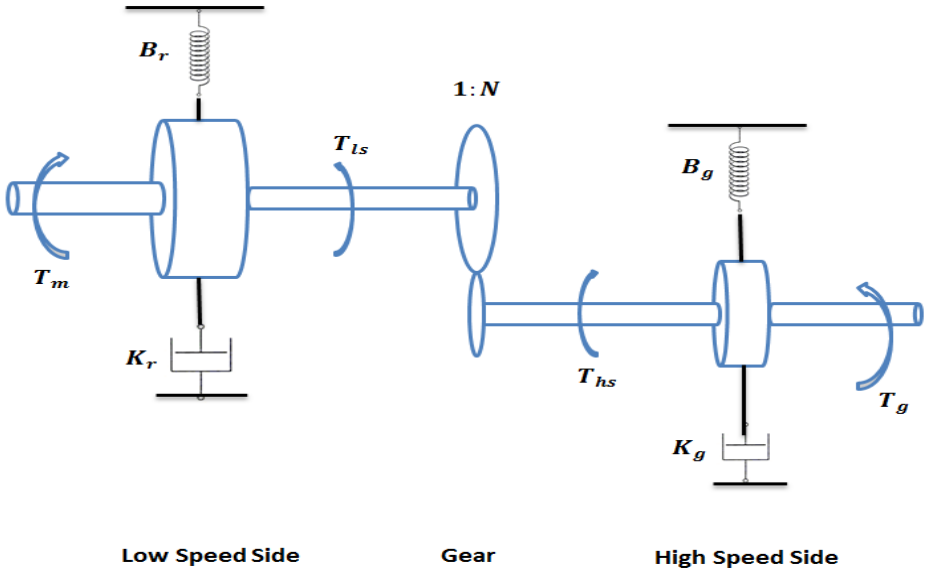

Fig. 5.12 Drive Train Model of MCECS

$$J_r \frac{\partial \omega_r}{\delta t} = T_m - K_r \omega_r - B_r \theta_r - T_{ls} - T_c \quad (5.104)$$

$$J_g \frac{\partial \omega_g}{\delta t} = T_g + T_c - K_r \omega_g - B_g \theta_g - T_{hs} \quad (5.105)$$

where B_r and B_g is the damping coefficient of rotor and generator, T_m and T_g is the hydrodynamic torque and electromagnetic torque of generator, T_c is the torque exerted by the coupler J_G and J_T are the generator and the rotor rotational inertias respectively, and N_G is the gear ratio. It must be noted that gearbox is considered because the analyzed system consists of a water turbine spininng at a very low speed. The rotor speed is increased by the gearbox ratio N_g to obtain the generator speed while the low speed torque is augmented. The gear ratio in the system can be expressed as:

$$N_G = \frac{\omega_g}{\omega_r} = \frac{T_{lm}}{T_{hg}} \quad (5.106)$$

The dynamic equation that determines the relationship between mechanical and electrical speed can be written as follows:

$$J_T \frac{\partial \omega_r}{\delta t} = T_m - K_t \omega_g - B_g \theta_g - T_g \quad (5.107)$$

where

$$J_T = J_r + {N_G}^2 J_G \quad (5.108)$$

$$B_T = B_r + {N_G}^2 B_G \quad (5.109)$$

$$K_T = K_r + {N_G}^2 \quad (5.110)$$

$$T_g = {N_G}^2 T_e \quad (5.111)$$

5.1.6 Three Phase Bridge Rectifier

The AC output voltages of a PMSG are converted into the dc voltage using an uncontrolled three phase full bridge diode rectifier [105] shown in Fig 5.13. The output voltage equation of the rectifier neglecting the commutation angle is shown in the following equation

$$V_R = \frac{3\sqrt{3}}{\pi} V_q \cos\alpha \tag{5.112}$$

$$i_d = i_q \tan\alpha \tag{5.113}$$

For an uncontrolled rectifier, the delay angle α is zero. As the delay angle α is zero, the d axis current i_d can be considered as zero. The output voltage V_R for an uncontrolled rectifier can be written as:

$$V_R = \frac{3\sqrt{3}}{\pi} V_q \tag{5.114}$$

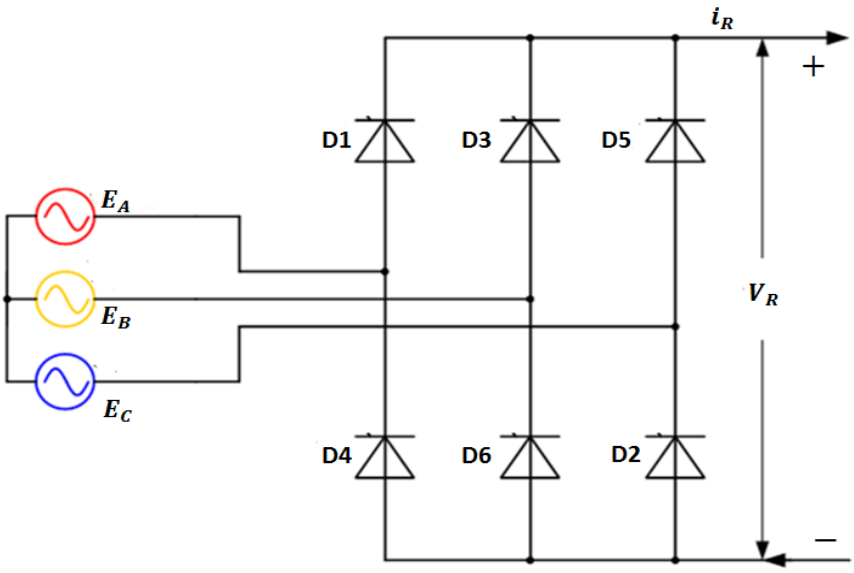

Fig. 5.13 Uncontrolled Diode Bridge Rectifiers

The instantaneous real power output of the AC generator side must be equal to the DC power of the rectifier side [106-107]. So the following equation must be satisfied:

$$\frac{3}{2}V_q i_q = V_R I_R = \frac{{V_R}^2}{R_r} \tag{5.115}$$

where I_R and R_r represent dc side current and resistance. Combining equation (5.115) and (5.116), dc side current and voltage can be expressed in terms of ac side quantities which are show in the following equations:

$$V_R' = V_R \frac{\pi}{3\sqrt{3}} = V_q \tag{5.116}$$

$$I_R' = I_R \frac{2\sqrt{3}}{\pi} = i_q \tag{5.117}$$

The resistance, inductance and capacitance of the dc side referred to rotor reference frame may be expressed as:

$$R_r' = R_r \frac{\pi^2}{18} \tag{5.118}$$

$$L' = L \frac{\pi^2}{18} \tag{5.119}$$

$$C' = C \frac{18}{\pi^2} \tag{5.120}$$

5.1.7 DC-DC Converter

The conversion of rectified DC voltage to any specified DC output voltage can be carried out employing a DC-DC converter. Fig 5.14 shows the schematic of boost converter. In this case a boost converter was used to regulate the output voltage and

operate the system at the optimum point [108-109]. The mathematical modeling of the converter yields the following relationship :

$$\frac{di_L}{dt} = \frac{E}{L_c} - (1-u)\frac{V_c}{L_c} \tag{5.121}$$

$$\frac{dV_c}{dt} = (1-u)\frac{i_L}{C_c} - \frac{V_c}{RC_c} \tag{5.122}$$

where E is the input dc voltage, V_o is the output dc voltage, i_L is the inductor current, R is the load resistance, L_c is the inductance and C_c is the capacitance. One can convert the dc side voltages, currents, resistances, inductances and capacitances to ac generator side i.e. to the rotor reference frame.

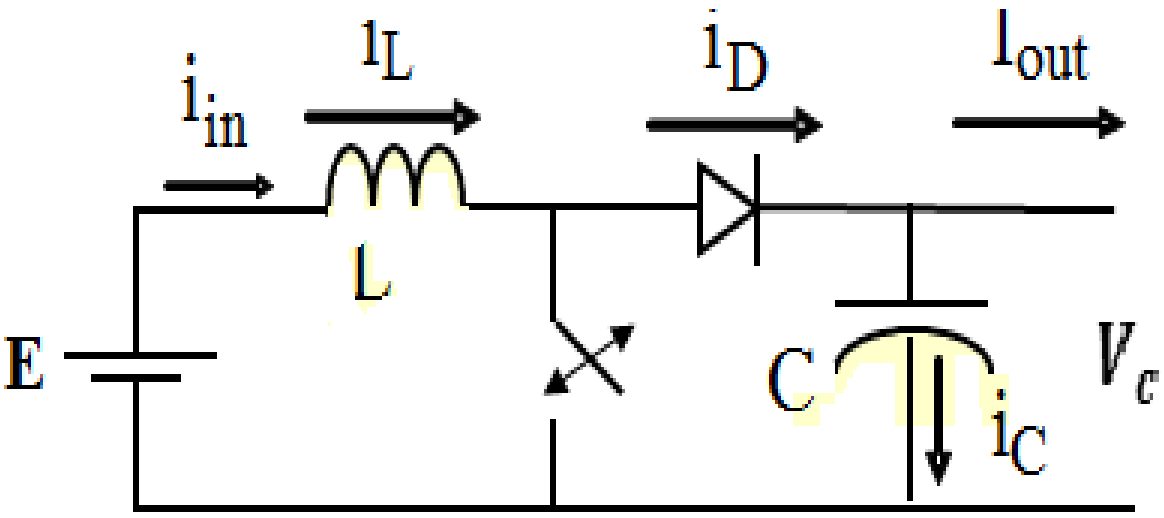

Fig. 5.14 DC-DC Boost Converter Schematic

5.2 Equivalent Circuit Model of MCECS

The electrical portion of the energy conversion system comprising of generator, dc –dc converter and load can be represented by conventional average equivalent circuit model. The equivalent circuit diagram of the MCECS is illustrated in Fig. 5.15. It enables to formulate a complete mathematical model of the electrical system.

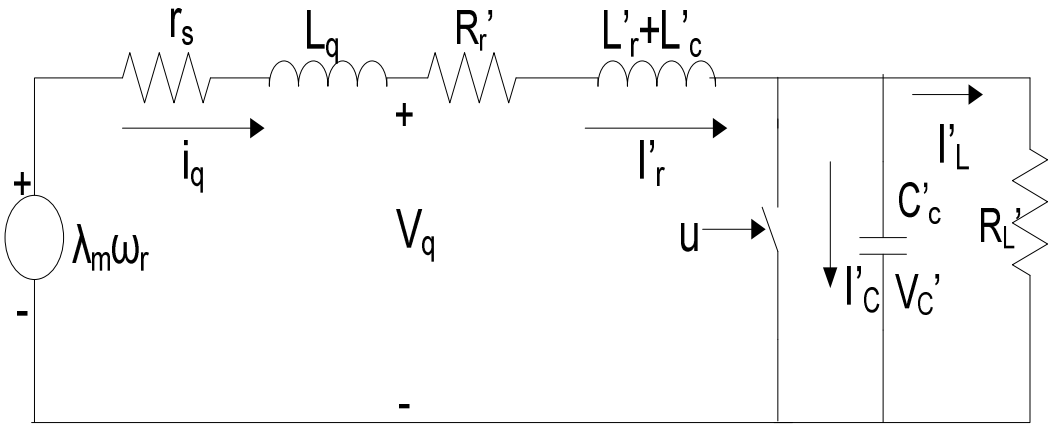

Fig. 5.15 Equivalent Circuit diagram of MCECS

From the equivalent circuit as shown in Fig 5.15, the set of differential equations governing the behaviour of the total system can be written as:

$$\frac{di_q}{dt} = -\frac{(r_s + R_r')}{L_q + L_{ac}} i_q + \frac{\lambda_m p \omega_{rm}}{L_q + L_{ac}} + (1-u)\frac{V_C'}{L_q + L_{ac}} \tag{5.124}$$

$$\frac{dV_C'}{dt} = (1-u)\frac{i_q}{C_c'} - \frac{V_C'}{R_L' L_{ac} C_c'} \tag{5.125}$$

$$T_{em} = \frac{3}{2} p L_d i_q \tag{5.126}$$

$$L_{ac} = L_r' + L_C' \tag{5.127}$$

where L_r' and L_C' are rectifier and boost converter inductances respectively, referred to the rotor reference frame. C_c' is the capacitance of the boost converter referred to the generator side.

5.3 Conclusion

In this chapter the theoretical hydrodynamics of the foil in a flow has been discussed. The unsteady foil theory explained in this chapter can be used to develop a numerical model of an ocean current turbine. The numerical models have to make several assumptions and corrections to account for the full three-dimensional, turbulent flow and dynamics around the turbine blades. CFD eliminates the need for many, but not all, of these assumptions. It also has the advantage of resolving the full time-dependent flow field, allowing for better understanding of the flow at the blade wall as well as in the wake of the turbine. However CFD comes with a much greater computation cost. Also a complete modeling of the marine current energy conversion system has been developed.

Chapter VI

Maximum Power Point Tracking of MCECS

6.0 Introduction

In this chapter different maximum power point techniques, suitable to any particular marine current turbine configuration, can be used. In most cases, classical PI or PID control are preferred. However, advanced control techniques can be used in order to ensure better performances, especially for guaranteeing robustness to modeling uncertainties. For example, adaptive back stepping control is a well-performing solution when dealing with dynamical feature uncertainties.

6.1 Maximum Power Point Technique

The maximum of the power curve for a particular flow speed occurs at a particular rotor speed. Due to the hydrodynamic characteristics of a water turbine, a small variation from the optimum rotor speed will cause a significant decrease in the power extracted from the wind. Generally turbines do not operate at the optimum speed for any given wind current because its rotor speed is dependent on the generator loading as well as the fluctuations in marine current. The hydrodynamics of a wind turbine (governed by the Cp function) shows that then same turbine angular speed for different wind speeds will result in different levels of extracted power. The optimum speed for maximum power extraction is different for each wind speed but the optimum TSR value remains the same. In order to maximize the amount of power captured by the turbine, variable-speed marine turbine systems are used because they allow turbine speed variation. A power extraction strategy

assess the flow conditions and then forces the system to adjust the turbine's rotational speed through power electronic control and/or mechanical devices so that it will operate at the turbine's highest efficiency. From the electronics point of view, this goal can be achieved through different converter topologies and maximum power point tracking (MPPT) algorithms. [110-115]. A tracker basically consists of two components, a switch-mode converter and a controller with tracking capability. The switch-mode converter is the core of the entire supply. The converter allows energy at one potential to be drawn stores as magnetic energy in an inductor, and then releases at a different potential. By setting up the switch-mode section in various topologies either high-to-low (buck converter) or low-to-high (boost) voltage converters can be constructed. The goal of a switch-mode power supply is to provide a constant output voltage or current. Many MPPT techniques are used nowadays but there are two main methods, which are the most popular:

A. Tip-Speed Ratio control (TSR),

B. Hill Climb Search (HCS).

A. Tip Speed Ratio

Tip speed ratio control method regulates turbine rotor speed to maintain an optimal TSR and requires measurement of both the flow speed and rotational speed of turbine. The optimal TSR for a given flow speed is obtained from the turbine-generator characteristics and varies from system to system. The block diagram of the tip speed ratio control method is shown in Fig. 5.1. Therefore this control approach requires extensive turbine knowledge and measurement of generator speed and water speed, thus increasing number

of sensors and complexity. This makes the practical implementation of the algorithm expensive and sometimes difficult to implement.

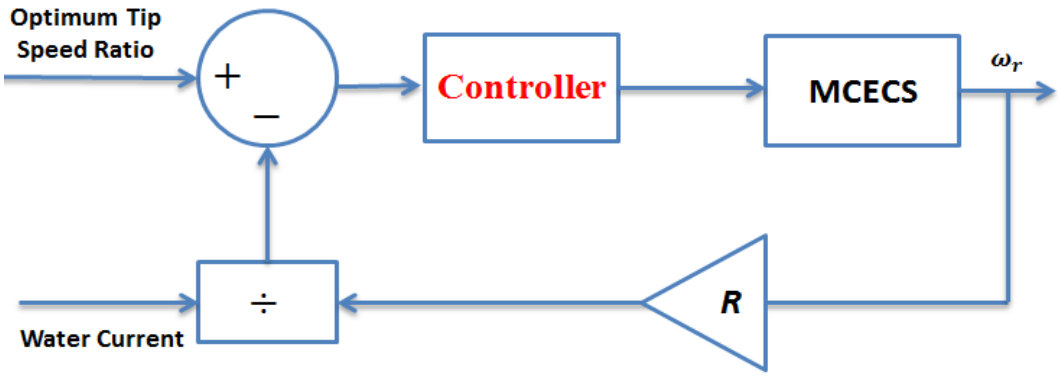

Fig 6.1 The block diagram of the tip speed ratio control

B. Hill Climbing Search

In order to avoid these difficulties, it is often recommended to use Hill Climbing Search Technique [116-122]. The algorithm continuously searches for the turbine peak output power by varying the generator speed/torque and change in power direction to determine the correct variation. While each of these three methods has their own merits and demerits, a number of variations of these methods have been proposed over the years using different techniques that address these issues.

6.2 MPPT Control Strategy of MCECS

The mechanical input power P_T to the PMSG generator from the marine turbine can be expressed as,

$$P_T = \frac{1}{2} A\rho C_p (v_w)^3 = \frac{1}{2} A\rho C_p \left(\frac{\omega_T R}{\lambda}\right)^3 \quad (6.1)$$

where A is the turbine blades' swept area (m^2), ρ is the density of the water, C_p is the power coefficient of the turbine, v_w is the flow speed of the water, ω_T is the rotational speed of the turbine and λ is the tip speed ratio. The optimum power output P_{T_opt} from a turbine is given by ,

$$P_{T\_opt} = \frac{1}{2} A\rho C_{p\_opt} \left(\frac{\omega_{T\_opt} R}{\lambda_{opt}} \right)^3 = K_{opt} \left({\omega_{T\_opt}}^3 \right) \tag{6.2}$$

The turbine optimum torque $T_{tur_{opt}}$ can be expressed as [123],

$$T_{tur_{opt}} = K_{opt} \left({\omega_{T_{opt}}}^2 \right) \tag{6.3}$$

where optimum co-efficient K_{opt} is given by,

$$K_{opt} = \frac{1}{2} A\rho C_{p_{opt}} \left(\frac{R}{\lambda_{opt}} \right)^3 \tag{6.4}$$

The optimum reference torque of the permanent magnet synchronous generator is [124-127]. It can be observed from the block diagram represented in Fig. 6.2, that the principle of this method is to adjust the PMSG torque according to a maximum power reference torque of the water turbine at a given wind speed.

$$T_{g_{opt}} = K_{opt} {\omega_g}^2 \tag{6.5}$$

where ω_g is rotational speed of the generator. The developed electromagnetic torque of a PMSG T_{em} is given by,

$$T_{em} = 1.5 p \lambda_m i_q \tag{6.6}$$

where p is the number of pole pairs, λ_m is the permanent magnet flux linkage and i_q is the q-axis stator current. The optimum q-axis stator current can be expressed as,

$$i_q^* = \frac{T_{g_{opt}}}{1.5 p \lambda_m} = \frac{K_{opt} {\omega_g}^2}{1.5 p \lambda_m} \tag{6.7}$$

The reference input dc current to the dc-dc converter can be determined from the following equation:

$$i_L^* = \frac{\pi * i_q^*}{2\sqrt{3}} \tag{6.8}$$

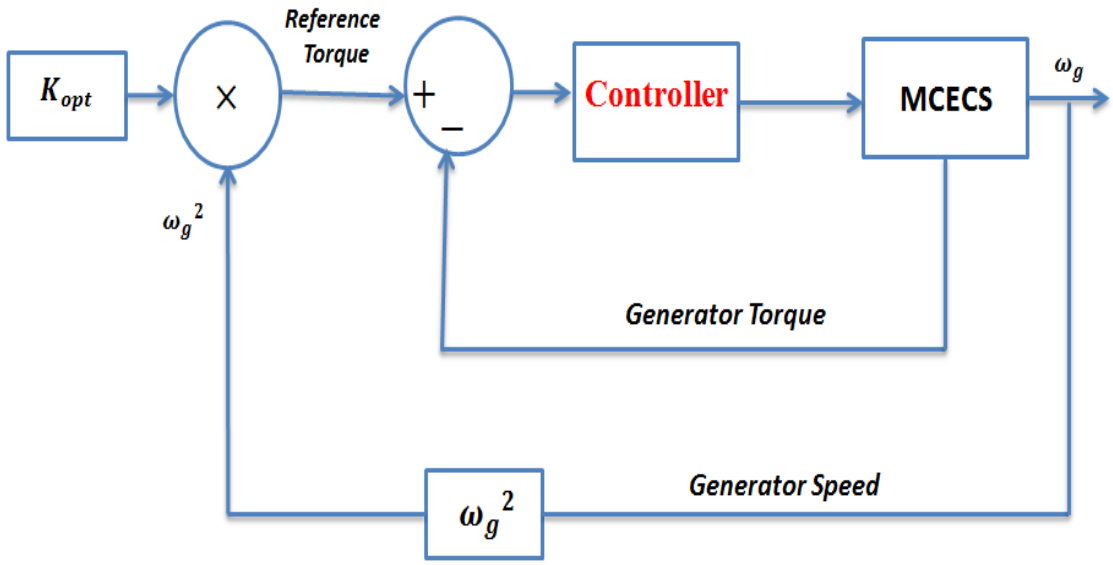

Fig. 6.2 The block diagram of optimal torque control MPPT method

In this approach, the developed electromagnetic torque of a PMSG is controlled so that the generator output power follows the optimum power curve. The generator shaft speed accelerates or decelerates based on the difference of the turbine output mechanical torque and the developed generator torque. As a result, both the generator torque and the turbine output torque reach the optimum torque points and, respectively and the turbine rotates at the maximum power point. This control strategy does not require any information about the flow speed of the water and thus the MPPT control is performed without the generator's inherent parameters. Fig 6.3 shows the power curve of the energy conversion system.

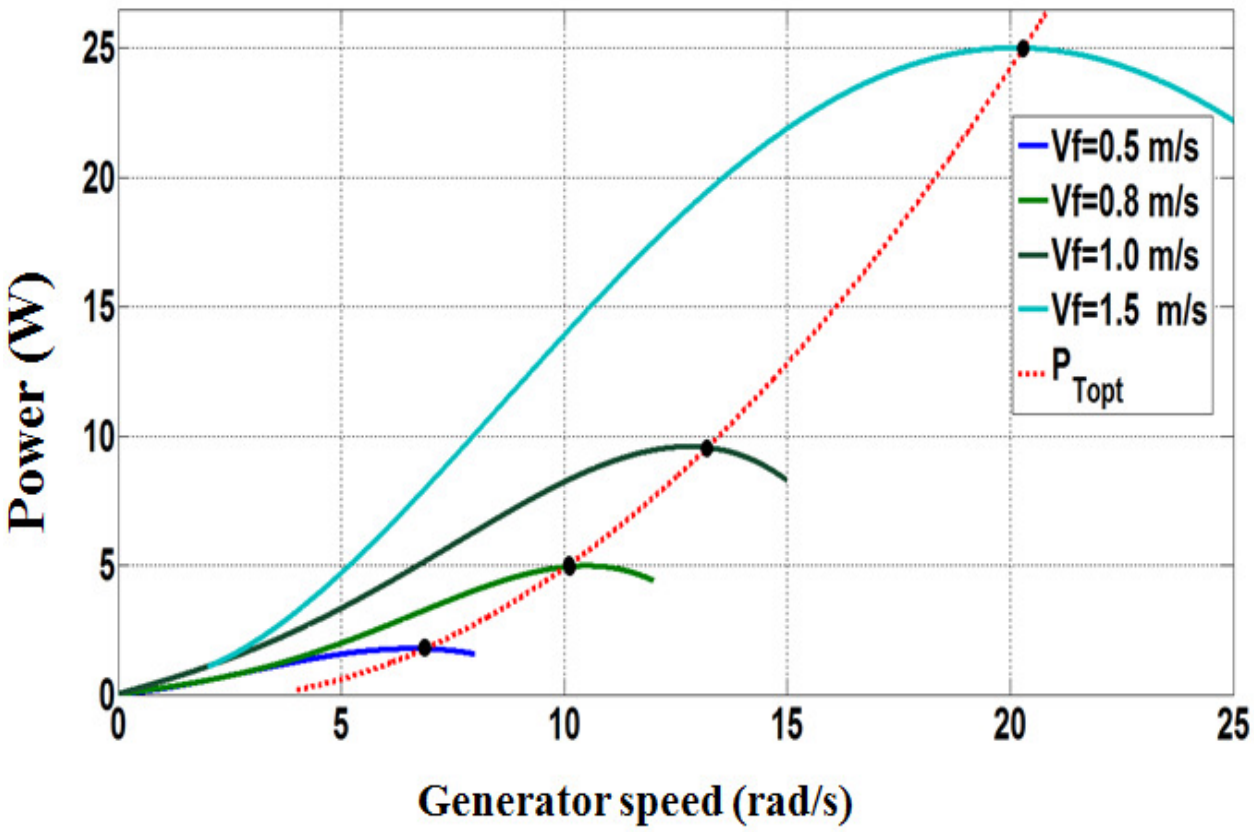

Fig. 6.3 Power Curve of Marine current energy conversion system

6.3 Classical Proportional Integral Control

The classical proportional integral control is popular and widely used in industry applications. The design of proportional integral controller is simple enough, and requires little feedback information and makes it easy to implement. It can also be employed over most plants having smooth models, in conjunction with other control and modeling techniques such as linearization, gain scheduling, etc. For fixed-pitch turbines, the captured energy maximum available in the tidal current can be achieved if the turbine rotor operates on the optimum point. This criterion can be obtained by tracking some target variables: the rotational speed reference, depending proportionally on the tidal speed, or the optimal rotor power, which proportionally depends on the cubed rotational

speed. The flow chart and the block diagram of the classical PI control have been shown in Fig.6.4 and Fig 6.5 respectively. The purpose is to control the duty cycle to extract maximum power from the system. The control algorithm can be breakdown into the following steps :

- Measure the speed of the generator ω_g.
- Estimation of reference torque.
- The reference torque is used to calculate the equivalent reference dc current by the expression in eq. 6.8.
- The error between the reference dc current and measured dc current is used to vary the duty cycle of the switch to regulate the output of the converter through a proportional–integral (PI) controller.

The generator torque is controlled in order to maintain optimum torque curve according to the generator speed. The acceleration or deceleration of the generator is determined by the difference of the generator torque T_g and the turbine torque T_m. If the generator speed is less than the optimal speed, the generator torque is smaller than the turbine torque, and the generator will pick up speed. The generator will be slowed down if the generator speed is higher than the optimal speed. As a matter of fact the turbine and generator torques settle down to the optimum torque point at any water speed, and the marine turbine will be operating at the maximum power point.

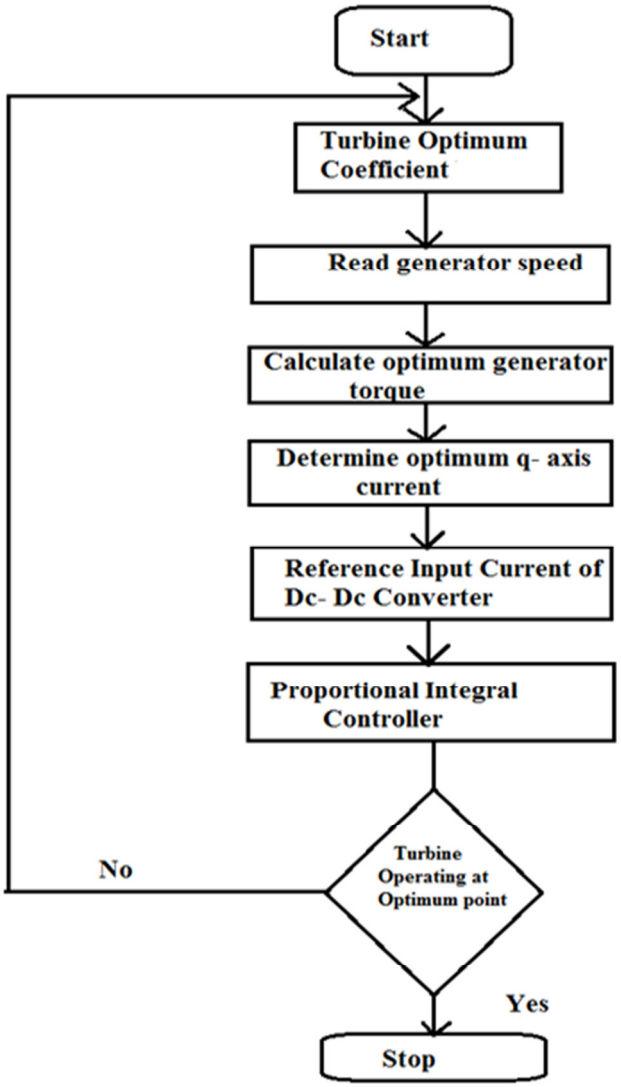

Fig. 6.4 Flow chart of the MPPT control strategy

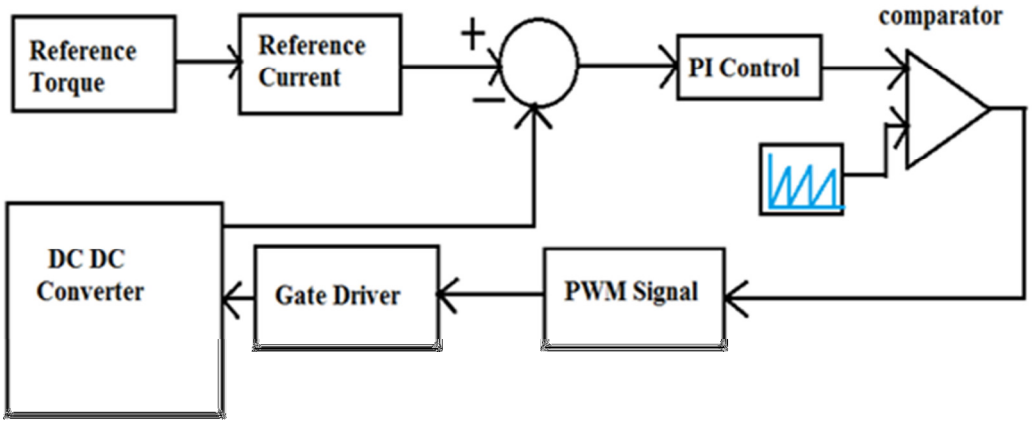

Fig. 6.5 Block diagram of the control algorithm

6.4 Stability Analysis of MCECS

A small signal model was developed to investigate the stability of the proposed energy conversion system during sudden changes in the load, flow speed or on the occurrence of disturbances and also to tune the parameters of the proposed control system. Linearizing around steady-state values, the linearization differential equations of the whole system can be obtained

A. Model of Marine Current Turbine

The rotor hydrodynamics are presented by the well-known static relations. The torque of the turbine can be expressed as:

$$T_m = \frac{1}{2}\rho A r C_T(\lambda) {V_w}^2 \tag{6.11}$$

Substituting the value of torque coefficient of the turbine in eq. 6.11 yields:

$$T_m = \frac{1}{2}\rho A r (a - b\lambda) {V_w}^2 \tag{6.12}$$

Simplification of the above equation results the following steps:

$$T_m = \frac{1}{2}\rho A r a {V_w}^2 - \frac{1}{2}\rho A r b \lambda {V_w}^2 \tag{6.13}$$

$$T_m = \frac{1}{2}\rho A r a {V_w}^2 - \frac{1}{2}\rho A r b \frac{\omega_r r}{V_w} {V_w}^2 \tag{6.14}$$

$$T_m = \frac{1}{2}\rho A r a {V_w}^2 - \frac{1}{2}\rho A r b \omega_r r V_w \tag{6.15}$$

Linearizing the turbine torque around steady values gives:

$$\Delta T_m = \frac{1}{2}\rho Ara(V_w + \Delta V_w)^2 - \frac{1}{2}\rho Arb\omega r(\omega_r + \Delta\omega_r)(V_w + \Delta V_w) \quad (6.16)$$

$$\Delta T_m = \rho Ara\Delta V_w V_w - \frac{1}{2}\rho Ar^2 b\frac{\omega_r}{N}\Delta V_w - \frac{1}{2}\rho Ar^2 b\frac{\Delta\omega_r}{N}V_w \quad (6.17)$$

B. Model of Permanent Magnet Synchronous Generator

The dynamic model of the PMSG is derived from the two phase synchronous reference frame, which the q-axis is 90° ahead of the d-axis with respect to the direction of rotation.

$$\frac{dI_{ds}}{dt} = p\omega_r I_{qs} - \frac{R_s}{L_S}I_{ds} - \frac{1}{L_S}V_{ds} \quad (6.18)$$

Linearizing the above equation around steady state values yields:

$$\frac{dI_{ds}}{dt} + \frac{d\Delta i_{ds}}{dt} = p\big(\omega_r + \Delta\omega_r)(I_{qs} + \Delta i_{qs}\big) - \frac{R_s}{L_S}(I_{ds} + \Delta i_{ds}) - \frac{1}{L_S}(V_{ds} + \Delta v_{ds}) \quad (6.19)$$

From equations (6.18) & (6.19) we can write

$$\frac{dI_{ds}}{dt} + \frac{d\Delta i_{ds}}{dt} = p\omega_r\Delta i_{qs} + p\Delta\omega_r I_{qs} - \frac{R_s}{L_S}\Delta i_{ds} - \frac{1}{L_S}\Delta v_{ds} \quad (6.20)$$

Linearization of the above equation gives:

$$\frac{d\Delta i_{ds}}{dt} = p\omega_r\Delta i_{qs} + p\Delta\omega_r I_{qs} - \frac{R_s}{L_S}\Delta i_{ds} - \frac{1}{L_S}\Delta v_{ds} \quad (6.21)$$

$$L_S\frac{di_{qs}}{dt} = p\omega_r\lambda_m - p\omega_r L_s i_{ds} - R_S i_{qs} - v_{qs} \quad (6.22)$$

$$\frac{di_{qs}}{dt} = \frac{1}{L_s}p\omega_r\lambda_m - p\omega_r i_{ds} - \frac{1}{L_s}R_S i_{qs} - \frac{1}{L_s}v_{qs} \quad (6.23)$$

At steady state condition the q axis current of the generator can be expressed as:

$$\frac{dI_{qs}}{dt} = \frac{1}{L_s} p\omega_r \lambda_m - p\omega_r I_{ds} - \frac{1}{L_s} R_S I_{qs} - \frac{1}{L_s} v_{qs} \tag{6.24}$$

Linearization of the eq. 6.24 at steady value yields:

$$\frac{dI_{qs}}{dt} + \frac{d\Delta i_{qs}}{dt} = \frac{1}{L_s} p\omega_r \lambda_m + \frac{1}{L_s} p\Delta\omega_r \lambda_m - \frac{R_s}{L_S} I_{qs} - \frac{1}{L_S} \Delta v_{qs} - \frac{R_s}{L_S} \Delta i_{qs} - p(\omega_r + \Delta\omega_r)(I_{ds} + \Delta i_{ds}) \tag{6.25}$$

From eq. (6.24) & (6.35)

$$\frac{d\Delta i_{qs}}{dt} = \frac{1}{L_s} p\Delta\omega_r \lambda_m - \frac{1}{L_S} \Delta v_{qs} - \frac{R_s}{L_S} \Delta i_{qs} - p\omega_r \Delta i_{ds} - p\Delta\omega_r I_{ds} \tag{6.26}$$

$$V_{dc} = \frac{3}{\pi} \sqrt{{v_{ds}}^2 + {v_{qs}}^2}) = \frac{3}{\pi} \sqrt{(v_{ds} + \Delta v_{ds})^2 + \left(v_{qs} + \Delta v_{qs}\right)^2} \tag{6.27}$$

$$I_{dc} = \frac{\sqrt{3}}{2} \sqrt{(I_{ds} + \Delta i_{ds})^2} + \left(I_{qs} + \Delta i_{qs}\right)^2 \tag{6.28}$$

C. Model of Boost Converter

The current flowing through the inductor in the boost converter at any time can be expressed as:

$$\frac{di_L}{dt} = -\frac{V_{out}}{L}\left(1 - \frac{V_{control}}{\hat{V}_{st}}\right) + \frac{V_{dc}}{L} \tag{6.29}$$

$$i_L = I_L + \Delta i_L \tag{6.30}$$

$$v_{control} = v_{control} + \Delta v_{control} \tag{6.31}$$

$$i_L = I_L + \Delta i_L \tag{6.32}$$

The steady state model of DC- DC converter can be expressed as:

$$\frac{dI_L}{dt} = -\frac{V_{out}}{L}\left(1 - \frac{V_{control}}{\hat{V}_{st}}\right) + \frac{V_{dc}}{L} \tag{6.33}$$

$$\frac{dI_L}{dt} = -\frac{V_{out}}{L} + \frac{V_{out}}{L}\frac{V_{control}}{\hat{V}_{st}} + \frac{V_{dc}}{L} \tag{6.34}$$

Linearizing the inductor current around steady values yields:

$$\frac{dI_L}{dt} + \frac{d\Delta i_L}{dt} = -\frac{V_{out}}{L} - \frac{\Delta V_{out}}{L} + \left(\frac{V_{control} + \Delta V_{control}}{\hat{V}_{st}}\right)\left(\frac{V_{out} + \Delta V_{out}}{L}\right) + \frac{V_{dc}}{L} + \frac{\Delta V_{dc}}{L} \tag{6.35}$$

Simplification of the above equation yields the following:

$$\frac{dI_L}{dt} + \frac{d\Delta i_L}{dt} = -\frac{V_{out}}{L} - \frac{\Delta V_{out}}{L} + \frac{V_{out}}{L}\frac{V_{control}}{\hat{V}_{st}} + \frac{\Delta V_{out}}{L}\frac{V_{control}}{\hat{V}_{st}} + \frac{\Delta V_{control}}{\hat{V}_{st}} + \frac{\Delta V_{control}}{\hat{V}_{st}}\frac{\Delta V_{out}}{L} + \frac{V_{dc}}{L} + \frac{\Delta V_{dc}}{L} \tag{6.36}$$

$$\frac{d\Delta i_L}{dt} = -\frac{\Delta V_{out}}{L} + \frac{\Delta V_{out}}{L}\frac{V_{control}}{\hat{V}_{st}} + \frac{\Delta V_{control}}{\hat{V}_{st}}\frac{V_{out}}{L} + \frac{\Delta V_{dc}}{L} \tag{6.37}$$

The voltage across the capacitor in the boost converter at any time can be expressed as:

$$\frac{dV_{out}}{dt} = \left(1 - \frac{V_{control}}{\hat{V}_{st}}\right)\frac{I_L}{C} + \frac{V_{out}}{R_L C} \tag{6.38}$$

$$V_{out} = V_{out} + \Delta v_{out} \tag{6.39}$$

$$\frac{dV_{out}}{dt} + \frac{d\Delta v_{out}}{dt} = \frac{I_L}{C} - \frac{V_{control}}{\hat{V}_{st}}\frac{I_L}{C} - \frac{V_{out}}{R_L C} \tag{6.40}$$

Linearizing the capacitor voltage around steady value gives the following:

$$\frac{dV_{out}}{dt} + \frac{d\Delta v_{out}}{dt} = \frac{I_L}{C} + \frac{\Delta i_L}{C} - \left(\frac{V_{control} + \Delta V_{control}}{\hat{V}_{st}}\right)\left(\frac{I_L + \Delta i_L}{C}\right) - \frac{V_{out}}{R_L C} - \frac{\Delta V_{out}}{R_L C} \tag{6.41}$$

Simplification of the above equation yields:

$$\frac{dV_{out}}{dt} + \frac{d\Delta v_{out}}{dt} = \frac{I_L}{C} + \frac{\Delta i_L}{C} - \frac{V_{control}}{\hat{V}_{st}}\frac{I_L}{C} - \frac{V_{control}}{\hat{V}_{st}}\frac{\Delta i_L}{C} - \frac{\Delta V_{control}}{\hat{V}_{st}}\frac{I_L}{C} - \frac{\Delta V_{control}}{\hat{V}_{st}}\frac{\Delta i_L}{C} - \frac{V_{out}}{R_L C} - \frac{\Delta V_{out}}{R_L C} \tag{6.42}$$

$$\frac{d\Delta v_{out}}{dt} = \frac{\Delta i_L}{C} - \frac{V_{control}}{\hat{V}_{st}}\frac{\Delta i_L}{C} - \frac{\Delta V_{control}}{\hat{V}_{st}}\frac{I_L}{C} - \frac{\Delta V_{out}}{R_L C} \tag{6.43}$$

$$\Delta i_{dc} = \frac{\sqrt{3}}{2}\left(\sqrt{{\Delta i_{ds}}^2 + {\Delta i_{qs}}^2}\right) \tag{6.44}$$

The current flowing through the capacitor of the boost converter can be expressed as:

$$C\frac{dV_{dc}}{dt} = I_{dc} - i_L \tag{6.45}$$

Linearization around the steady values gives the following:

$$\frac{d\Delta V_{dc}}{dt} = \frac{1}{C}\left[\frac{\sqrt{3}}{2}\left(\sqrt{{\Delta i_{ds}}^2 + {\Delta i_{qs}}^2}\right) - \Delta i_L\right] \tag{6.46}$$

The linearized drive equation of the MCECS can be expressed as below:

$$\frac{d\Delta\omega_r}{dt} = \frac{1}{J}(\rho Ara\Delta V_w V_w - \frac{1}{2}\rho Ar^2 b\frac{\omega_r}{N}\Delta V_w - \frac{1}{2}\rho Ar^2 b\frac{\Delta\omega_r}{N}V_w - 1.5p\lambda_m\Delta i_{qs}) \quad (6.47)$$

Simplification of the above equation yields:

$$\frac{d\Delta\omega_r}{dt} = (\frac{1}{J}\rho AraV_w - \frac{1}{2J}\rho Ar^2 b\frac{\omega_r}{N})\Delta V_w - \frac{1}{2J}\rho Ar^2 b\frac{V_w}{N}\Delta\omega_r - \frac{1.5}{J}p\lambda_m\Delta i_{qs} \quad (6.48)$$

The calculated reference current to operate MCECS at optimum point can be expressed as:

$$I_{ref} = \frac{\pi}{2\sqrt{3}}\frac{K_{opt}{\omega_r}^2}{1.5p\lambda_m} = C{\omega_r}^2 \quad (6.49)$$

$$\frac{dI_{ref}}{dt} = 2C\frac{d\omega_r}{dt} \quad (6.50)$$

The controlled voltage based on PI controller can be expressed as:

$$\frac{dV_{control}}{dt} = 2K_p C\omega_r\frac{d\omega_r}{dt} - K_p\frac{di_L}{dt} + K_I(C{\omega_r}^2 - i_L) \quad (6.51)$$

Linearizing the control signal around steady values yields:

$$\frac{dV_{control}}{dt} + \frac{d\Delta V_{control}}{dt} = 2K_p C(\omega_r + \Delta\omega_r)(\frac{d\Delta\omega_r}{dt} + \frac{d\omega_r}{dt}) - K_p(\frac{di_L}{dt} + \frac{d\Delta i_L}{dt}) + K_I(C(\omega_r + \Delta\omega_r)^2 - i_L - \Delta i_L) \quad (6.52)$$

Simplification of eq. 6.52 yields the following

$$\frac{d\Delta V_{control}}{dt} = 2K_p C\omega_r \frac{d\Delta\omega_r}{dt} - K_p \frac{d\Delta i_L}{dt} + K_I C 2\omega_r \Delta\omega_r - K_I \Delta i_L) \tag{6.53}$$

$$\begin{aligned}\frac{d\Delta V_{control}}{dt} = {} & \Delta\omega_r(-2CK_P K_1\omega_r + 2CK_I\omega_r) + \Delta i_{qs}(-2CK_P\omega_r K_2) + \Delta V_{dc}\left(-\frac{K_P}{L}\right) \\ & - K_I\Delta i_L + \Delta V_{out}\left(\frac{K_P\hat{V}_{st} - K_P V_{control}}{L\hat{V}_{st}}\right) + \Delta V_{control}\left(-\frac{K_P V_{out}}{L\hat{V}_{st}}\right) \\ & + \Delta V_w(2CK_p\omega_r K_3)\end{aligned} \tag{6.54}$$

The complete linearized small signal model of MCECS is given in eq. 6.55

$$\frac{d\Delta x}{dt} = A\Delta x + Bu \tag{6.55}$$

where Δx is the state vector and *u* is the input and they are given as follows:

$$\Delta x = \begin{bmatrix}\Delta\omega_T & \Delta i_{qs} & \Delta i_L & \Delta V_{dc} & \Delta V_{out} & \Delta V_{control}\end{bmatrix}$$

$$\boldsymbol{A} = \begin{bmatrix} \boldsymbol{A_{11}} & \boldsymbol{A_{12}} & \boldsymbol{0} & \boldsymbol{0} & \boldsymbol{0} & \boldsymbol{0} \\ \boldsymbol{A_{21}} & \boldsymbol{A_{22}} & \boldsymbol{0} & \boldsymbol{A_{24}} & \boldsymbol{0} & \boldsymbol{0} \\ \boldsymbol{0} & \boldsymbol{0} & \boldsymbol{0} & \boldsymbol{A_{34}} & \boldsymbol{A_{35}} & \boldsymbol{A_{36}} \\ \boldsymbol{0} & \boldsymbol{A_{42}} & \boldsymbol{A_{43}} & \boldsymbol{0} & \boldsymbol{0} & \boldsymbol{0} \\ \boldsymbol{0} & \boldsymbol{0} & \boldsymbol{A_{53}} & \boldsymbol{0} & \boldsymbol{A_{55}} & \boldsymbol{A_{56}} \\ \boldsymbol{A_{61}} & \boldsymbol{A_{62}} & \boldsymbol{A_{63}} & \boldsymbol{A_{64}} & \boldsymbol{A_{65}} & \boldsymbol{A_{66}} \end{bmatrix}$$

Where the matrix co-efficient can be expressed as:

$$\boldsymbol{A_{11}} = -\frac{\boldsymbol{slope}}{\boldsymbol{J}} \qquad \boldsymbol{A_{12}} = -\frac{\boldsymbol{1.5pN\pi\lambda_m}}{\boldsymbol{J}}$$

$$\boldsymbol{A_{21}} = \frac{\boldsymbol{pN\pi\lambda_m}}{\boldsymbol{L_s}} \qquad \boldsymbol{A_{24}} = -\frac{\boldsymbol{\pi}}{\boldsymbol{3\sqrt{3}L_s}}$$

$$A_{34} = -\frac{1}{L} \qquad A_{35} = \frac{1}{L}\frac{V_{control} - V_{st}}{V_{st}} \qquad A_{36} = \frac{1}{L}\frac{V_{out}}{V_{st}}$$

$$A_{42} = \frac{\pi}{2\sqrt{3}C_{in}} \qquad A_{43} = -\frac{1}{C_{in}}$$

$$A_{53} = \frac{1}{C}\frac{V_{st} - V_{control}}{V_{st}} \qquad A_{55} = -\frac{1}{R_L C} \qquad A_{56} = -\frac{1}{C}\frac{I_L}{V_{st}}$$

$$A_{61} = \frac{2CK_I\omega_t - 2CK_p\omega_t}{J} \qquad A_{62} = -\frac{3\pi pNCK_p\omega_t\lambda_m}{J} \qquad A_{63} = -K_I$$

$$A_{64} = -\frac{K_P}{L} \qquad A_{65} = -\frac{K_P}{L}\frac{V_{control} - V_{st}}{V_{st}} \qquad A_{66} = -\frac{K_P}{L}\frac{V_{out}}{V_{st}}$$

The stable initial condition has been calculated for flow speed of 0.6 m/s. The calculated eigenvectors of state matrix A are presented in Table 6.1. The system can be considered stable with introduction of a small disturbance as all the eigenvalues have negative real parts. There is no oscillation in the system as none of the eigenvalues have any complex parts in it. All of the modes present in the system are evanescent modes.

Table 6.1 Parameters of turbine, PMSG and Boost Converter

Eigen vectors	**Eigenvalues**
λ_1	-56178
λ_2	-3893
λ_3	-211
λ_4	-42
λ_5	-4
λ_6	-20

The normalized participation factors disclose the relationship between the modes and the variables. The participation factors are shown in Table 6.2. It can be seen that the eigenvalue λ_2 is highly sensitive to the state variable Δi_{qs} and is affected by K_{PI} and K_{II}. The remaining Eigen values are not highly sensitive to any state variable, but it is

evanescent mode, so there is no electromechanical oscillation mode in this system. Fig. 6.6 indicates that the system is stable regardless of the change in values of gains. The Nyquist and Bode plot of the energy conversion system is shown in Fig 6.7.

Table 6.2 Participation Factors

States	λ_1	λ_2	λ_3	λ_4	λ_5	λ_6
$\Delta\omega_T$	0	0	0.02	0.03	0.44	0.5
Δi_{qs}	0	0.94	0.05	0	0	0
Δi_L	0.14	0	0.17	0.16	0	0.53
ΔV_{dc}	0	0.02	0.41	0	0.42	0.16
ΔV_{out}	0	0	0.02	0.34	0.3	0.34
$\Delta V_{control}$	0.4025	0.02	0.41	0.13	0.06	0

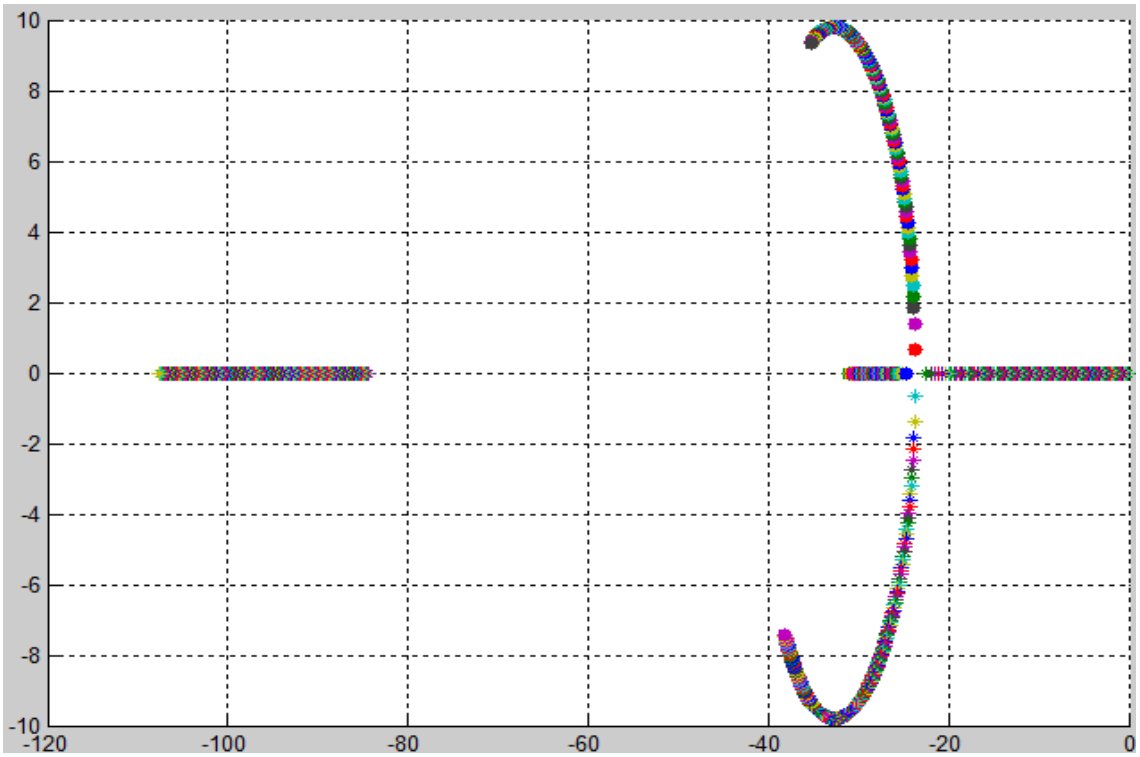

Fig. 6.6 Change of $\lambda_{5\text{-}6}$ when K_I is changed from 10 to 1000 i.e. $10 \leq K_I \leq 1000$

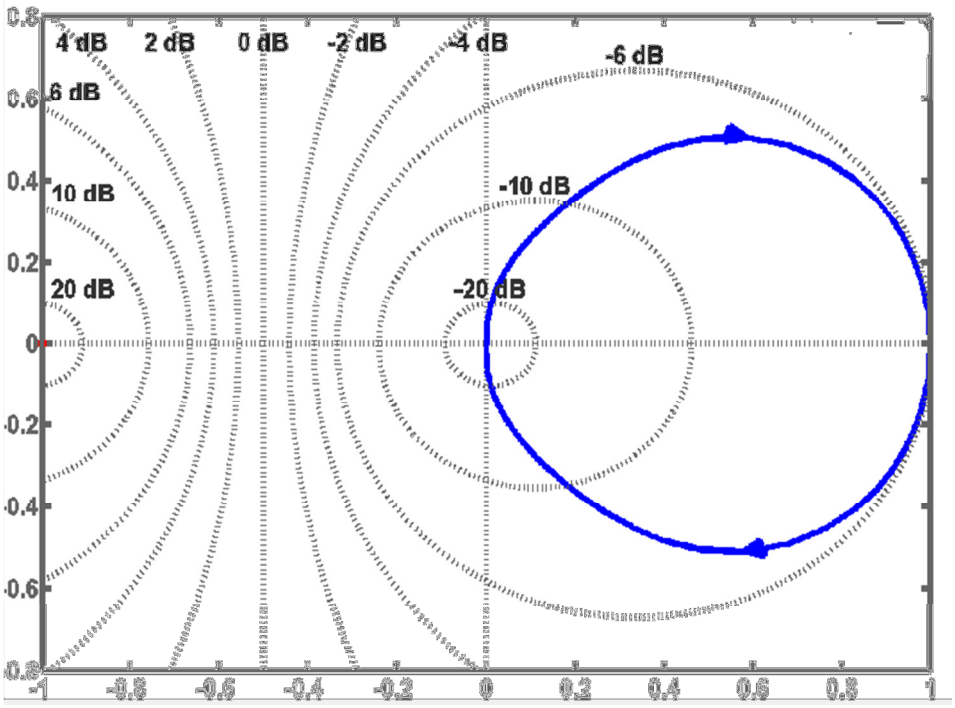

Fig. 6.7(a)

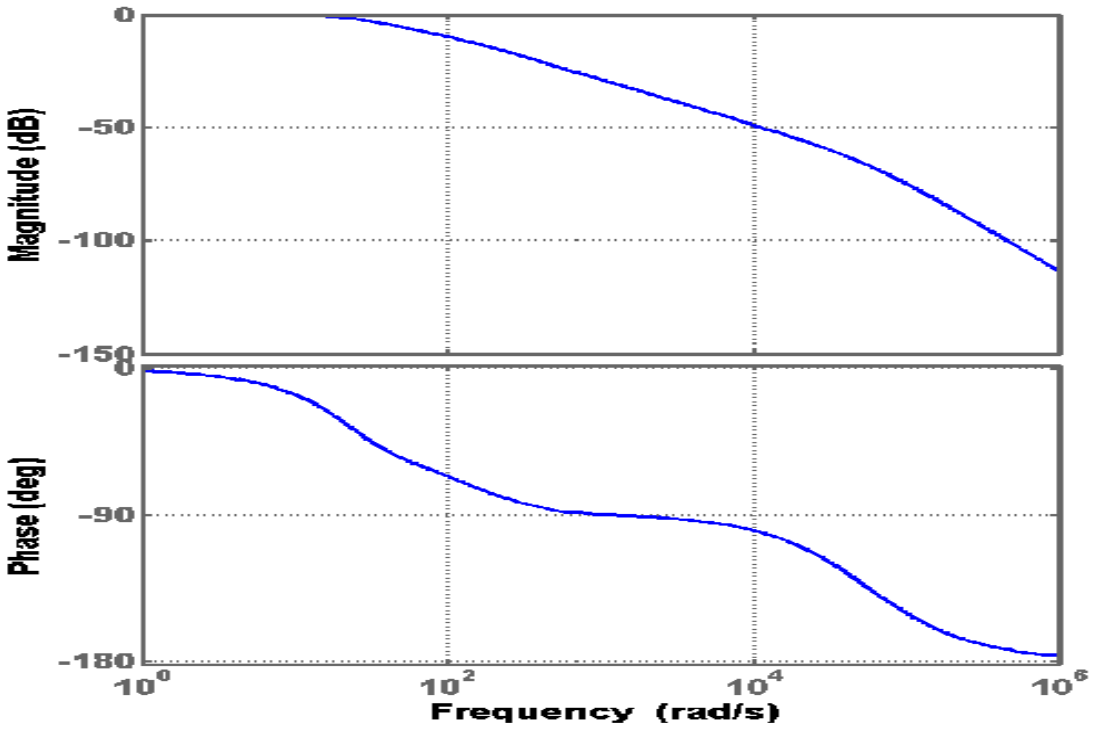

Fig. 6.7(b)

Fig. 6.7 (a) Nyquist Plot (b) Bode Plot of MCECS

The overall conversion system consists of stable subsystems. Inspection shows that the system has no unstable poles. The clockwise rotations are considered positive and counter clockwise rotations are considered negative. Therefore the net clockwise rotations are equal to the number of zeros which shows the system is stable. The positive gain margin and phase margin also depicts that the system is stable. This kind of controller is well-known for its simplicity for constant references. Its gains are computed by compensating the larger system time-constant and by guaranteeing a constant tracking error when the reference is a ramp. However, in case of a marine current turbine, the generated reference signals are time-varying and the current sources may be turbulent. In that case the proportional integral controller may not be so efficient.

6.5 Adaptive Backstepping Control

The idea of breaking a dynamic system into subsystems is not unusual in the design of nonlinear controllers. Sliding mode control can be regarded as one of the candidate. Generally design of a sliding controller includes two major steps:

1) Design a stable sliding surface to achieve the control objective, and

2) Make the sliding surface attractive by pushing system states toward the surface.

To facilitate the synthesis of a sliding controller, the sliding surface is designed in such a way that the relative degree from the control input to the sliding surface variable is one. Therefore, it is easier to control system states toward the sliding surface than it is to control the original dynamic system, even in the face of plant nonlinearity and modeling uncertainty. However, robust sliding control for uncertain nonlinear systems requires the uncertain terms enter the state equation at the same point as the control input. One of the

advantages of backstepping design is that the matching condition can be matched for a class of nonlinear systems satisfying the so called strict feedback form. Control design for this class of nonlinear systems can be achieved by recursive designs of scalar subsystems. Another feature of backstepping designs is that they do not force the designed system to appear linear, which can avoid cancellations of useful nonlinearities. Furthermore, additional nonlinear damping terms can be introduced in the feedback loop to enhance robustness.

Adaptive backstepping method combines backstepping control and adaptive laws. The backstepping design starts from the first state equation where the first state variable has the highest integration order from the control input. Then the second state variable can be defined as *virtual control,* and replace it with a stabilizing function. The term "backstepping" means that we use the latter state as a virtual control to stabilize the previous one. Lyapunov direct method is utilized as the stabilization method for the errors between each virtual control and its stabilizing function [127]. It has been demonstrated that controlling systems with the adaptive backstepping controllers, compared to the certainty-equivalence controllers [128], leads to possible significant improvements of the transient performance, without increasing the control effort. Stability analysis, which represents a major drawback of the traditional adaptive controllers, can also be easily performed via the backstepping method. Backstepping method provides a systematic step-by-step algorithm for designing stabilizing controllers [129-134]. A step by step design procedure of adaptive backstepping for a class of nonlinear systems with unknown parameters is shown in Appendix E.

Fig. 6.8 presents the flow chart of the control structure of fixed frequency dc-dc converter. The block diagram of the implementation of the controller is shown in Fig 6.9. In order to reduce the number of sensors, a Lyapunov observer is developed for the construction of parameter adaptation laws. The observed states and the estimated values of the parameters are fed into the backstepping controller. It also includes useful system nonlinearities into account and provides global asymptotic stability.

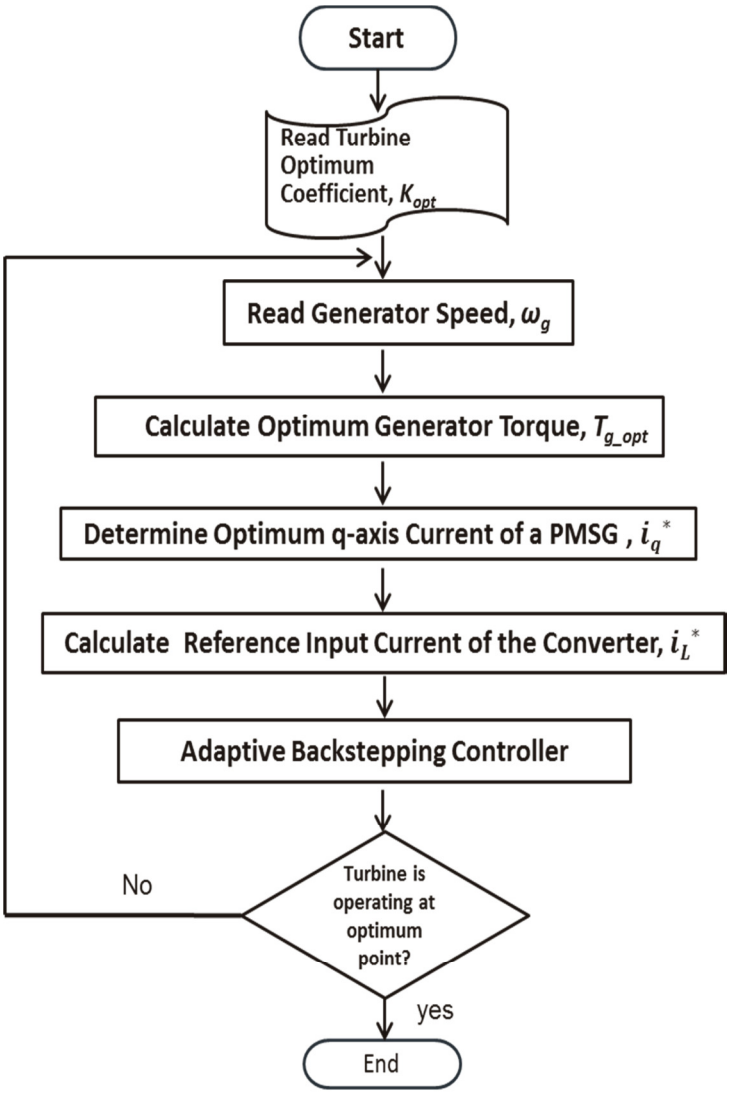

Fig. 6.8 Flow chart of the MPPT control strategy of MCECS

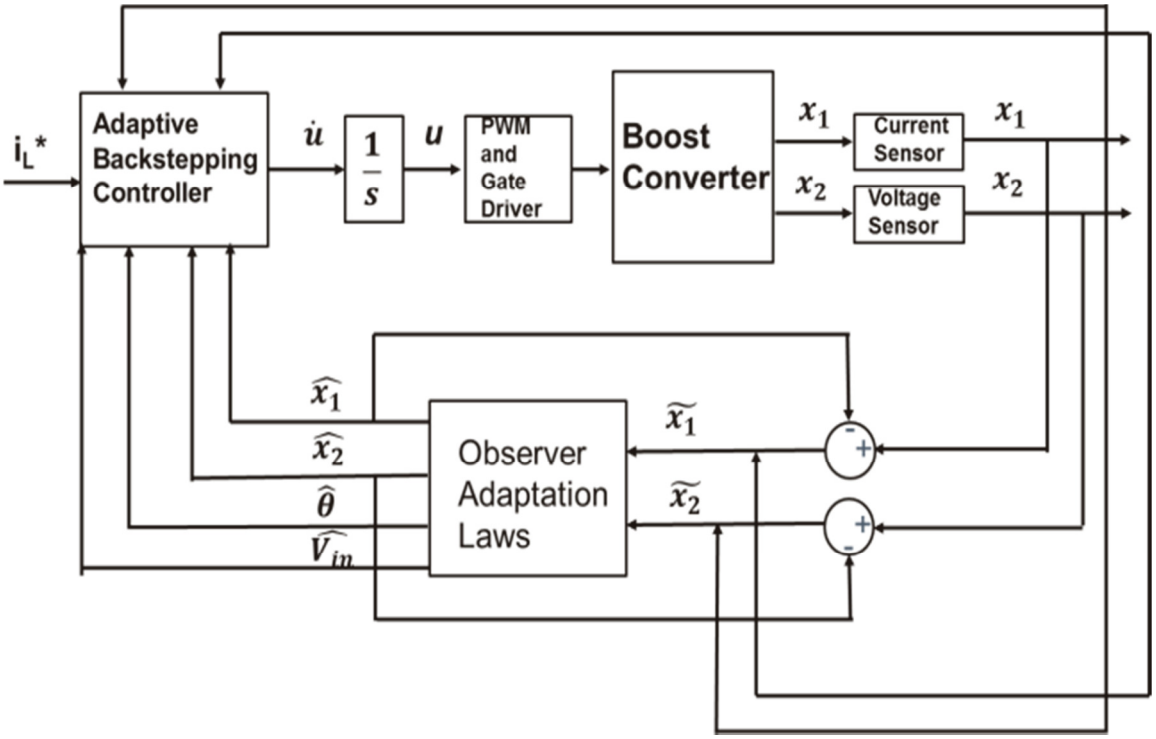

Fig. 6.9 Block diagram of the control algorithm

6.5.1 Design of Adaptive Backstepping Controller

The main objective behind using backstepping control methodology is to design a state feedback controller in order to make the origin asymptotically stable. The algorithm for the proposed backstepping style adaptive nonlinear controller is designed using systematic step-by-step procedures and is explained in details below,

$$\dot{\hat{x}}_1 = -(1-u)\frac{\hat{x}_2}{L} + \frac{\hat{V}_{in}}{L} + K_1(x_1 - \hat{x}_1) \tag{6.56}$$

$$\dot{\hat{x}}_2 = (1-u)\frac{\hat{x}_1}{C} - \frac{\hat{\theta}}{C}x_2 + K_2(x_2 - \hat{x}_2) \tag{6.57}$$

Step 1: Introduce the tracking error: $z_1 = \hat{x}_1 - I_{ref}$ where I_{ref} denotes the desired constant output reference. Achieving the tracking objective amounts to enforcing the error z_1 to vanish. The time derivative of z_1 is given as:

$$\dot{z}_1 = \dot{\hat{x}}_1 = -(1-u)\frac{\hat{x}_2}{L} + \frac{\hat{V}_{in}}{L} + K_1(x_1 - \hat{x}_1) \tag{6.58}$$

$$= -(1-u)\frac{\hat{x}_2}{L} + \frac{\hat{V}_{in}}{L} + K_1\tilde{x}_1 \tag{6.59}$$

Step 2: Assume $\widehat{x_2}$ is the control variable. Let α_1 is defined as a variable stands as a virtual control input

$$z_2 = \hat{x}_2 - \alpha_1 \tag{6.60}$$

$$\dot{z}_1 = -(1-u)\frac{(z_2 + \alpha_1)}{L} + \frac{\hat{V}_{in}}{L} + K_1\tilde{x}_1 \tag{6.61}$$

$$= -(1-u)\frac{z_2}{L} - (1-u)\frac{\alpha_1}{L} + \frac{\hat{V}_{in}}{L} + K_1\tilde{x}_1 \tag{6.62}$$

Step 3: In this step, the control objective is to design a virtual control law $\alpha_1$such that $z_1 \longrightarrow 0$ as $t \longrightarrow \infty$. Consider a control Lyapunov function,

$$V_1 = \frac{1}{2}{z_1}^2 \tag{6.63}$$

The time derivative of V_1 is given by,

$$\dot{V}_1 = z_1[\,-(1-u)\frac{z_2}{L} - (1-u)\frac{\alpha_1}{L} + \frac{\hat{V}_{in}}{L} + K_1\tilde{x}_1] \tag{6.64}$$

$$\dot{V}_1 = -(1-u)\frac{z_1 z_2}{L} + z_1[-(1-u)\frac{\alpha_1}{L} + \frac{\hat{V}_{in}}{L} + K_1\tilde{x}_1] \quad (6.65)$$

Now, the virtual control α_1 is defined as follows,

$$\alpha_1 = \frac{\hat{V}_{in} + LK_1\tilde{x}_1}{(1-u)} + c_1 z_1 \quad (6.66)$$

where c_1 is a strictly positive constant. Hence, clearly, if $z_2 = 0$, then

$$\dot{V}_1 = -(1-u)\frac{c_1}{L}z_1^2 \quad (6.67)$$

And z_1 are guaranteed to converge to zero asymptotically.

$$\dot{V}_1 = -(1-u)\frac{z_1 z_2}{L} - (1-u)\frac{c_1 {z_1}^2}{L} \quad (6.68)$$

If $z_2 = 0$ then we can write above equation as:

$$\dot{V}_1 = -(1-u)\frac{c_1 {z_1}^2}{L} \quad (6.69)$$

Which is asymptotically stable 0<μ<1 and this gives

$$\dot{\alpha}_1 = \frac{1}{(1-u)}\dot{\hat{V}}_{in} + \frac{\dot{u}}{(1-u)^2}V_{in} + \frac{LK_1\dot{\tilde{x}}_1}{(1-u)} + \frac{\dot{u}}{(1-u)^2}LK_1\tilde{x}_1 + c_1\dot{z}_1 \quad (6.70)$$

$$\dot{\alpha}_1 = \frac{1}{(1-u)}\dot{\hat{V}}_{in} + \frac{\dot{u}}{(1-u)^2}V_{in} + \frac{LK_1\dot{\tilde{x}}_1}{(1-u)} + \frac{\dot{u}}{(1-u)^2}LK_1\tilde{x}_1 + c_1\left[-(1-u)\frac{\hat{x}_2}{L} + \frac{\hat{V}_{in}}{L} + K_1\tilde{x}_1\right] \quad (6.71)$$

$$\dot{\alpha}_1 = \frac{1}{(1-u)}\dot{\hat{V}}_{in} + \dot{u}[\frac{1}{(1-u)^2}V_{in} + \frac{1}{(1-u)^2}LK_1\tilde{x}_1] + \frac{LK_1\dot{\tilde{x}}_1}{(1-u)} + c_1[-(1-u)\frac{\hat{x}_2}{L} + \frac{\hat{V}_{in}}{L} + K_1\tilde{x}_1] \quad (6.72)$$

Step 4: A second control Lyapunov function is chosen as:

$$V_2 = V_1 + \frac{1}{2}{z_2}^2 \tag{6.73}$$

The time derivative of V_2 is given by,

$$\begin{aligned}\dot{V}_2 &= \dot{V}_1 + z_2\dot{z}_2 \\ &= -(1-u)\frac{c_1{z_1}^2}{L} - (1-u)\frac{z_1 z_2}{L} + z_2\dot{z}_2\end{aligned} \tag{6.74}$$

Also,

$$z_2 = \hat{x}_2 - \alpha_1 \tag{6.75}$$

Step 5: The error dynamics for the control law z_2 is given as

$$\dot{z}_2 = \dot{\hat{x}}_2 - \dot{\alpha}_1 \tag{6.76}$$

$$= (1-u)\frac{\hat{x}_1}{C} - \frac{\hat{\theta}}{C}x_2 + K_2(x_2 - \hat{x}_2) - \dot{\alpha}_1 \tag{6.77}$$

$$\begin{aligned}\dot{z}_2 = (1-u)\frac{\hat{x}_1}{C} - \frac{\hat{\theta}}{C}x_2 + K_2(x_2 - \hat{x}_2) - \frac{1}{(1-u)}\dot{\hat{V}}_{in} \\ - \dot{\mu}\left[\frac{1}{(1-u)^2}V_{in} + \frac{1}{(1-u)^2}LK_1\tilde{x}_1\right] - \frac{LK_1\dot{\tilde{x}}_1}{(1-u)} - c_1[-(1-u)\frac{z_2}{L} \\ - (1-u)\frac{\alpha_1}{L} + \frac{\hat{V}_{in}}{L} + K_1\tilde{x}_1]\end{aligned} \tag{6.78}$$

$$\begin{aligned}\dot{V}_2 = -(1-u)\frac{c_1{z_1}^2}{L} - (1-u)\frac{z_1 z_2}{L} + z_2[(1-u)\frac{\hat{x}_1}{C} + \frac{\hat{\theta}}{C}x_2 + K_2(x_2 - \hat{x}_2) \\ - \dot{\alpha}_1]\end{aligned} \tag{6.79}$$

$$\dot{V}_2$$
$$= -(1-u)\frac{c_1 {z_1}^2}{L} - (1-\mu)\frac{z_1 z_2}{L} + z_2[(1-u)\frac{\hat{x}_1}{C} - \frac{\hat{\theta}}{C}x_2 + K_2\tilde{x}_2 - [\frac{1}{(1-u)}\dot{\hat{V}}_{in}$$
$$- \dot{u}\left[\frac{1}{(1-u)^2}V_{in} + \frac{1}{(1-u)^2}LK_1\tilde{x}_1\right] - \frac{LK_1\dot{\tilde{x}}_1}{(1-u)} - c_1[-(1-u)\frac{\hat{x}_2}{L} + \frac{\hat{V}_{in}}{L}$$
$$+ K_1\tilde{x}_1]] \qquad (6.80)$$

$$\dot{V}_2 = -(1-u)\frac{c_1 {z_1}^2}{L} - (1-u)\frac{z_1 z_2}{L}$$
$$+ z_2\left[-(1-u)\frac{z_1}{L} + (1-u)\frac{\hat{x}_1}{C} - \frac{\hat{\theta}}{C}x_2 + K_2\tilde{x}_2 - \frac{1}{(1-u)}\dot{\hat{V}}_{in} - \frac{LK_1\dot{\tilde{x}}_1}{(1-u)}\right.$$
$$\left. - \dot{\mu}\left[\frac{1}{(1-u)^2}V_{in} + \frac{1}{(1-u)^2}LK_1\tilde{x}_1\right] + c_2 z_2 - c_1\dot{\hat{x}}_1\right] - c_2 {z_2}^2 \qquad (6.81)$$

Step 6: The control input u˙ is selected to make the first order system asymptotically stable. The control input is given as,

$$\dot{u} = \frac{(1-u)^2}{\hat{V}_{in} + LK_1\dot{\tilde{x}}_1}[-\frac{(1-u)}{L}z_1 + \frac{(1-u)}{C}\hat{x}_1 - \frac{\hat{\theta}}{C}x_2 + K_2\tilde{x}_2 - \frac{1}{(1-u)}\hat{V}_{in}$$
$$- \frac{1}{(1-u)}LK_1\dot{\tilde{x}}_1 + c_2 z_2 - (1-u)^2 c_1\dot{\hat{x}}_1] \qquad (6.82)$$

$$\dot{u} = \frac{1}{\hat{V}_{in} + LK_1\dot{\tilde{x}}_1}\left[-\frac{(1-u)^3}{L}z_1 + \frac{(1-u)^3}{C}\hat{x}_1 - \frac{\hat{\theta}}{C}x_2(1-u)^2 + (1-u)^2K_2\tilde{x}_2\right.$$
$$\left. - (1-u)\hat{V}_{in} - (1-u)LK_1\dot{\tilde{x}}_1 + (1-u)^2 c_2 z_2 - (1-u)^2 c_1\dot{\hat{x}}_1\right] \qquad (6.83)$$

where c_2 is a strictly positive constant. The resulting time derivative of V_2 is given as:

$$\dot{V}_2 = -\frac{(1-u)}{L}c_1 z_1^2 - \frac{(1-u)}{L}z_1 z_2 \qquad (6.84)$$

LaSalle's invariance theorem provides that $z_1, z_2 \longrightarrow 0$ as $t \longrightarrow \infty$ and since z_1 and I_{ref} are bounded, x_1 is also bounded from $x_1 = I_{ref}, x_2$ is also bounded as z_2 and α_1 are

bounded. As x_1, x_2, z_1 and z_2 are bounded, the control input $\dot{u}$ is also bounded. As a result, the system is asymptotically stable.

6.5.2 Design of Online Parameter Estimator

The state space average model of a boost converter can be expressed by

$$\dot{x}_1 = -(1-u)\frac{x_2}{L} + \frac{V_{in}}{L} \tag{6.85}$$

$$\dot{x}_2 = -(1-u)\frac{x_1}{L} + \frac{\theta}{L}x_2 \tag{6.86}$$

An estimator/observer of the dc -dc converter is developed using the estimated values of input voltage and the load resistance and the equations are given below. The estimates of θ, V_{in} can be written as $\hat{\theta}$ and $\hat{V}_{in}$ respectively. The error in the estimation can be expressed as:

$$\tilde{\theta} = \theta - \hat{\theta} \tag{6.87}$$

$$\tilde{V}_{in} = V_{in} - \hat{V}_{in} \tag{6.88}$$

$$\tilde{x}_1 = x_1 - \hat{x}_1 \tag{6.89}$$

$$\tilde{x}_2 = x_2 - \hat{x}_2 \tag{6.90}$$

Using the estimated values of θ and V_{in}

$$\dot{\hat{x}}_1 = -(1-u)\frac{\hat{x}_2}{L} + \frac{\hat{V}_{in}}{L} + K_1(x_1 - \hat{x}_1) \tag{6.91}$$

$$\dot{\hat{x}}_2 = -(1-u)\frac{\hat{x}_1}{C} + \frac{\hat{\theta}}{C} + K_2(x_2 - \hat{x}_2) \tag{6.92}$$

Where K_1 and K_2 are positive observer gains

$$\dot{\tilde{x}}_1 = -(1-u)\frac{\tilde{x}_2}{L} + \frac{\tilde{V}_{in}}{L} - K_1\tilde{x}_1 \tag{6.93}$$

$$\dot{\tilde{x}}_2 = -(1-u)\frac{\tilde{x}_1}{C} + \frac{\tilde{\theta}}{C} - K_2\tilde{x}_2 \tag{6.94}$$

For the generation of adaptation law, the following quadratic Lyapunov function is selected

$$V = \frac{1}{2}L\tilde{x}_1{}^2 + \frac{1}{2}C\tilde{x}_2{}^2 + \frac{1}{2\gamma_1}\tilde{\theta}^2 + \frac{1}{2\gamma_2}\tilde{V}_{in}{}^2 \tag{6.95}$$

where γ_1, γ_2 are positive design parameters. The time derivative of the proposed Lyapunov function is given by:

$$\dot{V} = L\tilde{x}_1\dot{\tilde{x}}_1 + C\tilde{x}_2\dot{\tilde{x}}_2 + \frac{\tilde{\theta}}{\gamma_1}\dot{\tilde{\theta}} + \frac{\tilde{V}_{in}}{\gamma_2}\dot{\tilde{V}}_{in}$$

$$= L\tilde{x}_1[-(1-u)\frac{\tilde{x}_2}{L} + \frac{\tilde{V}_{in}}{L} - K_1\tilde{x}_1] + C\tilde{x}_2[(1-u)\frac{\tilde{x}_1}{L} + \frac{\tilde{\theta}}{L} - K_2\tilde{x}_1] + \frac{\tilde{\theta}}{\gamma_1}\dot{\tilde{\theta}} + \frac{\tilde{V}_{in}}{\gamma_2}\dot{\tilde{V}}_{in}$$

$$= -K_1L\tilde{x}_1{}^2 - K_2C\tilde{x}_2{}^2 - \tilde{\theta}\left(\frac{\dot{\hat{\theta}}}{\gamma_1} + x_2\,\tilde{x}_2\right) + \hat{V}_{in}\,(\tilde{x}_1 - \frac{\dot{\hat{V}}_{in}}{\gamma_2}) \tag{6.96}$$

In order to make the function $\dot{V}$ negative semi definite, the terms in the brackets must be zero. Using this constraint, the following parameter adaptation laws are developed,

$$\frac{\dot{\hat{\theta}}}{\gamma_1} + x_2\,\tilde{x}_2 = 0$$

$$\dot{\hat{\theta}} = -\gamma_1 x_2\,\tilde{x}_2 \tag{6.97}$$

$$\tilde{x}_1 - \frac{\dot{\hat{V}}_{in}}{\gamma_2} = 0$$

$$\dot{\hat{V}}_{in} = \gamma_2\tilde{x}_1 \tag{6.98}$$

Hence, if $\widetilde{x_1}, \widetilde{x_2} = 0, \dot{V} = 0$ and $\dot{V} < 0$ for all other values of $\widetilde{x_1}$ and $\widetilde{x_2}$. Now, by Lasalle's invariance principle, the origin is asymptotically stable. So, as $t \to \infty, \hat{\theta} \to \theta, \hat{V}_{in} \to V_{in}$, $\widehat{x_1} \to x_1$ and $\widehat{x_2} \to x_2$.

6.6 Conclusion

In this chapter a different maximum power point tracking algorithm has been proposed which does not require the information of flow speed. The two control technique was evaluated for permanent magnet synchronous generator based marine current turbines: classical PI control and more advanced control techniques, namely adaptive backstepping control technique. We have used normalized adaptive backstepping control law which reduces the number of uncertain terms in control law. Therefore, the control algorithm is simple and considerably reduces the computational complexity. The control algorithm uses continuous switching function to prevent the controller becoming unstable due to high rate of change of parameters during adaptation.

Chapter VII

Simulation Results

7.0 Introduction

In this chapter the simulation results of the marine current energy conversion system has been discussed fully. Flow 3D software package has been used to develop the computational fluid dynamic model of the marine current turbine. Also Matlab/Simulink has been selected to carry out the overall modeling task of MCECS. The software package allows user to use Simulink in conjunction with Matlab to develop algorithm, numerical computation and data visualization. A complete simulation model of the MCECS is developed using SimPower Systems toolbox of Matlab/Simulink Software.

7.1 CFD Simulation Results

CFD simulations predict the motion of a flow within a domain by discretizing the governing Navier-Stokes equations and solving the resulting set of algebraic equations. The commercial CFD package FLOW *3D* was used to solve the incompressible Navier-Stokes equations using finite difference approximations. To ensure numerical stability, a combination of central and upwind differences is used for the convective terms. One important feature known as the General Moving Object (GMO) can simulate the complex motions of floating bodies in steep waves. The motions of the bodies can be prescribed or they can be coupled to the motion of the fluid. It allows for extremely complicated motions and flows. For the simulation, the rotor was first drawn in

SolidWorks. The geometry file was imported into ***FLOW 3D*** as an **STL** file. The thickness of the blades of the rotor was made two time actual so that the grid employed could discretize them. The density of the rotor was adjusted to keep the total inertia of the rotor equal to the original prototype. The accuracy of any CFD simulation depends on the type of grid utilized (e.g. structured or unstructured) and obviously the grid resolution. Structured grids are the most desirable because they inherently provide highly accurate numerical solutions. As such, they have generally been used in CFD simulations of turbines. The disadvantage of using structured grids is that the grid generation process is a manually intensive and time consuming task. In contrast, the creation of unstructured grids is a more automated process that can be performed easily. However, when using unstructured grids, we should insure that the grid quality (e.g. grid element skewness, aspect ratio, and density) does not adversely impact the accuracy of the numerical solution.

Fig. 7.1a shows the computational domain grid set up in **FLOW *3D*** to analyze the performance characteristics of marine current turbine. However, here each had a cell size of 5mm. Both the finer mesh and coarse size grid were used and they produced basically the same results. The rotor was modeled as a general moving object with freedom to rotate around the z- axis. The boundary conditions used for the simulation are shown in Fig. 6.1b. The k-ε Reynolds-averaged Navier-Stokes (RANS) model was used to simulate turbulence in the flow.A uniform steady velocity profile was assumed at the inlet of the computational domain. Thus we made the simplifying assumption that the turbulence intensity was 5% and uniform at the inlet of the computational domain. A pressure outlet boundary condition was applied at the outlet. To reduce flow

recirculations on the far-field boundaries and to improve the stability of the numerical solution, symmetry boundary condition was applied. A rotating reference frame model was used to simulate the rotation of the blade and hub. This method simulates rotation without the need to physically rotate the computational grid by forming the governing equations for the rotor domain in a reference frame that rotates with the turbine, while the outer domain remains in a stationary coordinate system. Fig 7.2 plots the power coefficient of the turbine with respect to tip speed ratio.

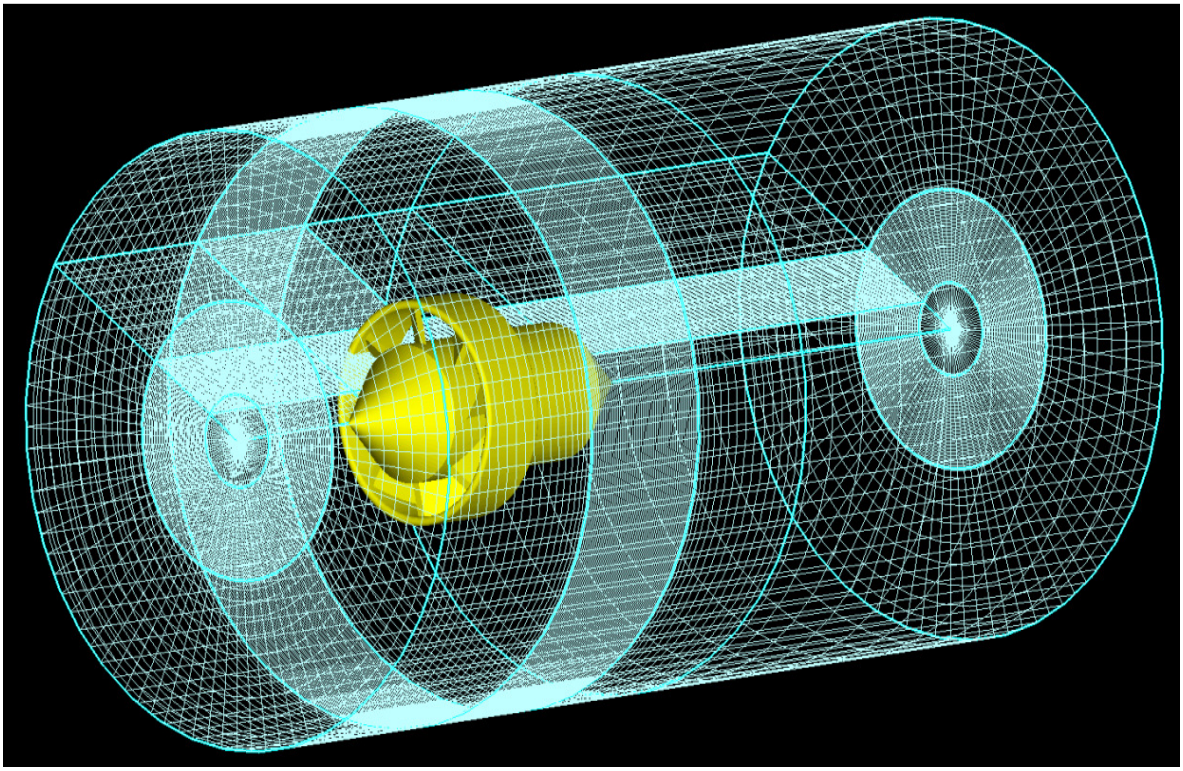

Fig. 7.1(a)

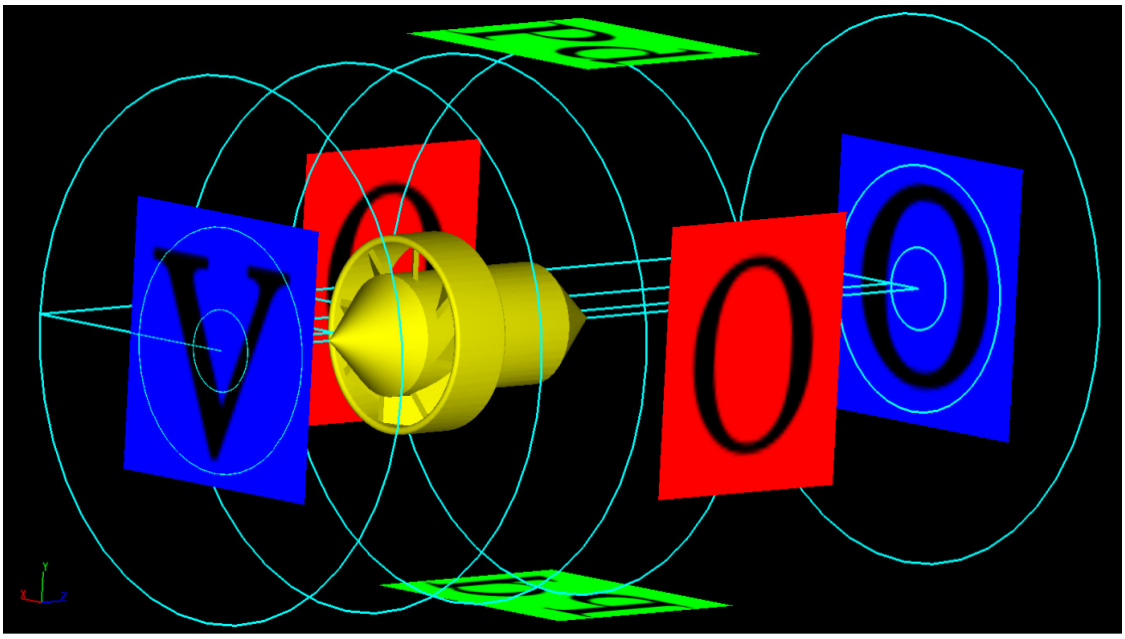

Fig. 7.1(b)

Fig. 7.1 CFD Software FLOW *3D* (a) Computational Domain Grid (b) Boundary condition of Marine Current Turbine

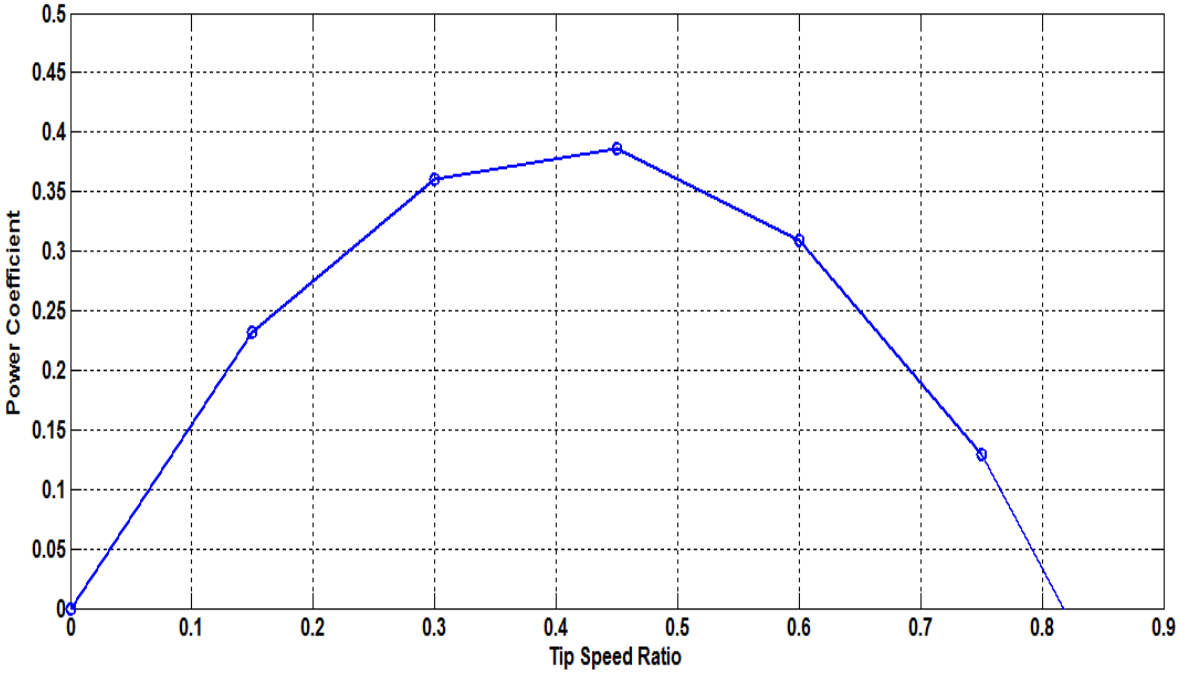

Fig. 7.2 Power Coefficient Curve of Marine Current Turbine

In order to run the turbine at the optimum speed proportional integral controller is incorporated in FLOW -3D subrotine so that turbine can operate at optimum speed for different flow speed. Fig 7.3a shows that the flow speed is varied from 0.8m/s to 1.25m/s. The rotor speed at different flow speed is captured in Fig. 7.3b. The output shows that

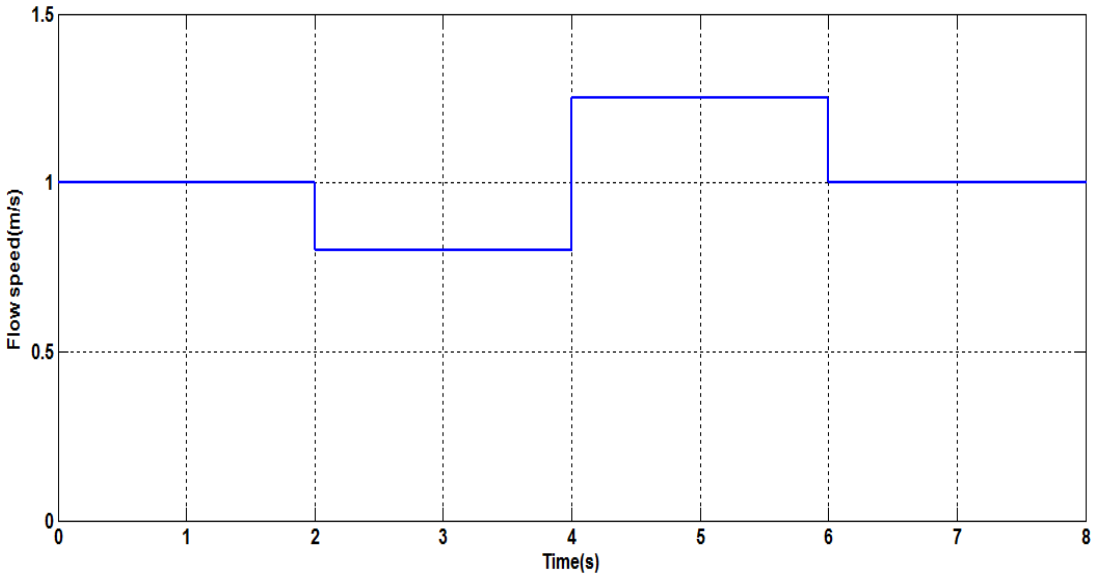

Fig. 7.3(a)

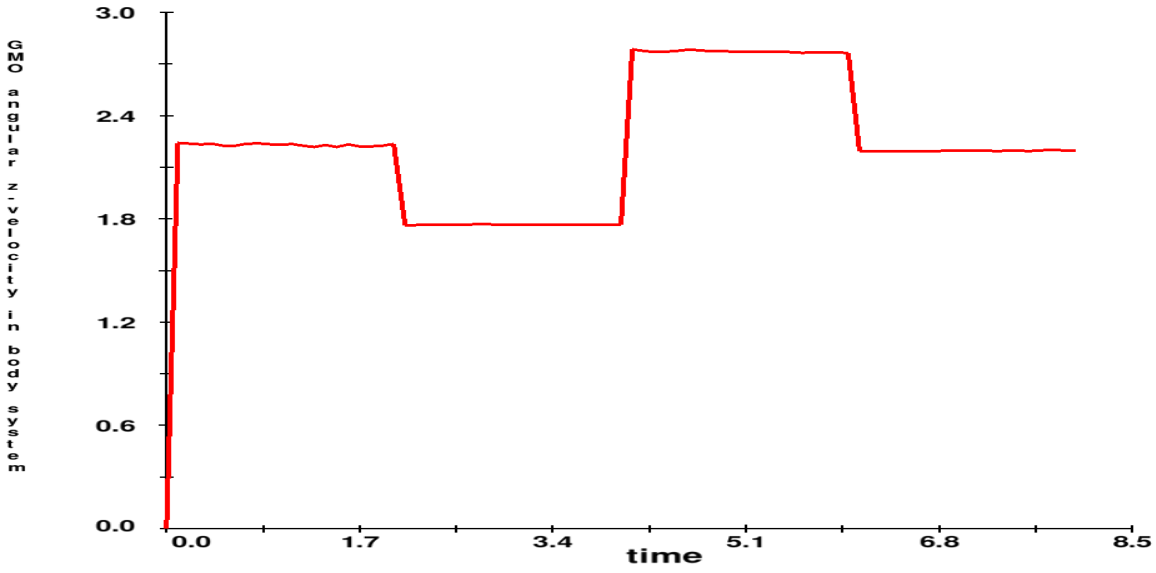

Fig. 7.3(b)

Fig. 7.3 Response of FLOW 3D Marine Current Speed (a) Step change in flow speed (b) Turbine Optimum Rotor Speed with Proportional Integral controller

PI controller can successfully operate the system at optimum speed. The optimization of the rotor design (pitch angle, geometry, number of blades) done using CFD. Simulation shows that rotor with curved blades improves the efficiency of the turbine. It should be noted that the CFD model only includes the turbine blade and hub geometries. Other turbine components, such as the clamp support, were not considered in this simulation. Nevertheless, the reasonable agreement between the CFD results and the blade element momentum method calculations provides confidence in the results obtained with both numerical methods. The CFD simulation represents is a step in the development of a CFD methodology to characterize the turbine performance. In future research should be done to develop a numerical model by considering realistic inlet velocity profiles and turbulence levels. Also include structural elements of the turbine, such as the support, in future simulations.

7.2 Matlab/ Simulink Simulation Results

Matlab/Simulink has been selected to carry out the overall modeling task of MCECS. Simulink is a platform, is often used for model-based design of dynamic systems. The software package provides an interactive graphical presentation of results and a customizable set of block libraries, and also options for specialized application. This makes it the best candidate for accomplishing the objective of fostering interdisciplinary integration (hydrodynamics and electro mechanics). In addition Simulink can be used in conjunction with Matlab to allow user to develop algorithm, data visualization, data analysis and numerical computation. It can also control physical setups. The time stepping of the simulation is chosen to be fixed.

The dimensions of the turbine are measured directly from the prototype. The efficiency of the turbine is derived through potential flow theory. Generator parameters are determined experimentally within the lab settings. Testing and steady-state analysis are carried out to determine generator efficiency. The PMSG inertia and damping constant are calculated analytically. Finally the generator model is validated through separate modelling exercises. The rectifier parameters are taken from manufacturer's specifications. The efficiency of rectifier is identified through lab testing. Similarly the parameters of customized boost converter are taken from the design and validated through testing.

% Subroutine for Turbine Simulation

```
function [Tm,wr_ref]= fcn(speed,wr_old,speed_ref)
          omega=wr_old/gearatio;
          r=rin+dr/2.0;
          c=cin+dc/2.0;
          a=ain+da/2.0;
        for i=1:s
             flow_char=flow(s,steps,dr,cin,ain,speed,span,piv,gamma);
            flow_tot=r*omega+flow_char;
            flow_tot=r*omega;
            angle=atan(flow_tot/speed);
            attack=a-angle;
            total=sqrt(speed.^2+flow_tot.^2);
            gamma=c*pi*total*sin(attack);
            r=r+dr; c=c+dc;a=a+da; arm=r;
            load=density*gamma*dr*total;
            moment=moment+load*cos(angle)*arm;
            drag=drag+load*sin(angle);
            lift=lift+load*cos(angle);
        end
    wr_ref=tsr_ref*speed_ref*gearatio/rout;
   Tm=-(blade_num*moment)/gearatio;
   Pow_Tur(z)=Tm*omega;
   Cp(z)=Pow_Tur(z)/(0.5*density*(pi*(rout-rin)^2)*(speed^3));
   Cs(z)=omega*rout/speed;
```

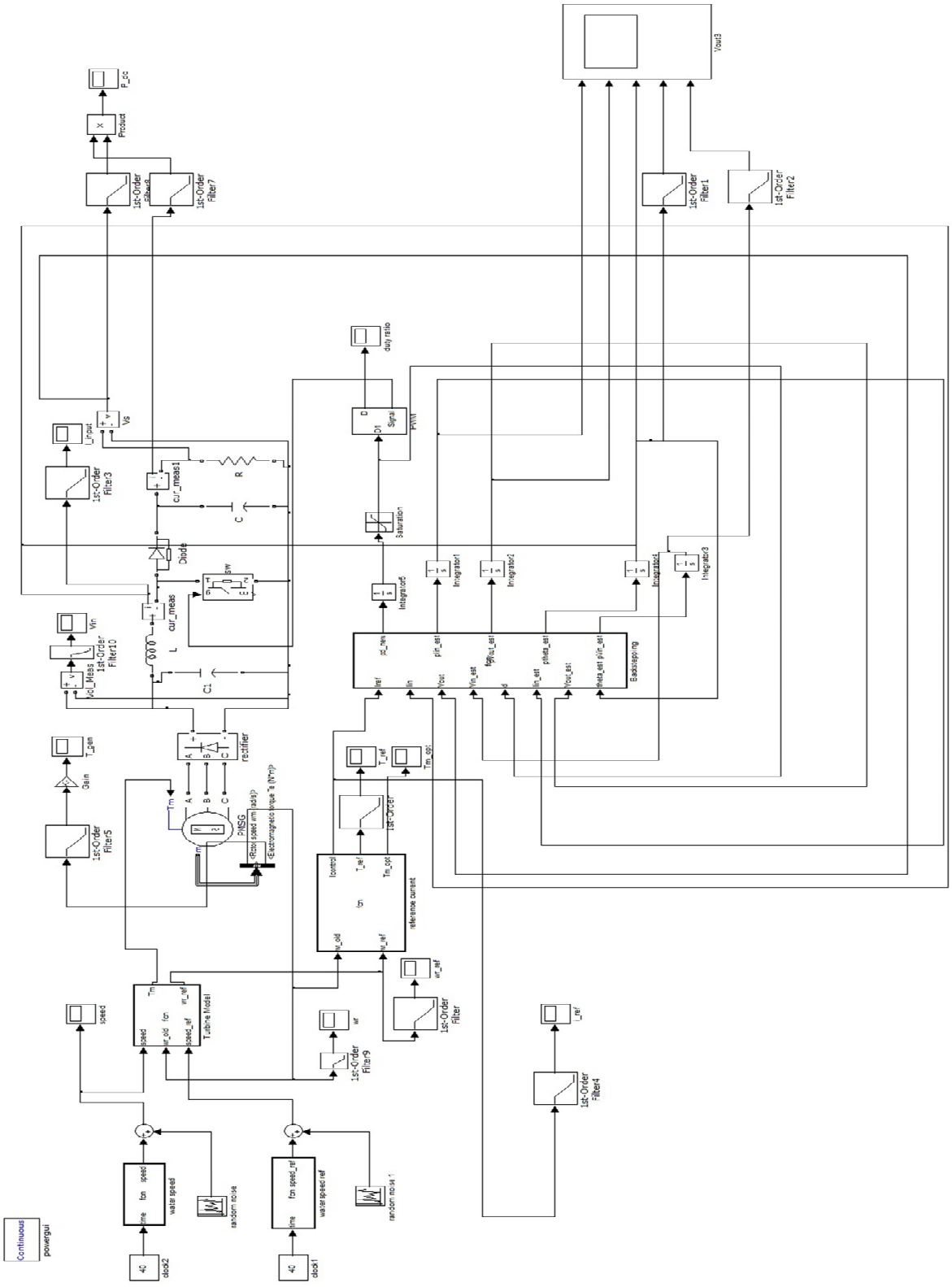

Fig. 7.4 Matlab/ Simulink Model of Marine Current Energy Conversion System

% Subroutine for MPPT Simulation

```
function [Icontrol,T_ref,Tm_opt] =fcn(wr_old,wr_ref)
   ang_speed=wr_old/gearatio;
   wr_ref=wr_ref/gearatio;
   Kopt=0.5*density*C_opt*pi*R_tur*R_tur*((R_tur/lambda_opt)^3);
   Tm_opt=Kopt*wr_ref*wr_ref;
   T_ref=Kopt*(ang_speed*ang_speed);
   Iref=T_ref/(1.5*p*magnet*gearatio);
   Icontrol=(Iref)*(pi/(2*sqrt(3)));
 end
```

% Subroutine for Adaptive Backstepping Simulation

```
function[pd_new, pIin_est, pVout_est, ptheta_est, pVin_est]=fcn(Iref, Iin,Vout, Vin_est, d,
Iin_est,Vout_est, theta_est)
   Iin_err=Iin-Iin_est;
   Vout_err=Vout-Vout_est;
   ptheta_est=-Vout*Vout_err*lambda1;
   pVin_est=lambda2*Iin_err;
   pIin_est=-(1-d)*(Vout_est/L)+(Vin_est/L)+K1*Iin_err;
   pVout_est=(1-d)*(Iin_est/C)-(theta_est*Vout/C)+K2*Vout_err;
   pIin_err=-(1-d)*Vout_err/L+pVin_est/L-K1*Iin_err;
   z1=Iin_est-Iref;
   alpha1=(Vin_est+L*K1*Iin_err)/(1-d)+c1*z1;
   z2=Vout_est-alpha1;
   pd_new=(1/(Vin_est+L*K1*Iin_err))*(c2*z2*((1-d)^2)-(z1/L)*(1-d)^3+(Iin_est/C)*(1-d)^3-
(Vout*theta_est/C)*(1-d)^2);
   pd_new=pd_new+(1/(Vin_est+L*K1*Iin_err))*(((1-d)^2)*K2*Vout_err-(1-d)*pVin_est-(1-
d)*L*K1*pIin_err-c1*pIin_est*(1-d)^2);
end
```

Table 7.1 shows the parameters of the marine turbine, PMSG, dc-dc converter used in the simulation. The sampling frequency used for the simulation is 100 kHz .

Table 7.1 Parameters of turbine, PMSG and DC-DC converter

Marine Current Turbine (MCT)	
Water density, ρ	1000 kg/m^3
Blades' swept area, A	0.062832 m^2
Outer radius of the blade, R_{out}	0.15 m
Inner radius of the blade, R_{in}	0.05 m
Optimum Coefficient, K_{opt}	0.7223 N.m./(rad./s)^2
Gear ratio, N	4
Permanent Magnet Synchronous Generator (PMSG)	
No. of phases	3
Magnet Position	Surface Mounted
Per phase stator resistance, R_s	3.4 Ω
Per phase stator inductance, L_s	0.000835 H
Permanent magnet flux linkage, λ_m	0.4022 V.s.
No. of pole pairs, p	2
Torque constant, K_t	1.2066 N.m./A
Inertia, J	0.004 kg.m^2
Dc-Dc Converter (Boost)	
Inductance, L_c	500 μH
Capacitance, C_c	1000 μF
Switch Type	Power Mosfet
Switching Frequency, f	5 kHz

Fig. 7.5 presents the step responses of the system for different flow speed. The flow speed is varied from 0.8 m/s to 1.25 m/s. The trajectory of the generator reference torque always follows the turbine optimum torque as shown in Fig. 7.5(b). Thus, at any flow speed, it is always possible to track the optimum turbine torque using the proposed control strategy without using any flow sensors. Fig. 7.5(c) shows the developed electromagnetic torque of the PMSG. The developed electromagnetic torque is controlled so that it always tracks the reference torque which is evident in the figures. In Fig. 7.5(d), the reference current and

the input dc current of the converter are displayed. The proportional integral controller ensures that the developed torque and the input current strictly follow the reference generator torque and the command current. Fig. 7.5(e) depicts the reference speed and the measured speed of the PMSG. It is observed that the PMSG always operates at the optimum reference speed for any given flow speed. Fig. 7.6 shows the output power of the proposed marine energy conversion system. The system always produces maximum power at any flow speed. Therefore the PI controller always operates the system at maximum power point. Also the controller provides good steady state and dynamic performances and exhibits excellent tracking capabilities.

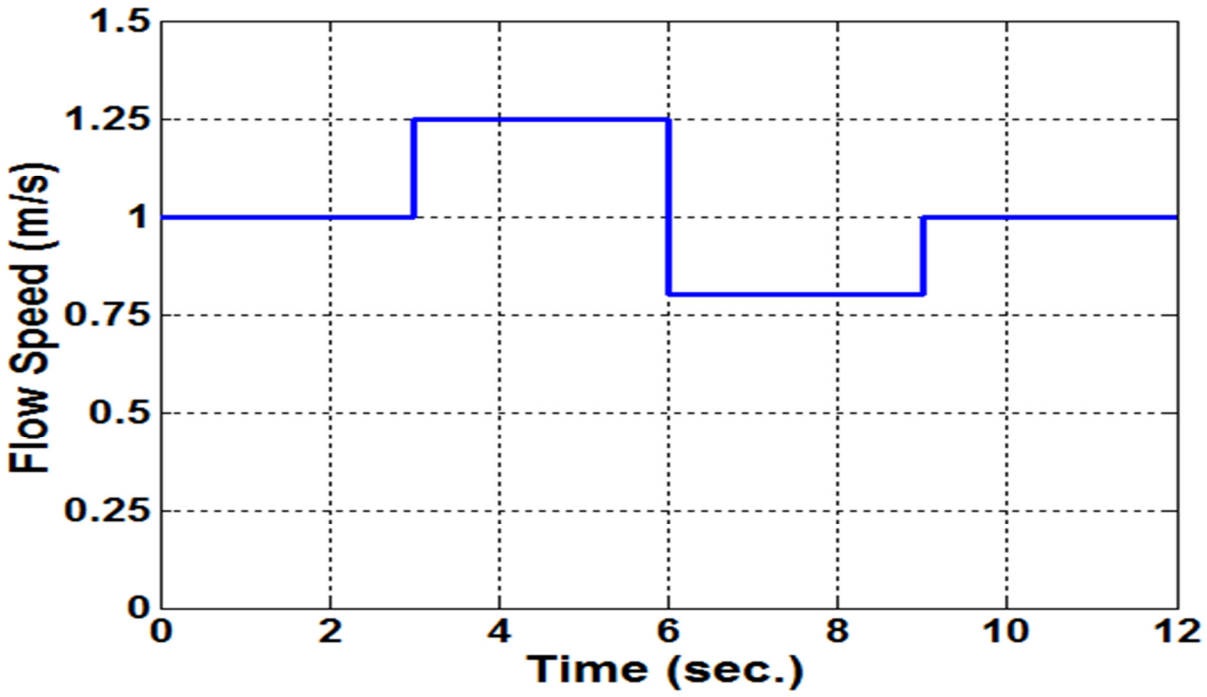

Fig. 7.5 (a)

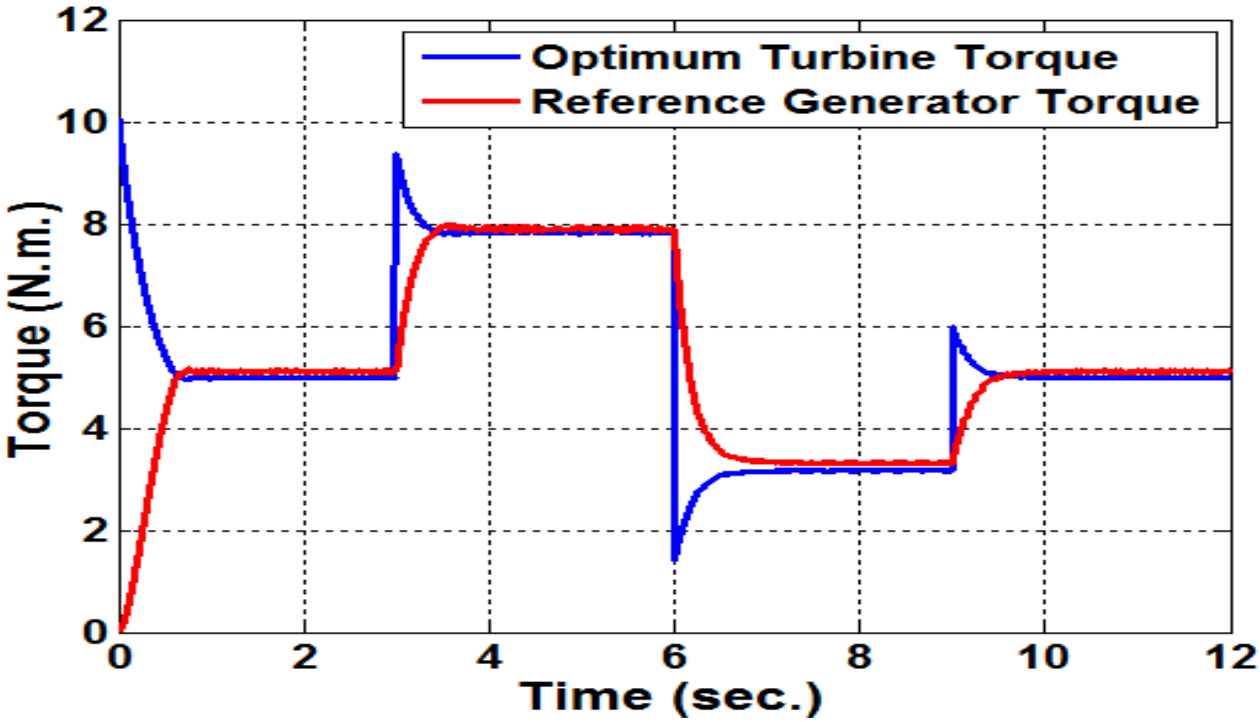

Fig. 7.5 (b)

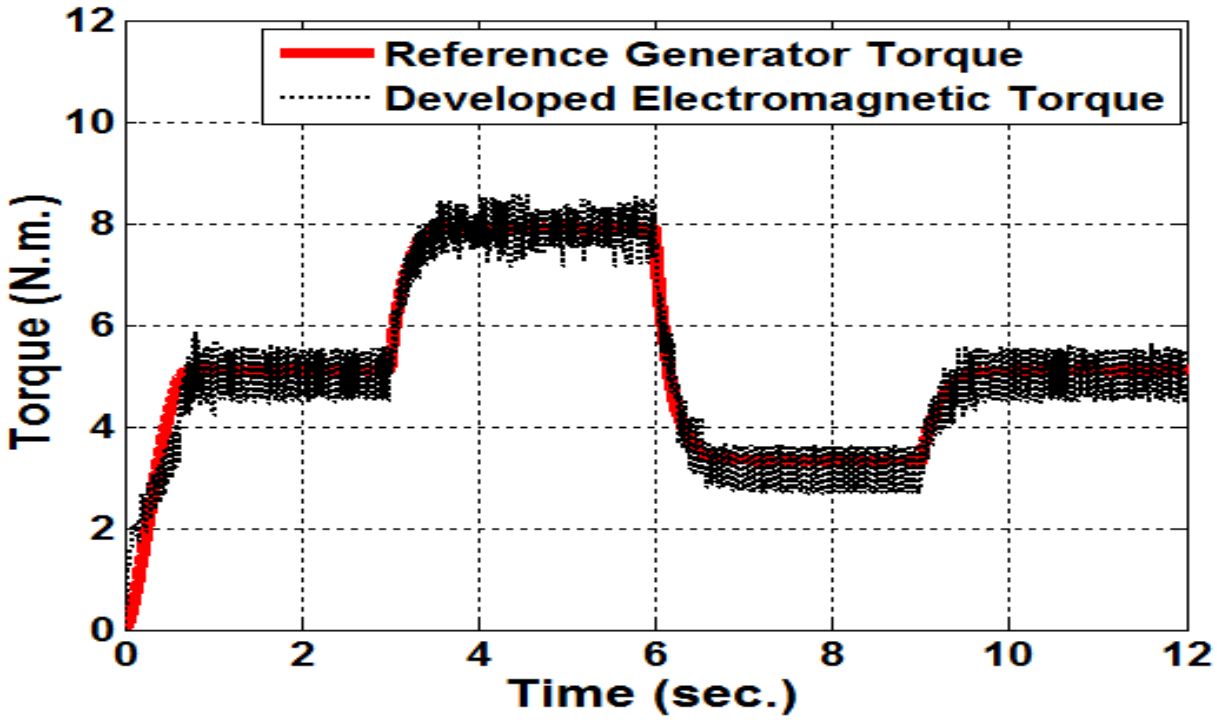

Fig. 7.5 (c)

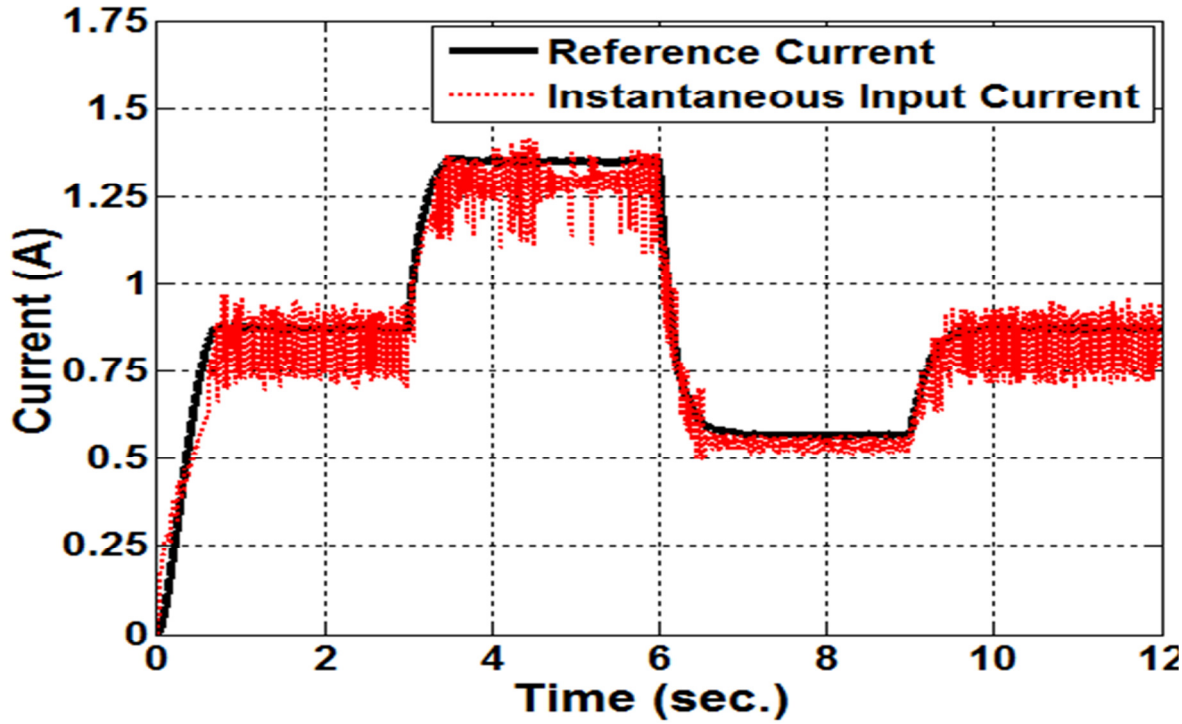

Fig. 7.5 (d)

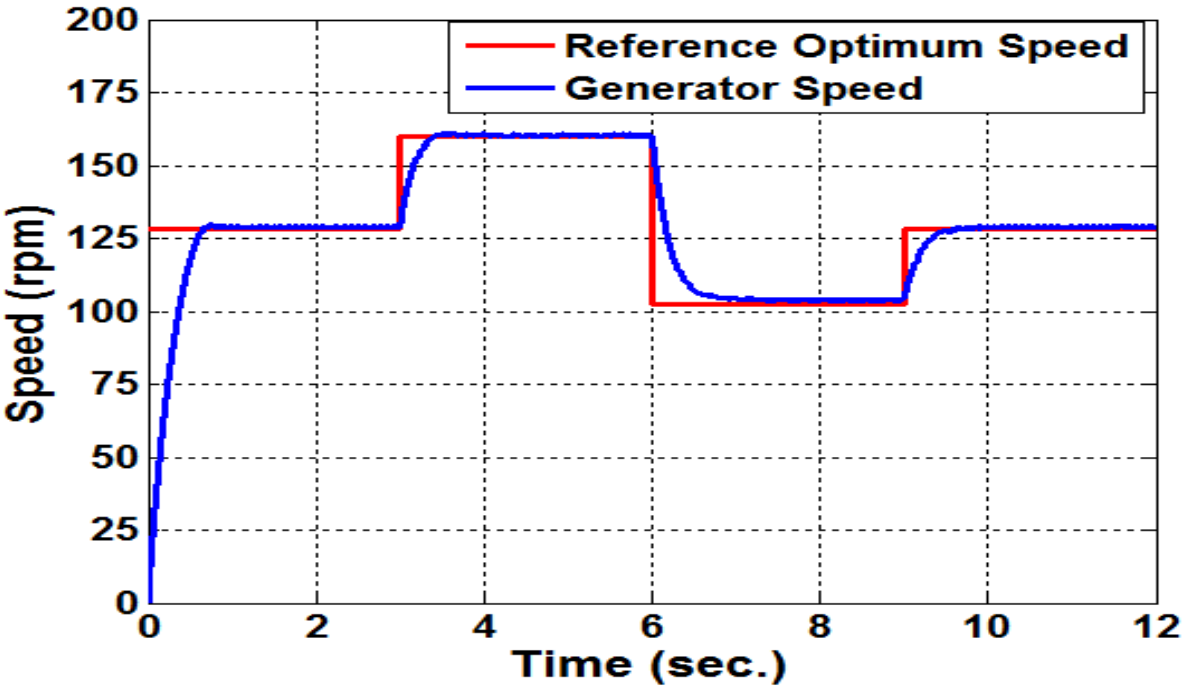

Fig. 7.5(e)

Fig. 7.5 Response of the system for step changes in flow speed: (a) flow speed, (b) optimum turbine torque and reference generator torque, (c) reference and developed generator torque, (d) reference current and instantaneous input current of the converter and (e) reference generator speed and instantaneous generator speed.

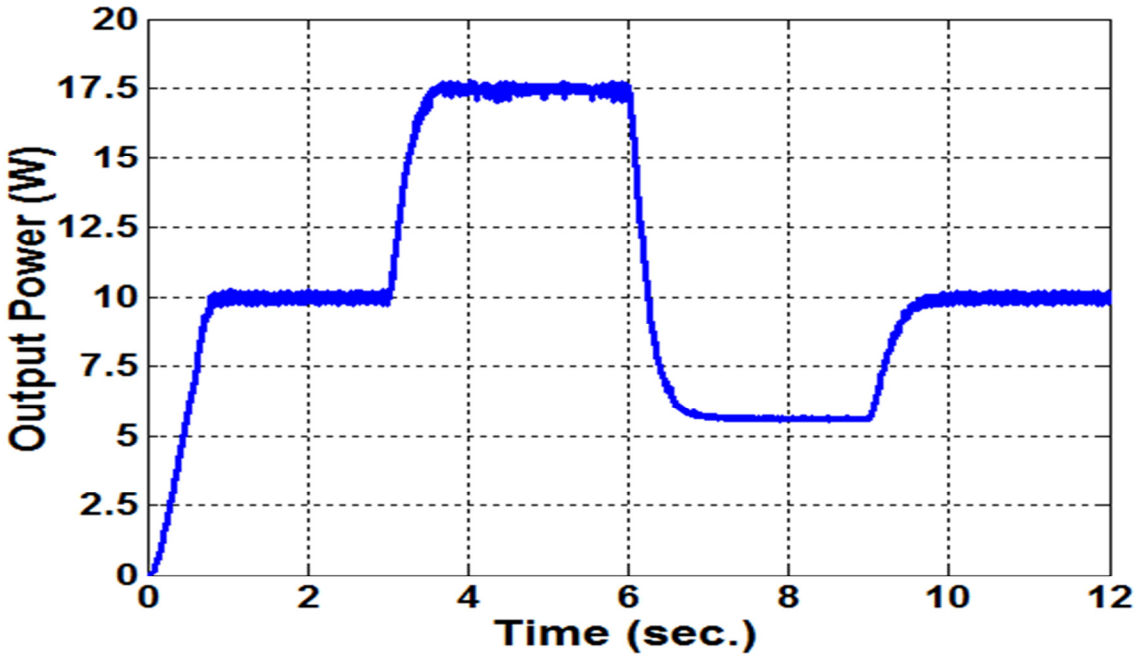

Fig. 7.6 Output power of Marine Current Energy Conversion System

Fig. 7.7 presents the step responses of the system for different flow speed. The speed is varied from 0.8 m/s to 1.5 m/s. The trajectory of the generator reference torque always follows the turbine optimum torque as shown in Fig. 7.7(b). Thus, at any flow speed, it is always possible to track the optimum turbine torque using the proposed control strategy without using any flow sensors. Fig. 7.7(c) shows the developed electromagnetic torque of the PMSG. The developed electromagnetic torque is controlled so that it always tracks the reference torque which is evident in the figures. In Fig. 7.7(d), the reference current and the input dc current of the converter are displayed. The backstepping controller ensures that the developed torque and the input current strictly follow the reference generator torque and the command current. Fig. 7.7(e) depicts the reference speed and the measured speed of the PMSG. It is observed that the PMSG always operates at the optimum reference speed for any given flow speed.

Fig. 7.8 illustrates the output voltage, the output current and the output power of the proposed marine energy conversion system. The system always produces maximum power at any flow speed. Thus, the proposed controller always operates the system at maximum power point. The adaptive performance of the proposed controller is depicted in Fig 7.9. The trajectories of the estimated load resistance and the estimated input voltage follow that of the actual load resistance and the actual input voltage. Thus, the proposed controller provides good steady state and dynamic performances and exhibits excellent tracking capabilities. Fig. 7.10 provides the boundless and stability of the proposed controller. The input current and the output voltage errors z_1 and z_2, respectively, converge to zero within finite time. The virtual control law α_1 also matches the output dc voltage of the system. This proves the stability of the proposed controller.

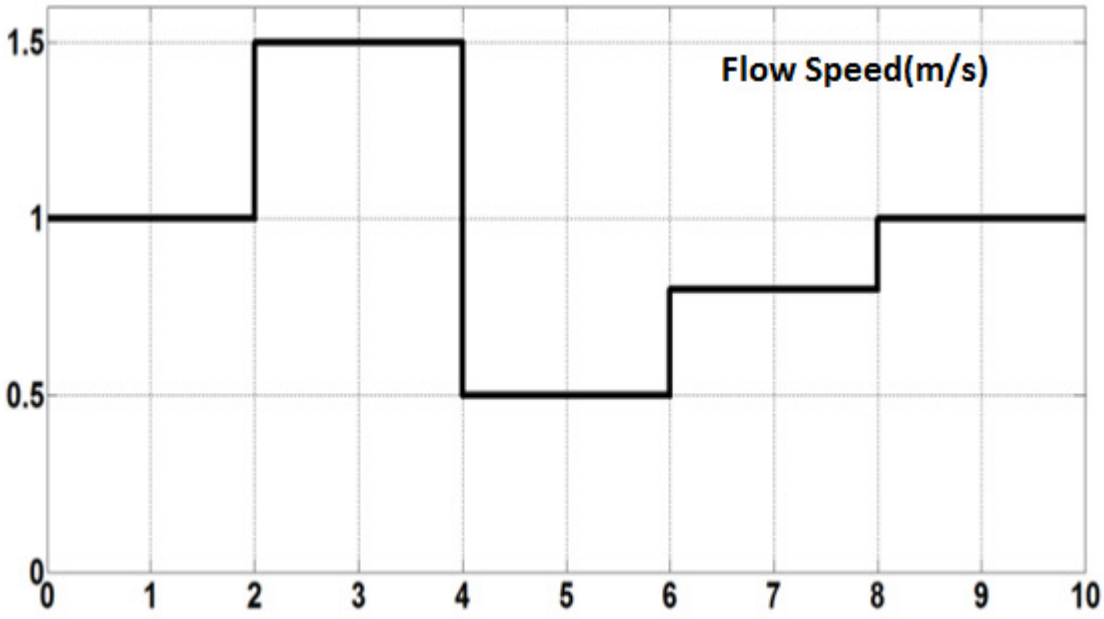

Fig. 7.7(a)

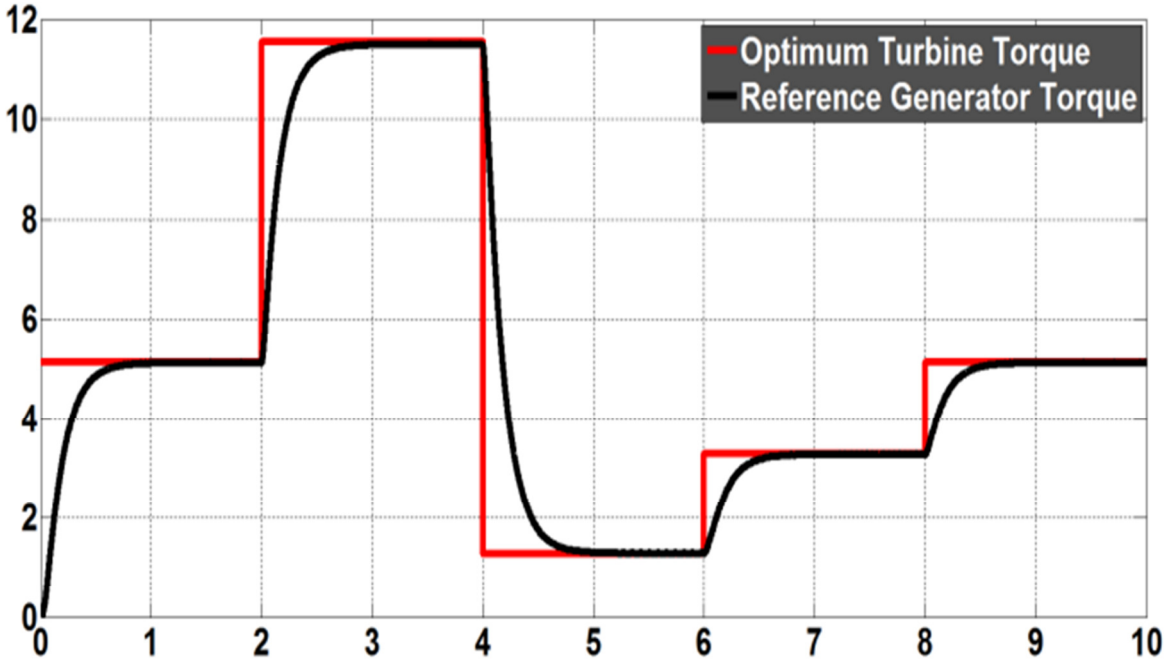

Time (s)

Fig. 7.7 (b)

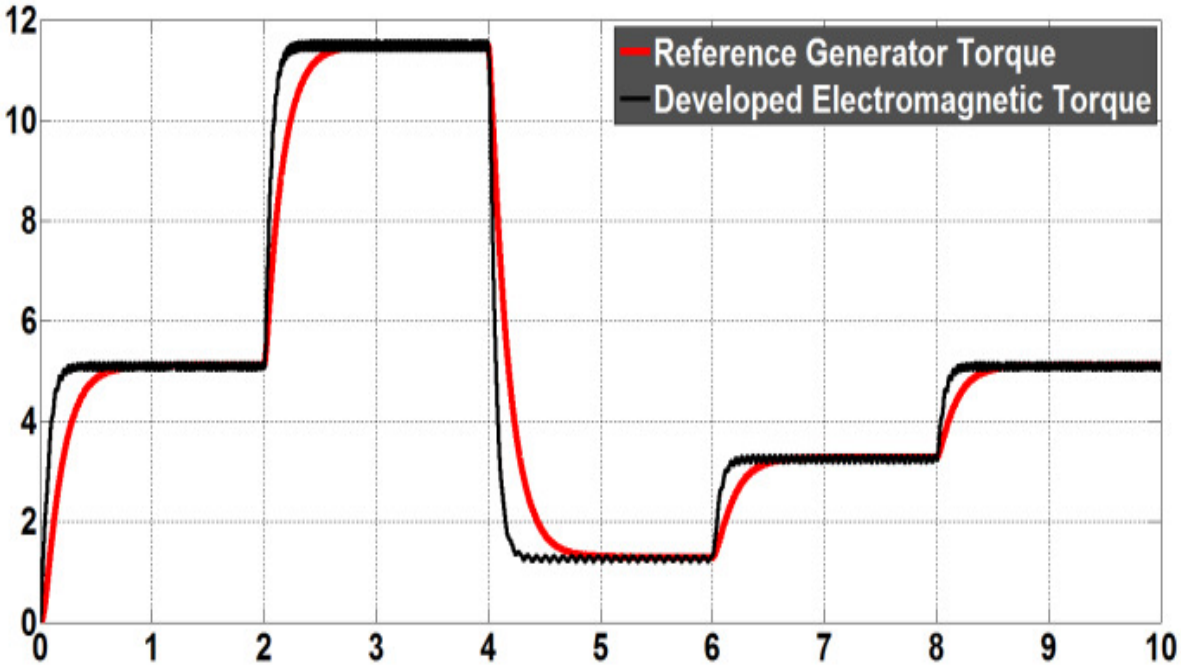

Time (s)

Fig. 7.7(c)

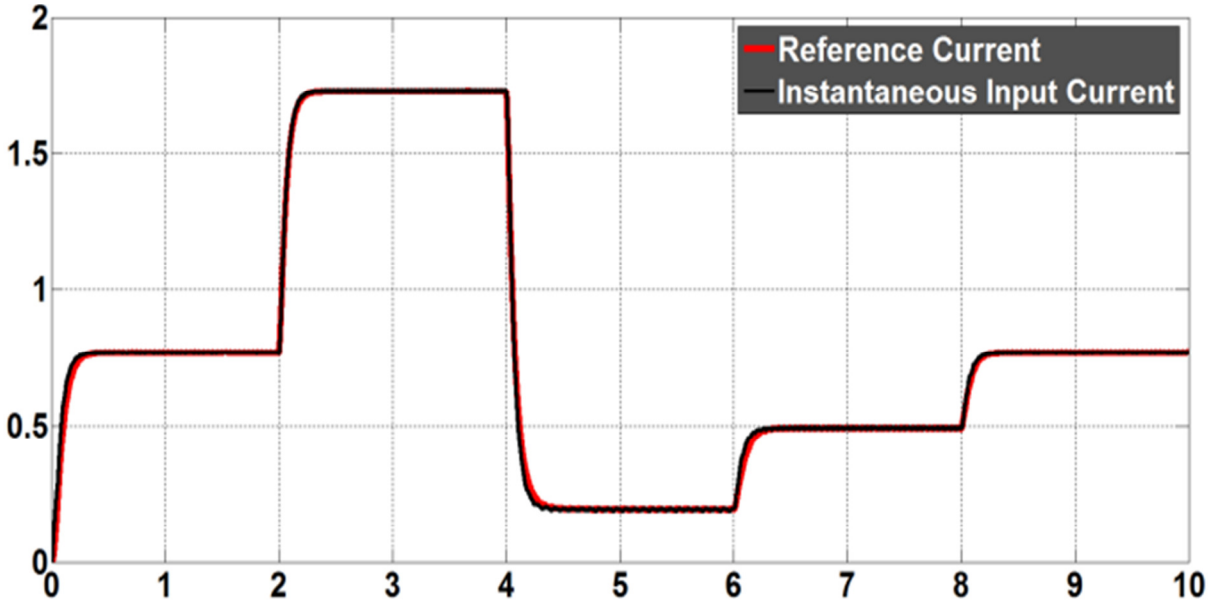

Time(s)

Fig. 7.7 (d)

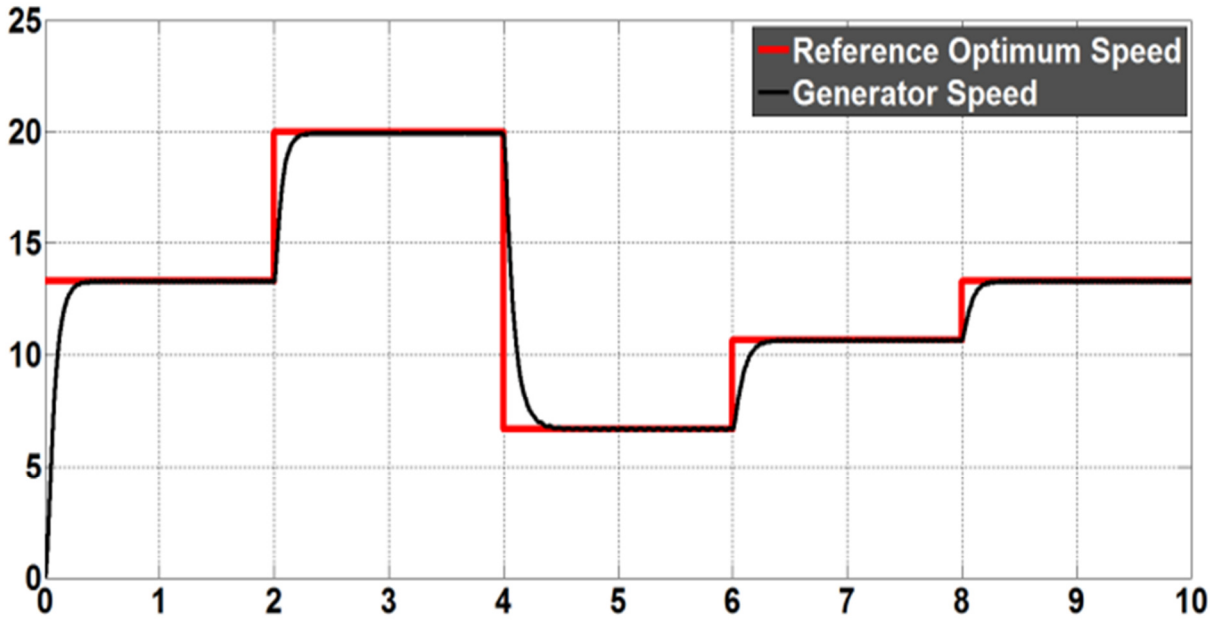

Time (s)

Fig. 7.7 (e)

Fig. 7.7 Response of the system for step changes in (a) flow speed(m/s), (b) optimum turbine torque and reference generator torque(N-m), (c) reference and developed generator torque(N-m), (d) reference current and instantaneous input current of the converter(A) and (e) reference generator speed and instantaneous generator speed(rad/s).

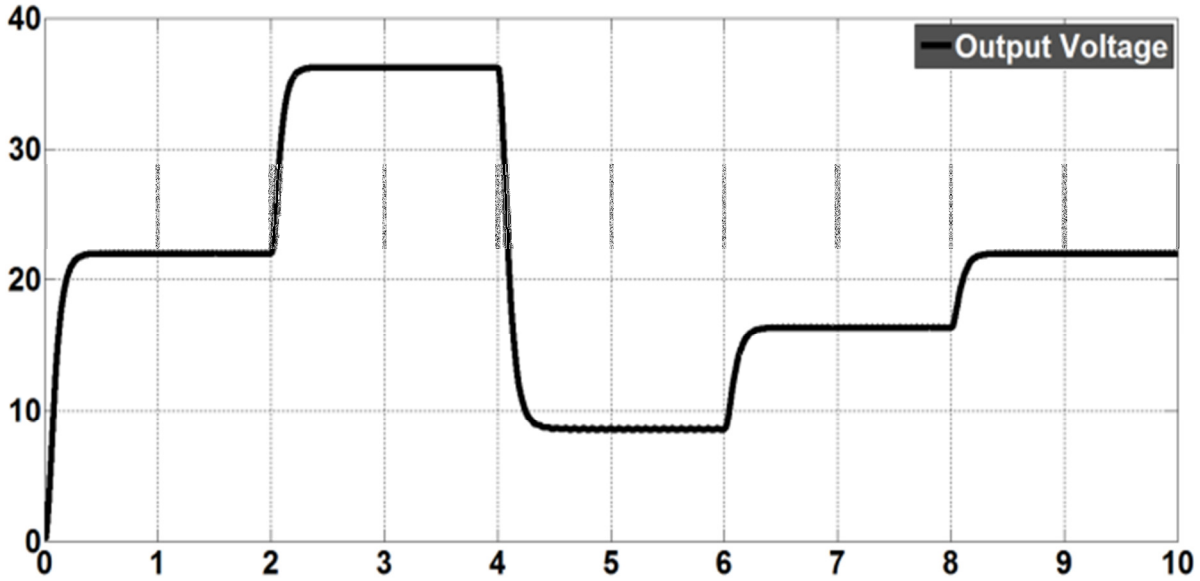

Fig. 7.8(a)

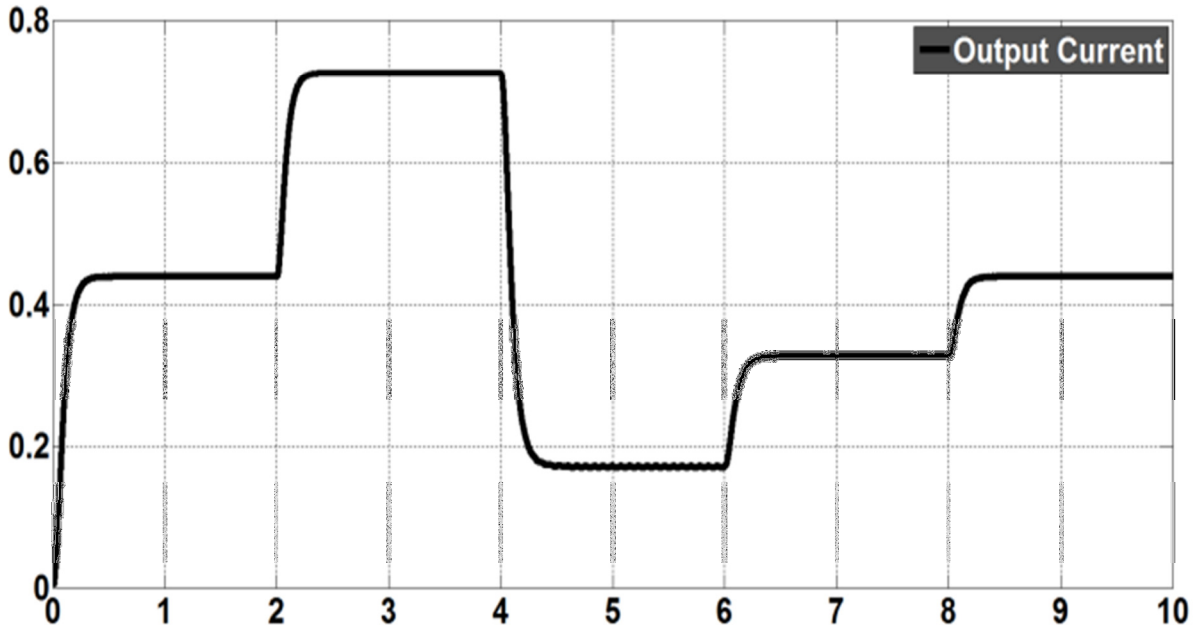

Fig. 7.8(b)

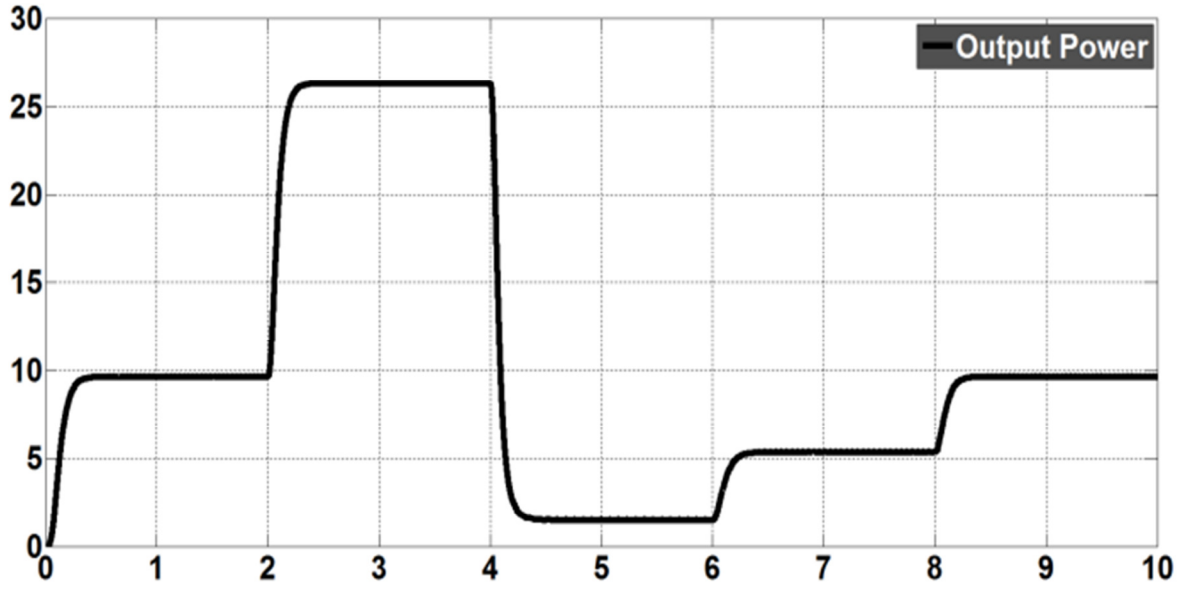

Fig. 7.8 (c)

Fig. 7.8 (a) Output load voltage (V), (b) output load current (A) and (c) Output power (W) of the system

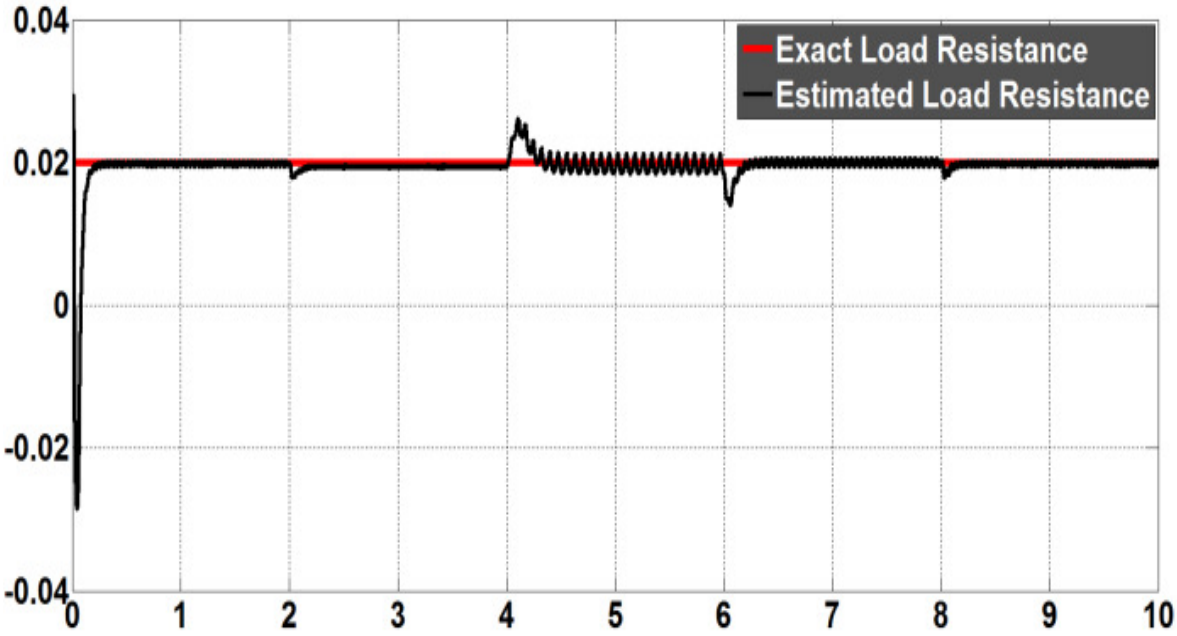

Fig. 7.9 (a)

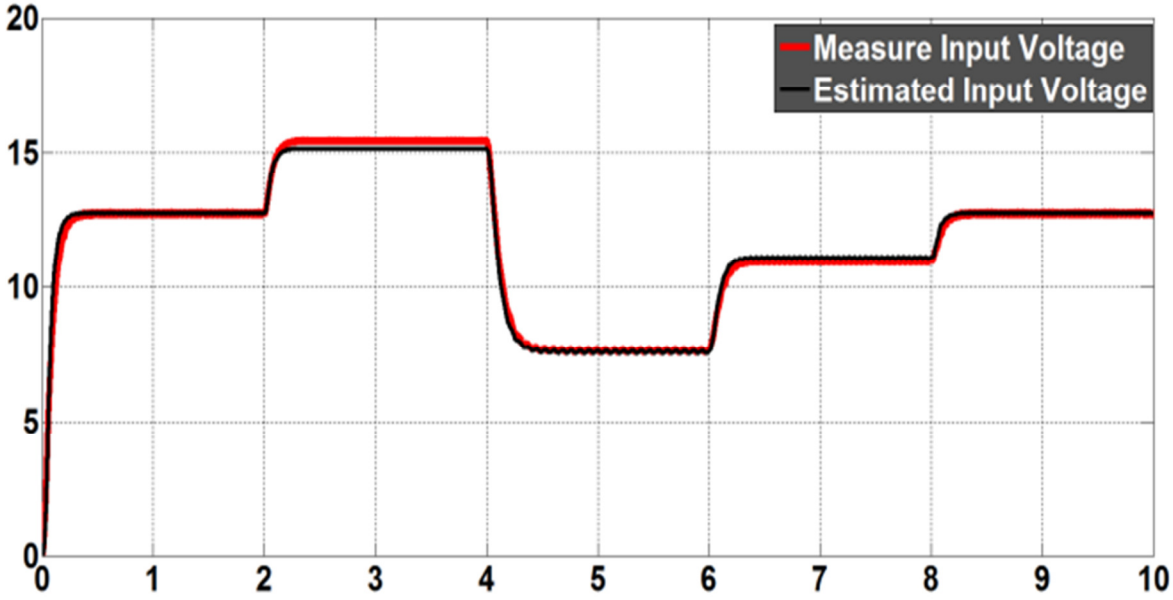

Fig. 7.9 (b)

Fig. 7.9 (a) Exact and estimated load resistance (ohm) and (b) exact and estimated input voltage (V)

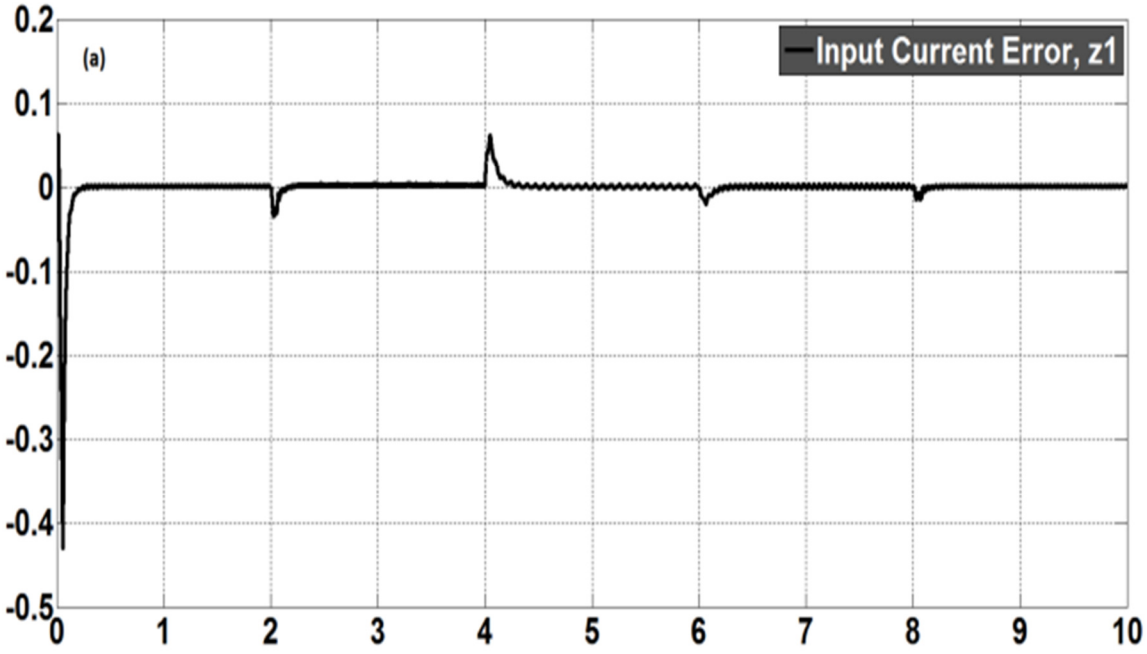

Fig. 7.10(a)

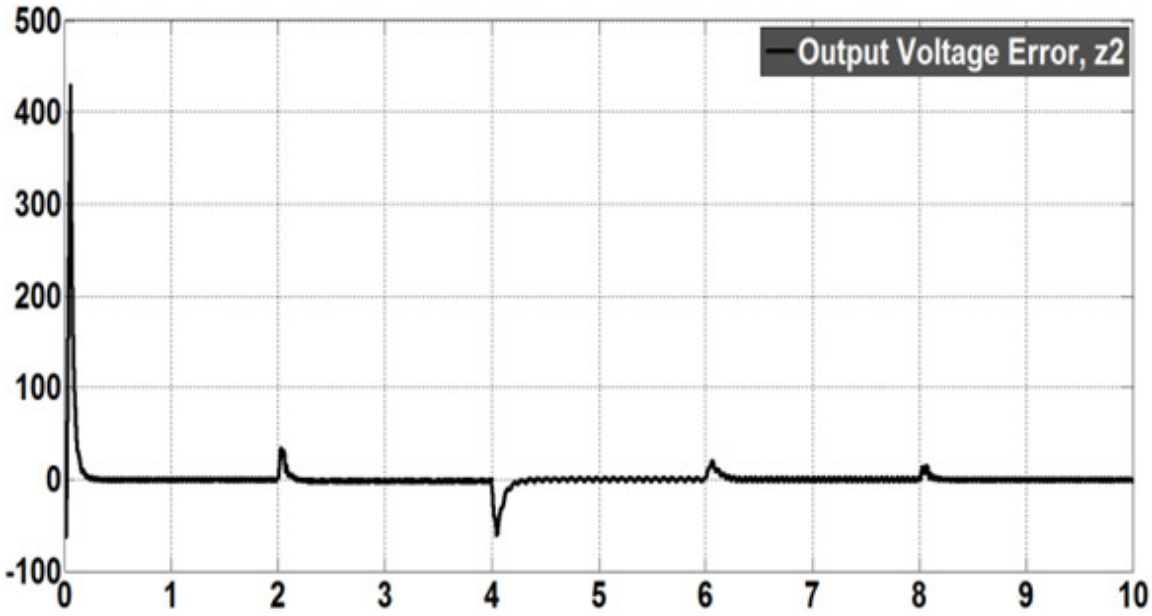

Time(s)

Fig. 7.10 (b)

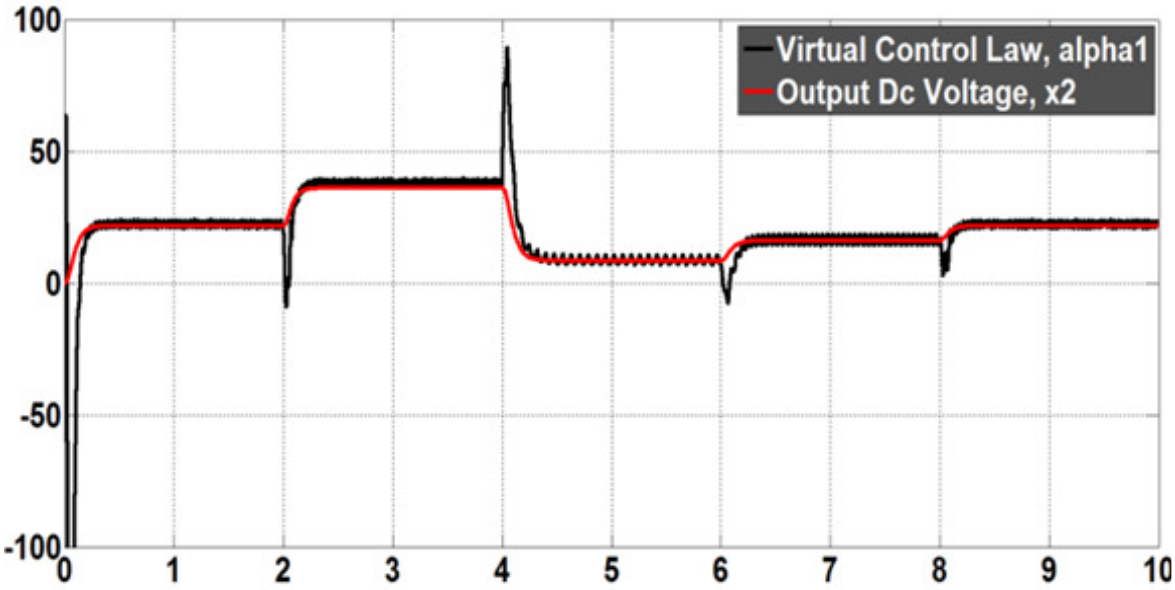

Time(s)

Fig. 7.10(c)

Fig. 7.10 Performance of the proposed controller (a) Input current error z_1, (b) Output voltage error z_2 and (c) Virtual voltage control law α_1

7.3 Non Turbulent Resource Simulation Results

The adaptive backstepping controller for MCECS was tested for tidal speed as explained in resource modeling. The hydrodynamic loads of the marine current turbine were evaluated for a filtered resource shown in Fig. 7.11a. The performances of the controller are shown in Figs 7.11 (b, c, d & e).The obtained results show good tracking performances of the PMSG rotor speed and the reference current.

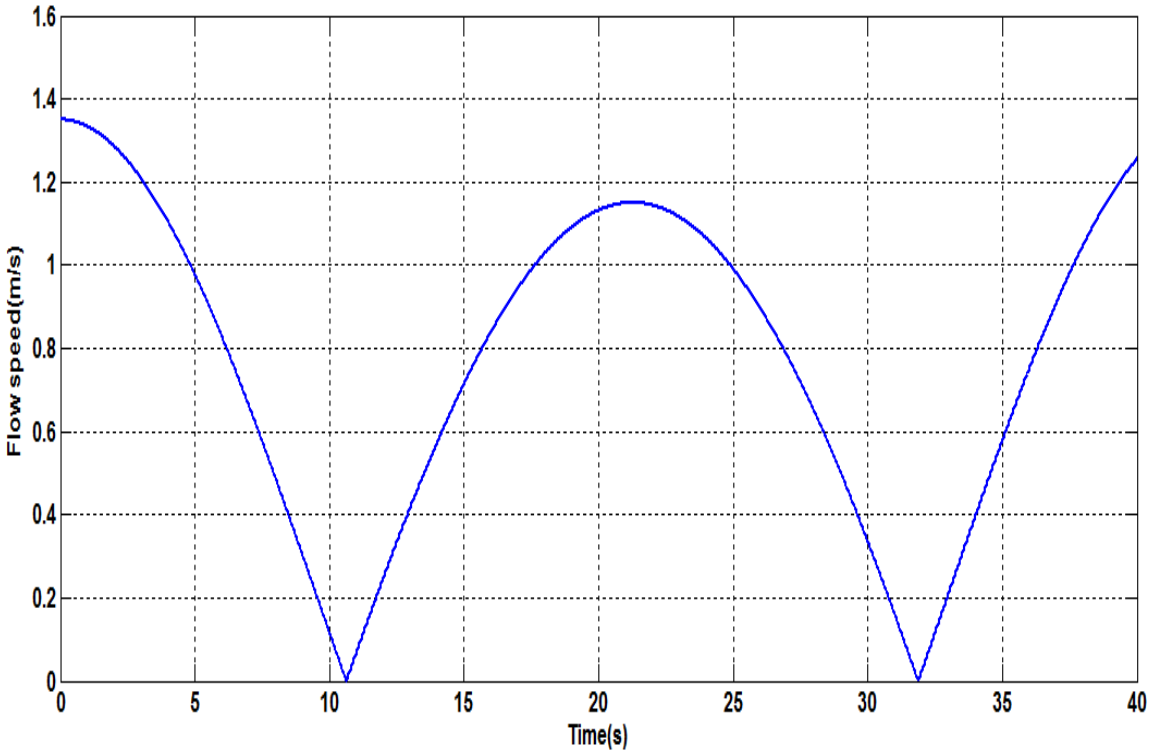

Fig. 7.11(a)

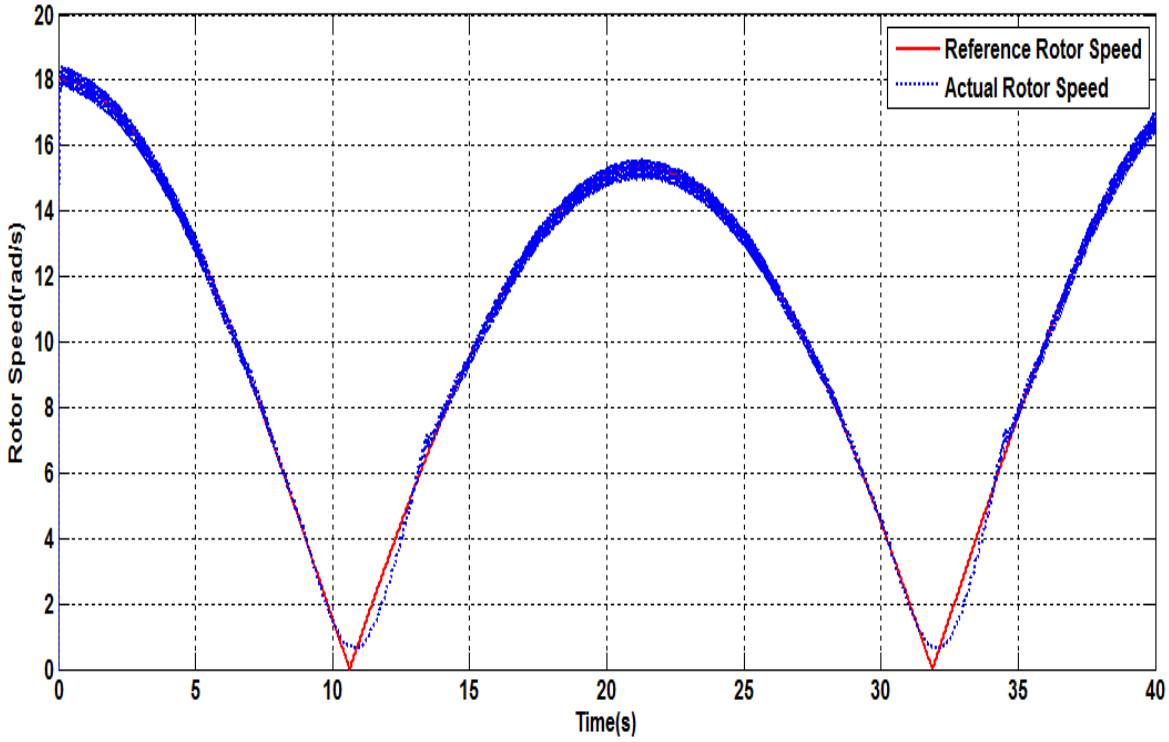

Fig. 7.11 (b)

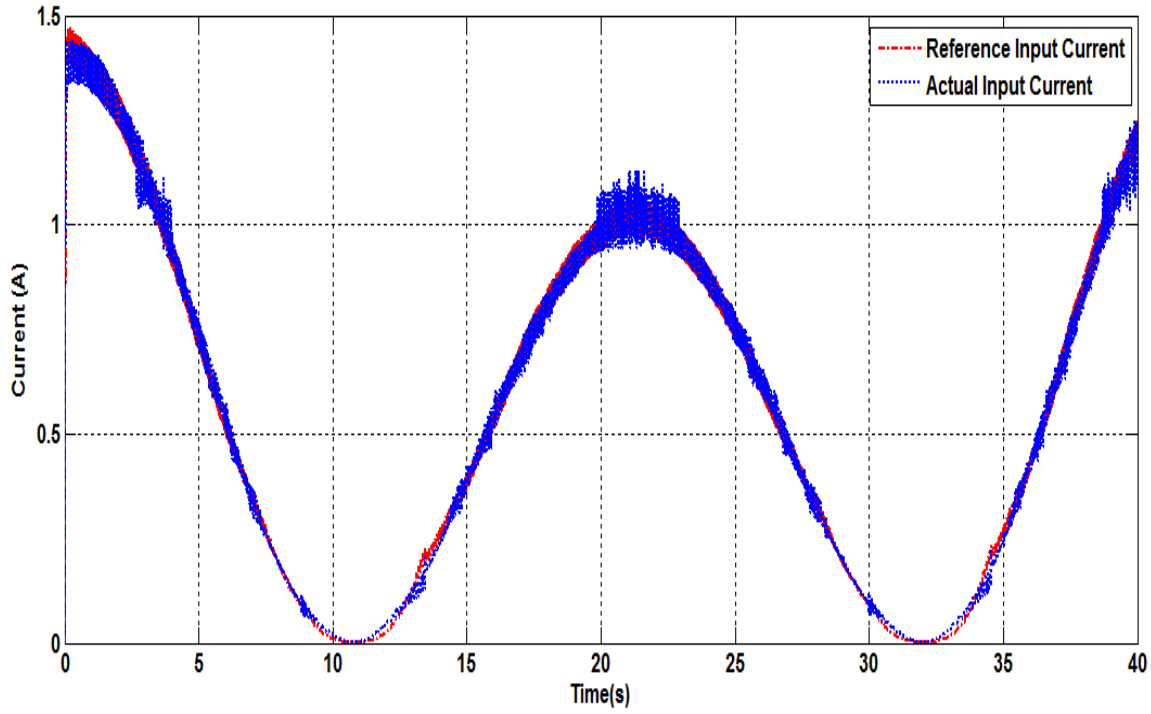

Fig. 7.11 (c)

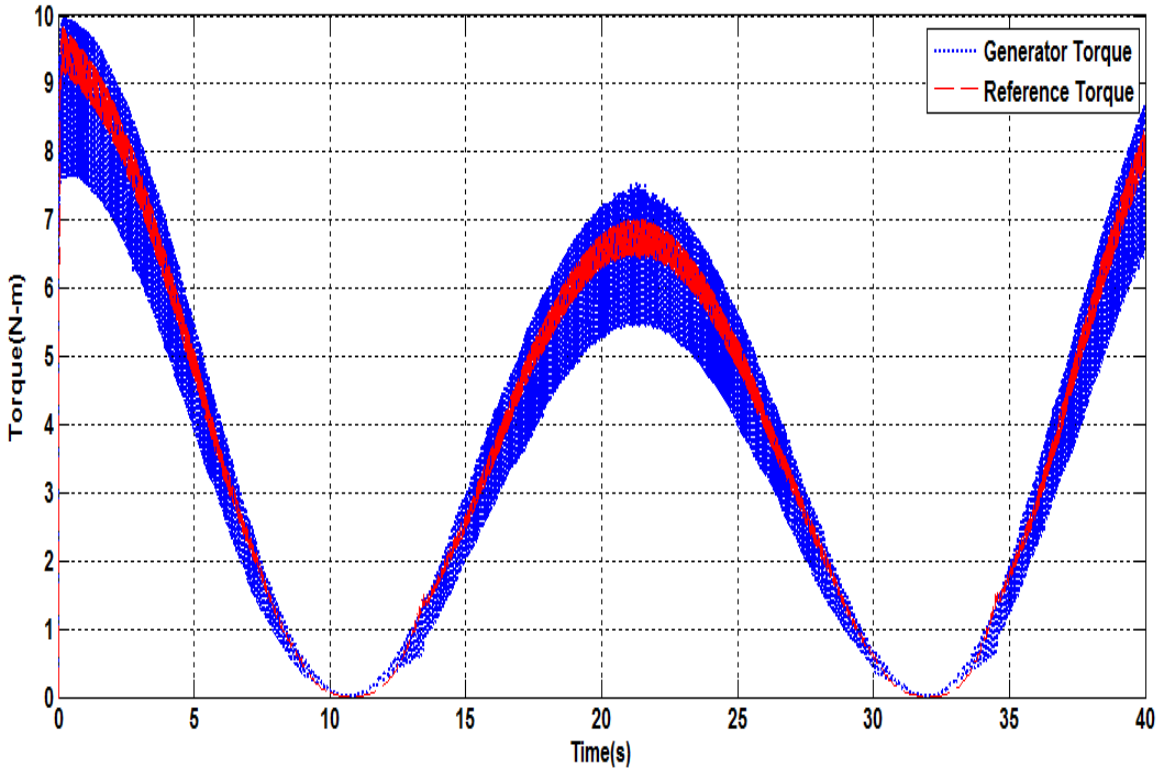
Generator Torque
Reference Torque
Torque(N-m)
Time(s)
0
1
2
3
4
5
6
7
8
9
10
0
5
10
15
20
25
30
35
40

Fig. 7.11(d)

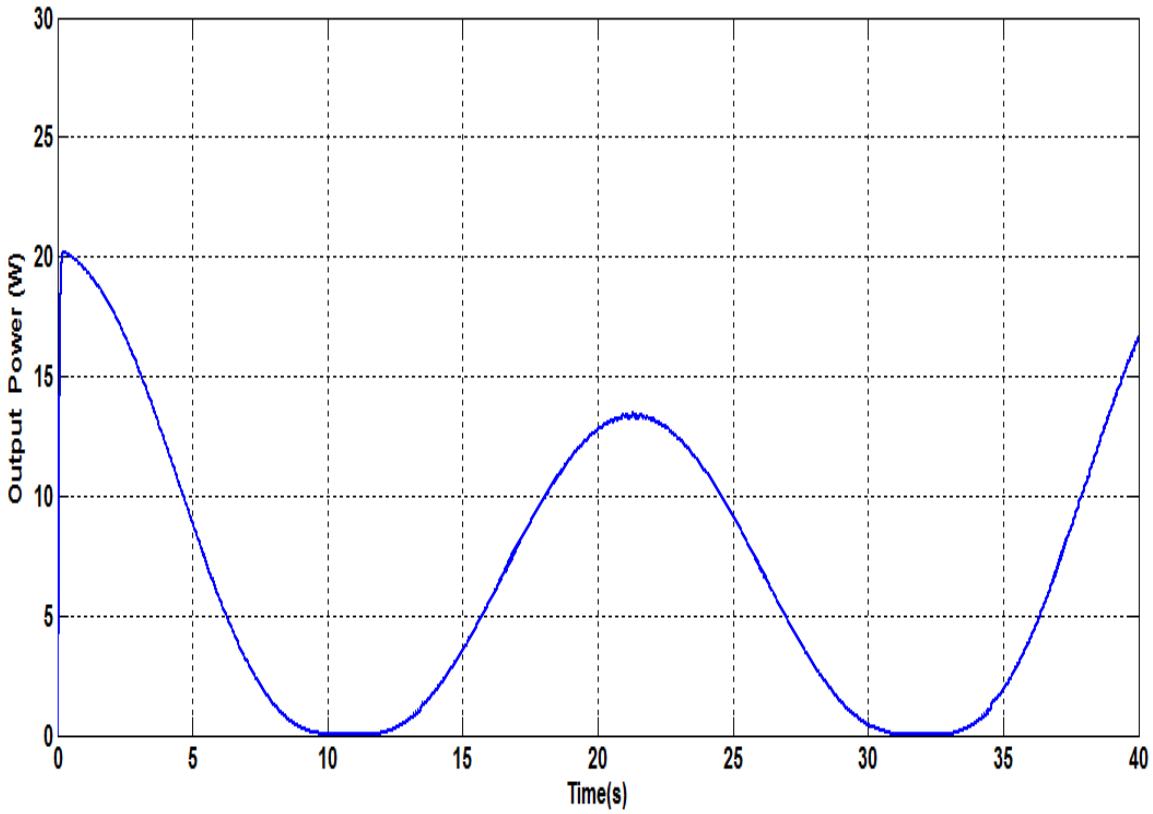

Fig. 7.11 (e)

Fig. 7.11 Response of the system for non-turbulent resource: (a) flow speed, (b) reference generator speed and instantaneous generator speed (c) reference current and instantaneous input current of the converter (d) reference and developed generator torque and (e) output DC power.

7.4 Turbulent Resource Simulation Results

The sensibility of the proposed adaptive backstepping control strategy was analyzed regarding the swell effect. The turbulent resource characteristics are given by Fig.7.12a. The PMSG-based marine current turbine control performances are shown by Figs. 7.12(b, c, d & e). The overshoot and oscillation in ADBT is less compared to PI control. But the settling time is nearly the same for both controllers. The transient performance in control efforts in ADBT is better than that of PI controller.

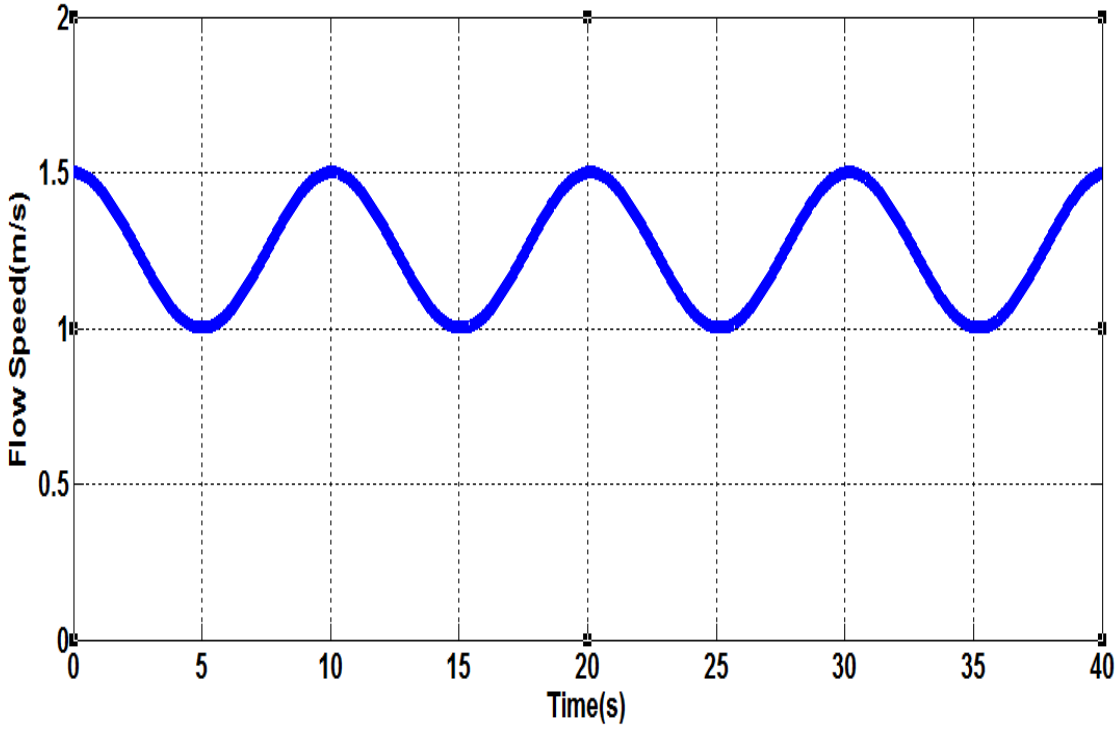

Fig. 7.12(a)

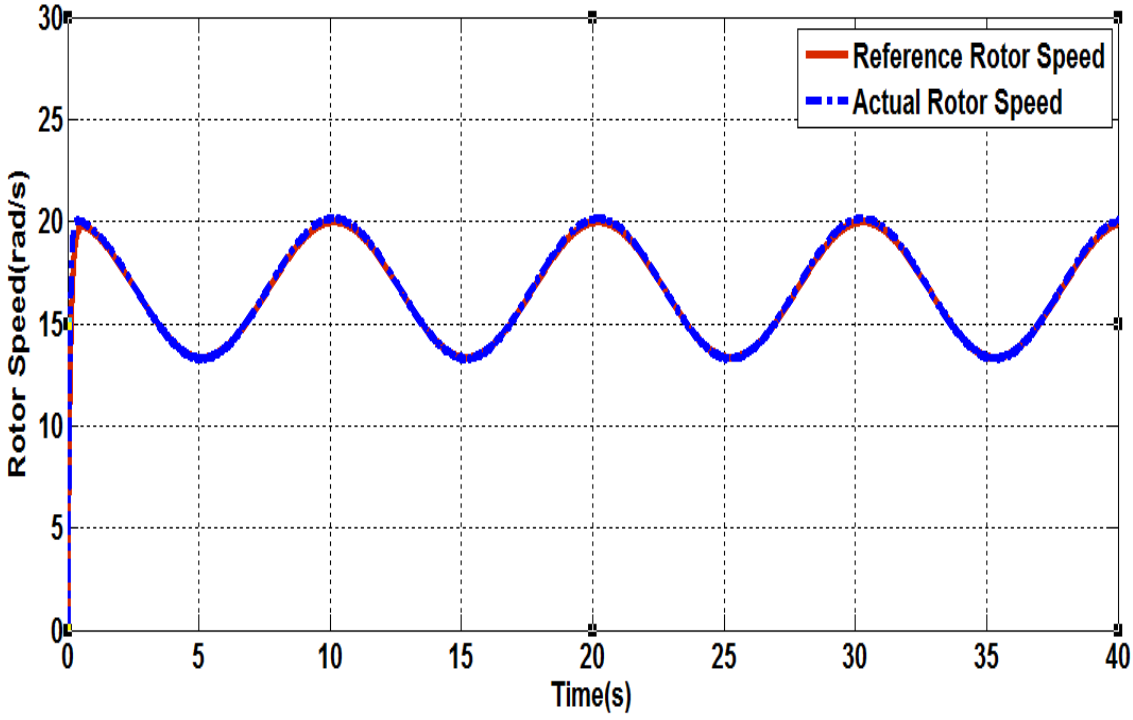

Fig. 7.12(b)

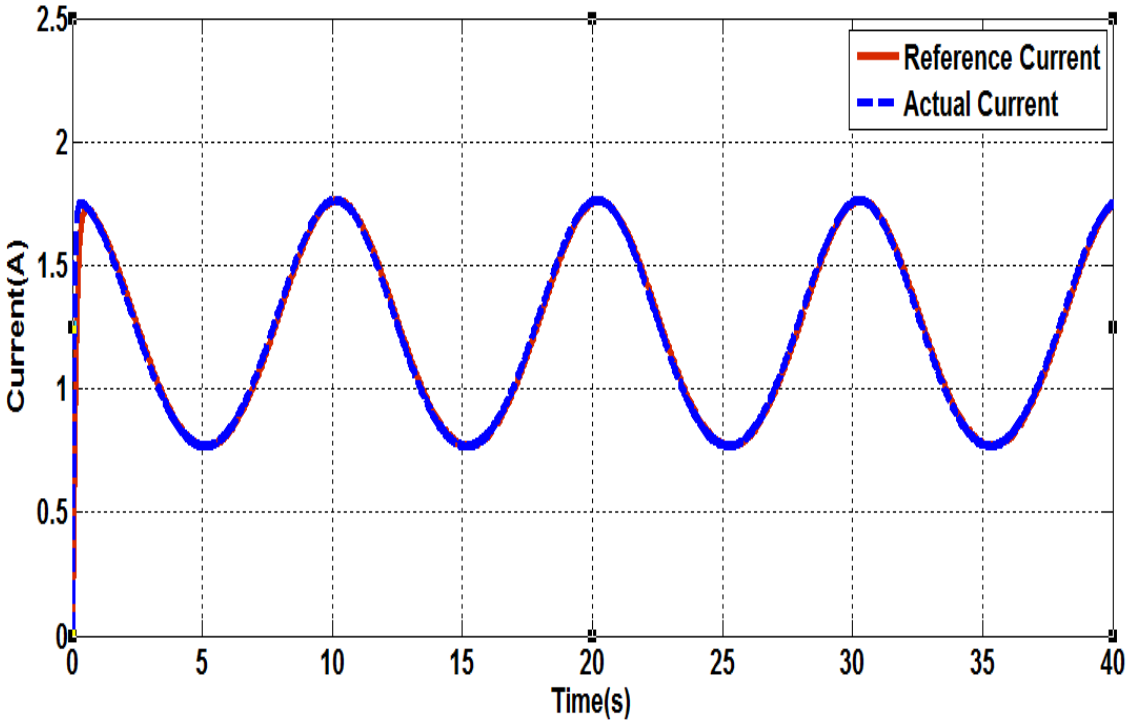

Fig. 7.12(c)

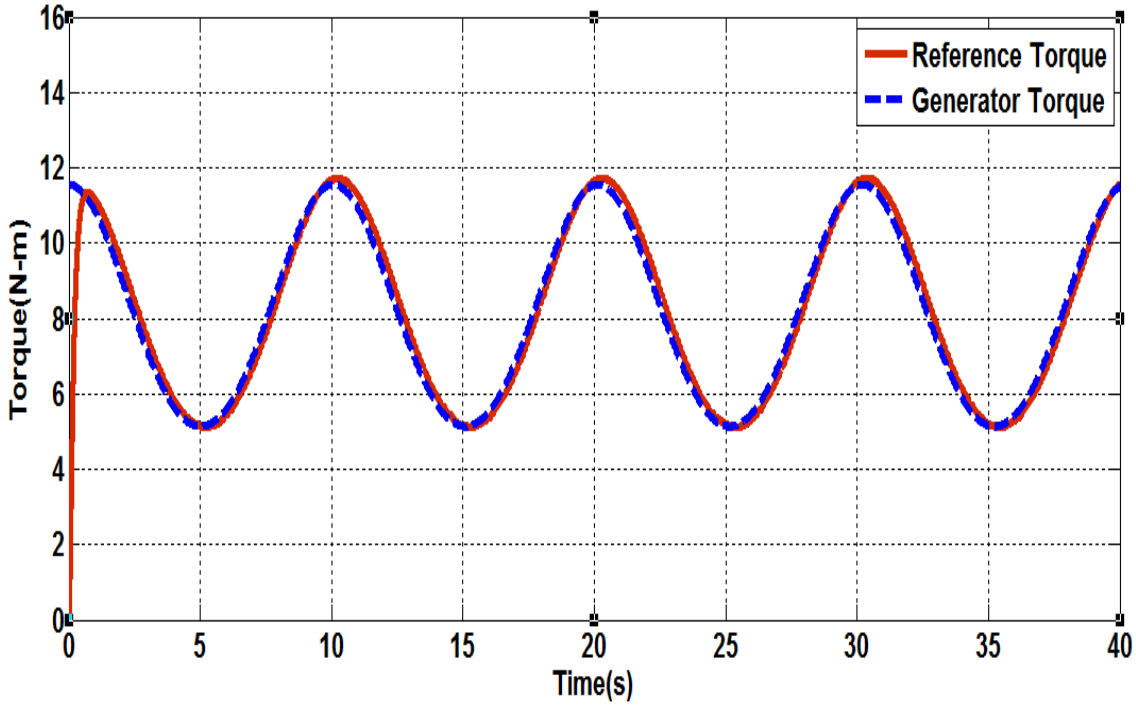

Fig. 7.12(d)

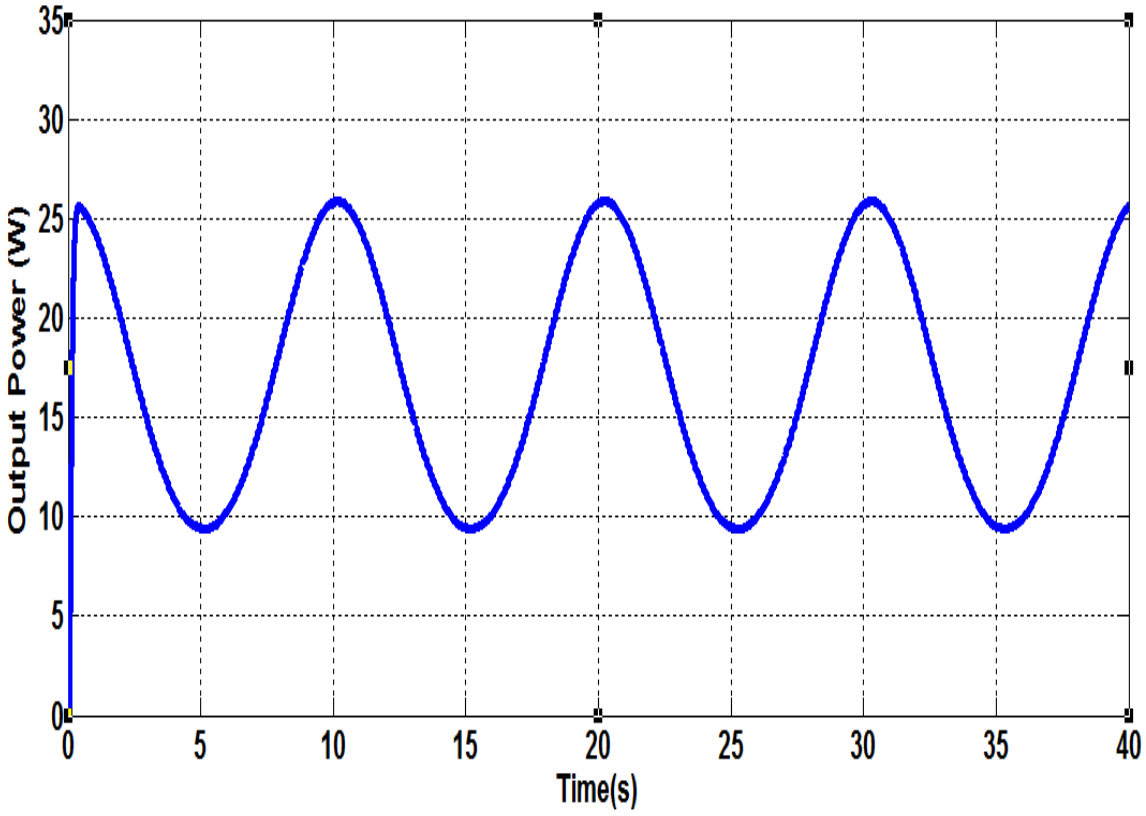

Fig. 7.12(e)

Fig. 7.12 Response of the system for turbulent resource: (a) flow speed, (b) reference generator speed and instantaneous generator speed (c) reference current and instantaneous input current of the converter (d) reference and developed generator torque and (e) output DC power.

Simulation results show that the proposed adaptive backstepping control strategy is effective in terms of speed tracking and following the reference current. Moreover, the sensitivity of the proposed control strategy has been analyzed regarding the swell effect. In Fig 7.12e peaks appeared in the generated power due to the acceleration and deceleration of the turbine speed due to the swell effect. The variation of the flow speed will impose consequently change in the rotor speed reference which is deduced from the MPPT strategy.

7.5 ADBT Robustness against Parameter Variations

The robustness of the adaptive backstepping control is briefly evaluated according to a well-known parameter variation under parameter perturbations was investigated. The parameter perturbations introduced in the control were set to the following values; 20% in the stator resistance, 20% in the *d* and *q* axes stator inductances, 20% in the rotor flux linkage. The results are shown in Fig.7.13. The results clearly show that stable operation and good performances are preserved although large perturbations are acting on the entire energy conversion system.

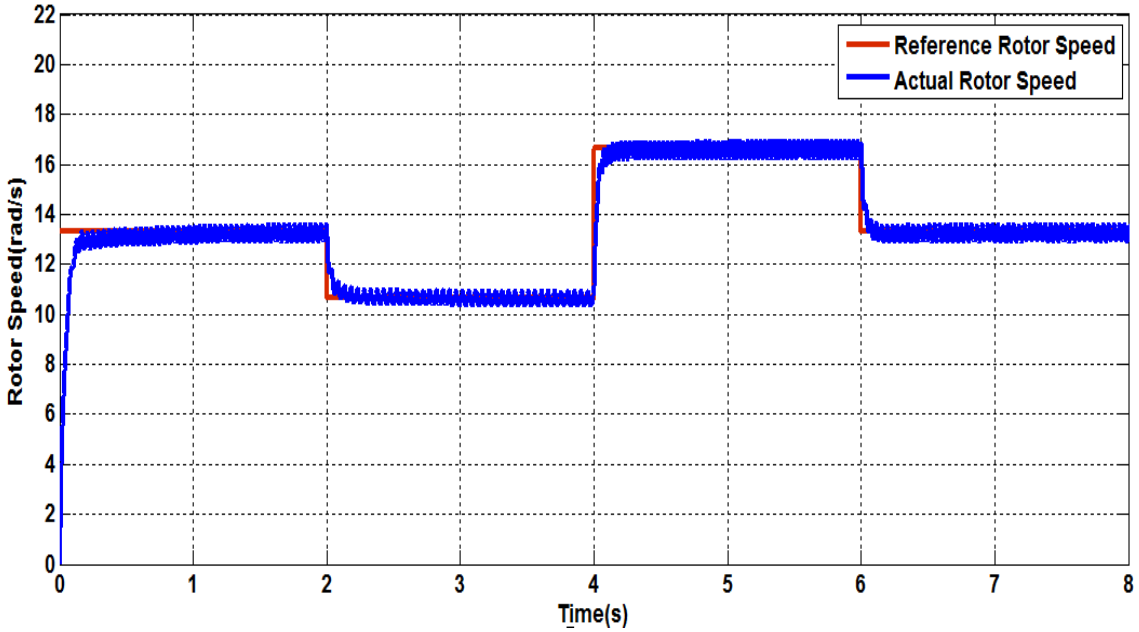

Fig. 7.13 Speed responses of the Adaptive Backstepping control with perturbed parameters

Therefore, using the proposed non-linear adaptive Backstepping control, the reference speed is insensitive to the parameter variations and disturbances. For comparison purposes, PI robustness was also evaluated. The findings of the simulation results was Adaptive Backstepping controller can quickly and accurately hacks the desired reference than the PI controller.

7.6 Comparison Study of Controllers

Although the control strategy is very efficient in terms of speed tracking, the marine current turbine is sensitive to high-frequency swell effect. To overcome this problem, the tidal speed must be filtered to avoid peaks in the generated power. In this section, a comparison between both the control strategies was done through different case studies. It should be noted that the simulations will also allow the evaluation of the resource model and its impact on the overall system power. Three types of resources taking into account external disturbance have been simulated in different cases are summarized in Table 7.1. The comparison is mainly based on the tidal speed values V_{actual} and V_{ref}.

Table 7.1 Simulation Cases

Case 1	$V_{actual} = 1.0+0.3Cos0.4t+0.2Cos0.6t$ $V_{ref} = 1.0+0.3Cos0.4t+0.2Cos0.6t$
Case 2	$V_{actual} = 1.0+0.3Cos0.4t+0.2Cos0.6t+b(t)$ $V_{ref} = 1.0+0.3Cos0.4t+0.2Cos0.6t+b(t)$
Case 3	$V_{actual} = 1.0+0.3Cos0.4t+0.2Cos0.6t+b(t)$ $V_{ref} = 1.0+0.3Cos0.4t+0.2Cos0.6t$
Case 4	$V_{actual} = 1.0+0.3Cos0.4t+0.2Cos0.6t$ $V_{ref} = 1.0$
Case 5	$V_{actual} = 1.0+0.3Cos0.4t+0.2Cos0.6t+b(t)$ $V_{ref} = 1.0$

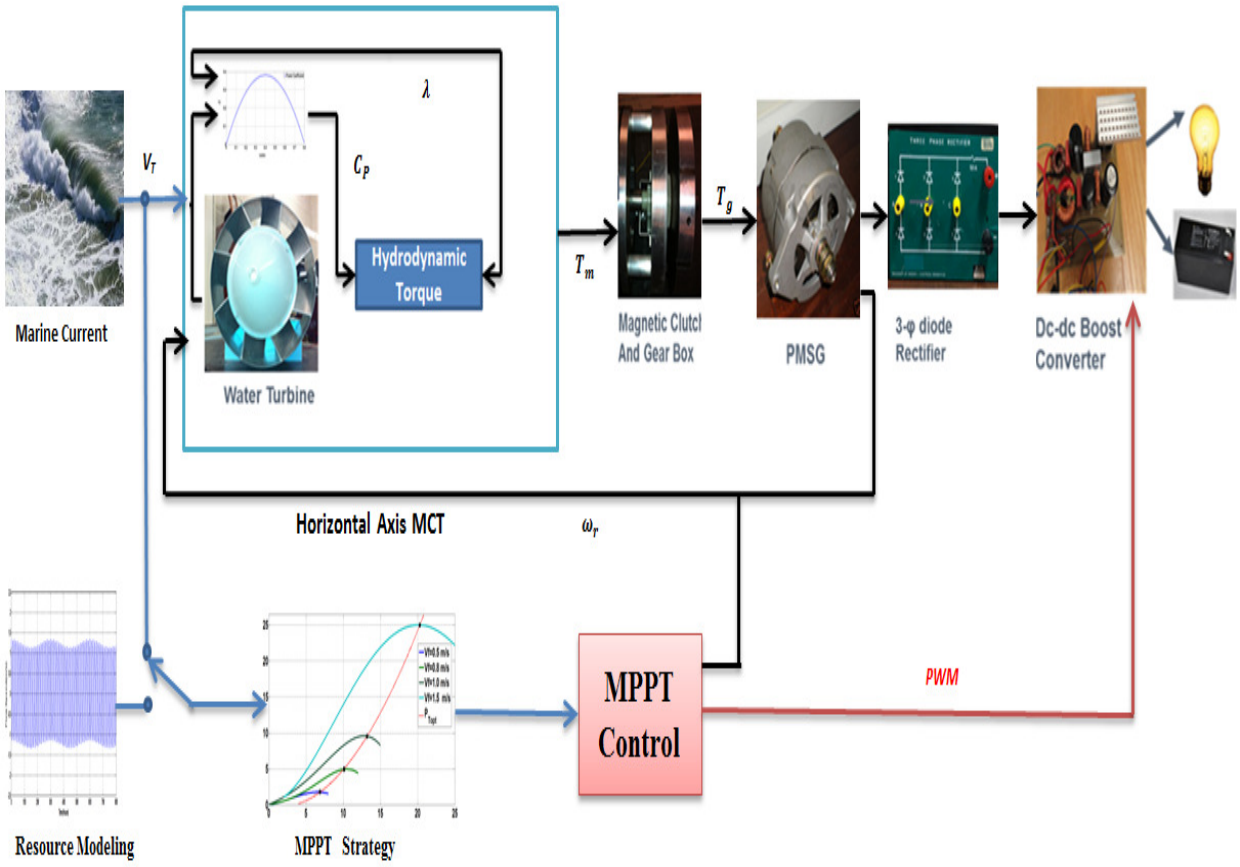

Fig 7.14 Maximum Point Tracking Based Control Strategy of MCECS

In this case V_{actual} is the tidal speed used as an input for the marine current turbine model. V_{ref} is the value of the tidal speed used as in input for the MPPT strategies as shown in Fig 7.14. The simulation time has been chosen to evaluate the influence of swell and sea surface effect disturbances which have time constants or periods of few seconds. In these conditions, the predicted average value of the tidal speed is assumed to be constant and equal to 1.0m/sec. Figs. 7.15, 7.16, 7.17 & 7.18 shows the simulation results for different cases. The obtained simulation results confirm that the adopted model that predicts the resource tidal speed is quite efficient as a reference for the MPPT control strategy.

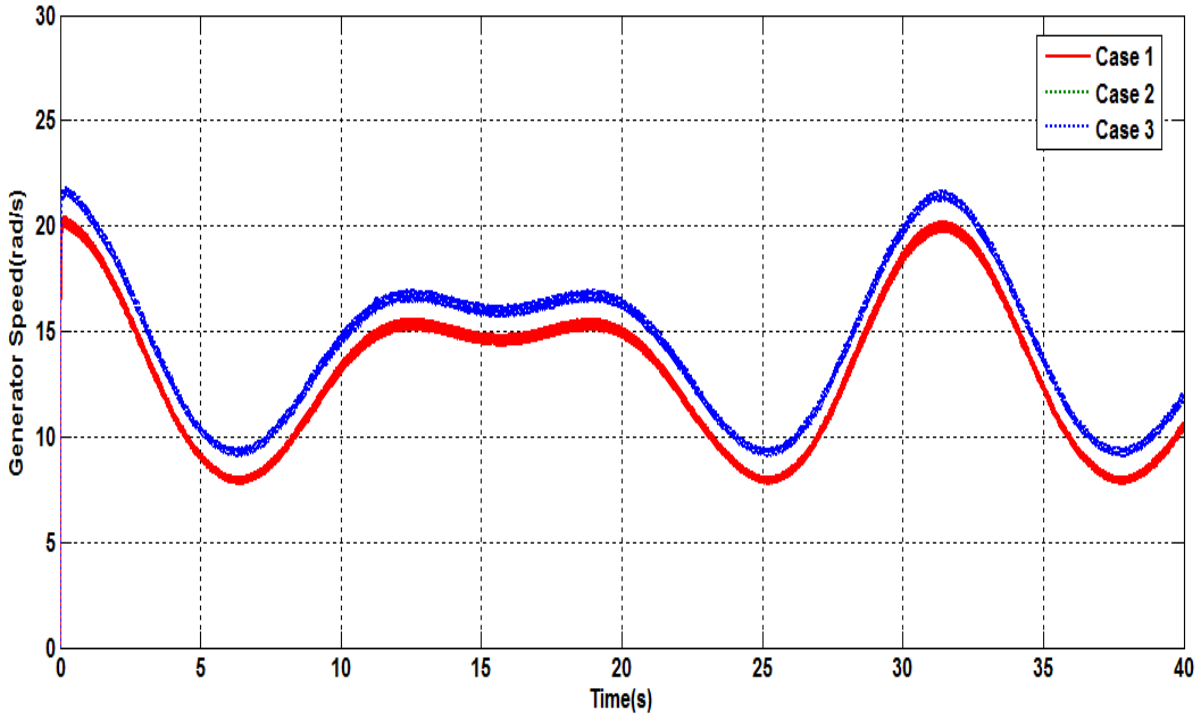

Fig. 7.15 (a)

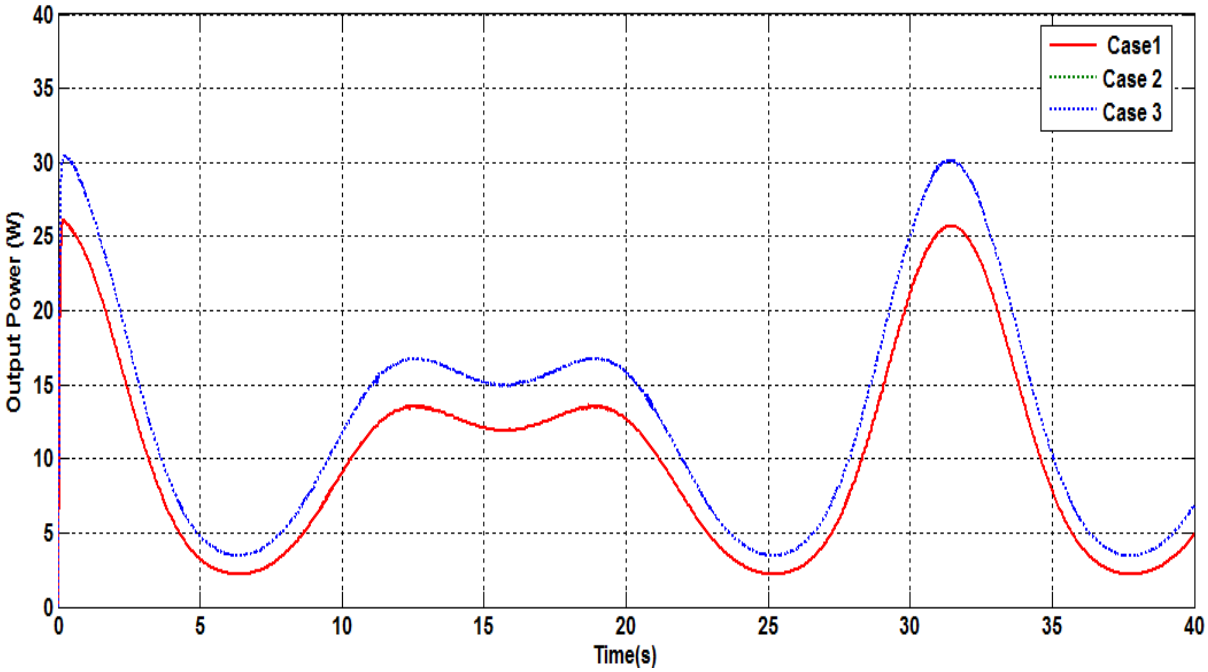

Fig. 7.15(b)

Fig 7.15 Turbulent resource for cases 1, 2 & 3 (a) Generator rotational speed and (b) Generated dc power for a PI control.

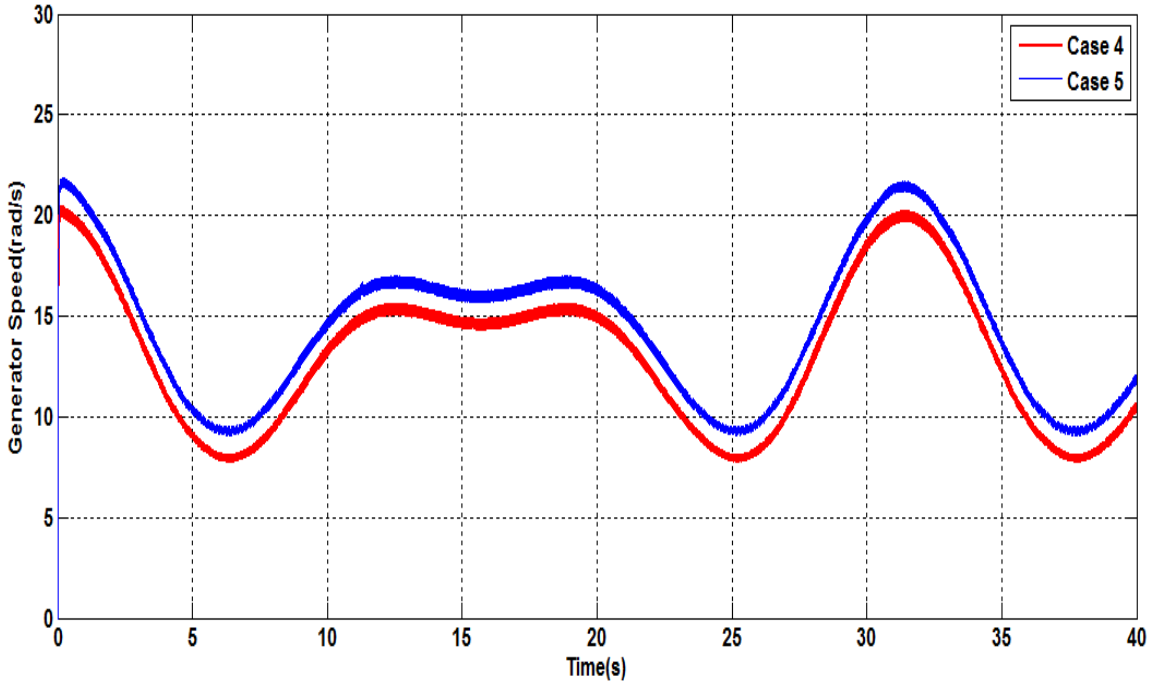

Fig. 7.16(a)

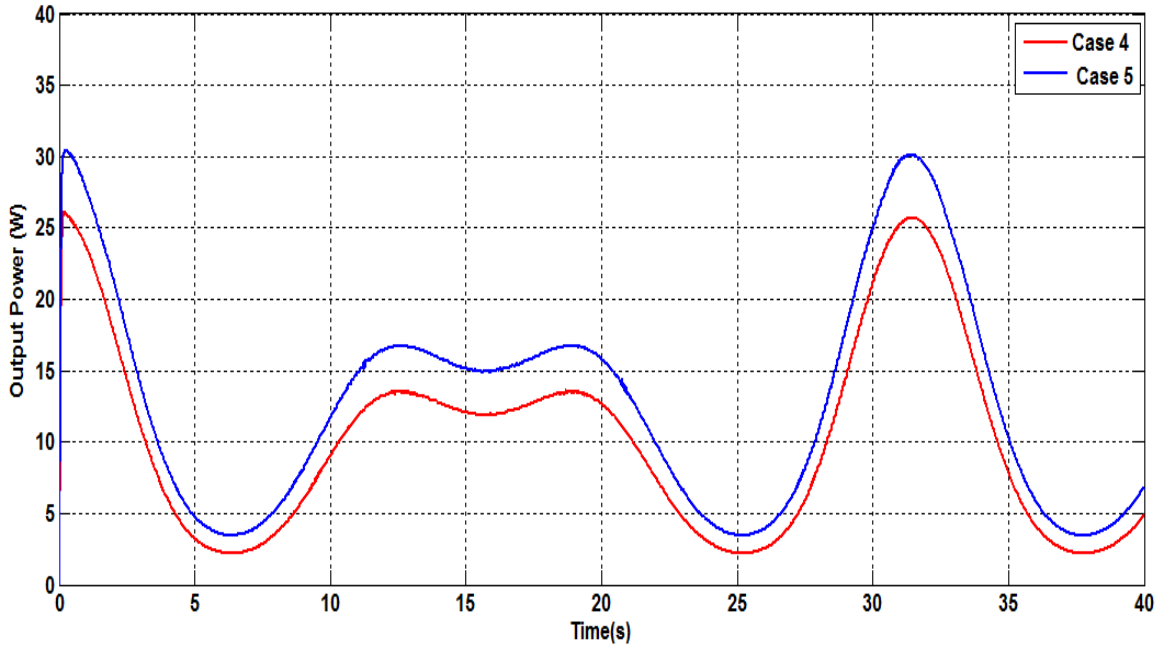

Fig. 7.16 (b)

Fig 7.16 Turbulent resource for cases 4 & 5 (a) Generator rotational speed and (b) Generated dc power for PI control.

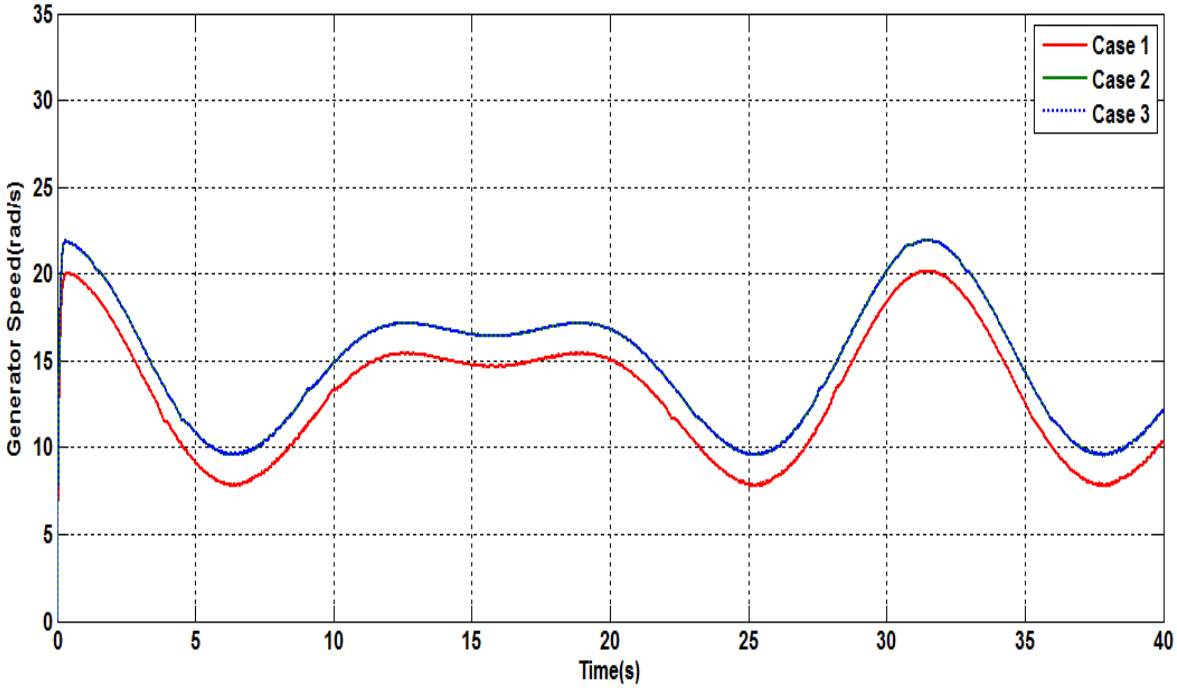

Fig. 7.17 (a)

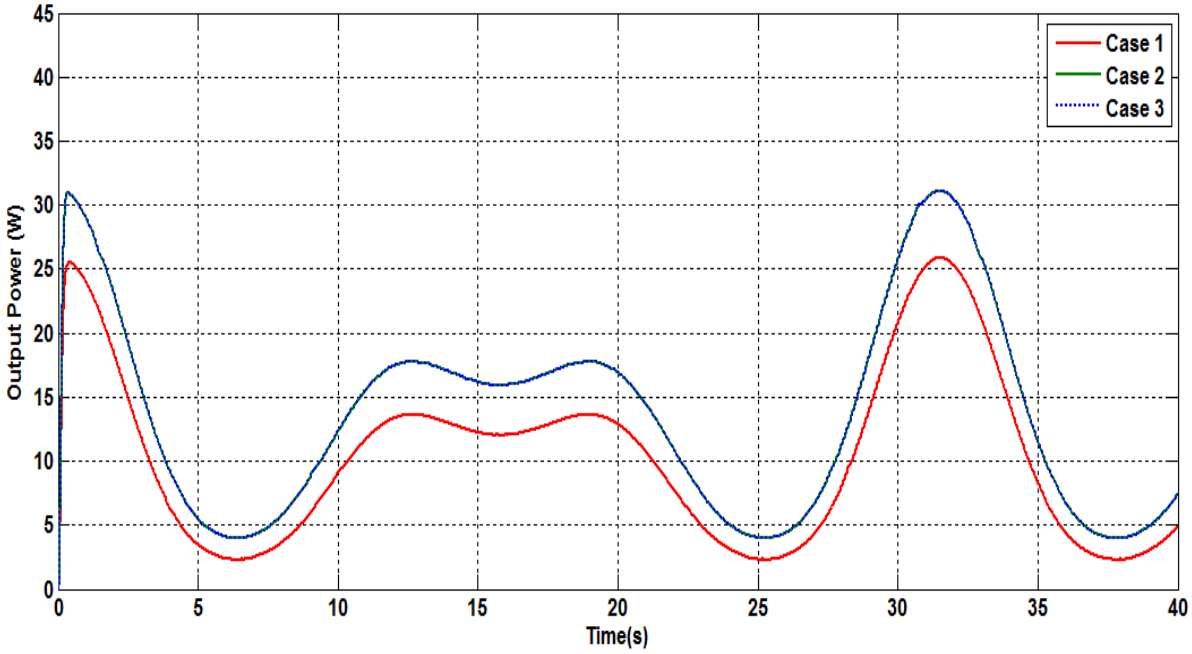

Fig. 7.17 (b)

Fig. 7.17 Turbulent resource for cases 1, 2 &3 (a) Generator speed and (b) Generated dc power for a ADBT control.

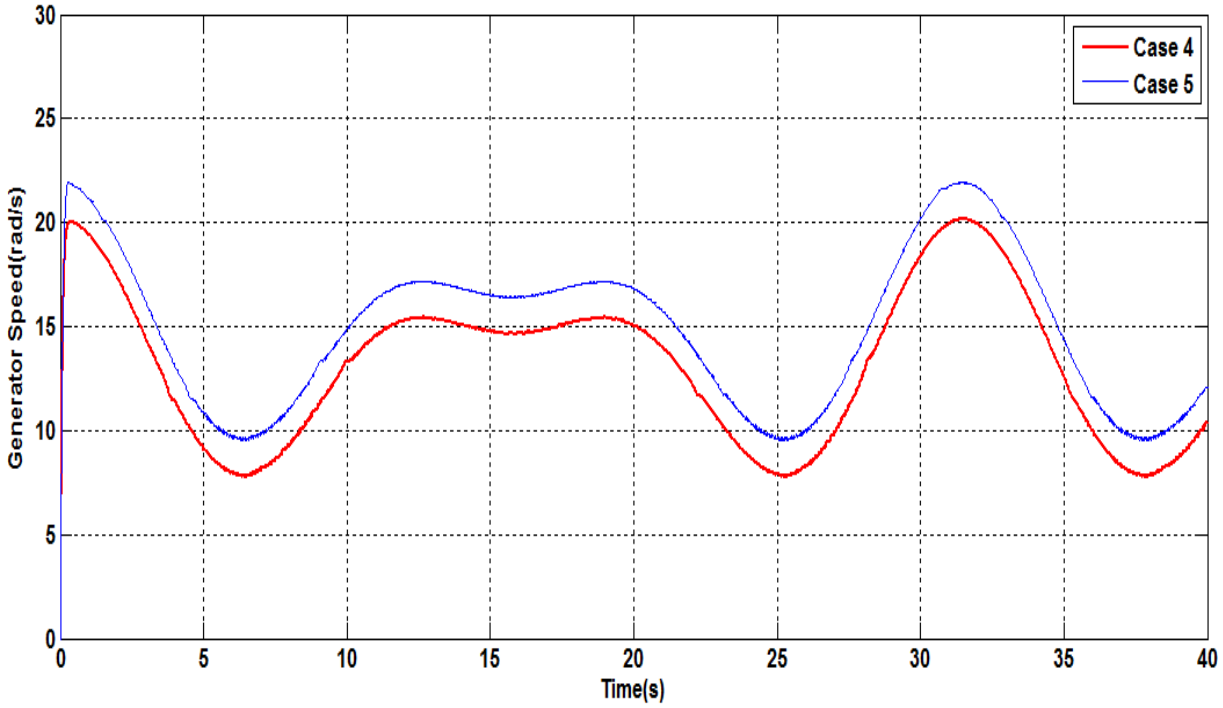

Fig. 7.18(a)

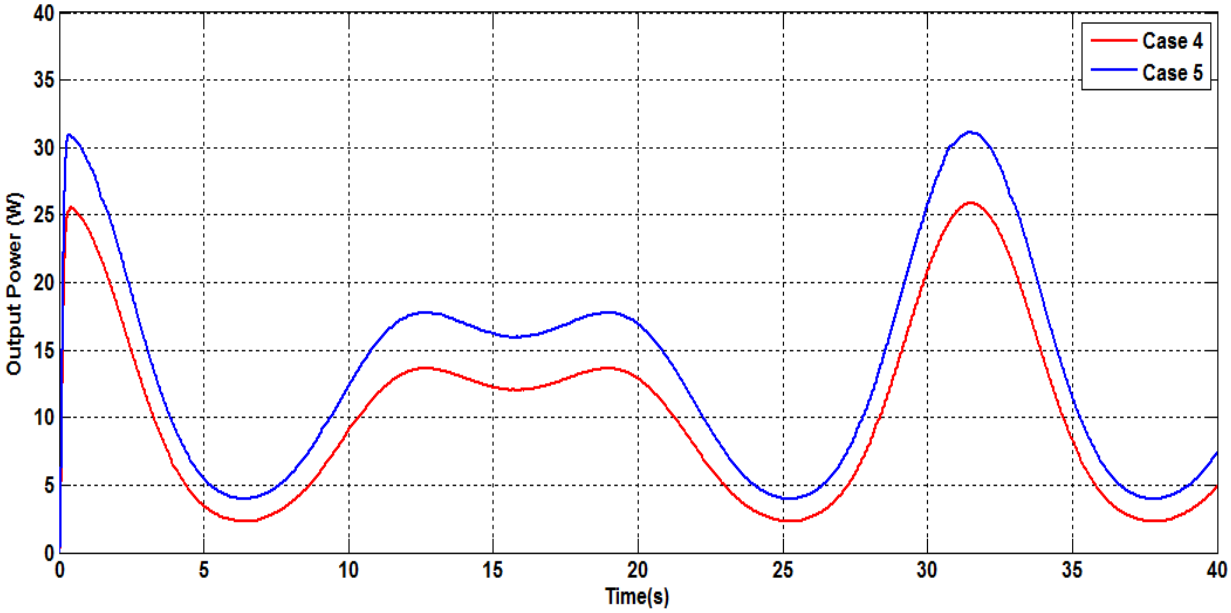

Fig. 7.18(b)

Fig. 7.18 Turbulent resource for cases 4&5 (a) Generator rotational speed and (b) Generated dc power for a ADBT control.

In the simulated cases, several waveforms for the tidal speed with and without disturbances have been considered. The resource models are composed of kinetic speed, the swell effect, and random signal $b(t)$ that represents all other disturbances. The simulated cases can be divided in two categories. The first one considers cases 1 and 2, in which, V_{actual} and V_{ref} were set equal. It is assumed that the tidal speed is well known. These cases give an idea about the performances of both control strategies in ideal operating conditions. However, the second category considers the cases 3, 4 and 5. These cases allow the use of the tidal predicted average speed as a reference for the MPPT calculations and therefore allow a sensorless control (no needs for tidal speed sensor for the MCT). The simulation results show the robustness of the control strategies. The results also prove that ADBT control is more robust when the tidal speed is not well known (cases 3, 4 and 5). In these three cases, it can be noted that the generated power is more important than those given by the proportional integral control.

7.7 Conclusion

The computer simulations proved to be a valuable tool in predicting the system behavior, designing a controller, and estimating the output generation of the MCECS. The simulation results obtained by using the Matlab/Simulink tool and CFD software show the effectiveness of the studied model. Two control strategy families were evaluated for PMSG-based marine current turbines: classical PI control and more advanced control techniques, namely adaptive backstepping control. The obtained results are very promising. Furthermore, simulation results also show that adaptive backstepping control seems to be a good candidate when there is an uncertainty in parameter.

Chapter VIII

Experimental Validation of MCECS

8.0 Introduction

This chapter describes the setup and test results of a small marine current energy conversion in a laboratory. A complete block diagram of the overall energy conversion system is shown in Fig. 8.1. The power system developed consists of horizontal axis blade rotor, permanent magnet synchronous generator, DC-DC converter, instrumentation and a dSpace based control system. The dSpace was used to implement the proportional integral controller to extract the maximum power from the system. This proposed system is designed to be installed at a site where the flow rate is greater than a knot. The magnetic clutch has been used to make sure that the system is completely water tight with zero leakage. Fig.8.2 exhibits the electrical schematic of the energy conversion system . The 3-φ output of the variable speed PMSG is converted into dc by a full bridge diode rectifier. The filtered dc voltage is fed into a dc-dc boost type converter. A sensorless indirect MPPT control strategy has been proposed that continuously determines the input reference current for the dc-dc converter. Thus, there are no need for any external flow sensor and parameters of the PMSG. A proportional integral controller has been used to control the duty cycle of the boost converter in order to ensure that the input current of the dc-dc converter strictly follows the trajectory of the command input reference current generated from the MPPT control algorithm.

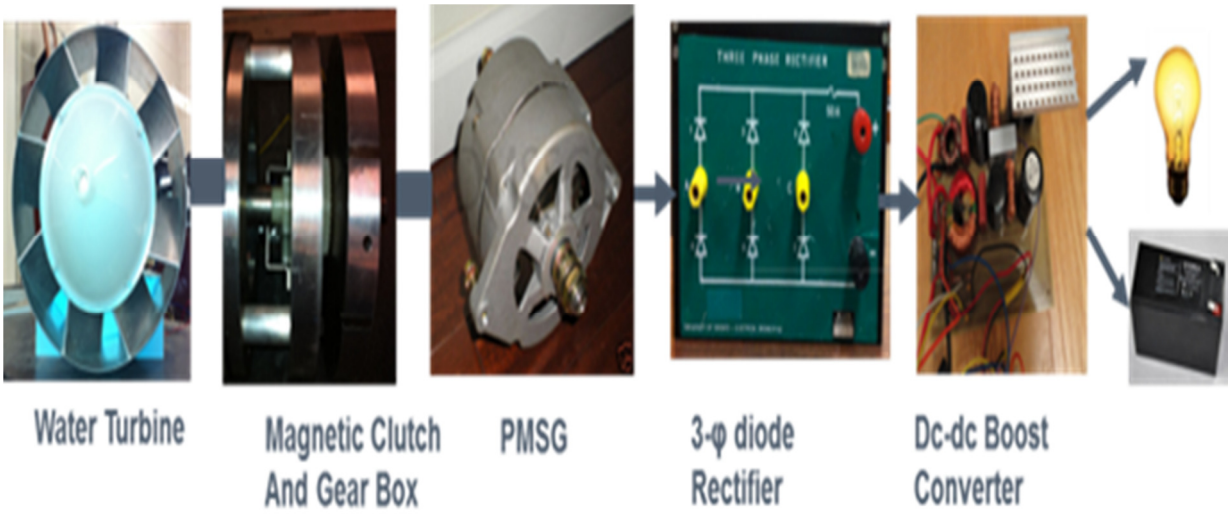

Fig. 8.1 Block diagram of the overall marine energy conversion system

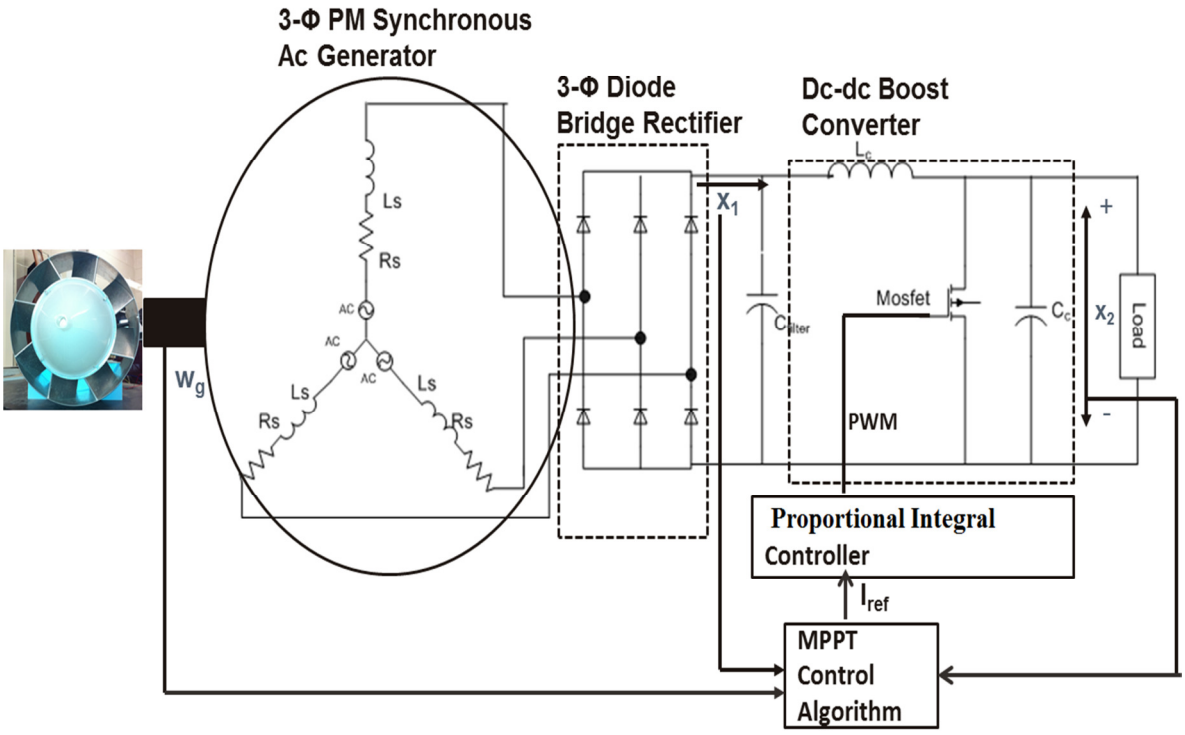

Fig. 8.2 Electrical Schematic of the marine current energy conversion system

8.1 Water Current Turbine Emulator

A water current turbine emulator (WCTE) is important equipment for developing marine current energy conversion systems. The emulator was used to drive an electrical generator in a similar way as the marine current turbine, by reproducing the torque developed by a marine current turbine for a given marine current. It offers a controllable test environment that allows the evaluation and improvement of control schemes for electric generators and which is hard to achieve with an actual water turbine since it is not possible to test the whole system in the wave tank all the time. A lab volt dc motor is the usual choice to provide the variable output torque because the torque it develops is proportional to the armature current. It is generally assumed that the proposed turbine will drive the generator at a constant tip speed ratio (TSR). The motor generator set will experience variable generator rotor speed depending on the current velocities. In order to test the energy conversion system a laboratory prototype is built using a permanent magnet dc motor driven by controlled dc voltage as shown in Fig. 8.3. A variable dc supply is being used to vary the speed of the generator and to observe the output at different operating speed. It is being considered that the generator will be connected to the turbine by a gear box. The electrical test bench allows checking the functionality of all the electrical apparatus (encoder, sensors, generators, rectifiers, dc-dc converter). The torque of the dc motor is varied based on the flow speed. In this particular case the PI controller is implemented to check if the system is running at the optimum point. The whole setup provides a better understanding of the system performance before testing in the tow tank.

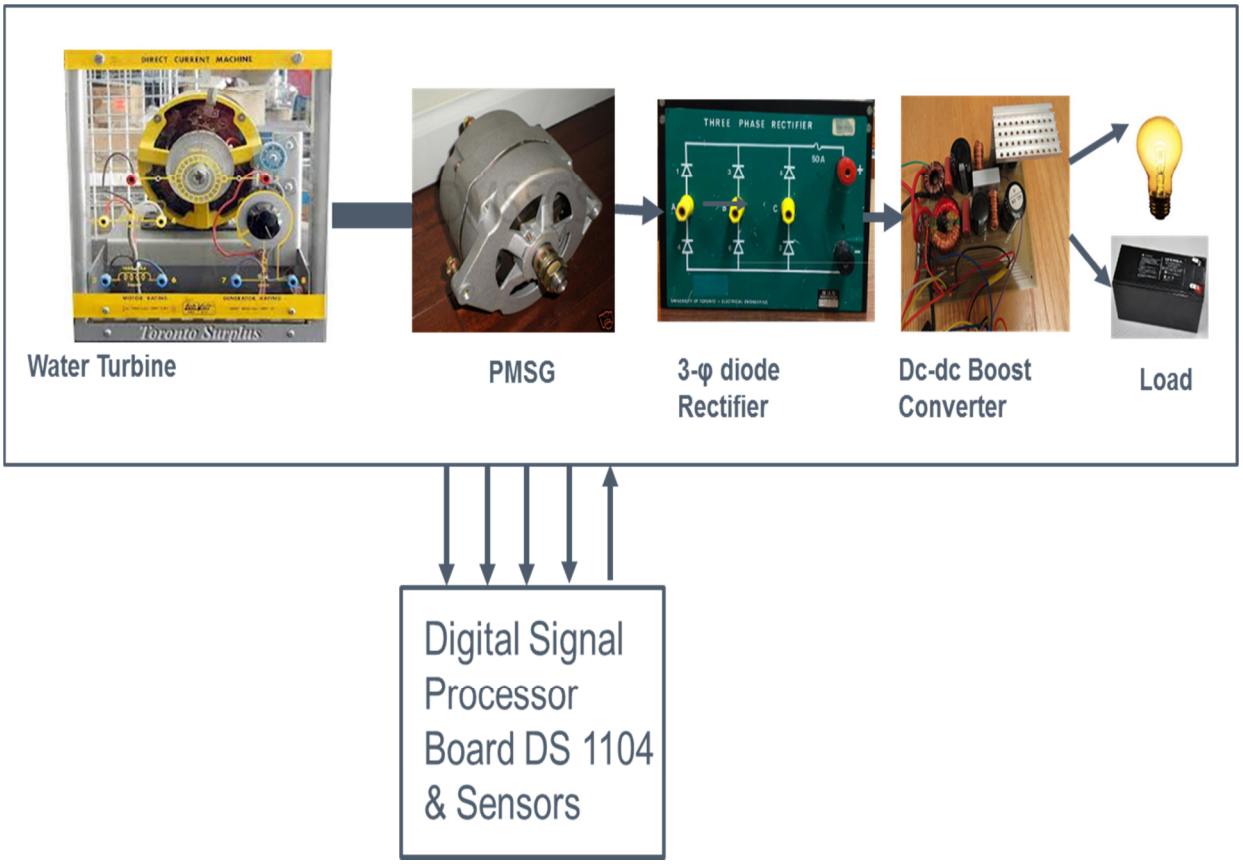

Fig 8.3 Testing of MCECS in the Energy Lab

8.2 Electrical Setup

The test bench presented in Fig 8.2 allows the physical simulation of the developed marine energy conversion system. The laboratory setup was required to tune the gains of classical proportional integral controller. Following are the parts of the energy conversion system:

a. A permanent magnet synchronous generator is used as the generator for the turbine. The generator is coupled to the DC motor and connected to the load via power electronic circuitry.

b. In order to measure the low RPM of the generator accurately, a high resolution encoder (Grayhill) with 256 cycles/rev have been used. A CPU of model Dell (Intel CORE i5) 2.9 GHz has been used to program the dSpace DS1104.

c. Interface circuits which are comprised of sensors and signal conditioners connected to the dSpace A/D converter.

d. DC- DC converter is used in order to control the generator in both topologies and to maintain the DC bus at the desired reference. One of the advantages of this type set up is its flexibility. The simulation conducted in Matlab/Simulink can be automatically implemented into the DSP. This adds flexibility and the established and simulated models can be easily modified. The following are the sequential operation of the set up to interface the system with computer.

    1. Matlab/Simulink is used for the studied system modeling and the control design and evaluation.
    2. RTI (Real Time Interface) is a dSpace library including different blocks which allow the implementation of the desired control. These blocks correspond to the Input/Output system and measure block.
    3. RTW (Real Time Workshop) compiles the Simulink files and adapts them to load into the dSpace.

8.3 Tow Tank Setup

The prototype has been tested has been tested at the tow/wave tank facility at Memorial University of Newfoundland. The whole assembly was mounted on a pole for easy installation in the tank. The maximum towing speed of the carriage is 5m/s. Fig 8.4a

shows the test rig device lifted to mount on the carriage frame. Fig 8.4b shows the test bench of the electrical setup of the energy conversion system for the instrumentation and control. The Simulink block to implement the MPPT using DSP is shown in Fig. 8.4c.

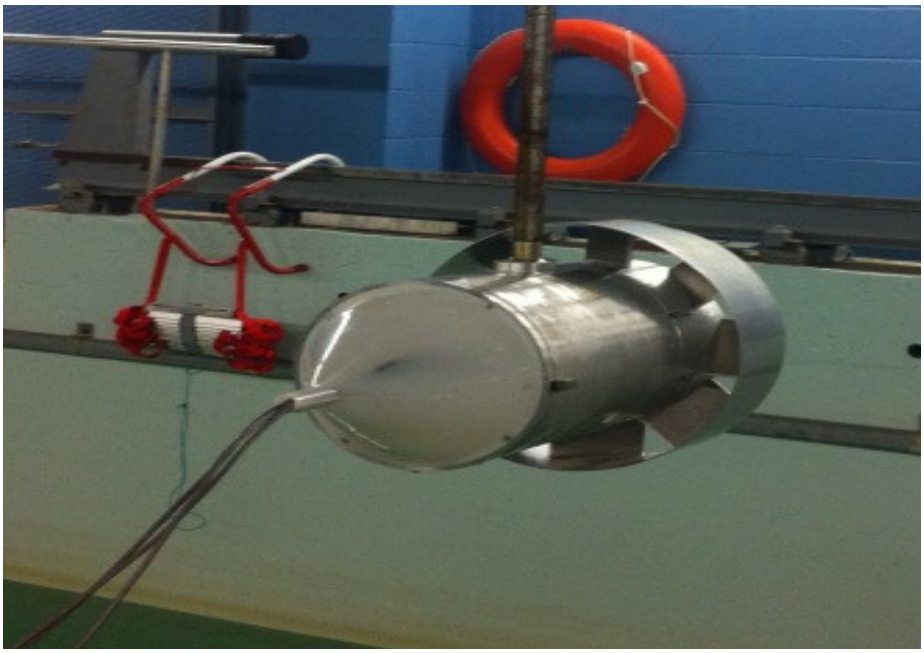

Fig. 8.4(a)

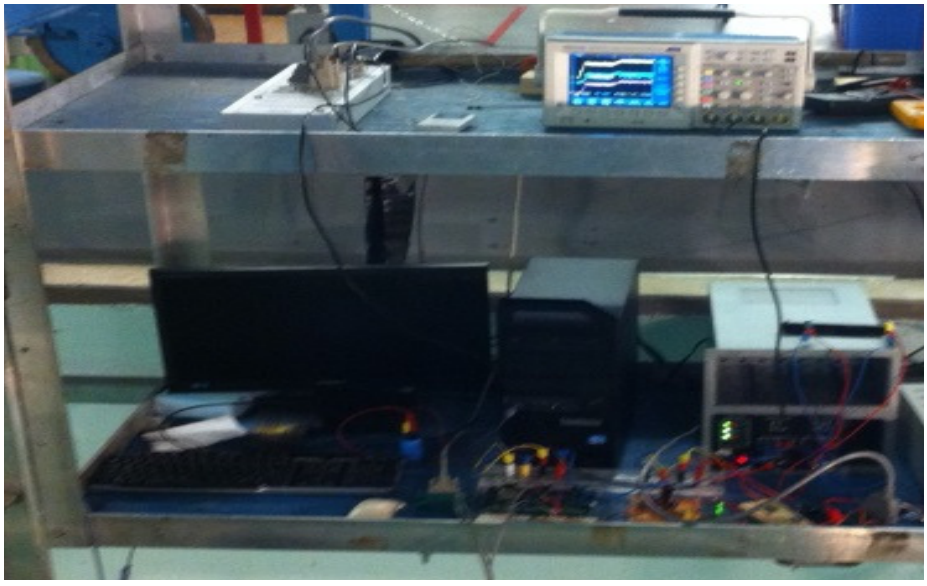

Fig. 8.4 (b)

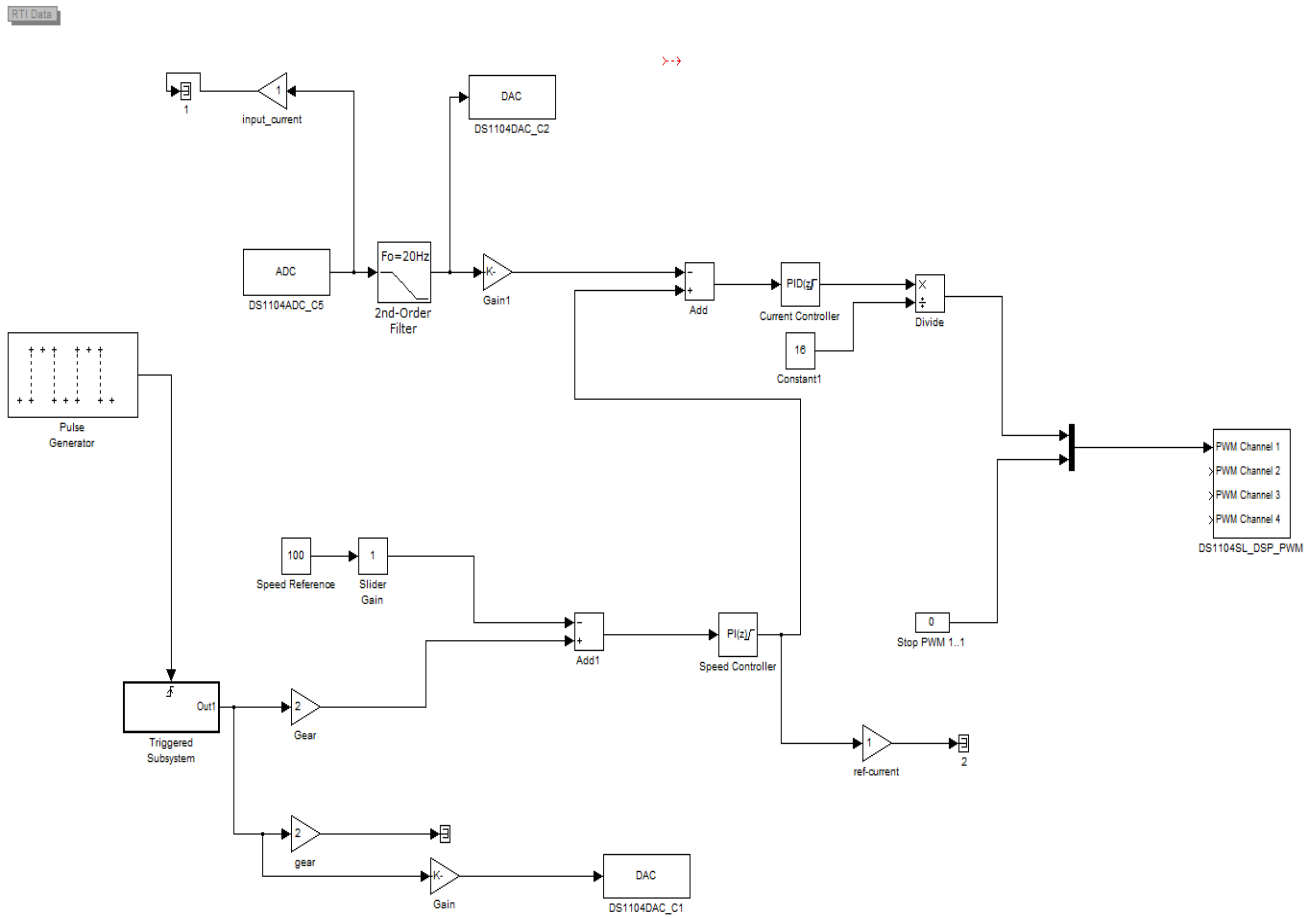

Fig 8.4(c)

Fig.8.4 Experimental Set up of MCECS in Wave Tank (a) Installation of MCECS in Tank (b) Electrical test bench to collect data (c) MPPT implementation using DSP

The customizable dSpace DS1104 made a significant contribution to the system modeling by collecting and storing data in computer. The dc current and voltage sensed both on the supply and load side was recorded. The speed of the turbine is sensed using an optical encoder mounted inside the water sealed chamber comprising of magnetic coupler, gear box and generator. The flow speed is measured using the setup installed in the carriage. All these signals fed back to dSpace contained noise components and different scaling factors. In order to read the signals accurately filtering were built. The MCECS has been tested in the tow-tank both in stable and unstable wake condition. The

unsteady or perturbed water flow at the start of each run, affects the overall performance of the system. For simplicity of modelling the system considers the steady flow condition. Due to short towing length and run times only a limited number of tests were performed under steady flow conditions. Prior to each run a carriage velocity was dialed manually. The prototype has been fully immersed in water at a depth of 2m from the water surface. The depth of rotor submersion (partial and full) will change the effective rotor area and output power. Also the free-surface proximity, boundary layer effects, and air suction due to funneling will play a critical role.

8.4 Testing Procedure and Results

The testing of the prototype in the tow tank was done by ramping up the flow/carriage speed, activate the controller, and allow rotor speed to reach the optimum point. All the collected performance data of the system are saved for subsequent analysis. Due to the limited availability and maintenance of tow tank facility the author only had the opportunity to test the proportional integral controller. In future the work can be revisited to implement adaptive backstepping controller. The tow tank doesn't have flow visualization options available to observe the wake characteristics of the blades. It is well known that horizontal axis turbine is inherently self- starting. But starting could be difficult sometimes due to friction in gears, generator cogging torque and load. The rotor is initially allowed to start up without any help. Also, the generator terminal is unloaded throughout the run. To identify the actual cut in speed of the turbine tests were carried out with the generator decoupled from the rotor. It was observed that the rotor, by itself, started to rotate at around 0.20 m/s to 0.24m/s of water velocity. With the generator

coupled to the rotor, the cut in speed of the rotor changes. After conducting a number of runs at increasing flow speeds, it became apparent that the rotor (with gears and PMSG) exhibits higher cut in speeds between 0.32 m/s and 0.36 m/s.

The simulated results were compared to the established experimental testing to verify reasonable agreement between theory and experiment. Fig. 8.5, 8.6 and 8.7 presents the responses of the system for different carriage speed varied from 0.75 m/s to 1.25 m/s. The horizontal axis turbines, due to their unique principle of operation, are subject to small torque ripples. The voltage output of a PMSG depends on the rotational speed. The oscillations in current are caused by torque ripples. The output current, as expected, carries the oscillating behavior at the load terminals. It should be noted that the total inertia of the rotor-generator unit and placement of a filter capacitor at the dc bus plays an important role in minimizing output ripples, especially at higher rotor speed. It is also identified that the ripple frequency is directly related to the rotor's rotational speed. To implement the controller in the real system one has to know the proper gains. Observation from the testing results shows that the generator speed and the input current can reach the reference values. This ensures the system can operate at the optimum point for any given flow speed when the controller is turned on.

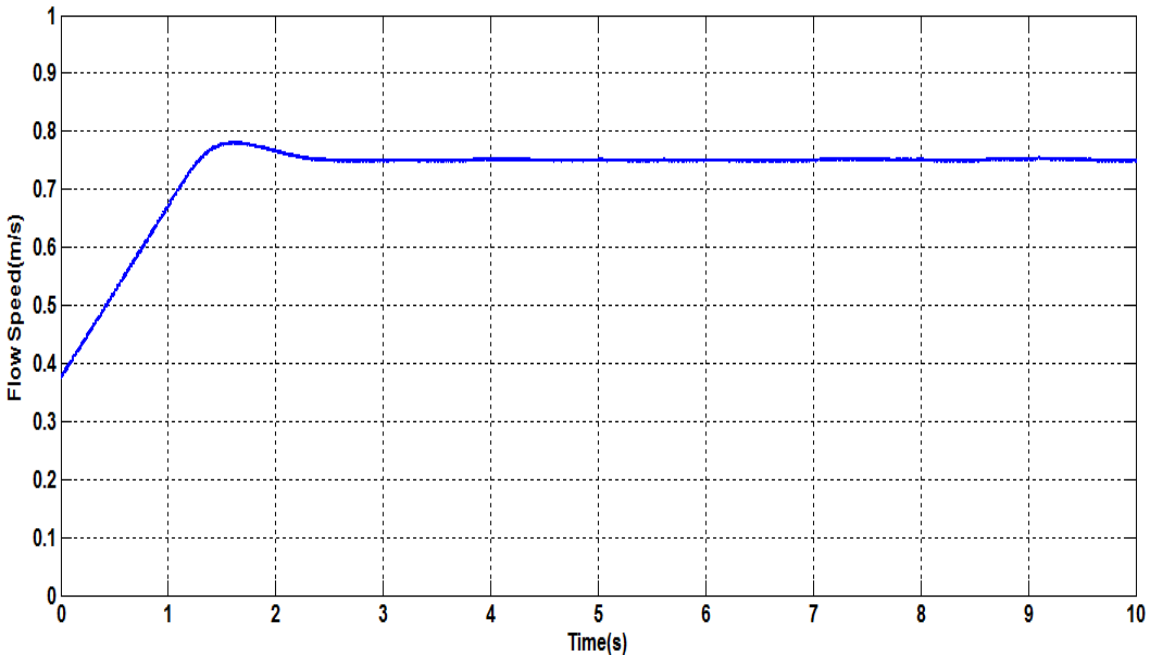

Fig. 8.5(a)

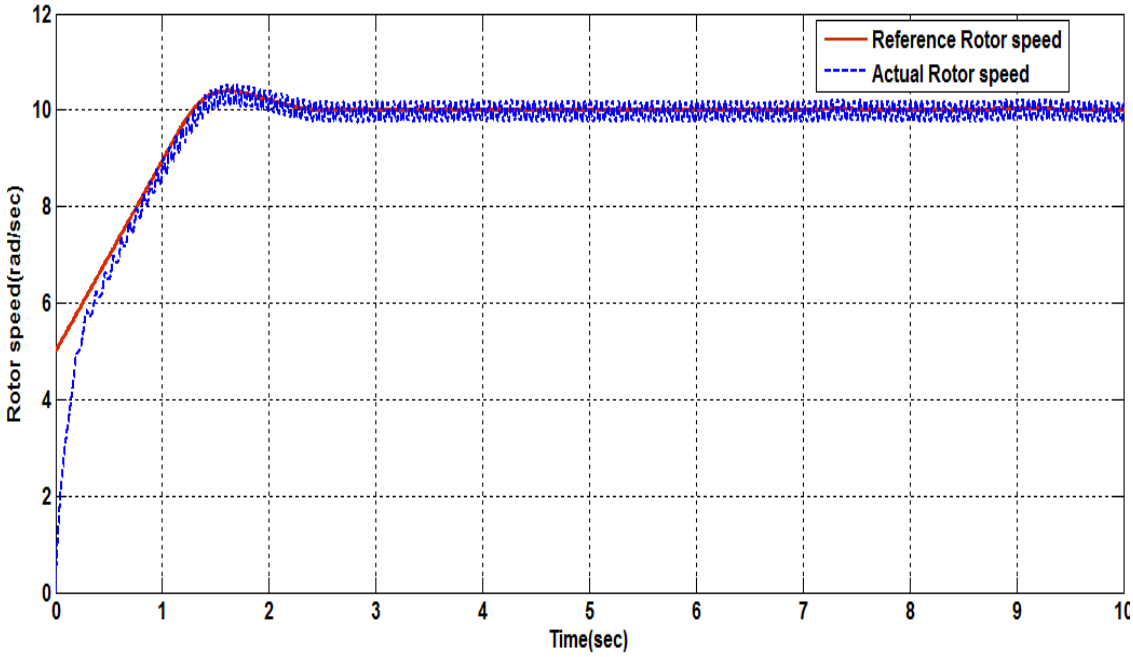

Fig. 8.5(b)

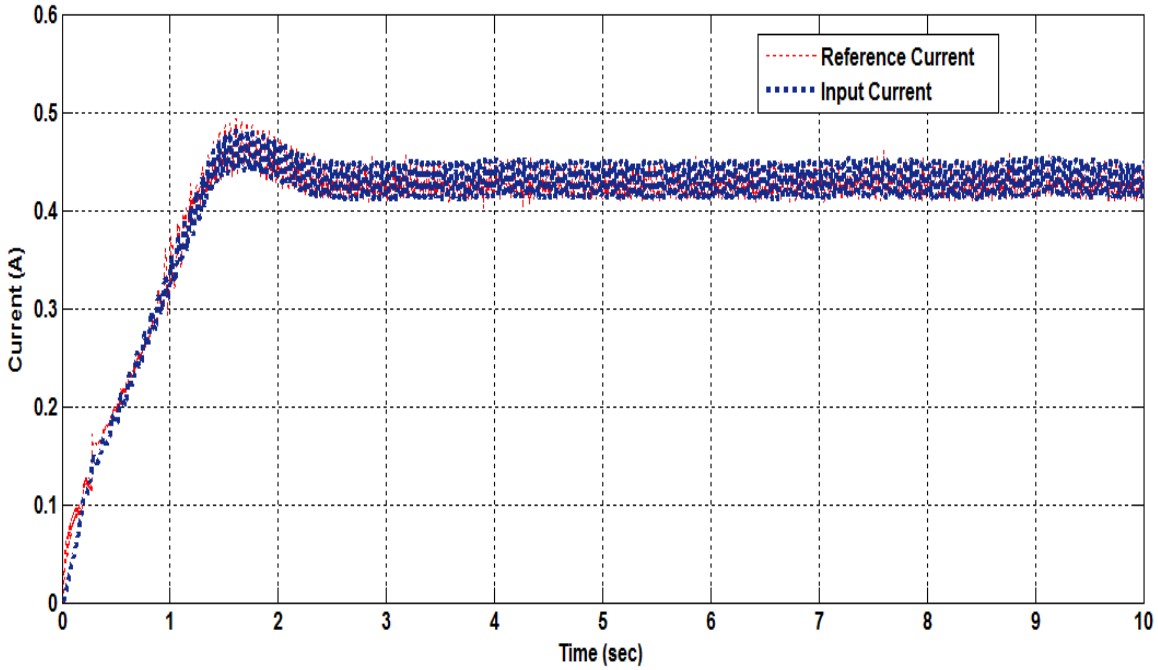

Fig. 8.5 (c)

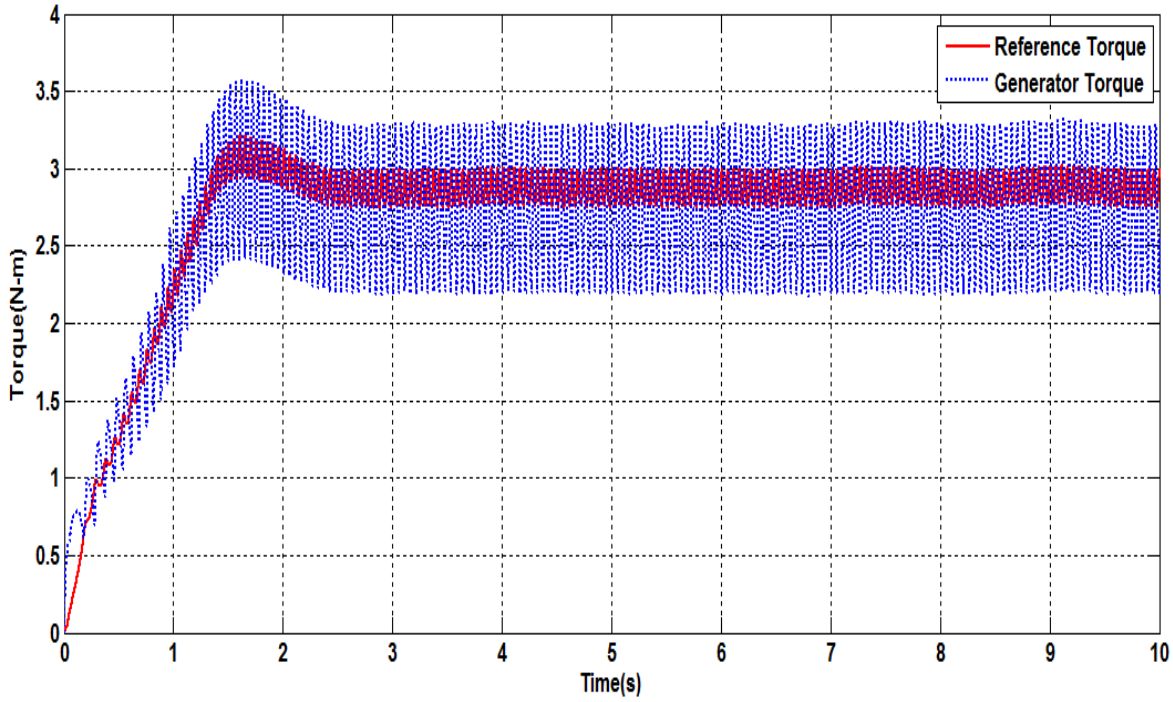

Fig. 8.5(d)

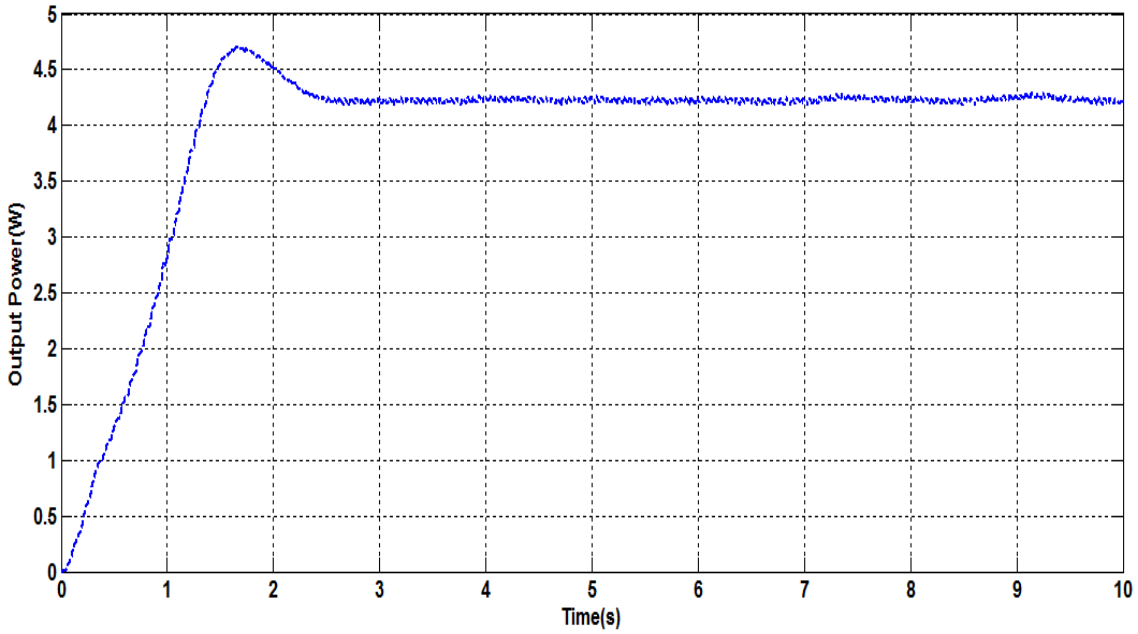

Fig. 8.5(e)

Fig. 8.5 Response of the system (a) Tow tank flow speed (b) Reference generator speed and instantaneous generator speed, (c) Reference current and instantaneous input current of the converter (d) Reference and developed generator torque and (e) Output dc power.

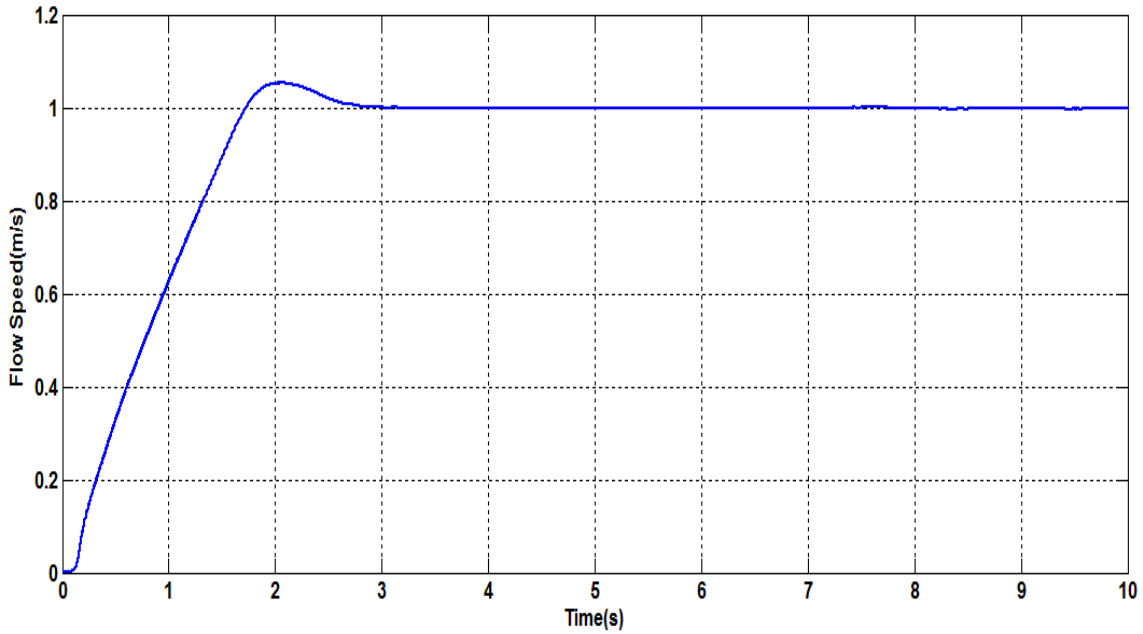

Fig. 8.6 (a)

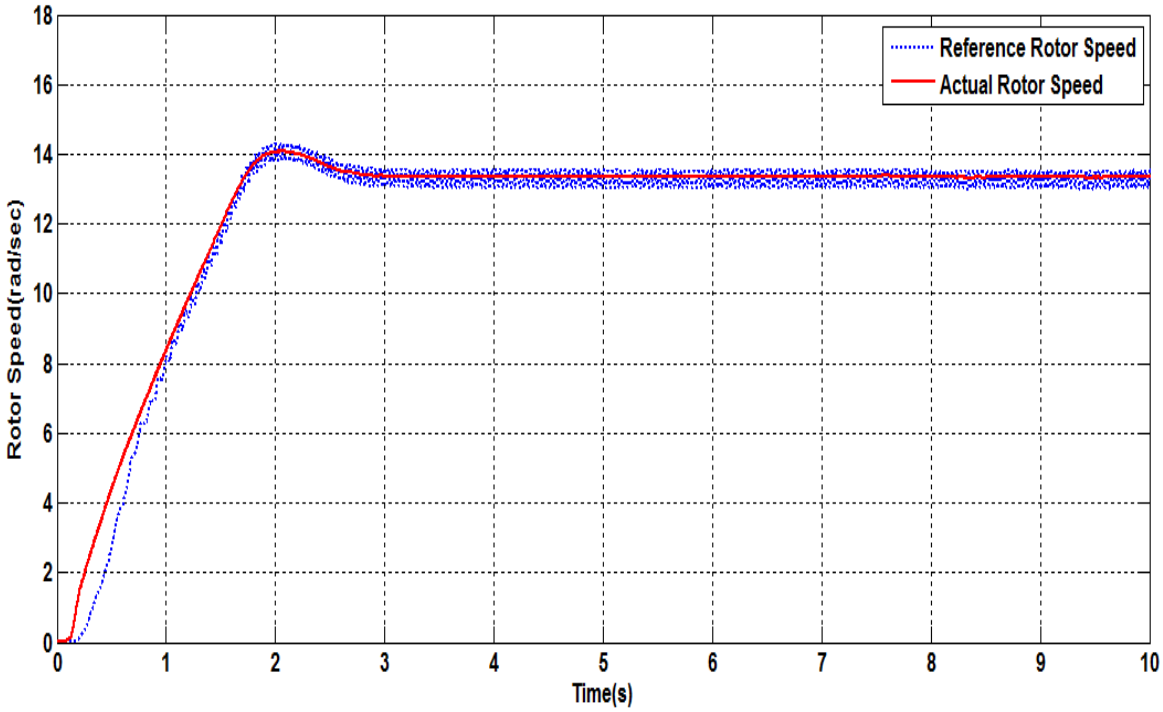

Fig. 8.6 (b)

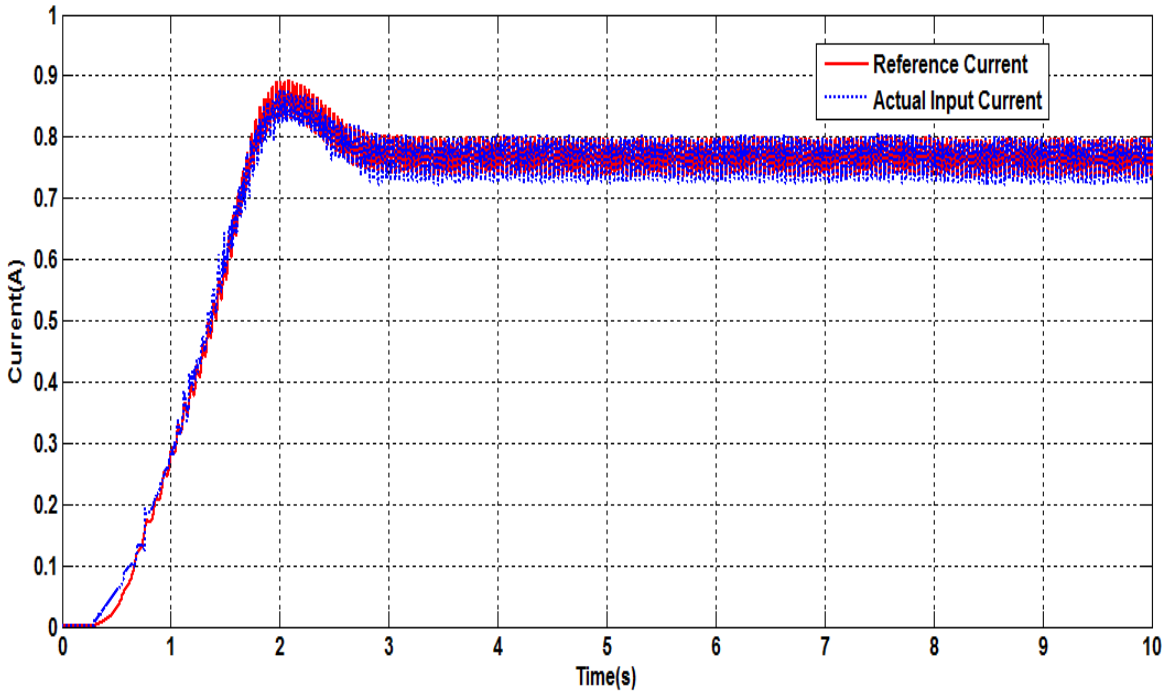

Fig. 8.6(c)

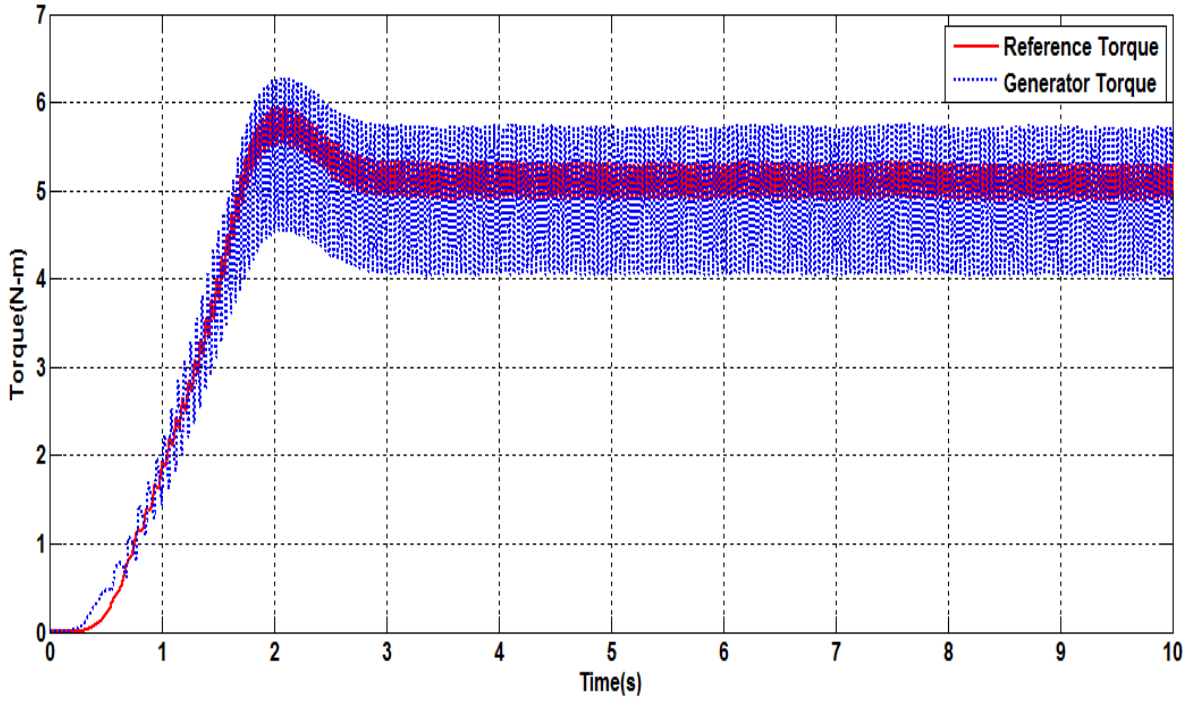

Fig. 8.6(d)

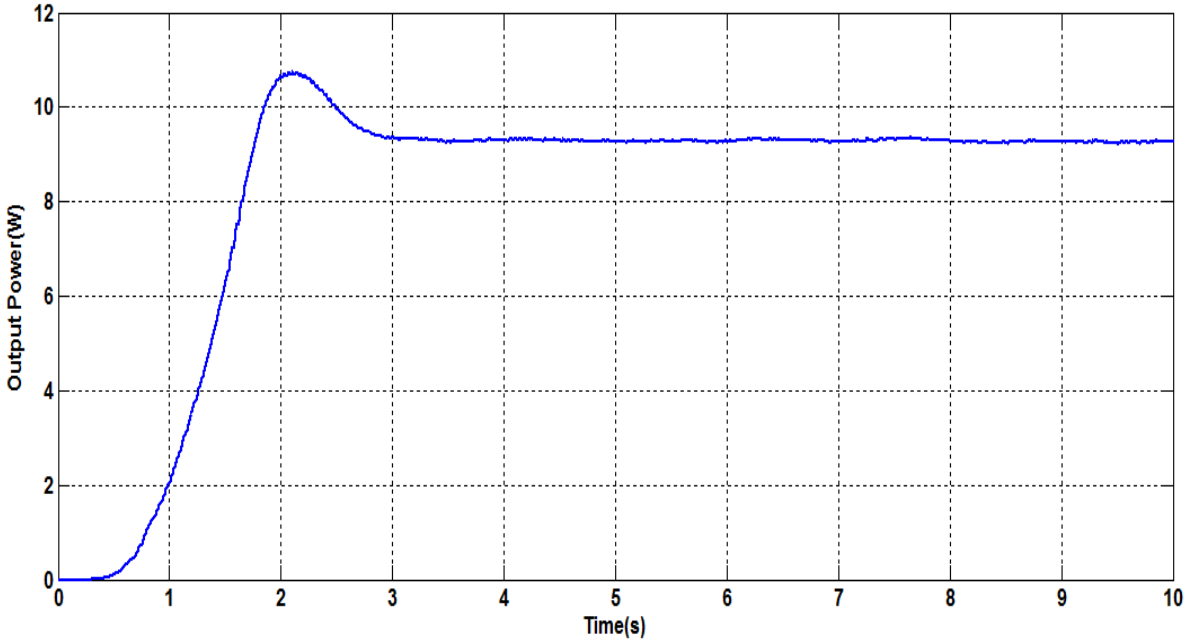

Fig. 8.6(e)

Fig. 8.6 Response of the system (a) Tow tank flow speed (b) Reference generator speed and instantaneous generator speed, (c) Reference current and instantaneous input current of the converter (d) Reference and developed generator torque and (e) Output dc power.

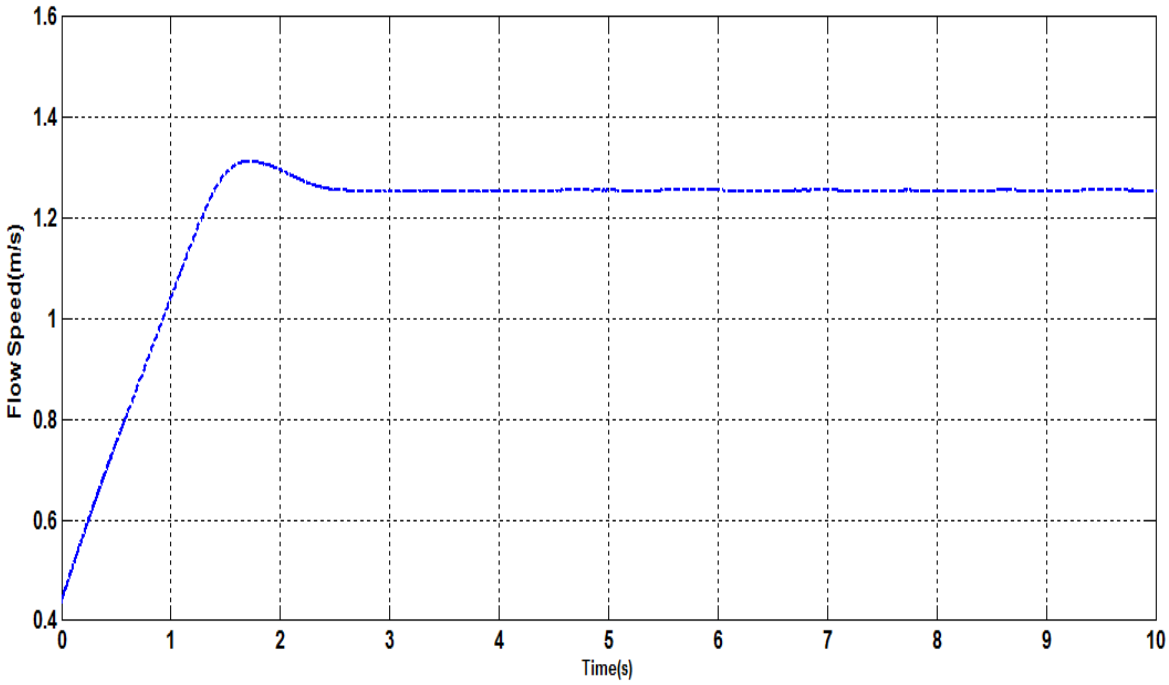

Fig. 8.7 (a)

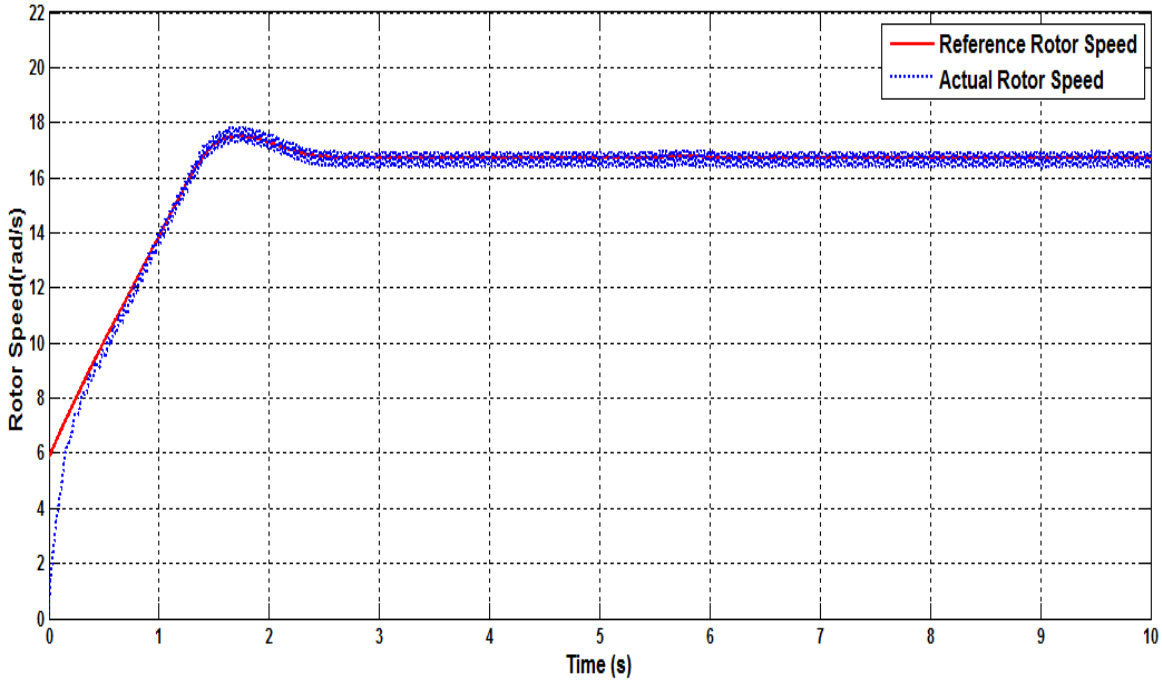

Fig. 8.7 (b)

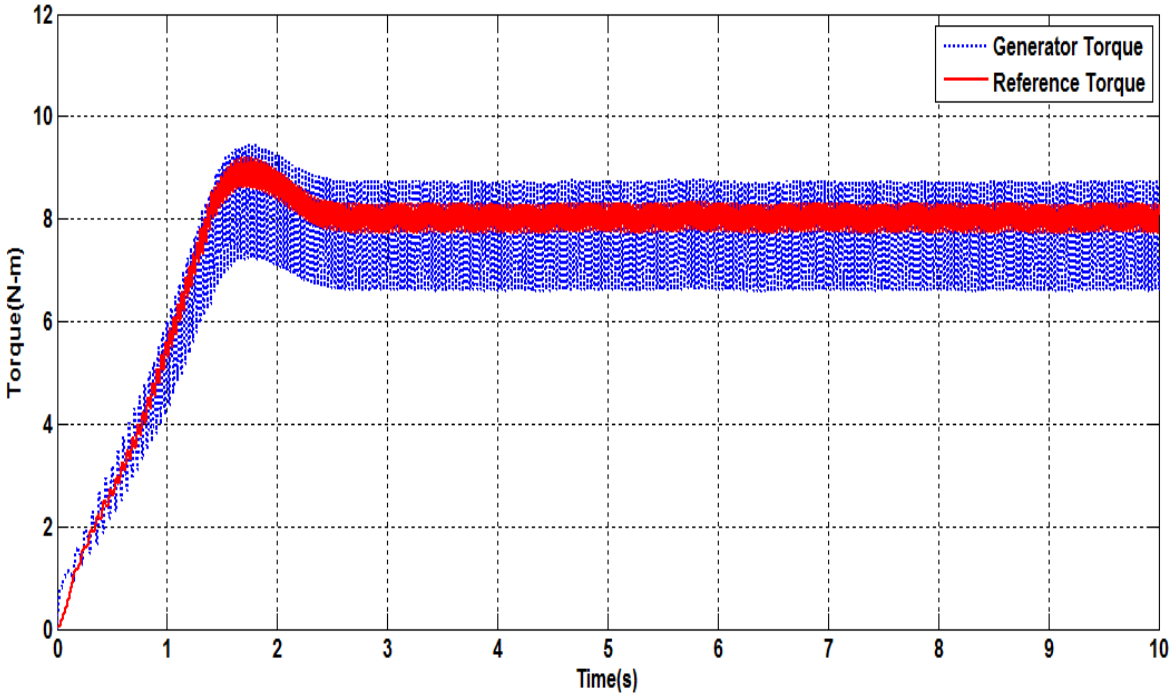

Fig. 8.7(c)

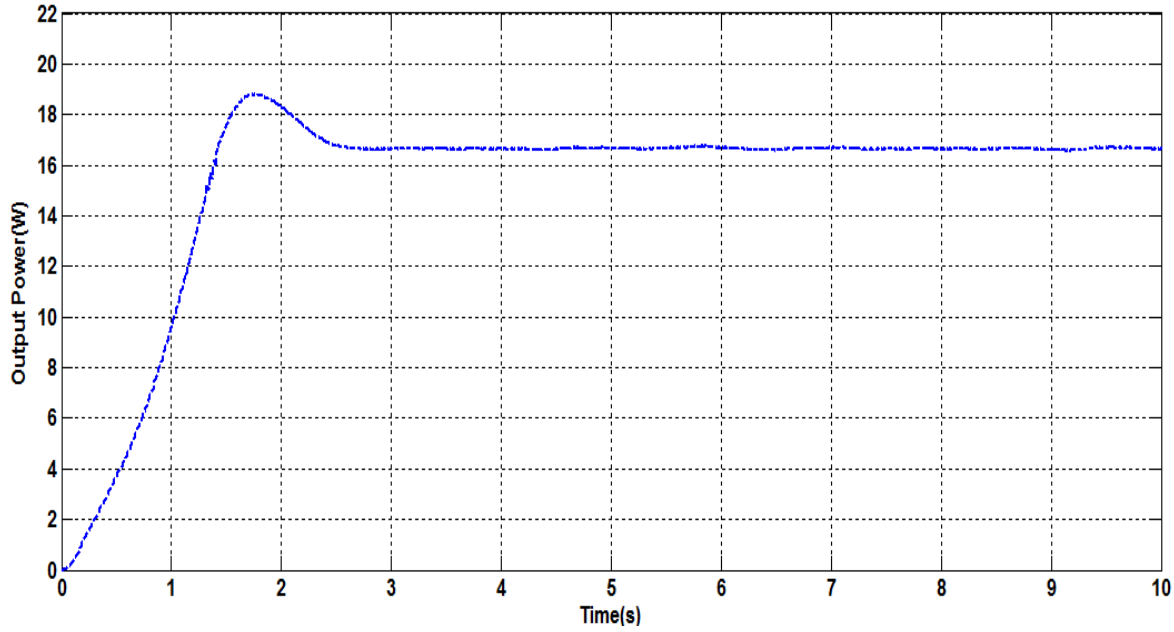

Fig. 8.7(d)

Fig. 8.7 Response of the system (a) Tow tank flow speed (b) Reference generator speed and instantaneous generator speed, (c) Reference current and instantaneous input current of the converter ,(d) Reference and developed generator torque and (e))Output dc power

To check the robustness of the controller a step response was introduced by changing the carriage speed. Fig. 8.8 shows the response of the system for the step input. The result shows that the system can also operate at optimum point for a sudden change in flow speed. One can see that the turbine responds very quickly to the changes in flow speed. The system did not exhibit any unstable behaviour. The system consists of two subsystems: an electrical subsystem that is fast and a mechanical subsystem that is slow. These subsystems are to some extent isolated from one another. Each subsystem is stable. It makes sense that the overall system is stable.

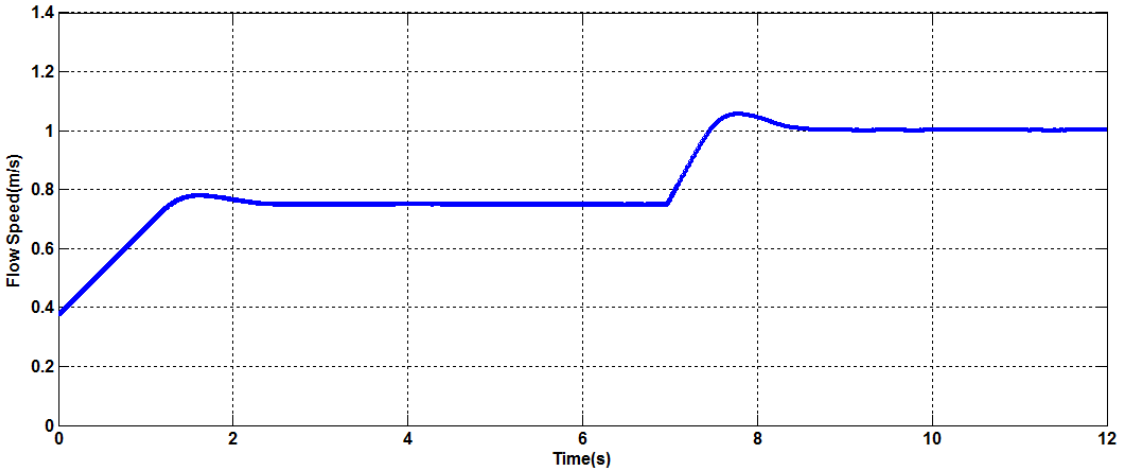

Fig. 8.8(a)

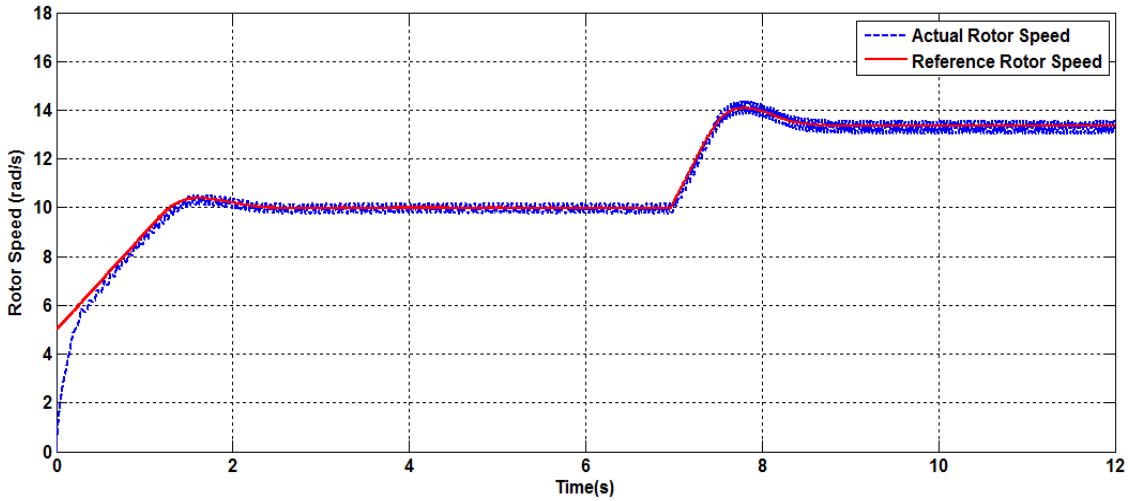

Fig. 8.8 (b)

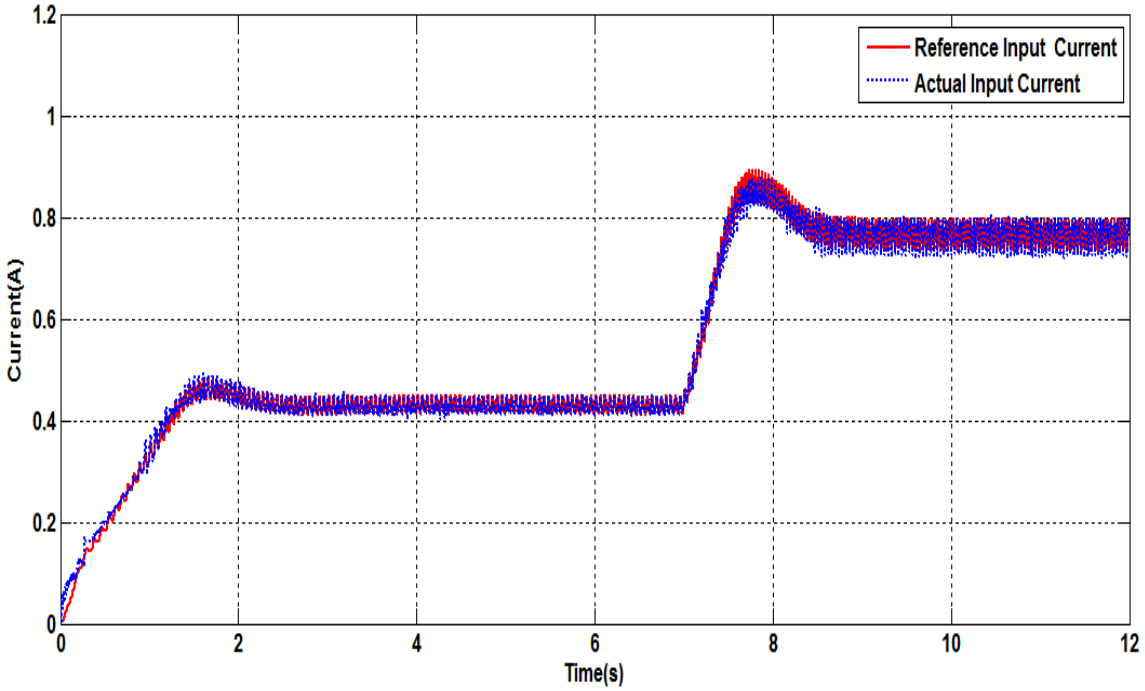

Fig. 8.8 (c)

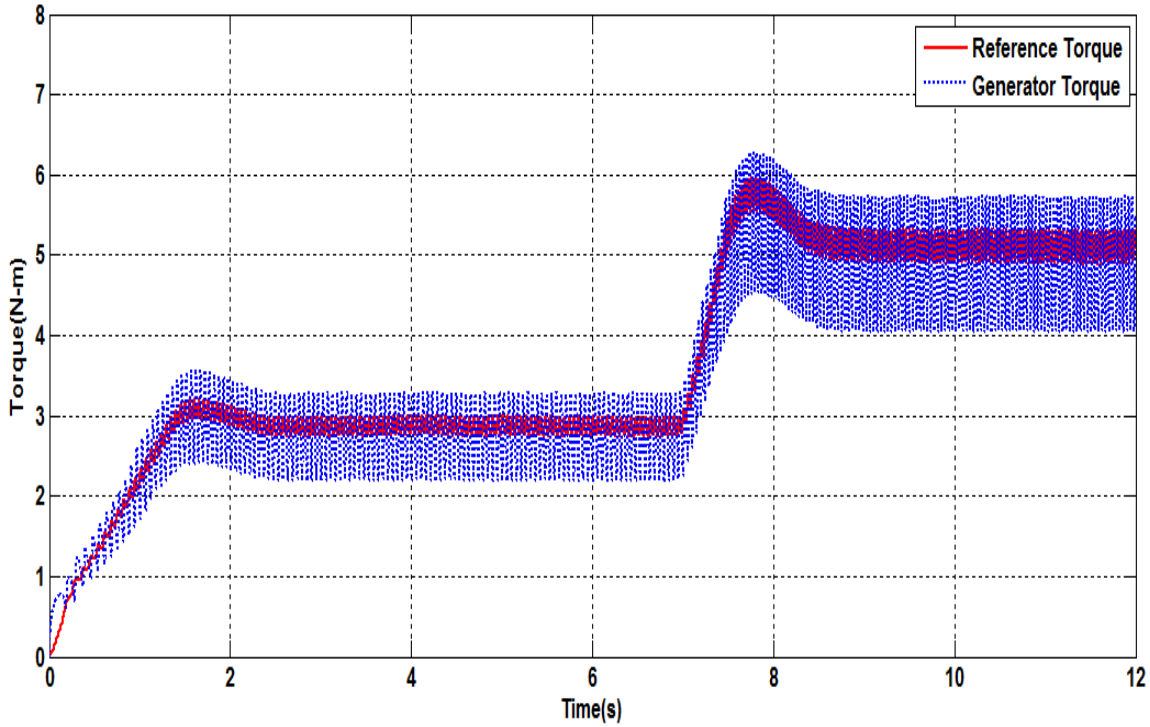

Fig. 8.8 (d)

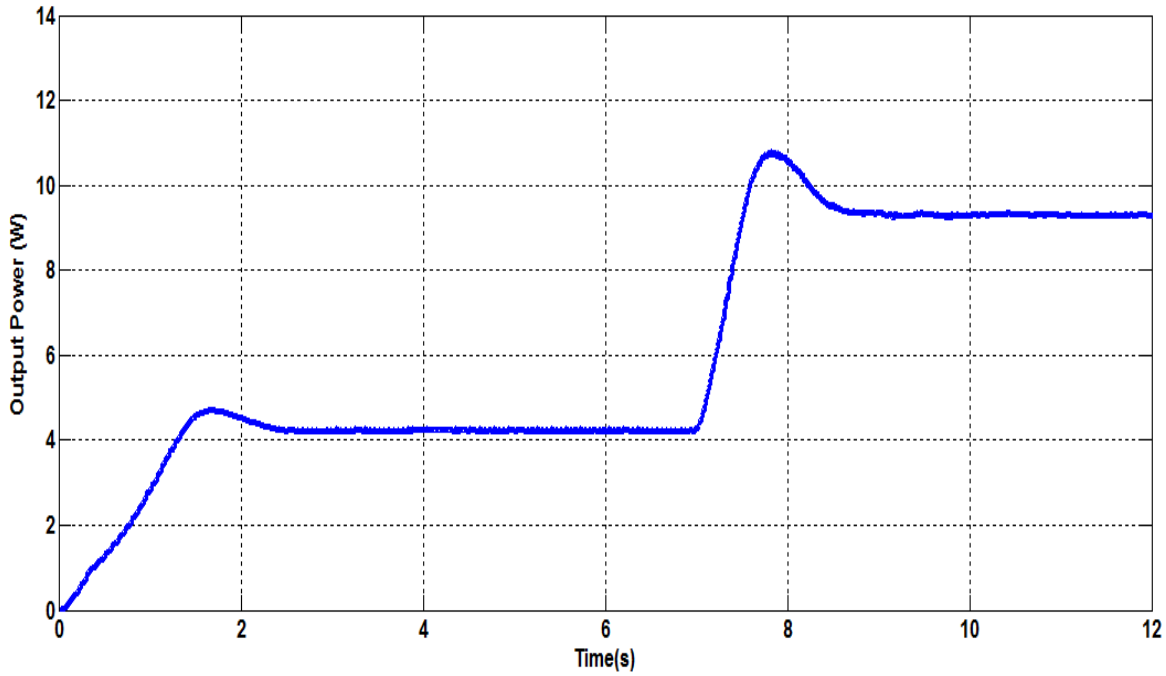

Fig. 8.8(e)

Fig.8.8 Response of the system for a step change (a) Tow tank flow speed (b) Reference generator speed and instantaneous generator speed (c) reference current and instantaneous input current of the converter (d) reference and developed generator torque and (e) output dc power

The modelling is successful in representing the dynamic states as well as the steady state condition. The comprehensive set of tests in the tow tank shows high degree of accuracy. It should be pointed out that the input power is dependent on water velocity. The output power is dependent on operating the device at optimum point. However, system efficiency is important to understand optimistic performance of the device. In this particular setup the overall losses (tank walls, gearing, bearing, generator, rectifier and converter) would be significant. As efficiency is a stead-state parameter, the transient data points should be ignored to reflect a more steady behavior. Fig. 8.9 shows the plot of system efficiency, (electrical output to fluid power ratio) and is not expressed in percentage. The overall system calculated system efficiency is 24%.

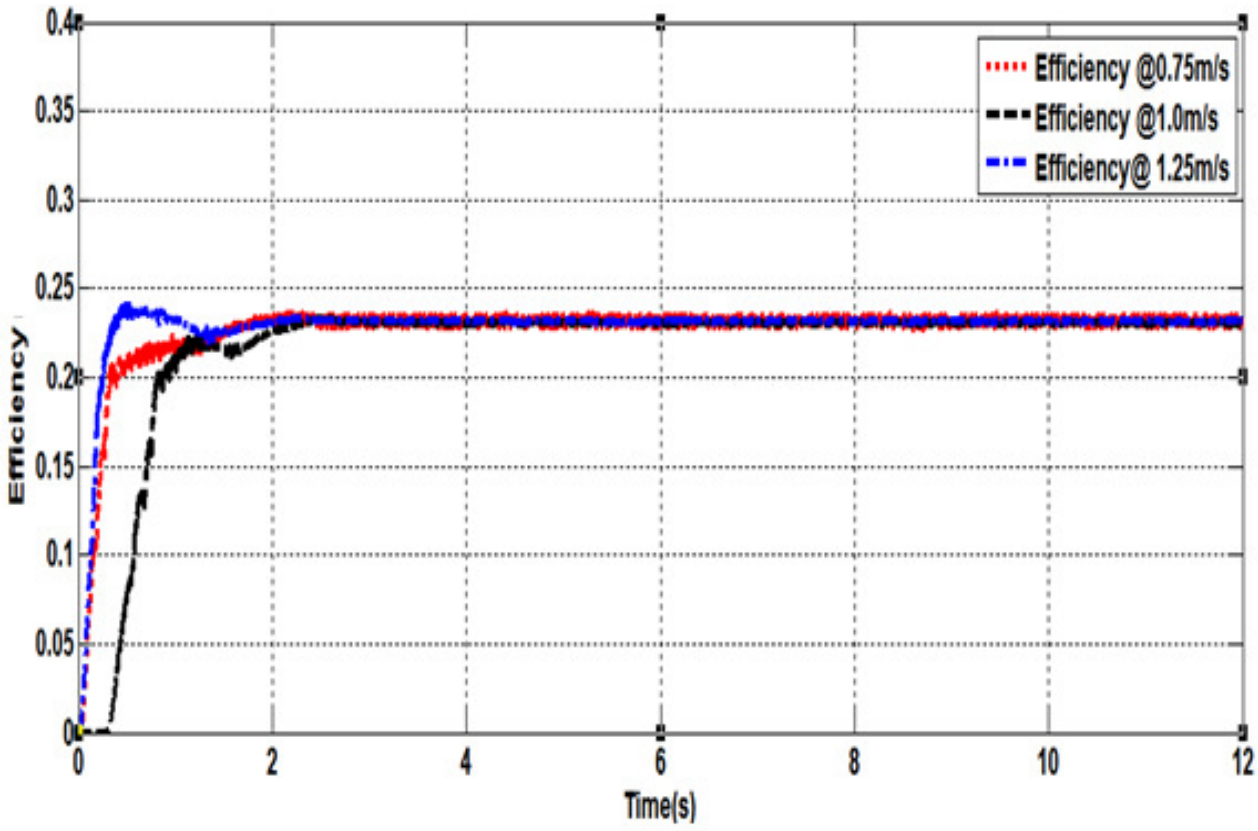

Fig 8.9 Efficiency of the MCECS at different flow speed

8.5 Conclusion

The prototype performance results are presented here at different tow tank speeds. The energy generated by the marine energy conversion system is recorded by a dSpace. The testing of the built prototype was done in a controlled environment using wave tank facility. The simulation results were compared to the test result of the prototype in order to verify reasonable agreement between theory, simulation and test results. The execution time of the control algorithm loop is very small. Since the ocean current is steady throughout, the system is expected to track effectively the maximum power at every instant.

Chapter IX

Conclusion Contribution and Future Work

9.0 Conclusion

A major outcome of the research is a robust small marine current energy conversion system that can extract power from the low marine current. It was tested in the towing tank in the Faculty of Engineering at Memorial University of Newfoundland. Power output was controlled using PWM and a DSP PI controller. A computational fluid dynamics simulation test bench was used to analyze the device. Two types of control strategies have been proposed. The first one used the well-known classical proportional integral controllers. The second one used a nonlinear control approach based on the so-called adaptive backstepping control that should handle torque oscillation smoothing and robustness against resource turbulences and load disturbances.

9.1 Contribution

The contributions of this research work are as follows:

- An autonomous, lightweight, low-cost, pressure-resistant energy marine current energy conversion system was designed and constructed. It was tested in the tow tank at MUN and gave reasonable power output.
- A theoretical model for the turbine was developed using potential flow theory. This model is relatively simple and computationally fast.

- A computational fluid dynamics model was developed for the turbine. It gave results close to test results. CFD allowed us to explore geometry variations too expensive to study experimentally.
- A simple proportional integral (PI) maximum power point tracking (MPPT) control strategy was developed for the turbine. The proposed control strategy was able to make the turbine rotor speed track an optimum speed. .
- An adaptive backstepping MPPT control strategy was developed for the turbine. Its main features are a chattering-free behaviour, a finite reaching time, and robustness with respect to external disturbances and unmodeled dynamics. Because of scheduling constraints, this was not tested in the tow tank.
- A marine current modeling procedure was developed that predicts the resource tidal speed from historical data.

9.2 Future Work

Some potential future work related to the thesis work includes:

- Better information about the ocean currents offshore NL is needed. This will guide the proper placement of turbines in areas where ocean currents are sufficiently strong.
- The geometry of the turbine needs to be optimized so that it has better efficiency and is highly-responsive to low-current velocities. This could be done more quickly using CFD which is much less expensive than tank tests.
- A generator designed specifically for the low rotational speeds of marine current devices needs to be developed.

- The turbine should be equipped with a tail arrangement to align in the direction of flow.
- The adaptive back stepping needs to be tested experimentally.
- A more robust prototype should be developed for tests at sea.
- There also exists ample room to improve the power output with design modifications such as design of magnetic gear arrangement, controlled rectifier.

References

[1] "The Kyoto Protocol, available at the United Nations Framework on Climate Change: http://unfccc.int/resource/docs/convkp/kpeng.pdf accessed 2005-08-17."

[2] "Status and research and development priorities," IEA/DTI report number FES-R-132 2003.

[3] J. A. Clarke, G. Connor, A. D. Grant, and C. M. Johnstone, "Regulating the output characteristics of tidal current power stations to facilitate better base load matching over the lunar cycle," *Renewable Energy*, vol. 31, pp. 173-180, 2006.

[4] M. Leijon, H. Bernhoff, M. Berg, and O. Ågren, "Economical considerations of renewable electric energy production - especially development of wave energy," *Renewable Energy* vol. 28, pp. 1201-1209, 2003.

[5] M. Leijon, A. Rehn, and A. Skoglund, "On the Physics, Engineering and Economics of Renewable Electric Energy Sources," *Submitted to Energy Policy* 2007.

[6] "Non Nuclear Energy - JOULE II, Wave energy project results, The Exploitation of Tidal Marine Currents," EU JOULE contract JOU2-CT94- 0355, 1996.

[7] I. G. Bryden, S. Naik, P. Fraenkel, and C. R. Bullen, "Matching tidal plants to local flow conditions," *Energy*, vol. 23, pp. 699-709 1998.

[8] M. D. Zaidman, V. Keller, A. R. Young, and D. Cadman, "Flow duration frequency behaviour of British rivers based on annual minima data," *Journal of hydrology*, pp. 195-213, 2003.

[9] A. S. Bahaj and L. E. Myers, "Fundamentals applicable to the utilization of marine current turbines for energy production," *Renewable Energy*, vol. 28,pp. 2205-2211, 2003

[10] Y. C. Chen and C. L. Chiu, "An efficient method of discharge measurement in tidal streams," *Journal of hydrology*, vol. 256, pp. 212-224, 2002.

[11] P. L. Fraenkel, "New development in tidal and wave power technologies, "presented at towards a renewable future: silver jubilee conference, Brighton, UK, 1999.

[12] "Tidal stream energy review," ETSU-T/05/00155/REP, 1993.

[13] "Non-Nuclear Energy - JOULE II, Wave energy project results, The Exploitation of Tidal Marine Currents," EU JOULE contract JOU2-CT94-0355, 1996.

[14] T.J. Hammons, "Tidal power," *Proc. IEEE*, vol. 3,pp. 419-433, March 1993.

[15] T.G. Pugh, *Tides, Surges and Mean Sea-Level*. London, UK: Wiley, 1987.

[15] D. Pugh, Changing sea levels, effects of tides weather and climate: Cambridge University Press, 2004.

[16] P. B. S. Lissaman and R. L. Radkey, "Coriolis Program - A review of the status of the ocean turbine energy system," presented at Oceans79, San Diego, USA, 1979.

[17] W. D. Liang, T. Y. Tang, Y. J. Yang, M. T. Ko, and W. S. Chuang, "Upper- ocean currents around Taiwan," Deep Sea Research Part II: Topical Studies in Oceanography, vol. 50, pp. 1085-1105, 2003.

[18] A. Kaneko, S. Mizuno, W. Koterayama, and R. L. Gordon, "Cross-stream velocity structures and their downstream variation of the Kuroshio around Japan," Deep Sea Research Part A. Oceanographic Research Papers, vol.39, pp. 1583-1594, 1992.

[19] M. H. Nielsen, "Baroclinic surface currents in the Kattegat," Journal of Marine Systems, pp. 97-121, 2005.

[20] J. Jachlewski, Wind solar project: Hybrid powered outdoor area lighting, Proceedings KGCOE 2005 of Multi disciplinary Engineering Design conference.

[21] T. Hayashi, Wind tunnel test on a different three phase Savonius rotor, vol 48, page 9-16, JSME 2005.

[22] *2005 IEEE Power Engineering Society General Meeting Panel Session*, "Harnessing the untapped energy potential of the oceans: Tidal, wave, currents and OTEC," San Francisco(USA), June 2005.

[23] Technomare SpA and IT Power Ltd., "Non Nuclear Energy—JOULE II, Wave energy project results: The Exploitation of tidal marine currents," *Non-Nuclear Energy R&D Component*, EU JOULE Contract JOU2-CT94-0355, 1996.

[24] P.W. Ullman, "Offshore tidal power generation – A new approach to power conversion of the oceans' tides," *MTS Journal*, vol. 36, no.4, pp. 16-24, 2002.

[25] I.G. Bryden et *al.*, "Choosing and evaluating sites for tidal current development," *Proc. IMechE*, Part A: *Journal of Power and Energy*, vol. 218, no.8, pp. 567-578, 2004.

[26] B.V. Davis, "Low head tidal power: A Major source of energy from the world's oceans,"*in Proceedings of IECEC'97*, vol. 3, pp. 1982-1989, Honolulu (USA), July-August 1997.

[27] I.G. Bryden et *al.*, "An assessment of tidal streams as energy sources in Orkney and Shetland," *Underwater Technology*, vol. 21, no.2, 1995.

[28] I.G. Bryden, "Tidal stream power for Orkney and Shetland?," *Underwater Technology*,vol. 9, no.4, 1993.

[29] I.G. Bryden et *al.*, "ME1 – Marine energy extraction: Tidal resource analysis," *RenewableEnergy*, vol. 31, pp. 133-139, 2006.

[30] http://www.marineturbines.com/home.htm (last accessed January 2009).

[31] http://www.teleos.co.uk/Home.htm (last accessed January 2008).

[32] http://www.bluenergy.com/ (last accessed January 2008).

[33] http://www.gcktechnology.com/GCK/ (last accessed January 2008).

[34] http://www.smdhydrovision.com/ (last accessed January 2008).

[35] T. Hayashi, "Wind tunnel test on a different three phase Savonius rotor," vol 48, page 9-16, JSME 2005.

[36] S. J. Savonius, "The S-Rotor and its Applications, Mechanical Engineering," Vol. 53, No. 5, May 1931, pp. 333-338.

[37] V.J Modi, N.J Roth., "A prototype design and performance of the Savonius rotor based irrigation system. M.A.Sc Thesis", University of British Columbia, March 1985.

[38] Menet J-L, Valde`s L-C, Me´nart B., "A comparative calculation of the wind turbines capacities on the basis of the L-r criterion." Renewable Energy Vol. 22 pp 491–506, 2001.

[39] Menet J-L, Me´nart B. Une proce´dure de comparaison de quelques e´oliennes classiques base´e surl'utilisation du crite`re L-sigma. In Proceedings of 15th French Mechanical Symposium, Nancy, France, September 3–7, 2001.

[40] J. L. Menet, "A double-step Savonius rotor for local production of electricity: a design study," Renewable Energy vol.19 September 2004, page 1843-1862.

[41] Ushiyama I. Nagai H., "Optimum design configurations and performances of Savonius rotors," Wind Engineering 1988;12(1):59–75.

[42] Fujisawa N., "On the torque mechanism of Savonius rotors," Journal of Wind Engineering Industrial Aerodynamics 1992; 40:277–92.

[43] Tsutomo Hayashi, "Wind tunnel tests on a different phase three stage Savonius rotor," JSME International Journal, Series B, Vol 48, No.1, 2005: 9-16.

[44] Grinspan, A. S., Suresh Kumar, P. Saha U. K. and Mahanta P., " Performance of Savonius wind turbine rotor with twisted bamboo blades," Proceedings of 19th Canadian congress of applied mechanics, Calgary, Alberta, Canada, Vol- 2, pp. 412 - 413, 2003.

[45] Merle C. Potter and David C. Wiggert, "Mechanics of Fluids," 2ed, 1997.

[46] J. M. Anderson, K. Streitlien, D. S. Barrett, and M. S. Triantafyllou, "Oscillating foils of high propulsive efficiency," *J. Fluid Mech.*, vol. 360,pp. 41–72, 1998.

[47] N. Bose and Y. Lien, "Propulsion of a fin whale (*Balaenoptera physalus*): Why the fin whale is a fast swimmer," in *Proc. Roy. Soc.Lond.*, vol. 237, 1989, pp. 175–200.

[48] P. R. Bandyopadhyay, J. M. Castano, J. Q. Rice, R. B. Philips, W. H. Nedderman, and W. K. Macy, "Low speed maneuvering hydrodynamics of fish and small underwater vehicles," *J. Fluids Eng.*, vol. 119, pp.136–119, 1997a.

[49] P. R. Bandyopadhyay, M. J. Donnelly, W. H. Nedderman, and J. M. Castano, "A dual flapping foil maneuvering device for low-speed rigid bodies," in *3rd Int. Symp. Performance Enhancement for Marine Vehicles*, Newport, RI, 1997b.

[50] P. R. Bandyopadhyay, J.M. Castano, M. J. Donnelly,W. H. Nedderman, and M. J. Donnelly, "Experimental simulation of fish-inspired unsteady vortex dynamics on a rigid cylinder," *J. Fluids Eng.*, vol. 122, pp.219–238, 2000.

[51] D. N. Beal, F. S. Hover, and M. S. Triantafyllou, "The effect on thrust and efficiency of an upstream Karman wake on an oscillating foil," in *Proc. UUST*, Durham, NH, 2001.

[52] C. E. Brown and W. H. Michael, "Effect of leading edge separation on the lift of delta wing," *J. Aerosp. Sci.*, vol. 21, p. 690, 1954.

[53] H. K. Cheng and L. E. Murillo, “Lunate-tail swimming propulsion as a problem of curved lifting line in unsteady flow. Part 1. Asymptotic theory,” *J. Fluid Mech.*, vol. 143, pp. 327–350, 1984.

[54] J. D. DeLaurier and J. M. Harris, “Experimental study of oscillating wing propulsion,” *J. Aircraft*, vol. 19, no. 5, pp. 368–373, 1982.

[56] M. H. Dickinson, “The effect of wing rotation on unsteady aerodynamic performance at low Reynolds numbers,” *J. Exp. Biol.*, vol. 192, pp.179–206, 1994.

[57] L. Luznik and N. Bose, “Propulsive thrust of an oscillating foil at large angles of attack: Experimental study,” in *Proc. Amer. Towing Tank Conf.*,Iowa, 1998.

[58] Triantafyllou, G. S., M. S. Triantafyllou, "Optimal Thrust Development in Oscillating Foils with Application to Fish Propulsion." Journal of Fluids and Structures vol.**7**, 205-224, 1993.

[59] Triantafyllou, M. S., Techet, A.H., Hover, "Review of Experimental Work in Biomimetic Foils." IEEE Journal of Ocean Engineering vol.29,2004.

[60] G. L. Johnson, *Wind Energy Systems*. Englewood Cliffs, NJ: Prentice- Hall, 1985.

[61] J. Kentfield, *The Fundamentals of Wind-Driven Water Pumpers*. Amsterdam, The Netherlands: Gordon and Breach, 1996.

[62] M. M. Duquette, “The Effect of Solidity and Blade Number on the Aerodynamic Performance of Small Horizontal Axis Wind Turbines,” M.Sc. Dissertation, Dept. Mech. Aero. Eng., Clarkson Univ., Potsdam, NY,2002.

[63] M. M. Duquette and K. D. Visser, “Numerical implications of solidity and blade number on rotor performance of horizontal-axis wind turbines,” *J. Solar Energy Eng.*, vol. 125, no. 4, pp. 425–432, Nov. 2003.

[64] H. Glauert, “Airplane propellers, division L,” in *Aerodynamic Theory*, W. F. Durand, Ed. New York: Dover, 1963, vol. IV.

[65] J. F. Manwell, J. G. McGowan, and A. L. Rogers, *Wind Energy Explained—Theory, Design, and Application*, 1st ed. New York: Wiley,2002.

[66] M.E.H. Benbouzid et *al.*, “The state of the art of generators for wind energy conversion systems,” *in Proceedings of ICEM'06*, Chania (Greece), September 2006.

[67] Sensorless Control of Permanent Magnet Synchronous Motor Drives, Chandana Perera, PhD Thesis, December 2008, Aalborg University.

[68] PM Wind Generator Comparison of Different Topologies, Yicheng Chen, Pragasen Pillay, Azeem Khan, IEEE Article.

[69] Electrical Machines and Drives, Peter Vas, Oxford University Press, 1992.

[70] Sensorless control of surface permanent magnet synchronous motor using a new method, Z. Song et al. Energy Conversion and Management, 2006.

[71] W. Baran and M. Knorr, “Synchronous couplings with Sm Co5 magnets,” in *2nd Int. Workshop on Rare-Earth Cobalt Permanent Magnets and Their Applications*, Dayton, OH, 1976, pp. 140–151.

[72] D. Weinmann *et al.*, “Application of rare earth magnets to coaxial couplings,” in *3rd Int. Workshop on Rare-Earth Cobalt Permanent Magnets and Their Applications*, San Diego, CA, 1978, pp. 325–347.

[73] J. P.Yonnet, “A new type of permanent-magnet coupling,” *IEEE Trans. Magn.*, vol. MAG-17, no. 6, pp. 2991–2993, Nov. 1981.

[74] V. V. Fufaev and A. Y. Krasil’nikov, “Torque of a cylindrical magnetic coupling,” *Elektrotekhnika*, vol. 65, pp. 51–53, 1994.

[75] E. P. Furlani, "Analysis and optimization of synchronous couplings," *J. Appl. Phys.*, vol. 79, pp. 4692–4694, 1996.

[76] E. P. Furlani, "A two-dimensional analysis for the coupling of magnetic gears," *IEEE Trans. Magn.*, vol. 33, no. 3, pp. 2317–2321, May 1997.

[77] S. M. Huang and C. K. Sung, "Analytical analysis of magnetic couplings with parallelepiped magnets," *J. Magn. Magn. Mater.*, vol. 239,pp. 614–616, 2002.

[78] E. P. Furlani, "Formulas for the force and torque of axial couplings," *IEEE Trans. Magn.*, vol. 29, no. 5, pp. 2295–2301, Sep. 1993.

[79] J. P. Yonnet *et al.*, "Analytical calculation of permanent magnet couplings," *IEEE Trans. Magn.*, vol. 29, no. 6, pp. 2932–2934, Nov. 1993.

[80] Y. Chen, K. Smedley, Three-phase boost-type grid connected inverter, IEEE Transaction on Power Electronics 23 (5) (2008) 2301-2309.

[81] Tidal stream energy review, UK DTI. Report ETSUT/05/00155/REP, prepared by Engineering and Power Development Consultants Limited, Binnie and Partners, Sir Robt. McAlpine and Sons Limited and IT Power Limited for the ETSU, UK Department of Energy. Crown Copyright 1993.

[82] The exploitation of tidal marine currents (non-nuclear energy JOULE II project results). Report EUR 16683EN, DG Science, Research and Development, The European Commission Office for Official Publications, Luxembourg, 1996.

[83] Feasibility study of tidal current power generation for coastal waters: Orkney and Shetland. Final Report, EU contract XVII/4 1040/92-41, ICIT, March 1995.

[84] T. J. Hammons, "Tidal power," *Proc. IEEE*, vol. 3, no. 3, pp. 419–433,Mar. 1993.

[85] “The exploitation of tidal marine currents,” Eur. Union Commission, Rep. EUR16683EN, 1996.

[86] L. Myers and A. S. Bahaj, “Simulated electrical power potential harnessed by marine current turbine arrays in the Alderney Race,” *Renew. Energy*, vol. 30, pp. 1713–1731, 2005.

[87] Tidal Current of the Brittany Western Coast: From Goulven to Penmarc’h French Navy Hydrographic and Oceanographic Service (SHOM), Paris, France, 1994.

[88] I. G. Bryden and S. J. Couch, “ME1 – Marine energy extraction: Tidal resource analysis,” *Renew. Energy*, vol. 31, pp. 133–139, 2006.

[89] Z. Zhou, M.E.H. Benbouzid, J.F. Charpentier, F. Scuiller, and T. Tang, “A review of energy storage technologies for marine current energy systems,” *Renewable and Sustainable Energy Review*, vol. 18, pp.390-400, Feb. 2013.

[90] Z. Zhou, F. Scuiller, J.F. Charpentier, M.E.H. Benbouzid and T. Tang, “Grid-connected marine current generation system power smoothing control using supercapacitors,” *in Proceedings of the 2012 IEEE IECON*, Montreal (Canada), pp.4035-4040, Oct. 2012.

[91]Y. Goda, *Random Seas and Design of Maritime Structures*. Advanced Series on Ocean Engineering, vol.33, World Scientific: Singapore, 2010.

[92] E. Bossanyi, *Wind Energy Handbook*. New York: Wiley, 2000.

[93] G. Mattarolo et *al.*, “Modelling and simulation techniques applied to marine current turbine,” *in Proceedings of the 2006 International Conference on Ocean Energy*, Bremerhaven (Germany), 2006.

[94] P.J. Moriarty et *al.*, “AeroDyn theory manual,” NREL/TP-500-36881, January 2005.

[95] Batten, W. M. J., Bahaj, A. S., Molland, A. F., and Chaplin, J. R., 2006, "Hydrodynamics of Marine Current Turbines," Renewable Energy, 31(2), pp.249–256.

[96] Batten, W. M. J., Bahaj, A. S., Molland, A. F., and Chaplin, J. R., 2008, "The Prediction of the Hydrodynamic Performance of Marine Current Turbines," Renewable Energy, 33(5), pp. 1085–1096.

[97] Bahaj, A. S., Molland A. F., Chaplin, J. R. and Batten, W. M. J., "Power and thrust measurements of marine current turbines under various hydrodynamic flow conditions in a cavitation tunnel and a towing tank," *Renew. Energy*, Vol. 32, No. 3, pp. 407–426, Mar. 2007.

[96] Katarina Yuen, Karin Thomas, Mårten Grabbe, Paul Deglaire, Mathias Bouquerel, David Österberg, Mats Leijon, "Matching a Permanent Magnet Synchronous Generator to a Fixed Pitch Vertical Axis Turbine for Marine Current Energy Conversion", IEEE Journal of Oceanic Engineering, Vol. 34, No. 1, Jan. 2009.

[97] P. C. Krause, *Analysis of electric machinery*. New York: McGraw-Hill,1986.

[98] L. Söderlund, J. T. Eriksson, J. Salonen, H. Vihriälä, and R. Perälä, "A permanent magnet generator for wind power applications," IEEE Transaction on Magnetics, vol. 32, pp. 2389-2392, 1996.

[99] P. Lampola and J. Perho, "Electromagnetic analysis of a low speed permanent magnetized wind generator," presented at Opportunities and advances in international power generation, 1996.

[100] E. Spooner and A. C. Williamson, "Direct coupled permanent magnet generator for wind turbine applications," presented at Electr. Power Appl.,1996.

[101] Borowy, B.S. and Salameh, Z.M., “Dynamic response of a stand-alone wind energy conversion system with battery energy storage to a wind gust”, IEEE Transactions on Energy Conversion, Vol. 12, No. 1, pp. 73-78, Mar. 1997.

[102] A. Grauers, "Design of direct drive PM generators for wind turbines," vol.PhD. Göteborg, Sweden: Chalmers University of Technology, 1996.

[103] A. E. Fitzgerald, C. Kingsley, and S. D. Umans, Electric machinery, Fifth edition ed: McGraw-Hill Inc, 1990.

[104] Borowy, B.S. and Salameh, Z.M., “Dynamic response of a stand-alone wind energy conversion system with battery energy storage to a wind gust”, IEEE Transactions on Energy Conversion, Vol. 12, No. 1, pp. 73-78, Mar. 1997.

[105] S. E. Ben Elghali, R. Balme, K. Le Saux, M. E. H. Benbouzid, J. F. Charpentier, and F. Hauville, “A simulation model for the evaluation of the electrical power potential harnessed by a marine current turbine,” IEEE J. Ocean. Eng., vol. 32, no. 4, pp. 786–789, Oct. 2007.

[106] Ben Elghali, S. E., Balme, R., Le Saux, K. , Benbouzid, M. E. H., Charpentier, J. F. and Hauville, F., “A simulation model for the evaluation of the electrical power potential harnessed by a marine current turbine,” IEEE J. Ocean. Eng., vol. 32, no. 4, pp. 786–789, Oct. 2007.

[107] K. Thomas, M. Grabbe, K. Yuen, and M. Leijon, “A low speed generator for energy conversion from marine currents—Experimental validation of simulations,” J. Power Energy, vol. 222, Part A: Proc. Inst. Mech. Eng., no. 4, pp. 381–388, 2008

[108] Ned Mohan ,”Power electronics : converters, applications, and design,” 3ed,2003.

[109] M. H.Rashid,”Power electronics: circuits, devices, and applications,” 3ed, 2004.

[110] K. Tan and S. Islam, “Optimal control strategies in energy conversion of PMSG wind turbine system without mechanical sensors,” IEEE Transaction Energy Conversion, vol. 19, no.2, pp. 392–399, Jun. 2004.

[111] R. Esmaili, L. Xu, D. K. Nichols, A new control method of permanent magnet generator for maximum power tracking in wind turbine application, IEEE PES 2005, vol.3, pp. 2090- 2095, June 2005.

[112] Raza, K.S.M. Goto, H. Hai-Jiao Guo Ichinokura, O. , “A novel speed-sensorless adaptive hill climbing algorithm for fast and efficient maximum power point tracking of wind energy conversion systems “,IEEE International conference on Sustainable Energy Technologies, No. 2008, pp 628-633

[113] I. Schiemenz and M. Stiebler, “Control of a permanent magnet synchronous generator used in a variable speed wind energy system,” in Proc.IEEE IEMDC, 2001, pp. 872–877.

[114] R. Datta and V.T. Ranganathan, “A method of tracking the peak power points for a variable speed wind energy conversion system”, IEEE Trans. Energy Conversion 18 (2003), pp. 163–168

[115] Tafticht, T. Agbossou, K. Cheriti, A., “DC bus control of variable speed wind turbine using a buck-boost converter”, IEEE Power Engineering Society General Meeting, 2006.

[116] H.E.Mena. Lopez, Maximum Power Tracking Control Scheme for Wind Generator Systems. Master's Thesis, Texas A&M University, Dec. 2007

[117] Srighakollapu, N. Sensarma, P.S. , “Sensorless maximum power point tracking control in wind energy generation using permanent magnet synchronous generator “, 34th Annual IEEE Industrial Electronics Conference, Nov. 2008

[118] T. Tanaka, T. Toumiya, and T. Suzuki, “Output control by hill-climbing method for a small scale wind power generating system,” Renewable Energy, vol. 12, no. 4, pp. 387-400, 1997.

[119] Morimoto S., Nakayama H., Sanada M., and Takeda Y., “Sensorless output maximization control for variable-speed wind generation system using IPMSG” IEEE Transactions on Industry Applications, Vol. 41, No. 1, pp. 60-67, Jan. 2005.

[120] Ben Elghali, S.E., El Hachemi Benbouzid, M., Ahmed-Ali, T. and Charpentier, J.F., “High-Order Sliding Mode Control of a Marine Current Turbine Driven Doubly-Fed Induction Generator” IEEE Journal of Oceanic Engineering, Vol. 35, No. 2, pp. 402-411, Apr. 2010.

[121] M. E. Haque, M. Negnevitsky and K.M. Muttaqi, “A novel control strategy for a variable-speed wind turbine with a permanent-magnet synchronous generator”, IEEE Transactions on Industry Applications, Vol. 46, No. 1, pp. 331-339, January 2010.

[122] S. Kazmi, H. Guo and O. Ichinokura, “A novel algorithm for fast and speed-sensorless maximum power point tracking in wind energy conversion systems”, IEEE Transactions on Industrial Electronics, Vol. 58, No. 1, pp. 29-36, January 2011.

[123] B. Beltran, T. Ahmed-Ali and M. El Hachemi Benbouzid, “High-order sliding mode control of variable-speed wind turbines”, IEEE Transactions on Industrial Electronics, Vol. 56, No. 9, pp. 3314 - 3321, September 2009.

[124] S. Benelghali, M. El Hachemi Benbouzid, J. F. Charpentier, T. Ahmed-Ali and I. Munteanu, “Experimental Validation of a Marine Current Turbine Simulator: Application to a Permanent Magnet Synchronous Generator-Based System Second-Order Sliding Mode Control”, IEEE Transactions on Industrial Electronics, Vol. 58, No.1, pp. 118- 126, January 2011.

[125] E. Koutroulis and K. Kalaitzaki “Design of a Maximum Power Tracking System for Wind-Energy-Conversion Applications,” IEEE Transactions on Industrial Electronics, Vol. 53, No. 2, pp. 486 - 494, April 2006.

[126] L. Baroteand, C. Marinescu and M. N. Cirstea “Control Structure for Single-Phase Stand-Alone Wind-Based Energy Sources,” IEEE Transactions on Industrial Electronics, Vol. 60, No. 2, pp. 764 - 772, February 2013.

[127] S. E. Ben Elghali, R. Balme, K. Le Saux, M. E. H. Benbouzid, J. F. Charpentier and F. Hauville, “A simulation model for the evaluation of the electrical power potential harnessed by a marine current turbine,” IEEE J. Ocean. Eng., Vol. 32, No. 4, pp. 786–789, October 2007.

[128] KRSTI´C M., KANELLAKOPOULOS I. and KOKOTOVI´C P.: ’Nonlinear and Adaptive Control Design’ (Wiley–Interscience Publication, 1995).

[129] KRSTI´C M., KANELLAKOPOULOS I. and KOKOTOVI´C P.: ’Nonlinear design of adaptive controllers for linear systems’, IEEE Transactions on Automatic Control, 1994, 39 pp. 738–752

[128] R. Lozano and B. Brogliato, “Adaptive control of a simple nonlinear system without a priori information on the plant parameters”, IEEE Transactions on Automatic Control, Vol. 37, No. 1, pp. 30-37, January 1992.

[129] S. Oucheriah and L. Guo, “PWM-Based Adaptive Sliding Mode Control for Boost DC-DC Converters”, IEEE Transactions on Industrial Electronics, Vol. 60, No. 8, pp. 3291 – 3294, August 2013.

[130] IKHOUANE F. and KRSTI´C M.: ’Adaptive backstepping with parameter projection: Robustness and asymptotic performance’, Automatica, 1998, 34 pp. 429–435.

[131] IKHOUANE F. and KRSTI´C M.: ’Robustness of the tuning functions adaptive backstepping design for linear systems’, IEEE Transactions on Automatic Control, 1998, 43 pp. 431–437.

[132] M. A. Rahman, D. M. Vilathgamuwa, M. N. Uddin and K. Tseng., “Nonlinear control of interior permanent-magnet synchronous motor” IEEE Transactions on Industry Applications, Vol. 39, No. 2, pp. 408-416, March 2003.

[133] H. El Fadil and F. Girt, “Backstepping Based Control of PWM DC-DC Boost Power Converters”, Proceedings of the IEEE International Symposium on Industrial Electronics, Vigo, 4-7 June 2007, pp. 395-400.

[134] J. Zhang, Z. Chen and M. Cheng, “Design and comparison of a novel stator interior permanent magnet generator for direct-drive wind turbines”, IET Renewable Power Generation, Vol. 1, No. 4, December 2007, pp. 203-210.

[135] Liao, Y., Liang, F., and Lipo, T.A.: ‘A novel permanent magnet motor with doubly salient structure’, IEEE Trans. Ind. Appl., 1995, 31, (5),pp. 1069–1077.

[136] Chau, K.T., Cheng, M., and Chan, C.C.: ‘Performance analysis of 8/6-pole doubly Power Syst., 1999, 27, pp. 1055–1067.

[137] Cheng, M., Chau, K.T., and Chan, C.C.: ‘Design and analysis of a new doubly salient permanent magnet motor’, IEEE Trans. Magn., 2001, 37, (4), pp. 3012–3020.

APPENDIX A MCECS COMPONENTS

Turbine

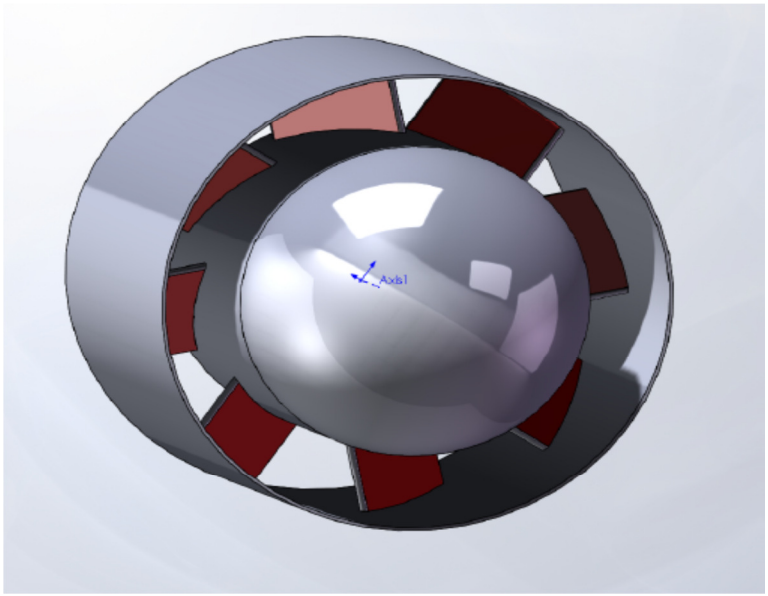

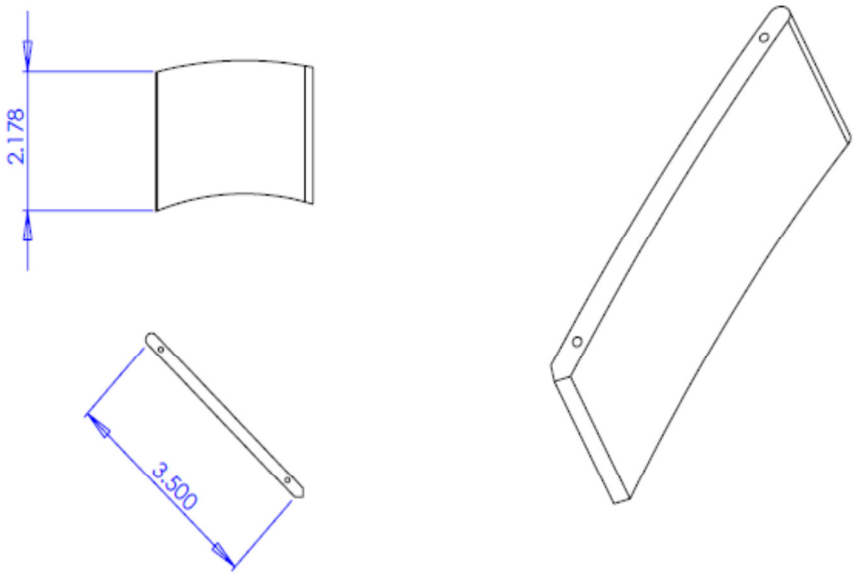

Fig. A.1 Turbine Dimension

Magnetic Coupler and Drive Train

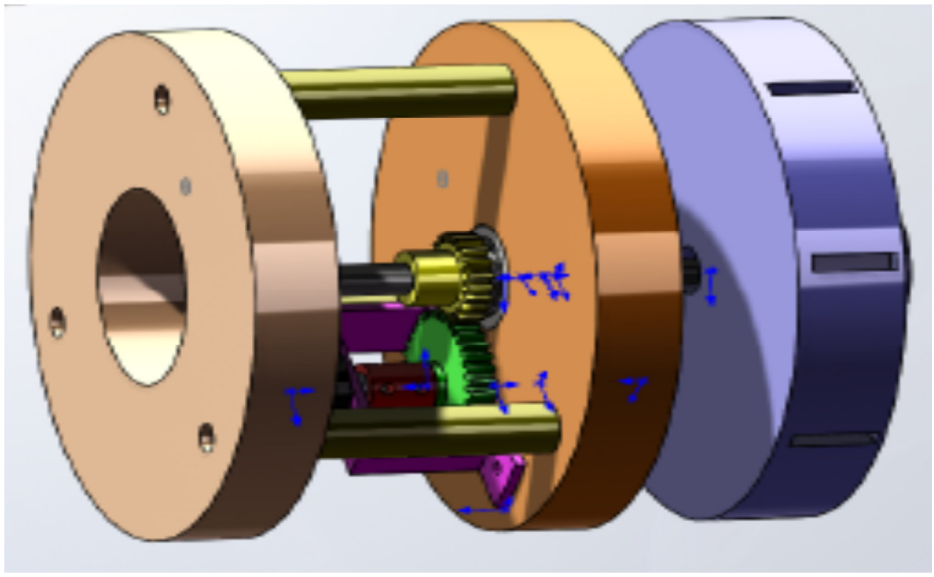

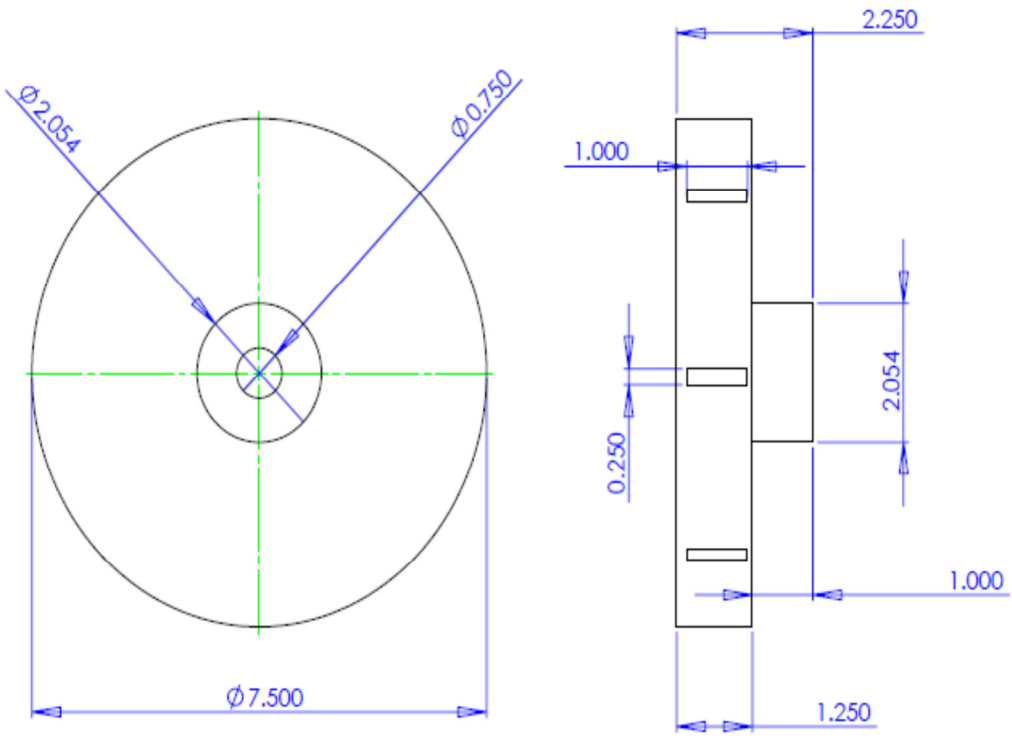

Fig A.2 Magnetic coupler Dimensions

MCECS Chamber

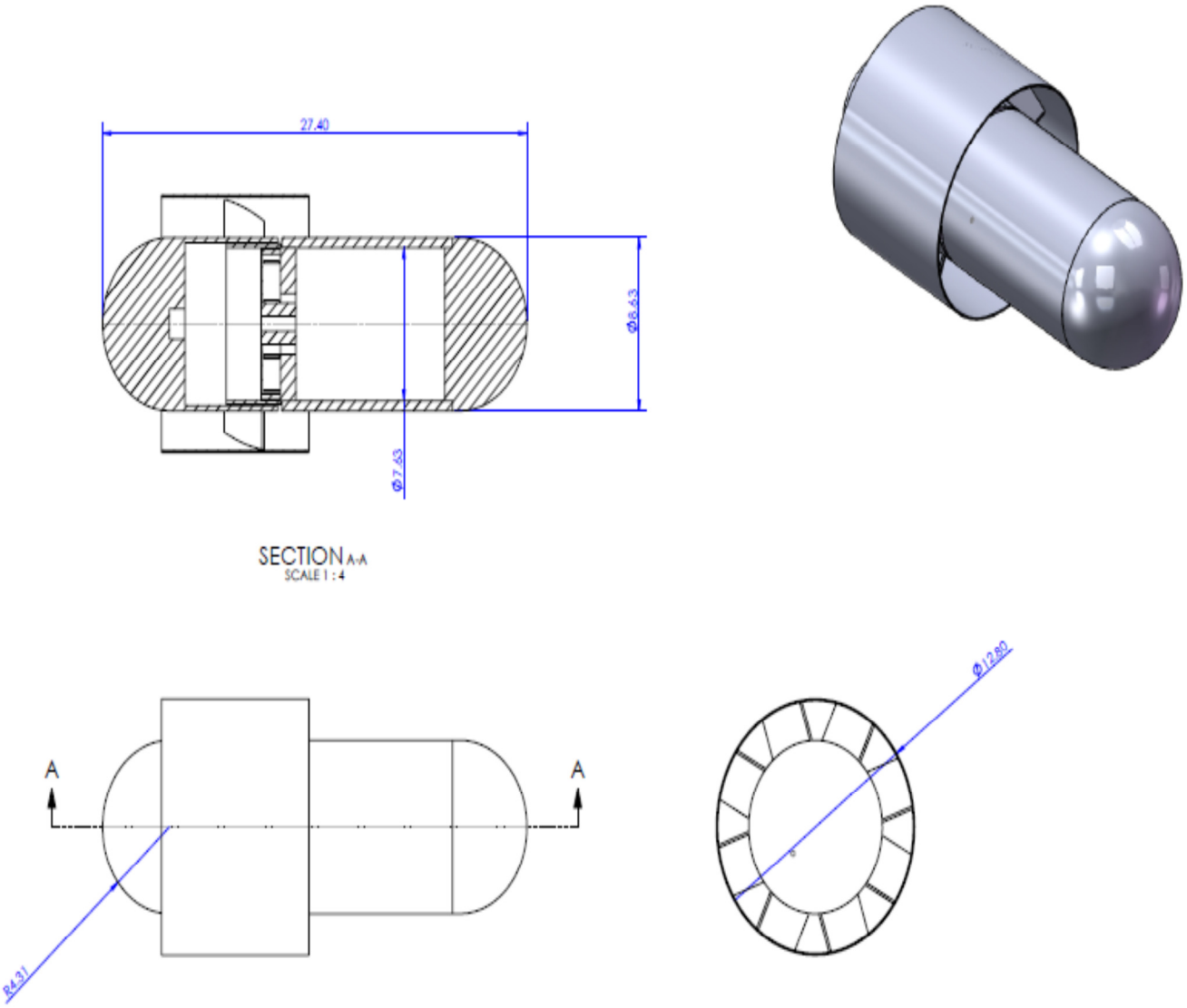

Fig A.3 MCECS Chamber Dimension

APPENDIX B LAGRANGIAN FORMULATION

The centre of gravity (C.G) of the foil can be found as the ratio of the mass and volume of foil. One can define the geometry of the working device in the x-y coordinate system as below:

$$X_A = A\cos\alpha \qquad B.1$$

$$Y_A = A\sin\alpha \qquad B.2$$

$$X_F = D\cos\alpha - B\cos\kappa \qquad B.3$$

$$Y_F = D\sin\alpha - B\sin\kappa \qquad B.4$$

Differentiation of the above equations *A.1* to *A.4* gives

$$\dot{X}_A = -A\,\dot{\alpha}\sin\alpha \qquad B.5$$

$$\dot{Y}_A = A\,\dot{\alpha}\cos\alpha \qquad B.6$$

$$\dot{X}_F = -D\,\dot{\alpha}\sin\alpha - B\,\dot{\alpha}\sin\kappa + B\,\dot{\beta}\sin\kappa \qquad B.7$$

$$\dot{Y}_F = D\,\dot{\alpha}\cos\alpha + B\,\dot{\beta}\cos\kappa - B\,\dot{\alpha}\cos\kappa \qquad B.8$$

This gives the kinetic energy of the device

$$K.E = \frac{M_A}{2}\left(\dot{X}_A{}^2 + \dot{Y}_A{}^2\right) + \frac{M_F}{2}\left(\dot{X}_A{}^2 + \dot{Y}_A{}^2\right) + \frac{I_A}{2}\dot{\alpha}^2 + \frac{I_F}{2}\dot{\beta}^2 \qquad B.9$$

The potential energy of the device is zero as it has no vertical motion. Thus the Lagrangian Formulation can be written as:

$$L = \frac{M_F}{2}(B^2 + D^2 - 2BD\cos\beta)\,\dot{\alpha}^2 + B^2\dot{\beta}^2 - 2(B^2 - BD\cos\beta)\dot{\alpha}\dot{\beta} + \frac{I_F}{2}(\dot{\alpha}^2 - \dot{\beta}^2) + \frac{M_A}{2}A^2\dot{\alpha}^2 + \frac{I_A}{2}\dot{\alpha}^2 \qquad B.10$$

A relationship is established between the real angle of attack and the speed of the device to extract maximum power out of the flow. The real angle of attack on the foil is:

$$\sigma = \beta - \alpha \qquad B.11$$

The instantaneous flow angle on the foil is:

$$\epsilon = \tan^{-1}\frac{W}{V} \qquad B.12$$

The virtual angle of attack on the foil is:

$$\gamma = \sigma - \epsilon \qquad B.13$$

In order to operate the foil at optimum angle of attack, the instantaneous angle of attack should be equal to half of the real angle of attack:

$$\epsilon = \frac{\sigma}{2} \qquad B.14$$

From the geometry of the device the relative speed of the foil can be written as follows:

$$W = \dot{\alpha}\, H \qquad B.15$$

The optimum speed of the device in order to capture maximum power from the flow:

$$\dot{\alpha} = \frac{v}{H}\, tan\, \frac{\sigma}{2} \qquad B.16$$

Also the optimum acceleration of the device can be expressed as follows:

$$\ddot{\alpha} = \frac{v}{H} cot\, \frac{\sigma}{2} - \frac{\dot{\alpha}^2}{2} \qquad B.17$$

In order to accommodate the process of putting over the foil into the model it is necessary to define conditions whereby the foil is either locked into place by the support mechanism at the extremes of the angle of attack range or free to rotate according to Newton's second law. The reason that the model is set up like this to be computational, easier to program and it prevents spikes in forces due to impulse loading messing up the

integration. As such, the device is modeled as if the foil is free to pitch until it hits a certain set angle, at which it is locked and pitch rate is then a function of the mechanical design of the device. At the end of the power stroke the angle of the foil is no longer locked to the mechanism and it is free to rotate under applied moments until reaching the opposite setting angle, where it is again locked into place. The foil reversal moment is applied at the end of the power stroke and is related to the total power generated through the stroke.The following are the steps describing the simulation of the device:

(a) The parameters specifying the geometry of the device is defined, setting the pitch of the foil relative to the foil support mechanism, given the values of the maximum angular displacement of the foil in two opposite directions. The additional parameters required are free stream velocity which is specified, time step length Δt of the foil geometry is taken to be smaller than the flow passing the foil, pivot of the foil, elastic axis of the foil, mass and inertia of the foil and arm.

(b) Initial conditions at *t=0* the angle is set at any angle less than the maximum set angle to start the device.

(c) The equation of motion of the device can be found by solving the matrix. The matrix is decoupled in order to find out the acceleration, velocity and position of the foil and the arm.

$$M_{11}\ddot{\alpha} + M_{12}\ddot{\beta} = N1$$

$$M_{21}\ddot{\alpha} + M_{22}\ddot{\beta} = N2$$

The time stepping equation can be written as below:

$$\dot{\alpha}_{new} = \dot{\alpha}_{old} + \Delta t\,\ddot{\alpha}$$

$$\dot{\beta}_{new} = \dot{\beta}_{old} + \Delta t \ddot{\beta}$$

$$\alpha_{new} = \alpha_{old} + \Delta t \, \dot{\alpha}_{old}$$

$$\beta_{new} = \beta_{old} + \Delta t \, \dot{\beta}_{old}$$

$$t_{new} = t_{old} + \Delta t$$

(d) In the simulation the effect of the vortices has been incorporated to make the simulation realistic and have a better understanding of the device performance. In addition the controller is set up so the optimum speed is maintained every instant to extract maximum power.

APPENDIX C PARK TRANSFORM

Generally Clarke and Park transforms are used in high performance drive (vector control) related to permanent magnet synchronous and induction machines. Through the use of the Clarke transform, the real (I_{ds}) and imaginary (I_{qs}) currents can be identified. The Park transform can be used to realize the transformation of the (I_{ds}) and the (I_{qs}) currents from the stationary to the moving reference frame and control the spatial relationship between the stator vector current and rotor flux vector. Fig. C.1 shows stator current in the *d-q* rotating reference frame and its relationship with the stationary reference frame *(a, b, c)*

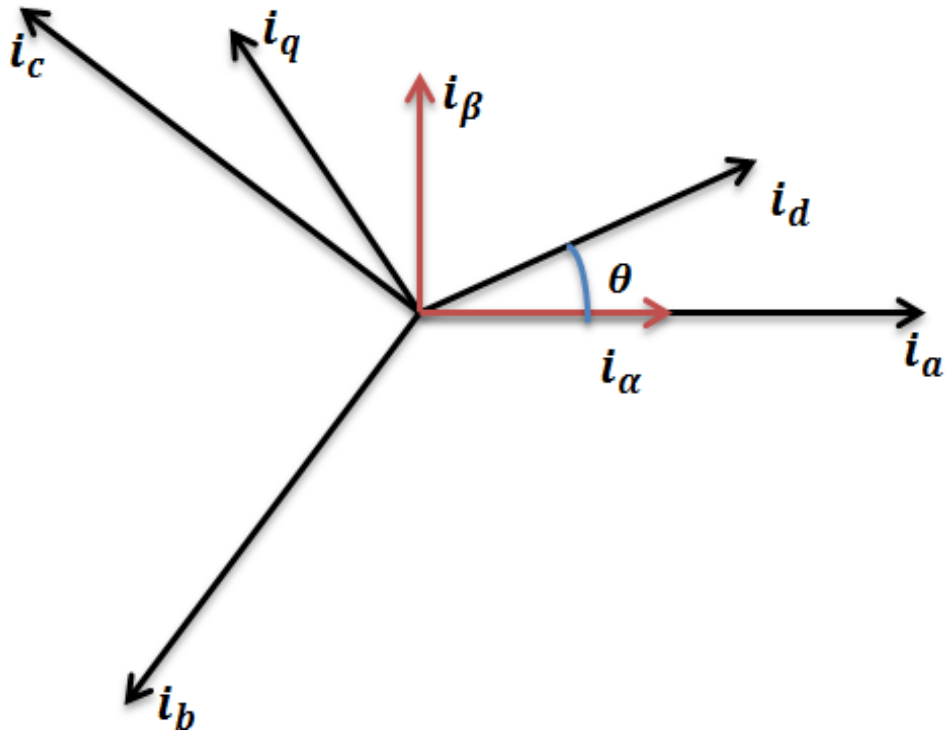

Fig. C.1 Stator current in the *d-q* rotating reference frame and its relationship with the stationary reference frame *(a, b, c)*

The Clarke Transform

The mathematical transformation called Clarke transform modifies a three-phase system to a two- phase orthogonal system.

$$i_\alpha = \frac{2}{3} i_a - (i_b - i_c) \qquad C.1$$

$$i_\beta = \frac{2}{\sqrt{3}} (i_b - i_c) \qquad C.2$$

$$i_o = \frac{2}{3} (i_a + i_b + i_c) \qquad C.3$$

The Park Transform

The two-phase α-β frame representation calculated with the Clarke transform is then fed to a vector rotation block where it is rotated over an angle θ to follow the frame d-q attached to the rotor flux. The rotation over an angle θ is done according to the formula.

APPENDIX D STATOR INTERIOR PERMANENT MAGNET GENERATOR

The fundamental characteristics of stator interior permanent magnet (SIPM) machine is split pole and full pitched winding [134]. The large torque capability makes it a potential candidate for low speed application. The flux density in air gap is high in SIPM. The peak flux density in air gap can be large and hence a large cogging torque is resulted. The flux switching technique can be adopted to overcome the cogging torque problem[134].

The proposed design includes a split type stator pole where laminated segments are used and permanent magnets (PM) are inserted into two stator segments teeth. The flux switching, the flux variation in a stator core can be described using Fig D.1. Fig D.1a shows that the rotor pole aligns with the stator segment tooth over which a winding is wound and the PM flux linked in this winding goes out of the rotor pole and into the stator segment tooth. When the rotor moves forward to align with the other stator segment tooth belonging to the same winding in Fig. D.2b, the PM flux linked in this winding goes out of the stator segment tooth and into the rotor pole. The flux switching can be achieving by adopting a symmetrical and unsymmetrical structure design where a smaller slot opening can be used [135].

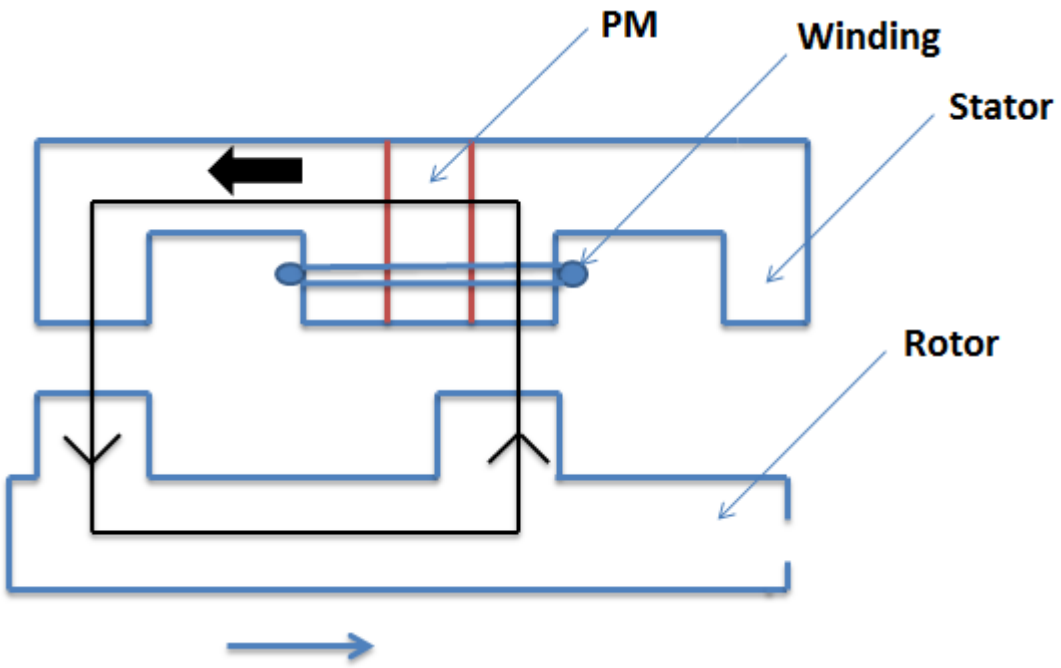

(a)

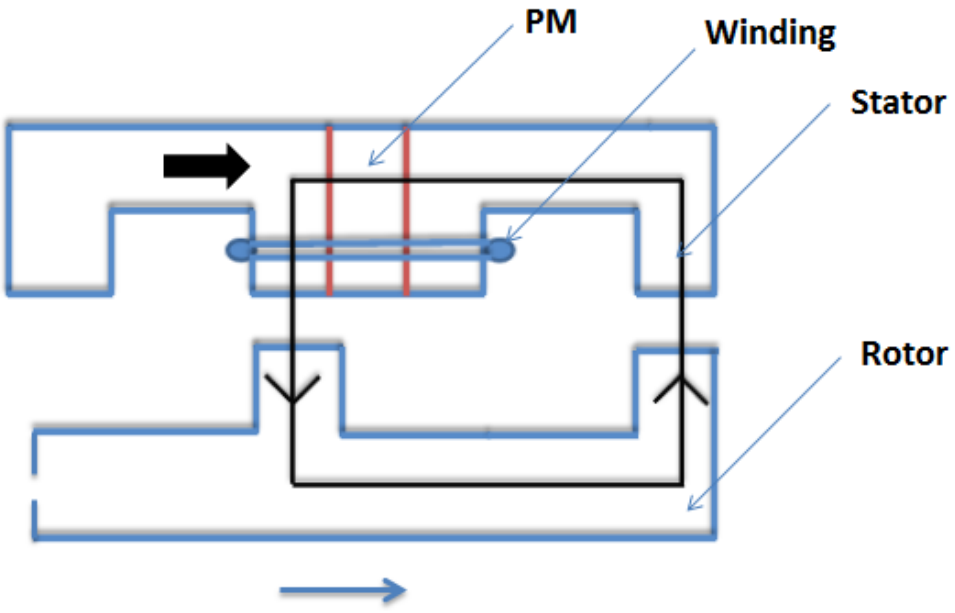

(b)

Fig. D.1 Flux switching Mode

A wide range of possible combinations among the phase numbers m, stator pole numbers p_s and rotor pole numbers p_r can be chosen for a SIPM machine design. For a single phase machine, the stator pole always has the same number as the rotor pole. For multiphase machine, the general relationship among p_s, p_r and m are given by

$$p_s = 4mk \qquad \text{D. 1}$$

$$p_r = (2m - \frac{1}{2}m)p_s \qquad \text{D. 2}$$

where k is a positive integer. Thus k = 1, m = 3 makes it a three phase 12/10-pole SIPM as shown in Fig. D.2.

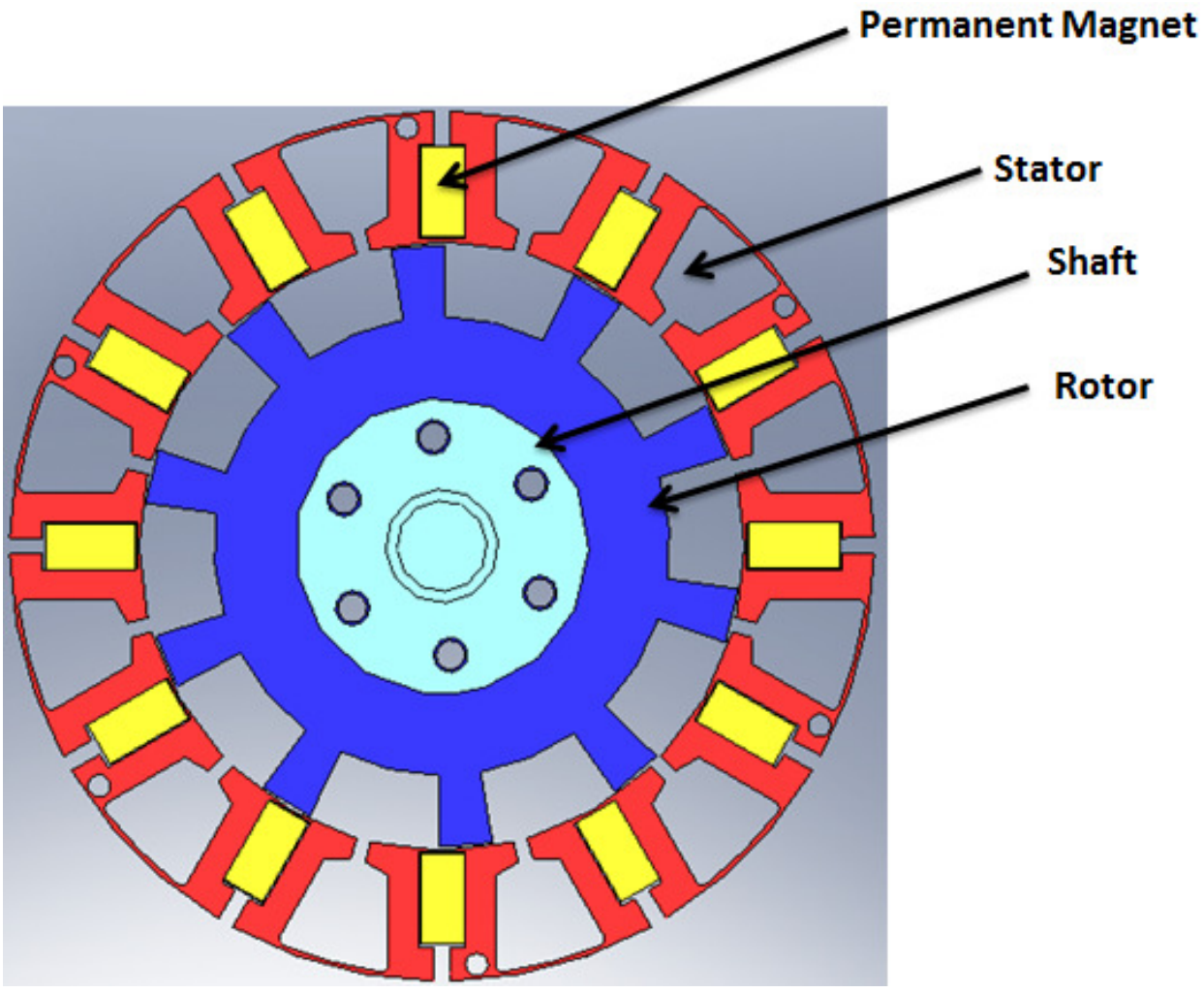

Fig.D.2 Cross-section of a 12/10-pole SIPM machine

When the rotor pole is fully aligned with stator segment tooth, the maximum flux linkage is linked by armature windings. This maximum flux linkage can be expressed as:

$$\varphi_m = k_d B_g \beta_s l_c \quad \text{D.3}$$

where B_g is the flux density in air gap when stator segment tooth and rotor pole is fully aligned, k_d is the flux leakage factor l_c is the stack length, β_s is the width of stator segment tooth. Therefore, the no-load voltage induced by flux linkage in a stator winding can be expressed as

$$E_p = \omega \frac{d\varphi}{dt} \quad \text{D.4}$$

$$E_p = \omega_r p_r k_m k_d B_g \beta_s l_c \quad \text{D.5}$$

where k_m is the waveform factor of the flux. The electrical power of the generator can be expressed as

$$P = m E_p I_P \quad \text{D.6}$$

$$P = m \omega_r p_r k_m k_d B_g \beta_s l_c I_P \quad \text{D.7}$$

The power is proportionally related with the product of air gap flux density B_g and stator tooth width β_s. The product of B_g and β_s is the maximum flux linkage in unit stack length when the stator segment tooth fully overlaps with a rotor pole. When the rotor angular velocity, phase current, winding turns and stack length of the SIPM machine are determined, the electrical power is identical if the product of B_g and β_s is kept as constant. This is one approach to diminish the cogging torque ripple can be carried out while keeping the SIPM machine at the same power capability [137].

Initial Sizing of Core Diameter and Stack Length

The sizing equation can be deduced as

$$D_{si}{}^2 l_c = \frac{P}{\left(\frac{0.87\pi^2}{120}\frac{p_r}{p_s}K_s K_d K_e K_i A_s B_\delta n_s\right)}$$

Generally the range of values of K_i, K_d and K_e are given below

K_i=*0.87,* K_d = 0.9~0.93, K_e =1.5~2.0

The value of A_s is generally kept within the range 10000~30000A/m. On the other hand, since the air gap flux density is usually the same as the tooth flux B_δ density is generally equal to 1.5T. Hence once the value of D_{si} is selected then the value of stack length l_c can be calculated. When the main dimensions are determined, the other structural dimensions, namely the stator outer diameter, pole heights and pole arcs can be specified.

Sizing of Permanent Magnets

When adopting neodymium–iron–boron (Nd–Fe–B) as the PM material the demagnetizing characteristic of PMs is almost linear. As shown in Fig. D.3, it gives

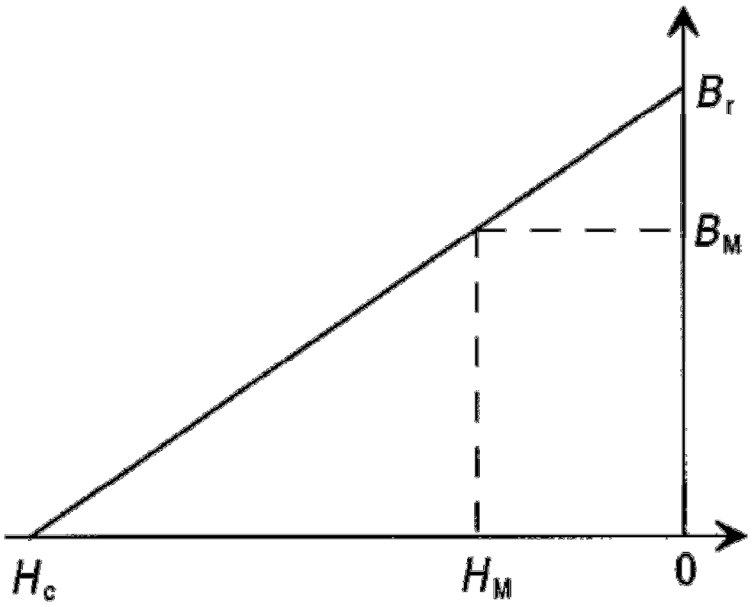

Fig.D.3 De-magnetizing characteristics of Permanent Magnet

$$B_M = B_r\left(1 - \frac{H_M}{H_C}\right) \quad \text{D.8}$$

$$H_M = H_r\left(1 - \frac{B_M}{B_r}\right) \quad \text{D.9}$$

where B_M and H_M are the flux density and field strength of PMs respectively at the operating point, while B_r and H_c are the remnant flux density and coercive force of PMs respectively. By applying Ampere's Law, it gives:

$$H_M h_{PM} = 2H_\delta g_o \quad \text{D.10}$$

Where H_δ is the field strength in air gap, and h_{PM} is the magnet thickness in the direction of magnetization.

$$h_{pm} = 2\frac{B_\delta g_o}{\mu_o H_c(1 - \frac{B_M}{B_r})} \quad \text{D.11}$$

Typically the value of $\frac{B_M}{B_r}$ = 0.7~0.95. The surface area S_{PM} of each PM is given below

$$S_{PM} = \frac{\varphi_m}{2}B_m = \sigma B_g \tau_S l_s \frac{\alpha_s}{2}B_M \quad \text{D.12}$$

where σ is the PM leakage factor. As the PM length l_{pm} in the axial direction is usually the same as the stack length, the PM width w_{pm} can be expressed as:

$$w_{pm} = \frac{S_{pm}}{l_{pm}} = \sigma B_g \tau_S \frac{\alpha_s}{2}B_M \quad \text{D.13}$$

Initial Calculation of Winding Turns

Number of winding turns per phase can be expressed as

$$\omega = \frac{30 p_s U \theta_\omega}{0.87\pi^3 K_d \alpha_s D_{si} l_c B_\delta} \quad \text{D.14}$$

Selection of Material

Generally low carbon steel is alloyed with small quantities of silicon to reduce eddy current losses in the core. These steels are available in an array of grades and thicknesses. Silicon steels are generally specified and selected on the basis of allowable core loss. The grades are addressed by increasing order of core loss by number M, such as M19, M27, M36 or M43. Each grade number specifying maximum core loss. The higher numbers means higher core losses and lower cost. The loss saved with each step down in performance is only few percent. Thinner laminations provides lower losses but is more expensive due to number of laminations required for a given stack height. The most common thicknesses are 0.014 in., 0.0185 in., and 0.025 in. In order to achieve the best performance, the laminations must be insulated from one another. The simplest way to do this is to specify a surface insulation on the raw material.

Fig D.4 shows a configuration of stator segment of SIPM machine. The stator segment tooth shoe expanded the width of stator segment tooth β_s. The magnets are inserted into the stator pole. The additional air gap can increase the anti-demagnetization performance of the machine. If the width at the middle of stator split pole does not change, the slot area will not vary and then the phase current can be seen as a constant while the current density is the same during optimization. There are three parameters, PM thickness l_m, and magnet length w_{pm} and slot gap width s to be optimized during the machine optimal design.

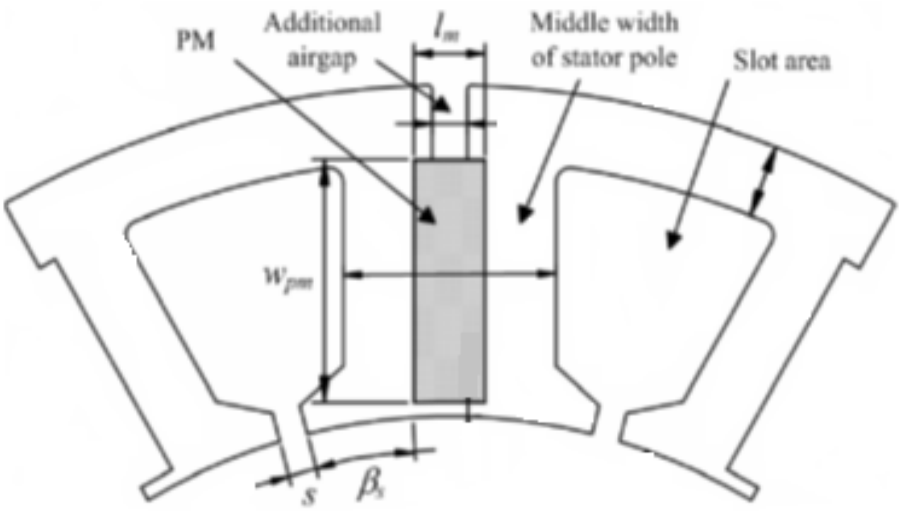

Fig.D.4 Configuration of stator segment[134]

The size of permanent magnet is determined at a particular point by the flux density in air gap and the width of stator segment tooth. The width of stator segment tooth can be expressed as

$$\beta_S = \frac{1}{2}(\tau_S - l_m - s) \qquad \text{D.15}$$

where τ_s is the stator pole pitch. For a given magnet thickness and slot gap width, the width of stator segment tooth β_s can be estimated using eq. D.15. It is recommended the cogging torque ripple decreases with small magnet thickness and the cogging torque does not drop significantly when the magnet thickness becomes smaller [134-136]. The stator and rotor are considered to be built up of laminated segments. As the PMs are embedded inside the stator pole, they have the advantages of anti-demagnetization performance and low induced eddy-current loss compared to surface mounted PMSG [134]. This is due to the fact that the magnets are not directly exposed to the reluctance variation of the salient rotor poles.

Table D.1 Design data of SIPM machine

Stack length	*76 mm*
Stator outer diameter	*130mm*
Stator inner diameter	*85mm*
PM thickness	*5mm*
PM length	*76mm*
Rotor pole arc	*10.42*
Slot gap width	*2mm*
Air gap length	*0.5mm*
Winding turns per phase	*280*

The schematic of the stator slots is shown in Fig D.5. The rotor of the generator has been shown in Fig D.6. A complete assembly of the SIPM generator consisting of magnets embedded in stator and rotor is shown in Fig D.7. One of the disadvantages of this design is that the current waveform is not sinusoidal. Also the manufacturing cost of this type of generator is expensive due to lamination and grade of cores. The design part needs to be revisited in future for further research.

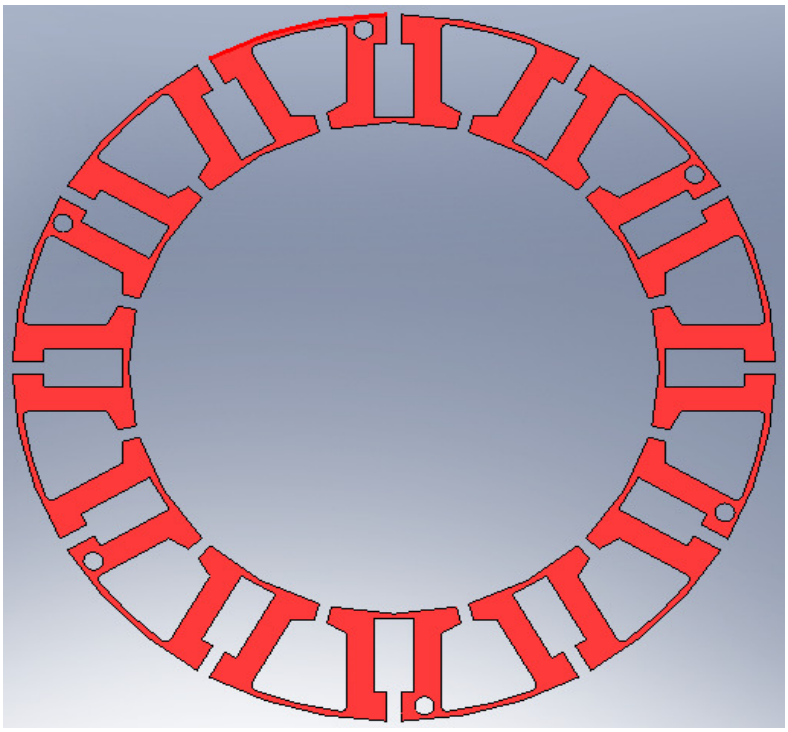

(a)

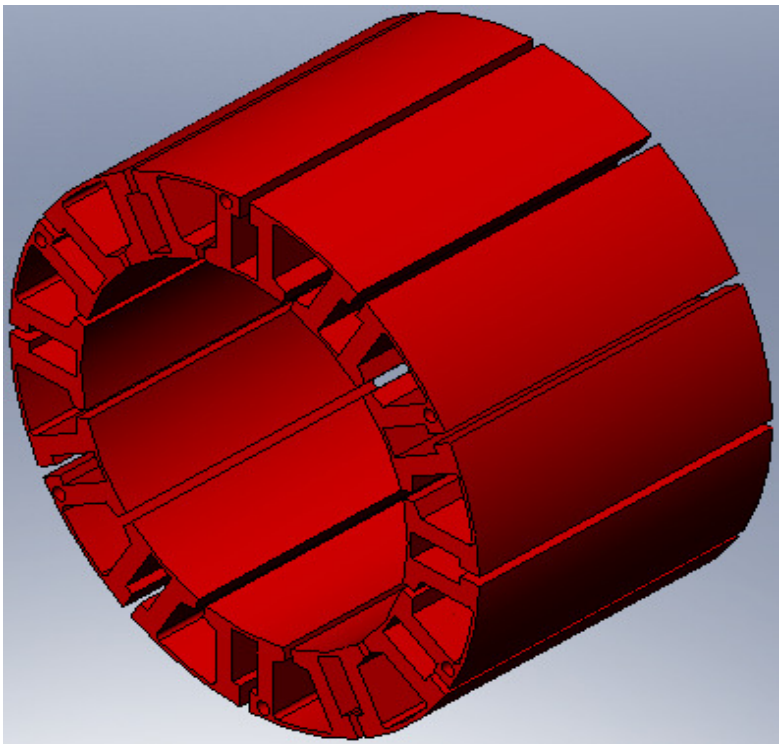

(b)

Fig D.5 SIPM Stator Slots

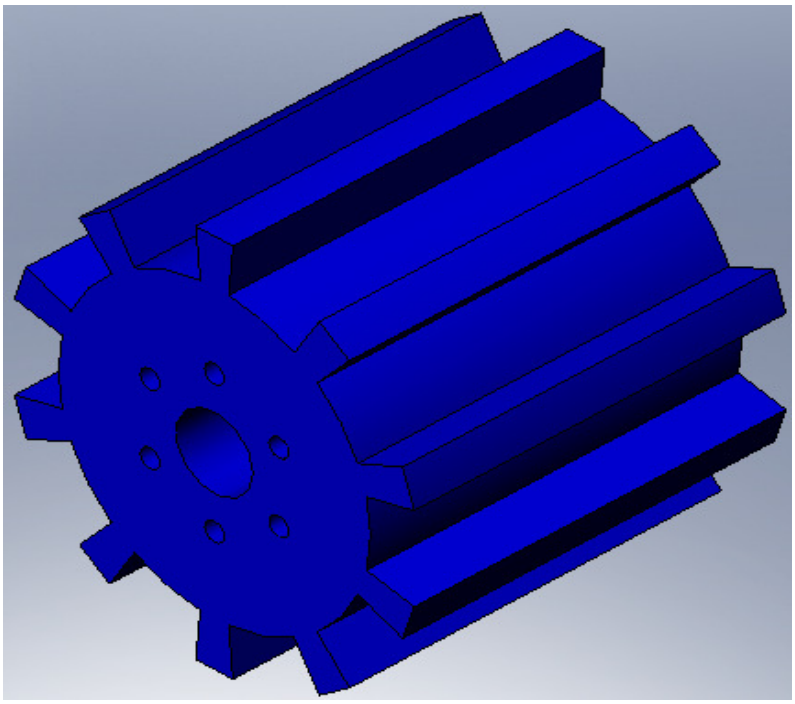

Fig D.6 Rotor of Generator

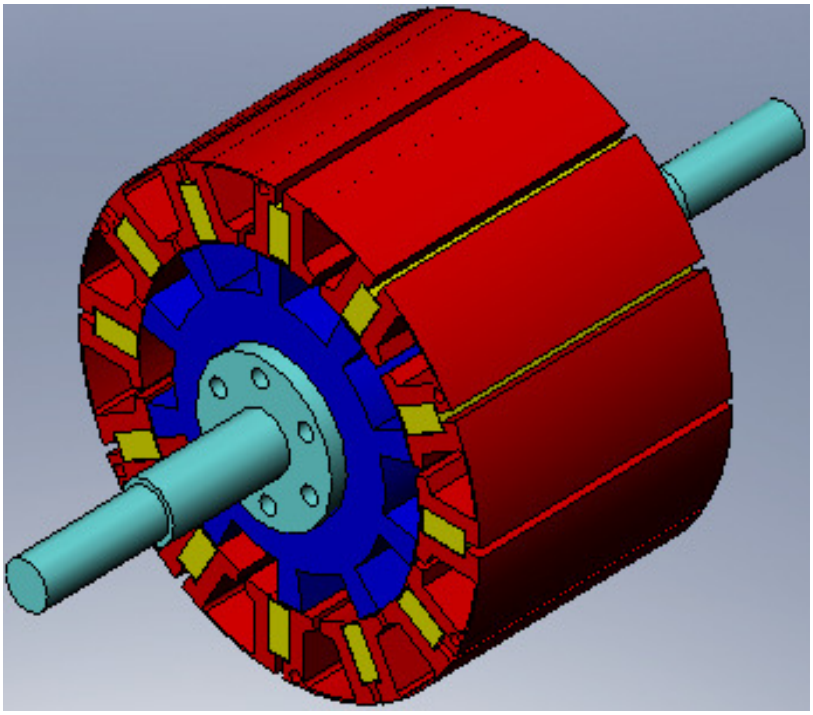

Fig D.7 Assembly of Stator and Rotor

APPENDIX E STRESS ANALYSIS

Aluminum has an Elastic Modulus around 70GPa, a Yield Strength or Failure Stress around 100MPa and a Poisson's ratio around 0.35. The chamber consists of an aluminum tube with two aluminum circular end caps. The tube has hoop or axial stresses and the end caps have in plane stresses. The tube can buckle under high enough pressure. Ignoring the end caps the hoop stress in the tube can be expressed as:

$$\sigma_H = \frac{Pr}{t} \qquad \text{D. 1}$$

where P is the pressure across the hull, r is the radius of the tube and t is the wall thickness of the tube. The axial stress can be expressed as:

$$\sigma_A = \frac{Pr}{2t} \qquad \text{D. 2}$$

The pressure across the hull can be calculated as:

$$P = \rho\, g\, h \qquad \text{D. 3}$$

where ρ is the density of water, g is the acceleration due to gravity and h is the depth of the hull below the water surface. For the hull h is 2m, r is 0.1m and t is 0.0125m. The calculated hoop and axial stress are 1.568 MPa and 0.784MPa respectively. The calculated stresses are well away from failure. Also the stress for support can be represented by the following expression:

For simple support

$$\sigma_S = 1.24\frac{Pr^2}{t^2} \qquad \text{D. 4}$$

Clamped support

$$\sigma_c = 0.75\frac{Pr^2}{t^2} \qquad \text{D. 5}$$

The calculated stress for simple and clamped support is 1.56 MPa and 0.94MPa respectively. Again, the calculated stresses are well away from failure. The critical pressure for buckling of a tube can be estimated roughly as:

$$P = 2.42\frac{E}{(1-\mu^2)^{\frac{3}{4}}} \times \left(\frac{t}{L}\right)^{\frac{5}{2}} \times \frac{1}{\left(\frac{L}{2r} - 0.45\left(\frac{t}{2r}\right)^{\frac{1}{2}}\right)} \qquad \text{D. 6}$$

where E is the Elastic Modulus, μ is the Poisson's Ratio and L is the tube length. Substitution into this gives a critical pressure 38MPa which is much larger than the test P.

APPENDIX E ADAPTIVE BACKSTEPPING CONTROL

The recursive backstepping design methodology is incorporated in adaptive control theory to formulate sequentially the feedback control law, the parameter adaptation law and the associated Lyapunov function for a class of nonlinear systems satisfying certain structured properties. In this article we will present the idea of adaptive backstepping design procedure for a class of nonlinear systems with unknown parameters. Consider

$$\dot{\hat{x}}_1 = x_2 + \theta\varphi(x_1) \qquad E.1$$

$$\dot{\hat{x}}_2 = u \qquad E.2$$

where θ is an known constant parameter.

Step 1

Let us first consider x_2 as a control input. Denoting $\hat{\theta}$ as the estimated value for the parameter θ and the estimation error $\theta - \hat{\theta}$ as $\tilde{\theta}$. Choosing the Lyapunov function candidate as follows:

$$V_1(x_1, \tilde{\theta}) = \frac{1}{2}{x_1}^2 + \frac{1}{2\gamma}\tilde{\theta}^2 \qquad E.3$$

It is easy to see that with the control law

$$x_2 = -k_1 x_1 - \hat{\theta}\varphi(x_1) \qquad E.4$$

$$\equiv \alpha_1(x_1, \hat{\theta})$$

The adaptation law can be expressed as:

$$\dot{\hat{\theta}} = \gamma\varphi(x_1)x_1$$

$$\equiv \gamma\tau_1 \qquad E.5$$

The derivative of the Lyapunov function candidate in eq. (E.3) is

$$\dot{V}_1 = -k_1 {x_1}^2 \leq 0 \qquad E.6$$

The function α_1 in eq. (E.4) is representing a stabilizing function for x_2, and τ_1 in eq. (E.5) is representing a tuning function.

Step 2

Since x_2 is not the control, we define the deviation of x_2 from the desired stabilizing function α_1 can be expressed as:

$$z = x_2 - \alpha_1(x_1, \hat{\theta}) \qquad E.7$$

This new error variable *z* declared in the system (E.1) can be rewritten as:

$$\dot{x_1} = -k_1 x_1 - \hat{\theta}\varphi(x_1) + z \qquad E.8$$

$$\dot{z} = \dot{x}_2 - \dot{\alpha}_1 = u - \dot{\alpha}_1 \qquad E.9$$

The derivative of the Lyapunov function V_1 can be expressed as:

$$\dot{V}_1 = x_1 \dot{x}_1 + \tilde{\theta}\dot{\tilde{\theta}}$$

$$= -k_1 {x_1}^2 + x_1 z + \tilde{\theta}(\tau_1 - \frac{1}{\gamma}\dot{\hat{\theta}}) \qquad E.10$$

Further, the dynamics of the error variable is

$$\dot{z} = \dot{x}_2 - \dot{\alpha}_1$$

$$= u - \frac{\partial \alpha_1}{\partial x_1}\left(x_2 + \theta\varphi(x_1)\right) - \frac{\partial \alpha_1}{\partial \hat{\theta}}\dot{\hat{\theta}}$$

$$= u - \frac{\partial \alpha_1}{\partial x_1}x_2 - \theta\frac{\partial \alpha_1}{\partial x_1}\varphi(x_1) - \frac{\partial \alpha_1}{\partial \hat{\theta}}\dot{\hat{\theta}}$$

$$= u - \frac{\partial \alpha_1}{\partial x_1}x_2 - \hat{\theta}\frac{\partial \alpha_1}{\partial x_1}\varphi(x_1) - \tilde{\theta}\frac{\partial \alpha_1}{\partial x_1}\varphi(x_1) - \frac{\partial \alpha_1}{\partial \hat{\theta}}\dot{\hat{\theta}} \qquad E.11$$

Augment the Lyapunov function by adding the error variable

$$V_2(x_1, z, \theta) = V_1\left(x_1, \tilde{\theta}\right) + \frac{1}{2}z^2 \qquad E.12$$

From eq. (E.9) and (E.11), the derivative of V_2 can be computed as:

$$\dot{V}_2 = \dot{V}_1 + z\dot{z}$$

$$= -k_1 {x_1}^2 + x_1 z + \tilde{\theta}\left(\tau_1 - \frac{1}{\gamma}\dot{\hat{\theta}}\right)$$

$$+z(u - \frac{\partial \alpha_1}{\partial x_1}x_2 - \hat{\theta}\frac{\partial \alpha_1}{\partial x_1}\varphi(x_1) - \tilde{\theta}\frac{\partial \alpha_1}{\partial x_1}\varphi(x_1) - \frac{\partial \alpha_1}{\partial \hat{\theta}}\dot{\hat{\theta}}) \qquad E.13$$

Grouping similar terms, we obtain

$$\dot{V}_2 = -k_1 {x_1}^2 + \tilde{\theta}\left(\tau_1 - \frac{\partial \alpha_1}{\partial x_1}\varphi(x_1)z - \frac{1}{\gamma}\dot{\hat{\theta}}\right)$$

$$+ z(u + x_1 - \frac{\partial \alpha_1}{\partial x_1}x_2 - \hat{\theta}\frac{\partial \alpha_1}{\partial x_1}\varphi(x_1) - \frac{\partial \alpha_1}{\partial \hat{\theta}}\dot{\hat{\theta}}) \qquad E.14$$

To make V_2 in (E.3) non positive, we can choose the control law

$$u = -k_2 z - x_1 + \frac{\partial \alpha_1}{\partial x_1}x_2 + \hat{\theta}\frac{\partial \alpha_1}{\partial x_1}\varphi(x_1) + \frac{\partial \alpha_1}{\partial \hat{\theta}}\dot{\hat{\theta}} \qquad E.15$$

The parameter adaptation law can be expressed as:

$$\dot{\hat{\theta}} = \gamma(\tau_1 - \frac{\partial \alpha_1}{\partial x_1}\varphi(x_1)z)$$

$$= \gamma(\varphi(x_1)z - \frac{\partial \alpha_1}{\partial x_1}\varphi(x_1)z) \qquad E.16$$

Therefore the derivative of V_2 becomes

$$\dot{V}_2 = k_1 {x_1}^2 + k_2 z^2 \leq 0 \qquad E.17$$

This implies that $x_1 \to 0$ and $z \to 0$ asymptotically.